Dissertation
submitted to the
Combined Faculties for the Natural Sciences and for Mathematics
of the Ruperto-Carola University of Heidelberg, Germany
for the degree of
Doctor of Natural Sciences

presented by

Dipl. Phys. Johann <u>Peter</u> Peiffer
born in   Bremen.

Oral examination: July 25, 2007

Liquid argon as active shielding and coolant for bare germanium detectors:

A novel background suppression method for the GERDA $0\nu\beta\beta$ experiment

Referees: Prof. Dr. Wolfgang Hampel

Prof. Dr. Wolfgang Krätschmer

Abstract

Two of the most important open questions in particle physics are whether neutrinos are their own anti-particles (Majorana particles) as required by most extensions of the Standard Model and the absolute values of the neutrino masses. The neutrinoless double beta ($0\nu\beta\beta$) decay, which can be investigated using ^{76}Ge (a double beta isotope), is the most sensitive probe for these properties. There is a claim for an evidence for the $0\nu\beta\beta$ decay in the Heidelberg-Moscow (HdM) ^{76}Ge experiment by a part of the HdM collaboration. The new ^{76}Ge experiment GERDA aims to check this claim within one year with 15 kg·y of statistics in Phase I at a background level of $\leq 10^{-2}$ events/(kg·keV·y) and to go to higher sensitivity with 100 kg·y of statistics in Phase II at a background level of $\leq 10^{-3}$ events/(kg·keV·y). In GERDA bare germanium semiconductor detectors (enriched in ^{76}Ge) will be operated in liquid argon (LAr). LAr serves as cryogenic coolant and as high purity shielding against external background. To reach the background level for Phase II, new methods are required to suppress the cosmogenic background of the diodes. The background from cosmogenically produced ^{60}Co is expected to be $\sim 2.5 \cdot 10^{-3}$ events/(kg·keV·y). LAr scintillates in UV (λ=128 nm) and a novel concept is to use this scintillation light as anti-coincidence signal for background suppression. In this work the efficiency of such a LAr scintillation veto was investigated for the first time. In a setup with 19 kg active LAr mass a suppression of a factor 3 has been achieved for ^{60}Co and a factor 17 for ^{232}Th around $Q_{\beta\beta}$=2039 keV. This suppression will further increase for a one ton active volume (factor $\mathcal{O}(100)$ for ^{232}Th and ^{60}Co). LAr scintillation can also be used as a powerful tool for background diagnostics. For this purpose a new, very stable and robust wavelength shifter/reflector combination for the light detection has been developed, leading to a photo electron (pe) yield of as much as 1.2 pe/keV. With this pe-yield a discrimination factor of $2 \cdot 10^6$ between γ-s and α-s and a factor $3 \cdot 10^3$ between γ-s and neutrons has been achieved by pulse shape analysis.

Zusammenfassung

Zwei der wichtigsten offenen Fragen in der Teilchenphysik sind die, ob Neutrinos ihre eigenen Antiteilchen sind, wie die meisten Erweiterungen des Standardmodells vorhersagen und was die absolute Masse der Neutrinos ist. Die höchste Sensitivität um dies zu untersuchen bietet der neutrinolose Doppelbetazerfall ($0\nu\beta\beta$) der mittels des $\beta\beta$ Isotops ^{76}Ge untersucht werden kann. Ein Teil der Kollaboration des ^{76}Ge Experiments Heidelberg-Moskau (HdM) hat eine Evidenz für die Entdeckung des $0\nu\beta\beta$-Zerfalls veröffentlicht. Das neue $0\nu\beta\beta$-Experiment GERDA wird ^{76}Ge-angereicherte Germaniumdetektoren in Flüssigargon (LAr) betreiben um diese Evidenz innerhalb eines Jahres (Phase I) mit 15 kg·y Statistik bei einem Untergrund von $\leq 10^{-2}$ cts/(kg·keV·y) zu überprüfen. Das LAr dient dabei als Kühlflüssigkeit und hochreine Abschirmung. Phase II wird mit 100 kg·y und einem Untergrund von $\leq 10^{-3}$ cts/(kg·keV·y) in höhere Sensitivitätsbereiche vorstoßen. Dafür sind neue Methoden zur Unterdrückung des kosmogenen Untergrunds der Dioden erforderlich, welcher für ^{60}Co $\sim 2.5 \cdot 10^{-3}$ cts/(kg·keV·y) beträgt. Flüssigargon ist ein Szintillator im UV Bereich (λ=128 nm) und ein neuartiges Konzept ist es, das Szintillationslicht als Anti-Koinzidenzsignal für die Untergrundunterdrückung zu nutzen. In dieser Arbeit wurde die Effizienz eines solchen Anti-Koinzidenz-Vetos mittels LAr-Szintillation erstmalig untersucht. Mit einem Testaufbau (aktive LAr Masse 19 kg) wurde ein Faktor 3 Unterdrückung für ^{60}Co und ein Faktor 17 für ^{232}Th im Bereich um $Q_{\beta\beta}$=2039 keV erreicht. Ein größeres aktives Volumen wird die Unterdrückung weiter verbessern (Faktor $\mathcal{O}(100)$ für 1t LAr für ^{232}Th und ^{60}Co). Darüber hinaus kann die LAr Szintillation zur Untergrunddiagnose eingesetzt werden. Dazu wurde eine neue, sehr stabile Wellenlängenschieber/Reflektor Kombination für den LAr-Szintillationslichtnachweis entwickelt, mit dem eine Lichtausbeute von 1.2 Photoelektronen pro keV erreicht wurde. Damit wurde durch Pulsformanalyse ein Diskriminationsfaktor von $2 \cdot 10^6$ zwischen α-s und γ-s und von $3 \cdot 10^3$ zwischen γ-s und Neutronen erreicht.

This work is dedicated to the memory of Dr. Burkhard Freudiger,
who taught me much about physics, life, the universe and everything.

Contents

List of Figures

List of Tables

Part I

Introduction

Chapter 1

Neutrino-physics

1.1 Neutrinos in the standard model of particle physics

In 1930 W. Pauli postulated a weakly interacting particle without electric charge to save the energy- and angular momentum conservation principle in the nuclear β-decay. This particle was later named 'neutrino' by E. Fermi. In 1956 F. Reines and C. Cowan succeeded in proving the existence of the neutrino experimentally. They used the induced reaction $p(\overline{\nu}, e^+)n$ to detect anti-neutrinos from a nuclear reactor [RC$^+$56].
In the Standard Model (SM) of particle physics, neutrinos are postulated as massless, point-like Dirac particles. Together with an associated charged lepton, they form a weak, left-handed isospin doublet. There are three known lepton families (e, μ, τ) and three corresponding neutrino flavours have been established. Also the analysis of the decay of the Z-boson [G$^+$00] proves that there are 3.00±0.06 weakly interacting light neutrino-flavours.

1.2 Neutrino detection

Since neutrinos participate only in the weak interaction (with cross sections as small as $(10^{-43} - 10^{-46})$ cm^2 [BKS95]) their detection is a challenging task that imposes two requirements on neutrino-experiments. First a large target mass is needed to balance the low cross sections for neutrino interactions at energies appearing in nuclear processes (order of magnitude 10 MeV and below). Second, a good background reduction is needed, since the background from other sources tends to be orders of magnitude higher than the signal produced by the neutrinos. All solar neutrino experiments and most other neutrino-related experiments are therefore situated in deep underground sites, to shield them from cosmic radiation.

1.2.1 Neutrino interaction channels

Neutrinos can interact with nuclei or with electrons and each interaction can occur via the charged or the neutral current of the weak interaction. The charged current reaction on a suitable nucleus is the inverse electron capture. This process was first proposed by B. Pontecorvo [Pon46] for the electron neutrino. The reaction is:

$$\nu_e + {}^A_Z X \rightarrow {}^A_{Z+1} Y + e^-$$

It can be written more generally for all neutrino flavours as:

$$\nu_l + {}^A_Z X \rightarrow {}^A_{Z+1} Y + l^-$$

where l stands for the lepton flavour and can be e, μ or τ. The neutral current interaction on nuclei leads to the excitation of the nucleus:

$$\nu_l + {}^A_Z X \to \nu_l + {}^A_Z X^*$$

In some cases this process may also lead to the fracture of the exited nucleus.

The interaction with electrons can either take the form of elastic scattering via the neutral current

$$\nu_l + e^- \to \nu_l + e^-$$

or, for high energy neutrinos, the form of interaction via the charged current:

$$\nu_l + e^- \to \nu_e + l^-$$

.

1.2.2 Detection methods

There are several possible types of detectors capable of detecting the various types of neutrino interaction.

Radio-chemical detectors

Historically, the first electron-neutrino detectors that were realised made use of the inverse electron capture. As target nuclei were chosen whose daughter nuclei ${}^A_{Z+1}Y$ are radioactive and have a half life of days or months. This allows the detection of the produced daughter nuclei via their decay, after their chemical separation from the target material. The need to separate few atoms of the daughter nucleus from the large target mass lead to the development of new, few-atom-chemistry techniques. Radiochemical detectors have the advantage of having comparatively low energy thresholds, depending on the target nucleus. However they measure only an integral neutrino flux over the time between two extractions of daughter nuclei. Examples of radio-chemical detectors are the Homestake chlorine experiment [DHH68], GALLEX [GAL99], SAGE [SAG99] and GNO [GNO00].

Cerenkov detectors

For neutrinos with energies in the MeV range or higher, the electrons scattered in neutrino-electron interactions are relativistic. When the speed of a charged particle, in this case the scattered electron, exceeds the local speed of light in the surrounding medium, the particle emits Cerenkov-radiation. This process was first observed by P. Cerenkov in 1934 [Cer37] and described mathematically by Frank and Tamm in 1937 [TF37]. The Cerenkov-light is emitted in a forward cone with an opening angle that depends on the speed of the particle and the refractive index of the medium. Using a medium that is transparent to it's own Cerenkov-light (e.g. water or ice) this process can be used to detect neutrinos on an event-by-event basis. The directional information is also retained within the limits imposed by the Cerenkov-angle. However, due to natural background in the energy range of a few MeV the effective energy-threshold is higher than it is for radio-chemical detectors. Examples of Cerenkov-detectors are Kamiokande [H+89], its successor Super-Kamiokande [F+01] and the Sudbury Neutrino Observatory SNO [AAB+04].

Scintillation detectors

A second possibility of real time neutrino-detection is the use of a scintillator as target. This has the advantage that the light-yield in scintillators is about 2 orders of magnitude higher than it is in Cerenkov-detectors. This leads to a better energy resolution and an improved signal-to-noise ratio, effectively lowering the energy threshold. However the directional information is not retained. Scintillation detectors are always sensitive to neutrino-electron scattering (e.g. Borexino [Bor02]) but with a suitable choice of a target nucleus they can also be sensitive to the charged-current interaction on nuclei (e.g. LENS-project [Mot04]). A real-time detection of the neutrinos is possible if either the half-life of the daughter nucleus is short compared to the time-constants of the light detection or if, as in the case of LENS, the interaction leads to the creation of an excited isomer that de-excites over intermediate states with characteristic time constants. This time correlation between the γ-s from the de-excitation of these nuclear states can be used as signature for the detection of a neutrino.

1.3 Neutrino physics beyond the standard model

1.3.1 The historical 'neutrino problems' and neutrino oscillations

When in 1970 the first solar neutrino experiment, the pioneering Homestake Chlorine Detector of Ray Davis [DHH68], started data taking, it became soon apparent that the neutrino-flux measured was only about 1/3 of that expected from the standard solar model (SSM). As SSM the model from [BP04] is taken. With increasing statistics the evidence for a deficit in the solar neutrino-flux became stronger. The Homestake final result [C⁺98] is a neutrino capture rate of: $R_\nu^{Cl} = 2.56 \pm 0.16(sys) \pm 0.16(stat)$ solar neutrino units (SNU), compared to $R_\nu^{Cl} = 7.6^{+1.3}_{-1.1}$ SNU expected from the SSM. 1 SNU is defined as 10^{-36} neutrino captures per target atom per second.

This discrepancy was named the 'solar neutrino problem'. The solution for this problem was at the time sought mostly in uncertainties of the SSM. Since the high energy ^{8}B neutrino flux depends strongly on the core temperature of the sun, a slight deviation of the actual core temperature from that predicted in the SSM might explain the solar neutrino deficit.

However, the subsequent solar neutrino experiments not only confirmed the solar neutrino problem, but also gave rise to more apparent discrepancies. The first real time solar neutrino detector, Kamiokande, observed a deficit as well. However, the deficit was lower: $\Phi_\nu^{Kam} = (2.82^{+0.25}_{-0.24} \pm 0.27) \cdot 10^6 cm^{-2}s^{-1}$ [FHI⁺96]. This is about 1/2 of the flux expected from SSM. If an incorrect calculation of the ^{8}B neutrino flux was the source of the discrepancy, Kamiokande, with a threshold of $\sim$7.5 MeV, should have been more strongly affected than Homestake, which had an energy threshold of 814 keV. So there was not only a discrepancy between the measured flux and the calculated flux, but there appeared also to be a discrepancy between the different solar neutrino experiments. This was named the 'second solar neutrino problem'.

Kamiokande also observed a deficit in the atmospheric neutrino flux, which can be calculated from the measured cosmic ray flux. This deficit was also observed by other experiments (MACRO and Soudan-2 [Gal05], IMB [BSBC⁺92]) and was named the 'atmospheric neutrino problem'.

The first detection of low energy solar pp-neutrinos was successfully done in the gallium experiments GALLEX [GAL99], its successor GNO [GNO00] and SAGE [SAG99]. The pp-neutrinos are the main contribution to the total solar neutrino flux since the pp-cycle is responsible for $\sim$98.5% of the solar energy production [BP04]. The GALLEX/GNO result is: $R_\nu^{Ga} = 69.3 \pm 5.5$ SNU (1σ) [ABB⁺05] and the SAGE result is: $R_\nu^{Ga} = 69.2^{+4.3}_{-4.2}(stat.)^{+3.8}_{-3.4}(sys.)$ SNU

[SAG02]. The SSM prediction is: $R_\nu^{Ga} = 128^{+9}_{-7}$ SNU. This deficit could not be explained by any slight variations of the solar model, unless the ^{7}Be neutrino flux was assumed to be zero. This, however, would be in contradiction with the previous experiments, since the neutrino flux detected by them proved the existence of the ^{8}B neutrinos and the production of ^{8}B in the solar fusion cycle requires the production of ^{7}Be. Also a reduction of the pp-neutrino flux could be excluded as explanation for the deficit observed, since any reduction of the pp-fusion large enough to explain the deficit would also lead to a lower energy production in the sun than that observed.

The SSM was also strengthened by another type of experiments. The helio-seismology experiments, both ground based and satellite based, measured the propagation of pressure waves and thereby the speed of sound in the sun. From that it is possible to calculate the pressure and temperature distribution in the sun and all results were in good agreement with the SSM [BPB01].

With an astrophysical explanation becoming strongly disfavoured and experimental errors becoming more and more unlikely, a different explanation which had already been proposed earlier came into focus. The favoured theory was now that a part of the electron-neutrinos 'disappears' by flavour oscillations. All solar neutrino experiments were either only sensitive to electron neutrinos or had at least a significantly higher sensitivity to electron neutrinos than to the other flavours. If the neutrinos underwent partial flavour transition between source and detection, all of the 'neutrino problems' would become explicable, since the flavour transition would in general be energy dependent. This process could therefore account for the 'missing' electron neutrinos and for the difference between the deficits at different energies.

1.3.2 Neutrino mixing and masses

The theory of flavour oscillations proposed as a solution of the historical neutrino problems requires the neutrino flavour eigenstates to be different from the mass eigenstates. This is possible if the neutrinos have a non-vanishing rest mass. This theory was proposed in 1957 by B. Pontecorvo [Pon57]. In analogy to the quark mixing, the flavour eigenstates become a linear superposition of the mass eigenstates: $|\nu_l\rangle = \sum_i U_{li}|\nu_i\rangle$ where $|\nu_l\rangle$ are the flavour eigenstates ($l = e, \mu, \tau$), $|\nu_i\rangle$ are the mass eigenstates ($i = 1, 2, 3$) and U_{li} is the unitary Pontecorvo-Maki-Nakagawa-Sakata (PMNS) mixing matrix [MNS62]. For massive dirac neutrinos the PMNS matrix has the form:

$$U^D = \begin{pmatrix} c_{12}c_{13} & s_{12}c_{13} & s_{13}e^{-i\delta} \\ -s_{12}c_{23} - c_{12}s_{23}s_{13}e^{i\delta} & c_{12}c_{23} - s_{12}s_{23}s_{13}e^{i\delta} & s_{23}c_{13} \\ s_{12}s_{23} - c_{12}c_{23}s_{13}e^{i\delta} & -c_{12}s_{23} - s_{12}c_{23}s_{13}e^{i\delta} & c_{23}c_{13} \end{pmatrix}$$

where $s_{ij} = \sin\Theta_{ij}$ and $c_{ij} = \cos\Theta_{ij}$ with $\Theta_{ij}(i < j)$ the neutrino mixing angles and δ is the CP-violating phase.

This form of the neutrino equation of state is valid for the case of pure vacuum oscillation. When neutrinos propagate through matter the oscillation probability can be enhanced. The reason is the following: while all flavours can interact with the electrons in matter via the neutral current, only electron neutrinos can interact via the charged current (at energies below the muon rest mass of 106 MeV). These interactions create an effective additional potential and significantly change the equation of propagation. This effect is known as the MSW (Mikheyev, Smirnov, Wolfenstein) effect and is described in detail in the original papers [Wol78] and [MS85].

The neutrino oscillation hypothesis has been proven. The analysis of the atmospheric neutrino data of the Super-Kamiokande experiment showed an asymmetry between downward

atmospheric neutrinos and upward atmospheric neutrinos that had passed through the earth [FHI$^+$99, AHI$^+$05]. This asymmetry, as well as the general atmospheric neutrino deficit, can be best explained by neutrino oscillations. Other strong evidence for neutrino oscillations came from the solar neutrino experiment SNO, the reactor neutrino experiment KamLAND and the accelerator experiment K2K.

The SNO is capable of measuring both the solar electron neutrino flux via the charged current interaction and the total solar neutrino flux via the neutral current interaction. In the electron neutrino flux a deficit was measured, while the total neutrino flux agreed with the expectations from the SSM [AAB$^+$04]. This means that the 'disappeared' electron neutrinos are detected as neutrinos of another flavour and is therefore a proof for the neutrino oscillation theory. An analysis of the day/night asymmetry in the solar neutrino flux [AAA$^+$02] supports the MSW solution. The best fit of the data is given by a model assuming a matter-enhanced oscillation when the neutrinos pass through the earth at night.

KamLAND measured a flux of anti-neutrinos from nearby nuclear reactors. The production rates of neutrinos in the reactors is well known and the measured flux was lower than the flux calculated without neutrino oscillations by a factor of 0.658 ± 0.044(stat)± 0.047(syst) [AEE$^+$05]. This shows a $\overline{\nu}_e$-disappearance and is a proof of anti-neutrino oscillations. The best-fitting model again includes the MSW effect. Similarly, K2K was able to show a ν_μ disappearance over a baseline of 250 km [AAA$^+$05]. The measured neutrino flux was a factor $0.709^{+0.056}_{-0.047}$ lower than the flux calculated without neutrino oscillations.

These results combined with a global analysis of all solar neutrino data leave only the so called Large Mixing Angle (LMA) solution for the neutrino oscillation [AEE$^+$05]. With this solution and the results from the atmospheric neutrino data some of the parameters of the PMNS matrix are known. The squared mass differences, $\Delta m_{ij}^2 = |m_i^2 - m_j^2|$ $(i < j)$, are:

$$\Delta m_{sol}^2 \equiv \Delta m_{12}^2 = (7.9^{+0.6}_{-0.5}) \cdot 10^{-5} \text{ eV}^2 \text{ ([AEE}^+05])$$

$$\text{and}$$

$$\Delta m_{atm}^2 \equiv \left| \Delta m_{23}^2 \right| = (2.1^{+1.3}_{-0.6}) \cdot 10^{-3} \text{ eV}^2 \text{ ([AHI}^+05]).$$

The errors given are the 90% C.L. ranges. Two of the mixing angles are also known:

$$tan^2 \Theta_{12} = 0.40^{+0.10}_{-0.07} \text{ (90\% C.L.) [AEE}^+05]$$

$$\text{which corresponds to}$$

$$\sin^2 2\Theta_{12} = 0.82 \pm 0.07$$

$$\text{and}$$

$$sin^2 2\Theta_{23} = 1.00^{+0}_{-0.08} \text{ (90\%C.L.)[AHI}^+05]$$

For the third mixing angle, Θ_{13}, there is only an upper limit from the CHOOZ experiment [AB$^+$03]:

$$sin^2 2\Theta_{13} \leq 0.16 \text{ (90\% C.L.)}$$

for $\Delta m_{31}^2 = 2 \cdot 10^{-3} \text{ eV}^2$.

The CP-violating phase δ remains unknown. Also unknown is the absolute mass scale of the neutrinos and the mass hierarchy. For the mass hierarchy there are three possible scenarios: the normal hierarchy $m_1 < m_2 < m_3$, the inverted hierarchy $m_3 < m_1 < m_2$ and, as a special case of

both, the degenerate mass scale, where the lightest neutrino mass is large compared to the mass differences. Since neutrino oscillations are only sensitive to the mass differences but not to the absolute neutrino mass scale, oscillation experiments cannot determine the absolute neutrino mass. For the lightest neutrino mass, which determines the mass scale, there are upper bounds. Direct searches, the Mainz [K$^+$05] and Troisk [Lob02] tritium-β-decay experiments, give an upper limit of $m_0 \leq 2.3$ eV. From the cosmological matter power spectrum an upper limit on the sum of neutrino masses can be deduced: $\sum_i m_i \leq (0.5 - 1.7)$ eV [BHH$^+$03, SVP$^+$03, FLM$^+$04].

Beyond the oscillation parameters cited above, there was a result from the LSND experiment that was consistent with a $\overline{\nu}_\mu \rightarrow \overline{\nu}_e$ oscillation with a Δm^2 at the $\mathcal{O}(1$ eV$)$ scale [AAB$^+$01]. A possible explanation for this observation, if it was confirmed, would have been the existence of a fourth, sterile neutrino flavour. Recently, however, the MiniBooNE experiment which was built to check the LSND result could exclude this oscillation scenario at a C.L. of 98% [Min07].

1.3.3 Neutrinos as Majorana particles

An important question that is yet unanswered is, whether the neutrinos are Dirac or Majorana particles. If the neutrinos are Majorana particles they satisfy the Majorana condition $\nu_i^c = \nu_i$ where $\nu_i^c = C\overline{\nu}_i^T$ is the charge conjugate with the charge conjugation matrix C. The neutrino mixing matrix then takes the form [BHP80]: $U = U^D S(\alpha)$. U^D is the PMNS matrix and $S(\alpha)$ is a diagonal phase matrix, characterised by two Majorana CP-violating phases. It can be written in the form: $S_{ik} = e^{i\alpha_i}\delta_{ik}$ with $\alpha_3 = 0$. The Majorana nature is predicted by several important extensions of the Standard Model of particle physics. In particular it is required by most See-Saw models, that could explain the smallness of the neutrino mass [MS80]. A Majorana nature of the neutrino would also allow an explanation of the baryon asymmetry of the universe [BPY05].

Neutrino oscillation experiments cannot determine the Majorana or Dirac nature of neutrinos. In order to test the Majorana nature of the neutrino it is necessary to investigate processes that violate the total lepton number conservation. Since Majorana particles are invariant under charge conjugation, the only distinguishing quantum number between ν and $\overline{\nu}$ for Majorana neutrinos would be the helicity. For massive particles the helicity is not a 'good' quantum number, since it is only conserved for particles moving at the speed of light. For massive Majorana neutrinos, processes that violate the total lepton number conservation by 2 are therefore possible. Such processes would be a good probe of the absolute mass scale of the neutrino, since the extent to which the helicity conservation is violated depends on (m/E), the mass over the energy the particle. Or put in different words: it depends on the amount by which the speed of the neutrino differs from the speed of light.

1.4 The neutrino-less double beta decay

In some even-even nucleus configurations that are not the energetically ideal isobar for their number of nucleons, the normal β-decay is forbidden because the neighbouring uneven-uneven isobars have less binding energy, i.e. more mass (see figure 1.1).

In such cases the double-β-decay is still possible. The 2-neutrino double-β-decay $(2\nu\beta\beta)$,

$$(A, Z) \rightarrow (A, Z + 2) + 2e^- + 2\overline{\nu}_e$$

is well studied and has been detected for 10 isotopes (^{48}Ca, ^{76}Ge, ^{82}Se, ^{96}Zr, ^{100}Mo, ^{116}Cd, ^{128}Te, ^{130}Te, ^{150}Nd, ^{238}U). For ^{136}Xe, which is another double-β-decay candidate up to now only a lower limit on the half-life could be deduced. The $2\nu\beta\beta$-decay is the independent, simultaneous β-decay of two independent nucleons in the nucleus. Figure 1.2 shows the Feynman diagram of
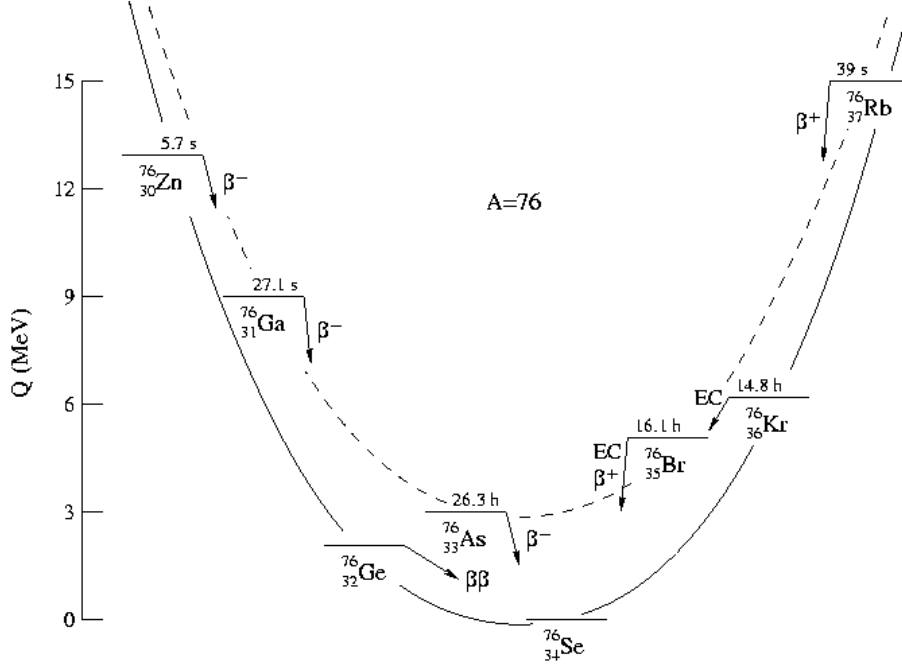
Figure 1.1: The relative mass for the different isobars at A=76. ^{76}Ge cannot decay by single-β-decay, but double-β-decay to ^{76}Se is possible.

the double β^- decay process. Equivalent processes in other isotopes are the double β^+-decay ($2\nu\beta^+\beta^+$) and the double electron capture ($2\nu ECEC$). The half-lives for this process range from $T_{1/2} = (7.7 \pm 0.7(\text{stat}) \pm 0.8(\text{syst})) \cdot 10^{18}$y for ^{150}Nd [Bar05] to $T_{1/2} = (7.2 \pm 0.3) \cdot 10^{24}$y for ^{128}Te [CBC$^+$93]. The half life of the $2\nu\beta\beta$ decay of ^{76}Ge is $T_{1/2} = (1.3 \pm 0.1) \cdot 10^{21}$ y [EV02].

If the neutrino is a massive Majorana particle, a different decay process is possible. The right-handed (anti-)neutrino emitted in one vertex of the decay can then be absorbed as left-handed neutrino at the second vertex, leading to an inverse electron capture. This is the so called zero neutrino double beta decay ($0\nu\beta\beta$-decay), which is a process that violates the lepton number conservation by 2. The Feynman diagram is shown in figure 1.3. The process balance is:

$$(A, Z) \to (A, Z + 2) + 2e^-.$$

For suitable nuclei the $0\nu\beta^+\beta^+$ decay and $0\nu ECEC$ processes are possible as well and there may be different double beta decay modes, like the decay under emission of a non-neutrino majoron [FS98].

The $0\nu\beta\beta$ decay is a very sensitive probe for the effective Majorana neutrino mass, $m_{\beta\beta} = \sum_i U_{ei}^2 m_i$, of the neutrino. The half life of the process depends quadratically on $m_{\beta\beta}$ [EV02]:

$$\frac{1}{T_{1/2}^{0\nu}(A, Z)} = |m_{\beta\beta}|^2 |M^{0\nu}(A, Z)|^2 G^{0\nu}(E_0, Z)$$

Here $M^{0\nu}(A, Z)$ is the nuclear matrix element (NME) and $G^{0\nu}(E_0, Z)$ is the known, energy dependent phase space integral, depending on the energy release E_0. The NME only depends on the properties of the nucleus. However, depending on the model used, there are different predictions for the value of the NME.

A detection of the $0\nu\beta\beta$-decay would not only prove the Majorana-nature of the neutrino, but would also set the mass scale of the neutrinos by determining the effective Majorana neu-
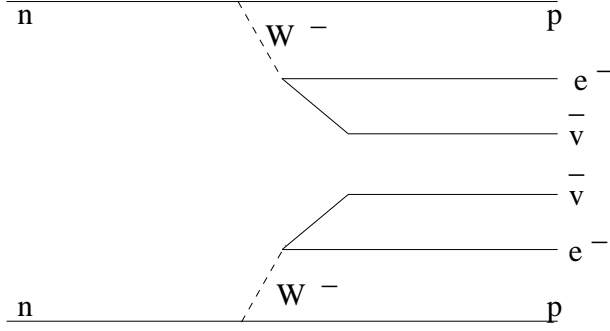
Figure 1.2: The Feynman graph for the $2\nu\beta\beta$-decay.
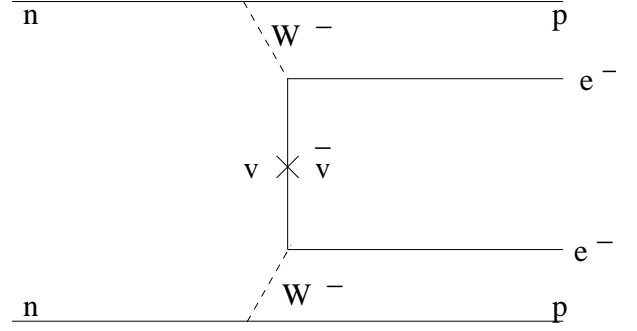
Figure 1.3: The Feynman graph for the $0\nu\beta\beta$-decay under exchange of a massive Majorana neutrino.

trino mass. Thereby it would decide the neutrino mass hierarchy. There is a claim of a 4.2σ evidence for a detection of the $0\nu\beta\beta$ decay of ^{76}Ge by a part of the Heidelberg-Moscow (HdM) collaboration [KKKC04]. However, these results are still under debate ([BBB$^+$05]) and need to be checked by an independent experiment. Apart from this claim the Heidelberg-Moscow experiment established the most stringent lower bound on the half life for the $0\nu\beta\beta$-decay of ^{76}Ge.

$$T_{1/2}^{0\nu}(^{76}\text{Ge}) \geq 1.9 \cdot 10^{25} \text{ years. (90\% C.L.) [KKDB}^+01]$$

Using the NME from [RFSV03] this translates to a upper bound on the effective Majorana neutrino mass of:

$$|m_{\beta\beta}| \leq 0.55 \text{ eV (90\% C.L. [BFGS05]).}$$

Chapter 2

GERDA

2.1 Motivation

As discussed above (in section 1.3.3) the fundamental question whether the neutrino is a Majorana particle, as most extensions of the standard model assume, is one of the 'hot topics' in particle physics. The most sensitive probe to investigate the Majorana nature of the massive neutrino is the $0\nu\beta\beta$-decay. If this lepton-number violating process is detected, the Majorana nature of the neutrino is proven.

One of the most promising $\beta\beta$-isotopes for the detection of the $0\nu\beta\beta$-decay is ^{76}Ge. There are several advantages in using germanium. One important advantage is, that the detector can be made out of the source material: germanium has been successfully enriched from the natural concentration of 7% ^{76}Ge to 85% in the past and industrial capabilities for the enrichment to 88% are available. A second advantage is, that there is a considerable experience with high purity germanium (HP-Ge) semi-conductor detectors and that there are various powerful methods of background rejection which will be discussed in section 2.3. Another advantage is that germanium diodes can be produced with very high purity levels and another one is the excellent energy resolution of germanium detectors of $\sim$3.3 keV at $Q_{\beta\beta}$=2039 keV. This Q-value of the $\beta\beta$ decay in ^{76}Ge, while not being the highest Q-value observed in $\beta\beta$-isotopes, has the advantage that it falls into a region where no significant contribution from full energy deposition lines from γ-s is expected. This facilitates the background suppression considerably (see below for details). Another advantage is the comparatively high density of 5.3 g/cm^2 of Ge which allows for a high target mass with a low surface area. For better clearness the advantages of ^{76}Ge are summarised in a list below:

- Germanium can be source and detector at the same time.

- Enrichment to 88% ^{76}Ge possible

- Favourable $Q_{\beta\beta}$ value of 2039 keV.

- HP-Ge-detector technology is well established.

- Intrinsic high purity.

- Powerful methods of background suppression possible.

- High density allows for a compact target with high mass.

The most stringent bound on the effective Majorana neutrino mass comes from the ^{76}Ge experiment HdM which was situated at the Gran Sasso laboratory in Italy (LNGS - Laboratori Nationale di Gran Sasso). From the same experiment, albeit only by a part of the collaboration, comes the only claim of a positive signal for the $0\nu\beta\beta$-decay so far. To check this claim and/or go beyond the limits set by the HdM experiment independent of nuclear matrix element (NME) uncertainties a new experiment using the same isotope is necessary, with an improved sensitivity. The parameters determining the sensitivity of a $0\nu\beta\beta$-decay experiment are the mass of the relevant isotope, M, the running time, T, and the background index B (usually quoted in units of counts/(keV·kg·y)) in the relevant energy range $Q_{\beta\beta} \pm \Delta_E$ with Δ_E being the energy resolution. When no events are observed in the energy window within the running time the limit on the effective Majorana neutrino mass $m_{\beta\beta}$ scales with $a/(M \cdot T)^{1/2}$ with a being the fraction of ^{76}Ge in the germanium. This limit is only possible in the background-free case. Once a non-zero background is observed the limit on $m_{\beta\beta}$ scales with $a \cdot [(B \cdot \Delta_e)/(M \cdot T)]^{1/4}$ [GER04]. With this observation it is apparent that the sensitivity of $0\nu\beta\beta$ experiments strongly depends on the background level.

The new $0\nu\beta\beta$ decay experiment GERDA (Germanium Detector Array [GER04]), which will be situated at the LNGS as well, aims at checking the results from HdM within one year of data taking (Phase I) amounting to ∼15 kg·y of statistics, with no background events in the $Q_{\beta\beta}$ range. To achieve this goal a total background index of of less than 10^{-2} cts/(keV·kg·y) is necessary. This is a reduction of one order of magnitude with respect to HdM. In GERDA bare high-purity germanium detectors (HP-Ge-detectors) will be operated in liquid argon, starting with the existing HP-Ge-diodes from the HdM and IGEX [A$^+$00] experiments. In Phase II, to go beyond the existing limits, new diodes will be added to increase the target mass aiming for a total of 100 kg·y of statistics. For this phase the aim is to reduce the total background index by another order of magnitude to $\mathcal{O}(10^{-3})$ cts/(keV·kg·y). The basic layout follows ideas proposed in 1995 [Heu95] and is similar to the GENIUS [KKBH$^+$99] and GEM [ZPT01] proposals. If required, later phases with a target mass of $\mathcal{O}(500)$ kg and a background index in the $\mathcal{O}(10^{-4})$ cts/(keV·kg·y) region are conceivable in the framework of a worldwide collaboration.

2.2 Detection principle

GERDA uses HP-Ge-diodes, made out of enriched germanium to detect the $\beta\beta$-decay. The use of Ge-diodes at cryogenic temperatures is a well known technique in γ-spectroscopy: The diodes are operated in reverse-bias and read out by a charge sensitive pre-amplifier. Energy deposition inside the diode leads to the creation of electron-hole pairs, which drift to the electrodes of the diode driven by the electric field. This leads to a signal in the charge sensitive pre-amplifier that is proportional to the energy deposited.

Since the detector material is at the same time the source, all $\beta\beta$ events will occur inside the diode. The electrons emitted in β-decays have a very limited range of $\mathcal{O}(1 \text{ mm})$ inside the germanium crystal and will therefore deposit all their energy apart from bremsstrahlung, which may escape, in the diode. In the case of the $2\nu\beta\beta$-decay (T$_{1/2} = (1.3 \pm 0.1) \cdot 10^{21}$ y [EV02]) a variable part of the energy is carried away by the neutrinos. This leads to an extended spectrum below $Q_{\beta\beta}$. In the case of the $0\nu\beta\beta$-decay no energy escapes the diode in form of neutrinos, so the signal expected for this decay is a full energy peak at $Q_{\beta\beta}$ with the energy resolution of the diode. The observation of such a peak would be clear evidence for the $0\nu\beta\beta$-decay. Figure 2.1 shows the $2\nu\beta\beta$ spectrum, which was calculated using the Primakoff-Rosen approximation [BV92, PR59] and the peak from the $0\nu\beta\beta$-decay as a mono-energetic line at 2039 keV

In GERDA the HP-Ge-diodes will be suspended in high-purity liquid argon (LAr) inside a
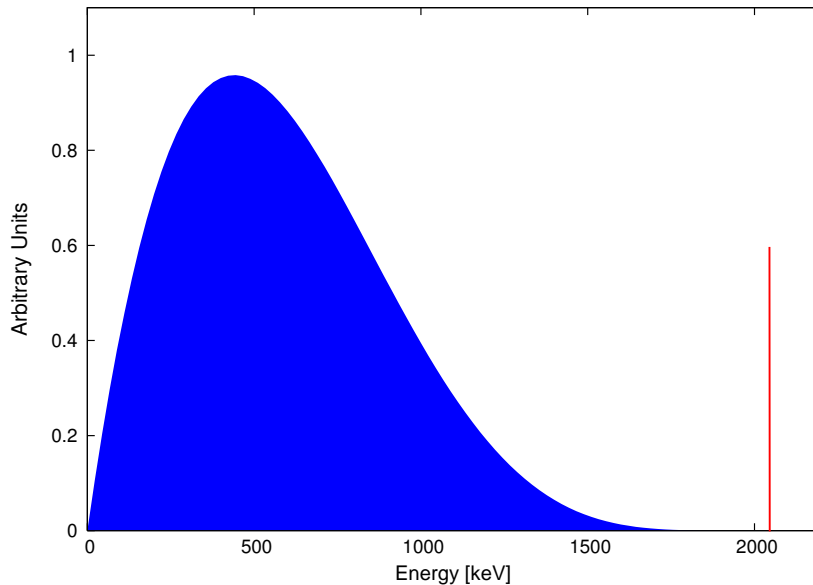
Figure 2.1: The spectrum for the $\beta\beta$-decay of ^{76}Ge. The extended spectrum to the left is that of the $2\nu\beta\beta$-decay mode. The mono-energetic peak at 2039 keV is the signal of the $0\nu\beta\beta$-decay that GERDA will be searching for (peak-height not drawn to scale).

stainless steel cryostat. The operating temperature is that of LAr: 87.3 K. The cryostat will be lined with copper, to shield the diodes from the activity of the steel. Around the cryostat there will be a water tank as gamma- and neutron shield. Figure 2.2 shows a schematic design of the GERDA detector and a detailed description of the final design can be found in [GER06].

2.3   Backgrounds in GERDA

There are three basic kinds of background in GERDA. One is the intrinsic background from contaminations in the diode material itself. Most important are the isotopes ^{60}Co and ^{68}Ge, which can be cosmogenically produced in the germanium. The other are surface contaminations on the diode and the external background from contaminations in any material surrounding the diodes. The external background is dominated by γ-s, since α-s and β-s have a comparatively small penetration power and are in general stopped in the LAr before they reach the diode.

To estimate the background in GERDA a good understanding of the background in the HdM experiment is helpful. Since the same HP-Ge-diodes will be used, any intrinsic contaminations will be inherited as well. For the energy range of 2000 to 2100 keV the background index was of the order of $\mathcal{O}(10^{-1})$ counts/(keV·kg·y). The primordial decay chains of U and Th external to the diodes were identified as the main contamination sources, contributing 38% and 41% of the total background rate respectively [DKK03]. ^{60}Co from the copper of the detector holder contributed 16% and the remaining 5% were attributed to anthropogenic contaminations and neutron- and muon-induced events. Within the limits of the experiment no intrinsic contamination was found by [DKK03].

The intrinsic cosmogenic contamination can however be estimated from the exposure time of the germanium to cosmic radiation during diode production [Mai96]. From this estimation, the time that the diodes were underground and the half life of the intrinsic isotopes produced, the intrinsic activity from ^{60}Co has been estimated to 36 μBq at the time of the start of the

13
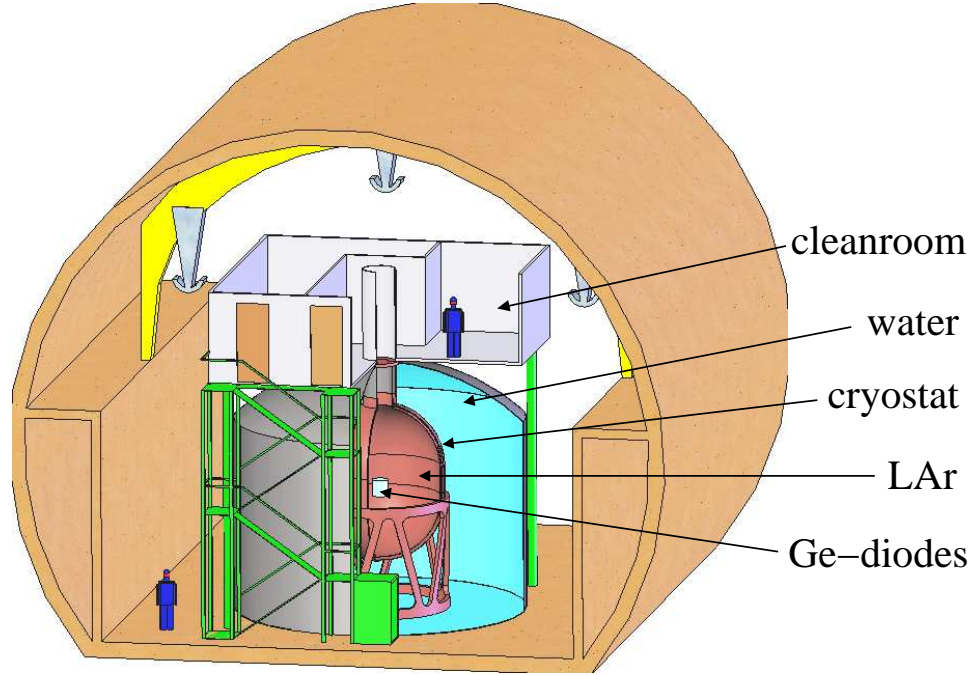
Figure 2.2: A schematic drawing of the GERDA experiment showing the location of the diodes, the cryostat, the water tank and the clean-room on top of the setup.

experiment in November 1995. This corresponds to ∼9% of the signal or $\mathcal{O}(10^{-2})$ cts/(keV·kg·y) at $Q_{\beta\beta}$. This number is in contradiction to the result from [DKK03] and the discrepancy is not yet fully resolved, but when using the number from [Mai96] and extrapolating it to the beginning of 2006 it yields a conservative estimation of the intrinsic background in the existing diodes for GERDA. This estimation is 10 μBq for the isotope ^{60}Co, which corresponds to ∼ $2.5 \cdot 10^{-3}$ cts/(keV·kg·y). ^{68}Ge is negligible due to its half life of 271 days [GER04].

The γ-spectra of the dominant isotopes contributing to the external background show no full energy lines in the region of interest (RoI) around $Q_{\beta\beta}$. This means that there are mainly two ways in which the γ-s from the external background can create a signal in the RoI: either when a γ with $E_\gamma > Q_{\beta\beta}$ is scattered in the Ge-diode (e.g. ^{208}Tl from the ^{232}Th chain or ^{214}Bi from the ^{238}U chain), or through (partial) summation of γ-s of lower energy that deposit energy in the diode at the same time (e.g. the γ-s from ^{60}Co).

As a note: there are some nuclei whose decay produces γ-s with an energy in the RoI [CEF99], but most of them are exotic and short lived isotopes that pose no danger of contributing to the background in GERDA. There are however three isotopes that need to be taken into account. One is ^{234m}Pa, a progenitor of ^{234}U in the ^{238}U decay chain. In the gamma spectrum from the decay of this isotope a line with an energy of 2041.2 keV has been detected [BGW$^+$04] which falls into the RoI within an assumed energy resolution of 3.5 keV. However the branching ratio of this line is only $1.1 \cdot 10^{-6}$. This means that the presence of enough ^{234m}Pa to create a signal in the RoI would be known from the detection of other characteristic lines with a higher branching ratio from the same isotope. The second relevant isotope emitting a gamma with an energy in the RoI is ^{77}Ge, which can be created by neutron capture on ^{76}Ge. ^{77}Ge decays with a half life

14

of 11.3 hours and emits a gamma of 2037.8 keV with a branching ratio of $6 \cdot 10^{-4}$. For Phase I the contribution is negligible, but for later phases a reliable detection of the neutron capture process as a tag for the possible creation of ^{77}Ge may be necessary to suppress this contribution to the background in the RoI. The third notable isotope is ^{56}Co which can be cosmogenically produced in germanium or the copper of the diode holders. Its decay emits a γ with an energy of 2034.8 keV at a branching ratio of 7.9%. While not being directly at $Q_{\beta\beta}$ this energy is still close enough that the isotope needs to be taken into account. The γ is emitted in a cascade with two other γ-s (with timescales of 0.6 ps and 6.1 ps), the detection of which can be used as veto signal. Also, the half life ($T_{1/2}$=77 d) is of an order of magnitude where storing the diodes/holder material underground and waiting for the isotope to decay is an option.

Other sources of background in GERDA and their estimated contribution to the total background (in cts/(keV·kg·y)) are: cosmic muons ($1.9 \cdot 10^{-3}$ [GER05]), delayed muon induced background ($(3\text{-}4) \cdot 10^{-4}$) [Pan06], contribution from the material of the signal cables ($1.5 \cdot 10^{-3}$ [KL05]), surface contaminations of the existing diodes, radon in the LAr and the contribution from the diode holder material ($6 \cdot 10^{-4}$, $2 \cdot 10^{-4}$ and $< 1 \cdot 10^{-3}$ respectively [GER04]).

The design of GERDA is such, that the external backgrounds are shielded to an extent where the total background, including the intrinsic background of the diodes which can not be shielded, is below the background index of 10^{-2} cts/(keV·kg·y) required for a 'background free' operation in Phase I. For Phase II, which requires a total background index of $\mathcal{O}(10^{-3})$ cts/(keV·kg·y), additional background reduction methods that allow a suppression of the intrinsic background of the diodes are necessary. The following section summarises the background reduction methods for both phases of GERDA.

2.3.1   Background reduction and suppression methods

There are several methods and precautions to reduce the background in the HP-Ge-diodes.

- Passive background reduction

  - Purity: All materials used in the detector construction have to meet very high radio-purity requirements. The closer to the diodes the materials are, the more stringent these requirements become (e.g. <10 mBq/kg activity in the steel of the top and bottom of the cryostat, <5 mBq/kg in the steel of the cryostat walls and <20 μBq in the copper inside the cryostat [GER06]). Apart from this, high requirements on diode handling have to be met, to prevent surface contaminations.

  - Reduction of material close to the diodes: Solid materials always contain non-negligible contaminations with primordial radio-nuclides, while gases like nitrogen or argon can be purified to very high levels [Sim05]. The diodes in GERDA will therefore not be operated in standard metal cryostats, but will be suspended naked in liquid argon, using a low-mass suspension made out of copper and PTFE.

  - Shielding: GERDA will use a graded shield. The water-tank around the cryostat will serve as shielding against γ-s from the rock and as neutron moderator. The γ-s from the cryostat material will be shielded by a copper lining inside the cryostat and the LAr serves as high purity shield against the γ-s from the copper shielding.

  - Waiting: Many cosmogenic isotopes have half-lives that are short enough that waiting for the decay while the material (i.e. the diodes) is stored underground protected from the cosmic radiation is a feasible option. For ^{68}Ge $\sim$60% of the nuclei decay in one year.

- Background suppression internal to diodes

  - Pulse shape analysis: The range of electrons in germanium is of the order 1 mm. This means that the energy deposition of the $0\nu\beta\beta$-signal is typically strongly localised inside the diode. The energy deposition from γ-s in the 2 MeV range in the diode, however, typically occurs by multiple interactions. When the background is due to the summation of two γ-s of lower energy, the energy deposition is also not localised. Due to the radial electric field there is a correlation between the location of the energy deposition and the relative drift-times for the electrons and holes created. This means that the time structure of the signal output of the charge sensitive pre-amplifier is generally different for a superposition of signals from multiple energy deposition sites in the diode than it is for the signal of a strongly localised single site event. This method has been used in the IGEX experiment [GMC$^+$03] and in the HdM experiment [MKK99, HK00] for Ge-diodes and in the GNO experiment for proportional counters [PCF04]. It has also been proposed for the MAJORANA ^{76}Ge-experiment [Maj03].

  - Segmentation of the diodes: For Phase II a segmentation of the diode readout for the new diodes is planned. Again the non-localised energy deposition for background events is used for background-suppression. The segmentation allows a localisation of the energy deposition inside the diode and events where more than one segment of the diode is triggered are discarded.

  - Coincidences in a decay chain: Some background events are intrinsically correlated to subsequent decays with a characteristic energy signature. For example the EC of ^{68}Ge ($\sim$10 keV energy deposition in $\sim$86% of the cases) is followed with a half life of $T_{1/2}$=68 min by the β^+-decay of ^{68}Ga, which has a Q-value above Q$_{\beta\beta}$ and is therefore a background candidate. The time correlation can, however, be used to veto these events.

- Anti-coincidence with events external to diode:

  - Cerenkov muon veto: The water tank, which serves as γ- and neutron shield, will be instrumented with PMTs. A muon or other fast charged particle going through the tank will give rise to Cerenkov light, which will be used as veto signal for the Ge-diodes.

  - Anti-coincidence between different diodes: As discussed above most sources of background events have a total Q-value that is higher than $Q_{\beta\beta}$. When one of these events deposits an energy close to $Q_{\beta\beta}$ in one diode, the remaining energy has to be deposited somewhere else. If it is deposited in a neighbouring diode, this coincidence between the events in different diodes is used to discard the event.

  - Scintillation light detection: Again the detection of the remaining energy of background events is used. The liquid argon used as cryogenic liquid is an efficient scintillator. The detection of the scintillation light as anti-coincidence signal is an option for phase II.

2.3.2 Anti-coincidence background suppression principle

As laid out, the $0\nu\beta\beta$-signal is a localised energy deposition inside the Ge-diode (figure 2.3, (1)), while the main contribution to the γ-background in the RoI in GERDA can be either due to the Compton scattering of γ-quanta of higher energy (2) or due to γ-s that are intrinsically coincident

with other events (3) within the time resolution of the detection or due to the summation of γ-quanta of lower energy (4). To suppress these background contributions it is necessary to detect the scattered γ-quantum or the other, coincident decays and to use this detection as anti-coincidence signal. To achieve this, barring the detection by the other diodes (5), the germanium-crystals must be surrounded by an active medium. Every event which is coincident with a detection of energy-deposition in the surrounding medium can be discarded. This kind of setup is called an anti-Compton-veto.
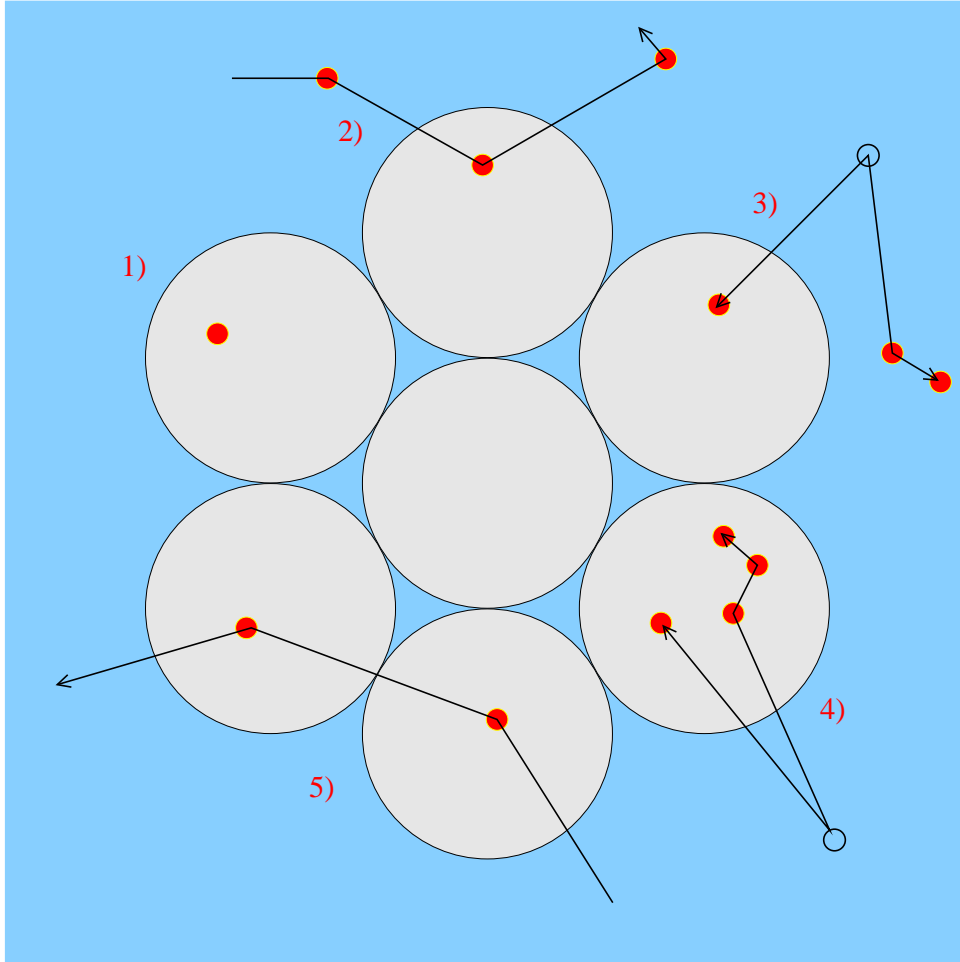
Figure 2.3: Examples of typical events. 1) $\beta\beta$ signal (single site energy deposition), 2) detection of a scattered γ, 3) detection of cascading γ-s, 4) multi site energy deposition in one diode, 5) energy deposition in neighbouring diodes. The locations of the energy deposition are marked as red dots.

It is of note that the anti-Compton background suppression principle is complementary to internal background suppression techniques like pulse-shape analysis and segmentation. The internal methods are ineffective against the single scattering of a high energy γ depositing an energy around $Q_{\beta\beta}$ in a single site inside the diode. However the active background suppression is effective, since the scattered γ can be detected. Conversely the active background suppression does not work against events where two (or more) low energy events in one diode sum up to $Q_{\beta\beta}$ and no energy is deposited outside the diode. However, this summation will be a multi-site energy deposition inside the crystal, so the internal background suppression methods are

effective. This property, that one suppression technique is effective where the other is not and vice versa means that the suppression-factors of these different techniques can be multiplied to predict the total suppression efficiency. This is often referred to as 'orthogonality'.

2.4 Physics reach

Generally, if no background events are observed, the limit on the half-life for the $0\nu\beta\beta$-decay of ^{76}Ge is given by:

$$T_{1/2} > 2.4 \cdot 10^{24} \cdot \epsilon \cdot a \cdot M \cdot t \text{ [y] [GER04]}$$

with the detection efficiency ϵ, the enrichment fraction a, the total active mass M and the measurement time t.

If background is observed and the number of background events is large enough to assume a Gaussian error, the limit on the half-life is given by:

$$T_{1/2} > 4.3 \cdot 10^{24} \cdot \epsilon \cdot a \cdot \sqrt{\frac{M \cdot t}{B \cdot \Delta E}} \text{ [y] [GER04]}$$

with the background index B in cts/(keV·kg·y) and the energy resolution at $Q_{\beta\beta}$ ΔE in keV. Both limits are at a confidence level (C.L.) of 90%.

2.4.1 Phase I

For the first phase of the experiment, the existing HP-Ge-diodes will be used. The total available mass is 17.9 kg. The average enrichment fraction is 86% and the detection efficiency is assumed to be 95%. Assuming that the background goal of an external background index of $\mathcal{O}(10^{-3})$ cts/(keV·kg·y) and a total background index of 10^{-2} cts/(keV·kg·y) can be reached and with the conservative assumption that one year of measurement time amounts to 15 kg·y of statistics, the physics reach is as follows:

For one year of data taking, assuming an energy resolution of 3.6 keV, the expected total background is 0.5 counts. If no event is observed, the limit on the half-life at 90% C.L. is $T_{1/2} > 3.0 \cdot 10^{25}$ y. This translates to an upper limit on the effective Majorana neutrino mass of $m_{\beta\beta} < 0.24 - 0.77$ eV, depending on the nuclear matrix element (NME) used. If one event is observed then the limit on the half-life becomes: $T_{1/2} > 2.2 \cdot 10^{25}$ and the upper limit on the effective neutrino mass becomes: $m_{\beta\beta} < 0.28 - 0.8$ eV (depending on the NME).

The claim for positive evidence for the $0\nu\beta\beta$-decay [KKDKC04] is based on an excess of 28.8±6.9 events for a total statistic of 71.7 kg·y. This would lead to a prediction of 6.0±1.4 events (above a background of 0.5 events) for 15 kg·y of statistic, after one year of data-taking with a similar efficiency. If no event is observed, this would rule out the claim at a C.L. of 99.6%. If one event is observed, the C.L. would be 97.8%. If 6 or more events are observed, however, this would be a five sigma confirmation of the claim.

2.4.2 Phase II

In the second phase new diodes will be added to increase the target mass. The new diodes will be segmented for an improved background reduction. The total background index aimed at is 10^{-3} cts/(keV·kg·y) and it is foreseen to accumulate $\sim$100 kg·y of statistics within 3 years. The total background expected for this time in the RoI with an energy resolution of 3.6 keV is 0.36 counts. The probability that no background event is observed, calculated from the Poisson

statistic is ∼70%. The limit on the half-life would then improve to $T_{1/2} > 2.0 \cdot 10^{26}$ y. This translates to an upper limit on the effective Majorana neutrino mass of $m_{\beta\beta} < 0.09 - 0.29$ eV depending on the NME used. If the background cannot be reduced to the envisioned level, a longer running time may be necessary to achieve the same sensitivity.

Figure 2.4 shows a plot of the allowed regions of the effective Majorana electron neutrino mass against the lightest neutrino mass [FSV03]. In the plot the areas corresponding to the sensitivity of the two phases of GERDA are visualised along with the claim of detection mentioned above. Phase I will cover the area of sensitivity required to scrutinize the claim and Phase II will cover the degenerate neutrino mass hierarchy. If no signal for the $0\nu\beta\beta$ decay is found, a ton scale ^{76}Ge experiment will be required to cover the inverted hierarchy region (depicted in green). Such an experiment might be undertaken in a worldwide collaboration, as for example in a joint effort with the MAJORANA [Maj03] collaboration.

A more detailed analysis of the physics reach and foreseen performance of GERDA can be found in [GER04].
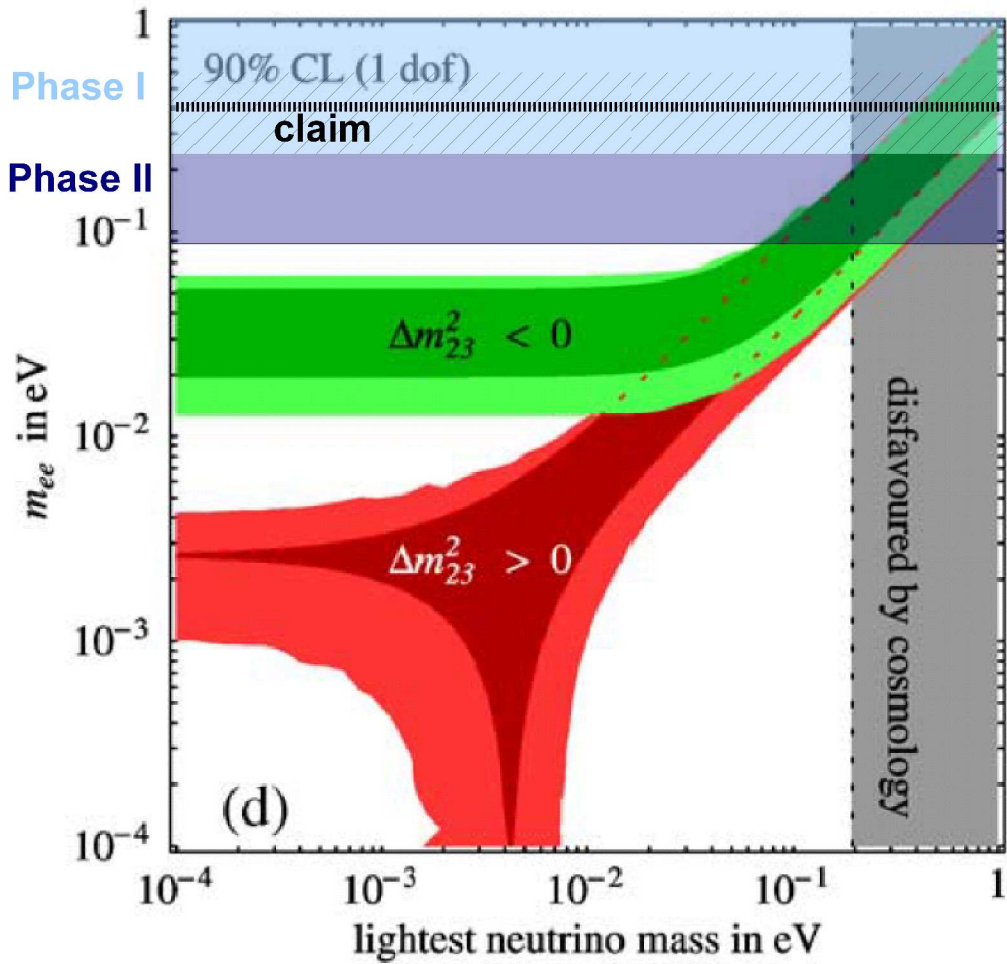
Figure 2.4: A plot depicting the sensitivity of the two phases of GERDA for the scale of the effective Majorana electron neutrino mass and the HdM claim. The region printed in green is the inverted hierarchy, the normal hierarchy region is shown in red.

Part II

Active background suppression using liquid argon (LAr) scintillation

Chapter 3

Liquid argon and the LArGe project

3.1 Liquid argon scintillation

It is known from literature that liquid argon (LAr), like all noble gas liquids, scintillates ([HTH$^+$81] and citations therein). Table 3.1 summarises some properties of LAr and its scintillation light. LAr will be used as cryogenic liquid for cooling the diodes and serve as high-purity passive shielding in GERDA. An option for a later phase in GERDA is the instrumentation of the LAr volume with photo-multiplier-tubes (PMTs) to detect the scintillation light induced by interactions of incident ionising radiation with the LAr. The detection of these events would then be used as anti-coincidence signal as discussed in section 2.3.2.

Material properties			
density in liquid phase	ρ	1.4 g/cm^3	
boiling point (at 1 bar)	T$_b$	87.3 K	
freezing point (at 1 bar)	T$_f$	83.8 K	
electron configuration		[Ne]3s^{2}3p^6	
Scintillation properties			Reference
light-yield$^{(*)}$	Y	41±2 photons per keV	[DHK$^+$02]
emission peak wavelength	λ_{max}	128 nm	
time constant singlet state	τ_s	6 ns	
time constant triplet state	τ_t	1.59 μs	[HTF$^+$83]
ratio singlet/triplet for β-s	$I_s/I_t(e^-)$	0.3	
ratio singlet/triplet for α-s	$I_s/I_t(\alpha)$	1.3	
ratio s/t for fission fragments	$I_s/I_t(ff)$	3	

Table 3.1: Properties of liquid argon and its scintillation. $^{(*)}$ The light-yield is given for excitation by electrons/γ-s. The scintillation properties depend strongly on LAr purity and pressure. The values given are for normal atmospheric pressure.

The investigation of the feasibility and efficiency of such an anti-Compton-veto using LAr scintillation light as anti-coincidence signal is the topic of this work. It is also one major goal of the 'Liquid Argon and Germanium hybrid detector' (LArGe) project, which this work is a part of. More details on the project can be found in section 3.2 below.

3.1.1 Excimer formation

When ionising radiation passes through argon, it can either excite or ionise the argon atoms. Kubota et al. [KHSR79] found the ratio of ionisation to excitation to be roughly 2:1. An excited argon atom possesses a binding potential towards regular argon atoms [Mul70] and can therefore form an excited dimer (excimer) in a three body collision. The formation of an excimer in a two body collision is forbidden because of angular momentum conservation.

In the case of the ionised atom, the electron thermalises in the surrounding medium on a timescale of $\mathcal{O}(100)$ ps and becomes in general trapped in the field of the parent ion. The effect of the cases where the electron escapes the field of its parent ion is discussed in section 3.1.2 below. The trapped electrons form an electron-hole pair with the hole in the electron shell of the parent ion. Analogous to solid-state physics this electron-hole pair is referred to as exciton. These excitons are initially mobile, but create a potential in which they themselves are trapped. This process is called 'self-trapping' [Mar71]. When the electron of these excitons recombines with the hole a photon with an energy equivalent to the binding energy of the electron is emitted. These photons have a high probability of being absorbed, creating secondary excitons. This means the argon is not transparent to these recombination photons. There is, however, the possibility that the initial ionised argon atom forms an ionised dimer with a neighbouring atom, before an exciton is formed, i.e. before the thermalisation of the electron. In this case the recombination with the electron leads to the dissociation of the ionised dimer and the formation of an highly excited atom, which de-excites non-radiatively to the regular exciton state. This exciton can then form an excimer as described above [DHK+02]. Below is a summary of the reaction equations leading to the creation of excimers.

$$\text{Direct exciton creation:} \quad \gamma' + Ar \rightarrow Ar^*$$

$$
\begin{aligned}
\text{or ionisation:} & \quad \gamma' + Ar \rightarrow Ar^+ + e^- \\
\text{followed by} & \quad Ar^+ + 2Ar \rightarrow Ar_2^+ + Ar \\
\text{recombination and} & \quad Ar_2^+ + e^- \rightarrow Ar^{**} + Ar \\
\text{exciton creation:} & \quad Ar^{**} \rightarrow Ar^* + heat
\end{aligned}
$$

$$\text{Excimer formation:} \quad Ar^* + Ar + Ar \rightarrow Ar_2^* + Ar$$
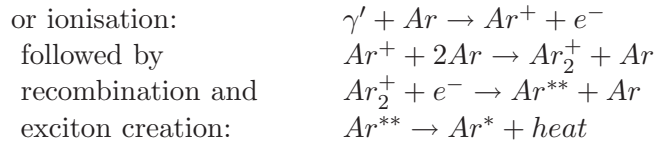
Here γ' denotes the energy deposition from ionising radiation via a (virtual) photon into the argon.

3.1.2 Light emission, time constants and photon yield

The argon excimers Ar_2^* formed in the processes described above are meta-stable and decay under emission of a photon with a wavelength of λ=128 nm. Argon is transparent to light of this wavelength. The excimers can be created either in a singlet-state or in a triplet state. The decay of the singlet state is allowed while the decay of the triplet state is forbidden by angular momentum conservation. It has therefore a much longer half-life. The singlet state decays with a time-constant of 6 ns and the triplet state decays with a time-constant of 1.59 μs.

$$Ar_2^* \xrightarrow[\tau_t=1.6\ \mu s]{\tau_s=6\ ns} 2Ar + h\nu \ (\lambda = 128 \text{ nm})$$
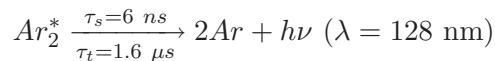
To estimate the light-yield it is necessary to take into account three processes that reduce the light-yield: the escape of electrons, 'stolen' electrons and bi-excitonic quenching.

The escape of electrons emitted in the ionisation process occurs when the electron thermalises beyond the so-called Onsager-radius [Ons38]. This is the critical distance where the thermalised electron escapes the field of the parent ion and does not form an electron-hole pair with its corresponding hole. In LAr this radius is 127 nm [DHK$^+$02]. The formation of an exciton is then delayed by up to $\mathcal{O}$(ms). This means that the probability of non-radiative de-excitation, which depends linearly on the available time, increases relatively to the de-excitation by emission of scintillation light. Even if the delayed exciton still de-excites by emission of scintillation light, this will not register on the time-scale of the light-detection of most LAr-scintillation experiments (typically $\mathcal{O}(\mu s)$). So the scintillation photon from this process is effectively lost.

The second process, the 'stolen' electron, is the capture of one free electron by electro-negative impurities in the argon, like for example oxygen. Again this process has to take place before the formation of an exciton ($\mathcal{O}(100$ ps)) and its probability therefore strongly depends on the amount of trace impurities in the argon. This means that the photo electron yield of the LAr scintillation strongly depends on argon purity.

The third process is the bi-excitonic self quenching [HDM92]. In this process two excitons combine, forming a non-excited atom and an ion:

$$Ar^* + Ar^* \rightarrow Ar + Ar^+ + e^-.$$

This is only possible as long as the excitons are not immobilised by the self-trapping process. The ion can then form another exciton as discussed above, but in the total balance one exciton is lost. The probability of this process scales with the density of the excitons, which depends on the ionisation density of the incident particle. The bi-excitonic self quenching is therefore expected to be stronger for particles of high ionisation density.

Taking into account the effects of escaping electrons and bi-excitonic self quenching the authors of [DHK$^+$02] give a theoretical estimation of the average energy necessary for the generation of one photon in pure LAr as $W_{ph}^{th}(\beta) = 24.4 \pm 1.3$ eV for excitation by electrons. This agrees well with the experimental value for ultra-high purity argon of $W_{ph}^{exp}(\beta) = 23.6 \pm 0.3$ eV [MTK$^+$74] and translates to a light-yield of $Y^{th}(\beta) = (41 \pm 2)$ photons/keV and $Y^{exp}(\beta) = 42.4 \pm 0.5$ photons/keV respectively.

For particles of high ionisation densities like α-s a 'quenching factor' q is defined as $Y(\alpha) = q \cdot Y(\beta)$. It is the factor by which the light-yield is reduced relative to the light-yield for excitation by electrons, $q=1$ means no quenching and $q=0$ would mean total quenching. Hitachi et al. found a quenching factor of $q = 0.71 \pm 0.04$ for 5.305 MeV alphas and $q = 0.73 \pm 0.04$ for 6.12 MeV alphas [HYDT87].

3.2   The LArGe project

A series of experimental studies have been carried out to investigate the properties of LAr and its potential as a cryo-liquid for the operation of bare HP-Ge-detectors. One focus of these studies was the investigation of the use of the scintillation light from the LAr as anti-coincidence signal for the HP-Ge-detectors. The experimental work was complemented by Monte Carlo studies that are also presented in this work (chapter 7) and by analytical energy transfer calculations that are part of a currently ongoing diploma thesis [Pol07]. The project started with a small test-setup at the MPI-K in Heidelberg called LArGe-TB (test-bench). It's main purpose was a basic feasibility study of the anti-Compton veto concept. The second step was the construction of an improved system with which most of the work of this thesis was done and which will be described in chapter 4. This system was named LArGe@MPI-K (Liquid Argon and Germanium

system <u>at</u> '<u>M</u>ax-<u>P</u>lank-<u>I</u>nstitut für <u>K</u>ernphysik') and it has been used to study the anti-Compton veto concept in more detail and also, without a Ge-diode inside, to study the properties of the LAr scintillation. The final step will be the operation of a ∼1 ton LAr scale ultra-low-background system currently under construction in the LNGS. In this final system an array of several HP-Ge-diodes will be operated in LAr.

The common concept of all LArGe setups is the detection of the LAr scintillation light by cryogenic photo-multiplier tubes (PMTs). Since the glass of PMTs is not transparent to the extreme ultra violet (XUV) scintillation-light (λ=128 nm) it has to be shifted before detection. To achieve this the PMT is coated by a wavelength-shifter (WLS) and the active volume is surrounded by a foil which acts both as WLS and as reflector in the optical range. The wavelength-shifter absorbs the XUV light and emits in the optical range (λ=410-450 nm depending on the WLS used). The reflector in the optical range is necessary to guide the shifted light to the PMT(s).

The general detection concept is to record the signal from the HP-Ge-diode(s) and that from the PMT(s) simultaneously whenever an energy deposition inside the diode(s) is registered. All data are recorded and retained for later analysis. The veto is then applied in the off-line data analysis. Every event where an energy deposition inside the LAr was registered within a time window of $\mathcal{O}(\mu s)$ with respect to the signal in the Ge-diode is discarded.

The time-window for the coincidence between the Ge-diode signal and the scintillation signal is determined by the data acquisition (DAQ) method and the number of photo electrons collected. For the straightforward method of integrating over the scintillation signal to collect most of the light, the time window is set by the slow component of the LAr scintillation. This method is necessary for low photo electron statistics and it also allows for an easy way to make use of the LAr scintillation not only as a pure veto trigger but also as a spectrometer. The length of the integration time-window also determines the maximal trigger rate in the LAr that the setup can handle with this DAQ mode: The requirement is $R \cdot G \ll 1$ (with the trigger rate R in Hz and the gate length G in seconds) and if it is fulfilled, the product $R \cdot G$ is the fraction of the dead time relative to the total time. If the product becomes greater than 1 the detector is blinded by the dead-time.

For pure veto-purposes it is also possible to use only the fast component of the LAr scintillation. This shortens the necessary time-window to $\mathcal{O}(10$ ns$)$. However, this also decreases the available number of photo electrons since the fast component contains only ∼23% of the total signal for excitation by electrons (see table 3.1). The achievable detection threshold depends on the photo electron yield and the number of photo electrons required for a veto signal. For example: assuming a photo electron yield of 1 pe/keV and the veto requirement of the simultaneous detection of 10 photo electrons would lead to a energy threshold of 44 keV, if only the fast component is used. This is sufficient for pure veto purposes.

Atmospheric argon always contains the cosmogenically produced radio-isotope ^{39}Ar. ^{39}Ar undergoes β-decay with a half-life of 269 y. This means that atmospheric argon has an intrinsic radioactivity and this radioactivity leads to an intrinsic scintillation event rate that is directly proportional to the active volume used.

The concentration of ^{39}Ar in atmospheric argon is given by [FM04] as $(7.9\pm0.3)\cdot10^{-16}$ g/g. Since LAr is in general produced from atmospheric argon it also contains the same fraction of ^{39}Ar. This corresponds to an intrinsic activity of (1.39 ± 0.05) Bq/l of LAr. The experimental value found by [B^{+}06] is $(1.41 \pm 0.11(syst) \pm 0.02(stat))$ Bq/l. With the density of LAr of 1.4 g/cm^3 this corresponds to ∼1 Bq/kg.

This determines the choice of the DAQ method for a given active volume. With 1.4 kHz trigger rate per cubic meter of LAr, an active volume of 1 m^3 and a time-window of ∼6.4 μs,

which corresponds to about 4 half-lives of the slow component, the product is $R \cdot G$ introduced above is ~ 0.01. So for an active volume of 1 m^3, which is the scale of the GERDA-LArGe system at Gran Sasso, the intrinsic ^{39}Ar activity is low enough to allow even the integration over the full LAr scintillation pulses. For GERDA, however, with a total volume of ~ 70 m^3 the simple integration over the full pulse is not possible unless the active volume is made significantly smaller than the total volume. So a different method of DAQ and data evaluation has to be used that allows for a much shorter time-window. One of the options is a flash ADC with a GHz sampling rate and a data evaluation including pulse shape analysis of the recorded signals. The principle of pulse shape analysis is discussed below.

3.3 Pulse shape analysis on LAr scintillation light

3.3.1 Pulse shape discrimination principle

The relative probability to excite an argon atom to the singlet or to the triplet state and consequently the population of the excimer singlet and triplet states depends on the ionisation density of the incident particle [KSR80]. This means that the time dependence of the scintillation light intensity $I(t)$, in other words the pulse shape, is dominated by two exponential decays. One with the time constant of the singlet state de-excitation τ_s (6 ns), the other with that of the triplet state de-excitation τ_t (1.6 μs, see table 3.1):

$$I(t) = I_0^{sing} \cdot e^{-t/\tau_s} + I_0^{trip} \cdot e^{-t/\tau_t}$$

with I_0^{sing} and I_0^{trip} being the initial intensities of the emissions from the singlet and triplet state respectively. These intensities depend on the relative population of these states.

It is therefore possible to define two components of the pulse shape: one fast component where the emission from the singlet state is dominant and one slow component, where the emission from the singlet state vanishes and that of the triplet state becomes dominant. By investigating the ratio of these components it is therefore possible to discriminate between different kinds of ionising radiation with different ionisation densities i.e. between β-s/γ-s, α-particles and fission fragments/fast nuclei. Since the detection of γ-s occurs only via their interaction with electrons which in turn ionise the argon, their pulse-shape is not distinguishable from β-particles. Fast nuclei can be for example recoil nuclei from interactions with neutrons or other neutral particles.

3.3.2 Reducing the dead time

Apart from the discrimination between different particles, there are further advantages to a good understanding of the LAr scintillation pulse shape. As discussed above, the intrinsic ^{39}Ar activity limits the capabilities for spectroscopy by simple integration over the scintillation signal. While it is possible with sufficient photo electron statistics to use only the fast component as anti-coincidence trigger, a good understanding of the pulse shape allows the separation of two pulses superimposed on each other. This means that a larger part of the pulses can be used which in turn increases the number of photo electrons available and thereby lowers the detection threshold. It also allows to retain the spectroscopic information from the pulses.

3.3.3 Additional physics potential

Apart from the use of the LAr scintillation light as anti-coincidence signal for the operation of HP-Ge-detectors there is the possibility for additional physics using the LAr veto detector as rare

event detector on its own. This requires a pulse shape discrimination that is powerful enough to distinguish the events of interest from the intrinsic background like ^{39}Ar. Of special interest is the detection of Cold Dark Matter in the form of weakly interacting massive particles (WIMPs). WIMPs can interact with argon via nuclear recoil and the recoil nuclei can be detected. As mentioned above, recoil nuclei have a high ionisation density and are in principle distinguishable from β/γ-s (like the intrinsic ^{39}Ar background) and from α-s. With the intrinsic ^{39}Ar activity of 1.4 Bq/l a discrimination power of $> 10^6$ is necessary to achieve a sensitivity of 10^{-10} pb for WIMP detection [BCC$^+$05, Sch03, Sch05].

If this discrimination power can be reached the dominant background to WIMP detection is due to neutrons. Neutrons are also detected via recoil nuclei and can therefore be indistinguishable from WIMPs by means of the pulse shape discrimination. A suppression of the neutron flux is therefore crucial to allow a WIMP detection. The total neutron-flux in the Gran Sasso Laboratories is dominated by neutron emission from decays of radio-isotopes in the sourrounding rock. It is $(3.78\pm0.25)\cdot10^{-6}$ $n \cdot cm^{-2} \cdot s^{-1}$ (Hall A) [WJRv04]. This will be reduced by the graded shield of the GERDA-LArGe setup at Gran Sasso which includes 20 cm of borated polyethylene. Taking into account the transmission factor through borated polyethylene for neutrons from a ^{252}Cf source from [SA00], the reduction factor is estimated as $\sim 2 \cdot 10^4$. The neutron energy spectrum from ^{252}Cf peaks around 2.5 MeV and extends up to $\sim$25 MeV. For lower energy neutrons the absorption is more efficient, e.g. for 1 MeV neutrons the reduction factor is estimated as $\sim 1 \cdot 10^5$). So the remaining flux is about $2\cdot10^{-10}$ $n \cdot cm^{-2} \cdot s^{-1}$ if one takes the attenuation factor for the integral flux and $\sim 3 \cdot 10^{-11}$ $n \cdot cm^{-2} \cdot s^{-1}$ if one takes that for 1 MeV neutrons respectively. In addition there is the flux of high energy neutrons induced by cosmic muons in the rock, which is difficult to shield due to the high neutron energy and is a challenge for all Dark Matter experiments. For the Gran Sasso Laboratories it is estimated as $5.5\cdot10^{-10}$ $n \cdot cm^{-2} \cdot s^{-1}$ [DGRS97]. The muon induced neutron flux produced in the argon and shielding material itself is estimated to be of the same order of magnitude [GER04], but can be suppressed by a muon veto.

The investigation of the sensitivity for WIMP detection under these conditions will be an additional topic of interest for the GERDA-LArGe setup at Gran Sasso. Therefore the investigation of the pulse shape discrimination method, which is a prerequisite for a possible WIMP detection, is an additional topic of this work.

3.4 A first test of HP-Ge detector performance in LAr

One of the first questions to be answered was whether the operation of a bare HP-Ge-diode in LAr deteriorates the performance of the diode. One possible origin of such a deterioration might be that the temperature of LAr is 10 K higher than the temperature of LN. Another possible origin might be the presence of the scintillation light. A test of this was performed in cooperation with the germanium-detector manufacturer DSG (Detector Systems GmbH) in Mainz. A 2 kg HP-Ge-diode was suspended in LAr in a test-setup at DSG. A ^{60}Co-source was suspended in the LAr in 6 cm distance from the diode and the energy spectrum from the detector was recorded. The spectrum is shown in figure 3.1. It shows the 1173 keV and 1332 keV peaks from the ^{60}Co source and the 1460.8 keV peak from ^{40}K of the natural background are visible.

The energy resolution at each of these peaks was determined. Figure 3.2 shows the fits of the peaks and table 3.2 lists the energy resolutions taken from the fits, given as 1σ, FWHM and relative energy resolution. The energy resolution agrees within the errors with the nominal energy resolution of the diode of (2.2 ± 0.03) keV FWHM at the 1332 keV line for the operation in a standard cryostat. The systematic variation can be estimated from earlier tests of the

same diode carried out by DSG in the same test setup in LN_2. In these tests the resolution of the diode ranged from 2.02 keV (3.11.2003) to 2.36 keV (12.01.2004), so the energy resolution measured in LAr in this test is the same as that in LN within the error of the measurement.

Source	Energy	1σ (LAr)	FWHM (LAr)	rel. resol. (FWHM)
^{60}Co	1173 keV	0.918 keV	2.16 keV	0.18%
^{60}Co	1332 keV	0.946 keV	2.22 keV	0.17%
^{40}K	1461 keV	1.06 keV	2.49 keV	0.17%

Table 3.2: The energy resolutions measured at different peaks in the spectra shown in figure 3.1. The nominal energy resolution of the 2 kg diode used, when operated in a standard cryostat, was (2.2±0.03) keV FWHM at the 1332 keV peak.

Since the 1173 keV or the 1332 keV γ-s are emitted in a cascade (with a time constant of 0.73 ps) and are therefore coincident within the time resolution of the Ge-diode, the detection of one of these γ-s in the diode has a high probability to be accompanied by scintillation light due to energy deposition from the second γ in the LAr. The decay of ^{40}K from the external background, which emits the single 1461 keV ^{40}K γ, however, is not intrinsically correlated to any other decay. This means that the probability that the detection of the 1461 keV ^{40}K γ in the Ge-diode is accompanied by an energy deposition in the LAr is less than it is for the ^{60}Co lines. The conclusion from this is, that if the scintillation light would have a deteriorating effect on the energy resolution of the diodes, the resolution measured at the ^{60}Co lines would be stronger affected than that measured at the ^{40}K line.

However, no such deterioration of the resolution at the ^{60}Co lines compared to the resolution at the ^{40}K line was observed. This proves that the scintillation light has no deteriorating effect on the performance of germanium diodes suspended in LAr. The conclusion of this test is, that there is no difference of the performance of HP-Ge-diodes when operated in LAr, as compared to the operation in LN_2. The use of LAr as shielding is therefore a feasible alternative to the use of LN_2.
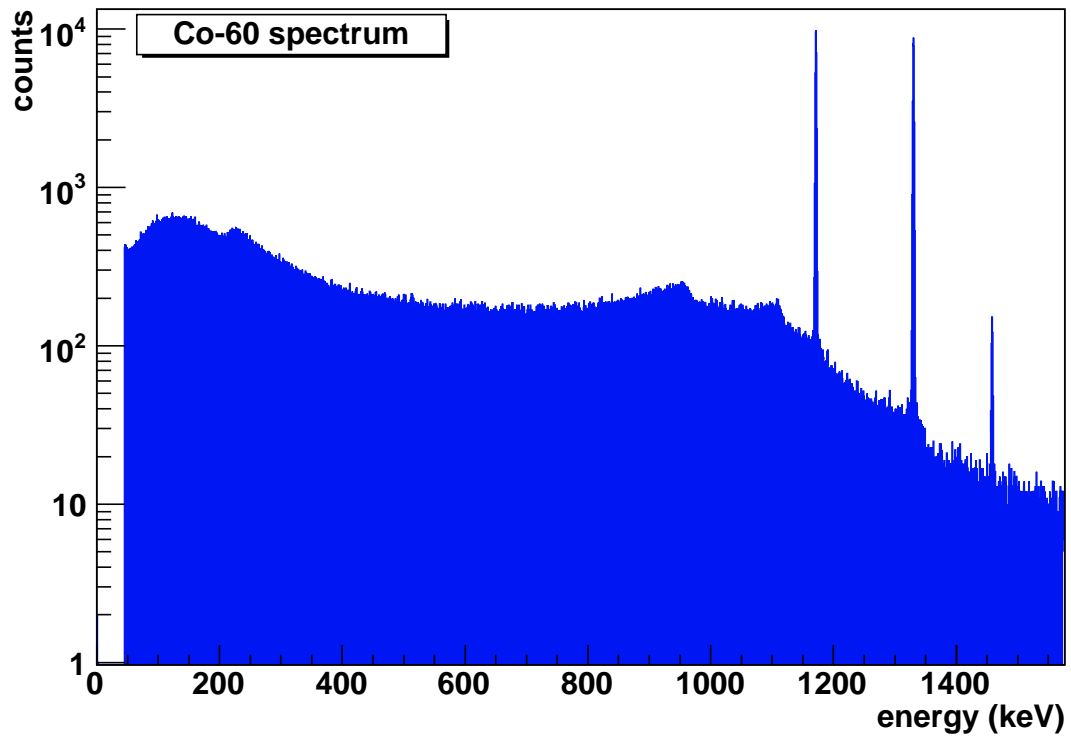
Figure 3.1: The spectrum of a ^{60}Co source taken in a test setup at DSG(Mainz) with a 2 kg HP-Ge diode suspended in LAr. Plotted in logarithmic scale. At 1461 keV the ^{40}K peak from the natural background is visible.
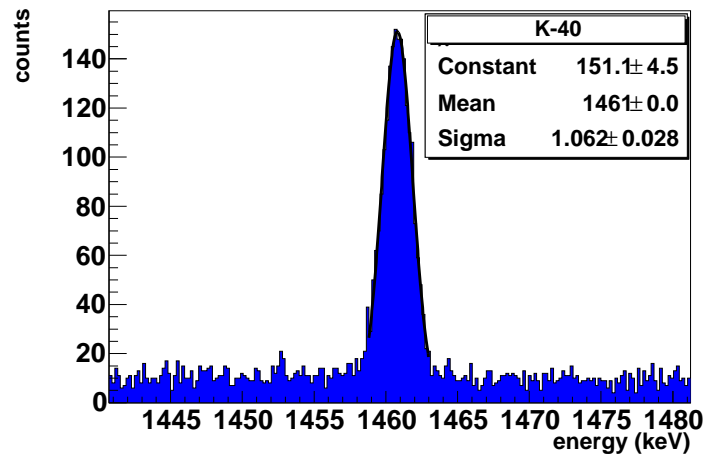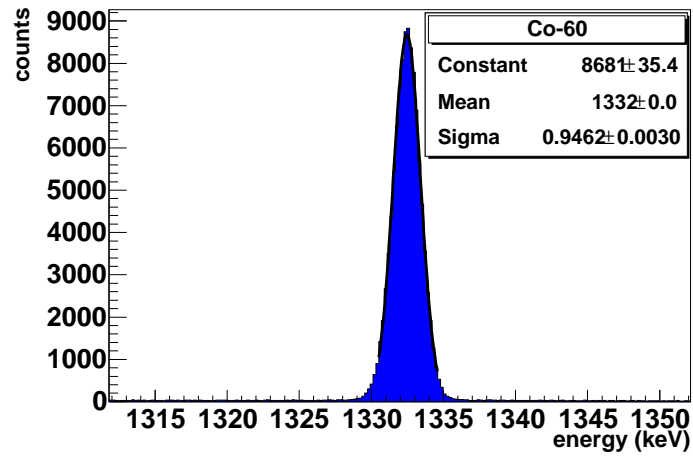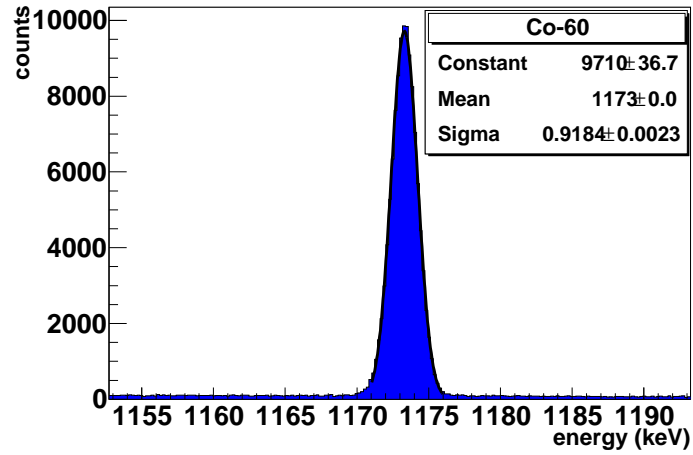
Figure 3.2: A comparison of the peaks in the spectrum shown in figure 3.1 along with the corresponding fits. Top: 1173 keV peak, middle: 1332 keV peak and bottom: 1461 keV ^{40}K peak from the natural background.

Chapter 4

The experimental setup

4.1 Requirements

The first tests of the LAr scintillation anti-Compton background suppression method were made with a pilot setup. While the suppression principle has been proven to work ([PMSS05]), the operation of this pilot setup revealed some requirements for a long term stability of an LAr scintillation experiment. The most important result was that an air-tight system is required, since even trace impurities of water and oxygen will reduce the light yield. Continuously flushing the setup with gaseous argon proved to be insufficient to reliably prevent a contamination of the LAr with air.

A system fulfilling the requirements learned from the pilot setup was designed and built. It will be hereafter referred to as LArGe@MPI-K (Liquid Argon and Germanium system at 'Max-Planck-Institut für Kernphysik'). The following list summarises specifications for the LArGe@MPI-K setup. An asterisk denotes the requirements learned from the first test.

- The system is designed for simultaneous operation of one HP-Ge-diode and light readout.

- The filling level is monitored by temperature sensors

- The PMT can be calibrated via an optical fibre.

- * To prevent contamination of the LAr with air, the system is designed with a leakage rate of less than 10^{-8} mbar·l/s (helium leakage rate).

- * The system is operated at an overpressure of 50 mbar

- * Radioactive sources can be inserted to a position close to the diode and removed without opening the system.

The LArGe@MPI-K setup is operated in an underground laboratory at the MPI-K, called the low-level-laboratory (LLL). The depth of the LLL is 15 meters water equivalent (m.w.e.).

4.2 Setup description

The schematic drawing of the LArGe@MPI-K setup is displayed in figure 4.1. It is mounted inside a stainless steel tank (h = 110 cm, $\varnothing$ = 35 cm) which is visible in the photo on figure 4.3. All the valves and feed-throughs as well as the pre-amplifier and voltage supply for the HP-Ge-diode are mounted on top of the tank. Inside the tank there is a glass dewar of 65 cm height and

29 cm in diameter. The dewar is filled with LAr. On top of the dewar there is an aluminium lid as convection barrier. Mounted on the aluminium lid there is an 8" PMT for light readout, the photo-cathode of which is immersed in the LAr. The voltage divider for the PMT is mounted on its neck. Around the PMT, also mounted on the aluminium lid, is an acrylic holding structure (figure 4.2), which carries the wavelength-shifter (WLS)/reflector for shifting the scintillation light into the visible range and to guide it to the PMT. The WLS consists of 3M radiant mirror foil (the former product name was VM2000) and defines the active volume (h = 43 cm, ∅ = 20 cm). The HP-Ge-diode is suspended 8 cm above the bottom of the active volume. The two tubes on the right of the pictures are for flushing the volume between the stainless steel tank and the dewar with gaseous argon (outer tube) and for flushing the dewar itself (inner tube). For a detailed system description including safety analysis and operations see [DPS05].

Figure 4.2 shows a photo of the inner part of the system. The acrylic structure for WLS- and diode mounting is visible as well as the PMT in the middle and the source insertion tube below it as well as the aluminium convection barrier above the PMT and the stainless steel lid of the tank on top. Figure 4.3 shows the closed tank with the flushing tubes and the pre-amplifier for the Ge-diode mounted on the stainless steel lid.

The system is shielded by the 15 m.w.e. of soil above the LLL and by a 5 cm thick wall built of lead bricks. In the lead wall there is a 5x5 cm window, at the hight of the diode. Radioactive sources can be placed either in front of this window in the lead-shielding or inserted into the source-tube, which extends close to the Ge-diode and allows the movement of the sources along the vertical axis. Table 4.1 summarises the dimensions and components of the setup.

Stainless Steel tank	h = 110 cm, ∅ = 35 cm
Dewar	h = 65 cm, ∅ = 29 cm
PMT	8" ETL 9357-KFLB
WLS	3M radiant mirror foil (VM2000)
Ge-Diode	Canberra p-type diode, 390 g
Active LAr volume	h=43 cm, ∅=20 cm $\hat{=}$ 13.5 l
Active LAr mass	∼ 19 kg
Operating pressure	50 mbar
Shielding	5 cm lead and 15 mwe underground lab

Table 4.1: Dimensions and components of the LArGe@MPI-K experimental setup.
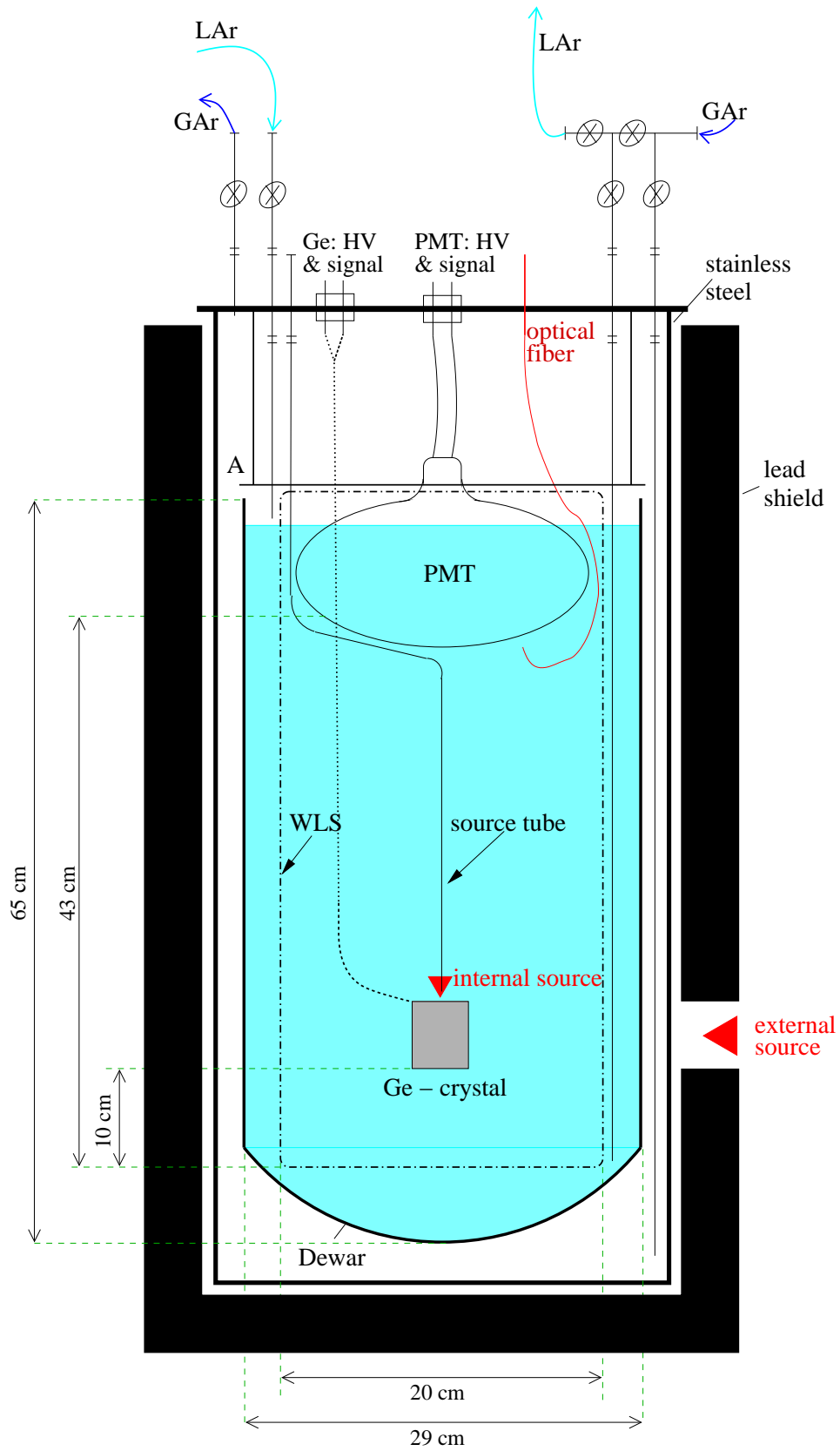
Figure 4.1: Schematic drawing of the LArGe test setup. Two important source positions are marked. GAr = gaseous argon, A = aluminium lid, WLS = wave length shifter.

Figure 4.2: The inner part of the LArGe@MPI-K system. From top to bottom: stainless steel lid, aluminium lid, PMT, source-tube and acrylic mounting structure for WLS and diode.

Figure 4.3: The closed LArGe@MPI-K system. Right: the flushing tubes. Middle: the preamplifier. Bottom: the unfinished lead shielding.

4.3 Front-end and DAQ electronics

4.3.1 Simultaneous readout of the Ge-diode and the PMT

The HP-Ge-diode operated in the liquid argon is supplied with high voltage (by a iseg NHQ 225M NIM-HV module) and read out by a pre-amplifier (custom made by DSG) mounted on the stainless-steel-lid of the system. Plugged into the HV-supply line to the pre-amplifier is a nano-ampere meter (home made) to monitor the leakage current over the diode. The pre-amplifier has two signal outputs, one fast signal for triggering and one shaped, charge-equivalent signal. The fast signal is fed into a leading-edge discriminator (LeCroy Mod.821 NIM) with variable threshold, which is placed just above the noise. Via a gate & delay unit (Phillips Scientific Mod.794 NIM) triggered by the discriminator a 6 μs gate for a peak-sensing ADC (Caen Mod.V785 VME module) is generated. The ADC is mounted in a VME-crate (Wiener) controlled by a Motorola PowerPC running on Debian Linux. It is programmable by a home made VME software [LMP01]. The shaped output of the pre-amplifier is integrated and amplified by a spectroscopy amplifier (Ortec Mod.572 NIM) with a shaping constant of 3 μs. The peak-hight of the output of the spectroscopy amplifier is proportional to the total charge of the Ge-diode signal. The signal is recorded by the ADC. The signal coming from the voltage divider of the PMT is shaped and amplified by a second spectroscopy amplifier (Ortec Mod.472 NIM) in the same way as the Ge-diode signal and recorded by a second channel of the same ADC within the 6 μs gate generated by the trigger on the Ge-diode signal.
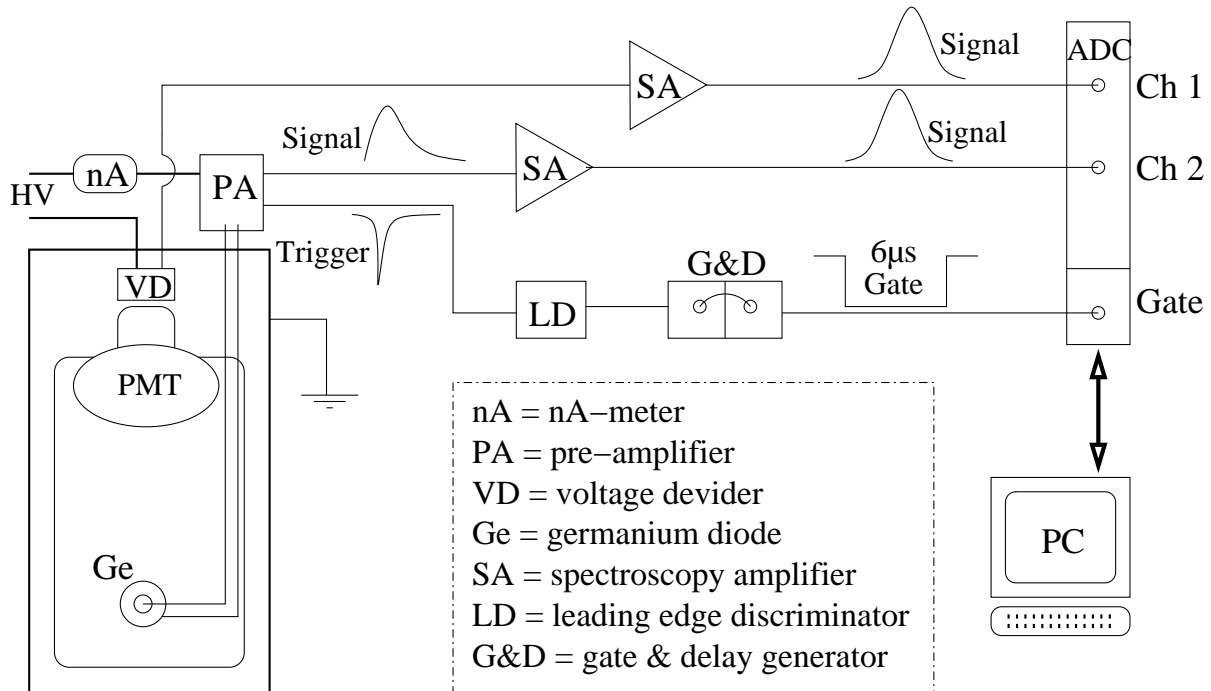
Figure 4.4: Schematic drawing of the front-end electronics for simultaneous readout of the HP-Ge-diode and the PMT with the Q-ADC system. The gate is generated by a trigger on the diode signal.

4.3.2 Calibration of the PMT

To calibrate the PMT a common trigger is generated by a flip-flop setup on a gate & delay unit. This generates a TTL signal which triggers an UV-LED with adjustable intensity (home made). The LED emits a short pulse (τ=3 ns) of UV-light ($\lambda = 380$ nm) which is guided to the photo-cathode of the PMT by an optical fibre. The same trigger generates the gate for the ADC, so that for each trigger to the LED the corresponding signal from the PMT is recorded. The signal from the PMT is shaped and amplified as above.
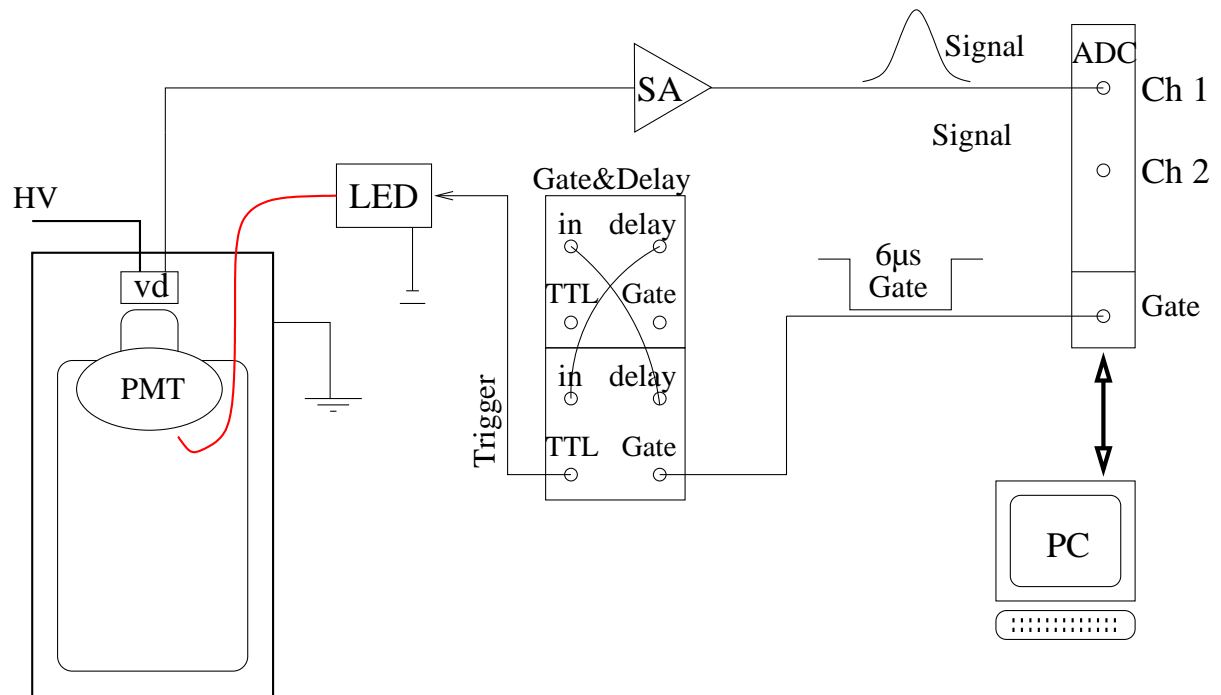
Figure 4.5: The front-end-electronics layout for the calibration of the PMT using an UV-LED.

4.3.3 Measuring with the digital oscilloscope

In the later stages of the experiment, for the investigation of LAr scintillation without operating a Ge-diode, the DAQ system was changed to recording each single pulse with a digital oscilloscope (Tektronix DPO 7054). This has the advantage of the possibility to study the pulse shape of each pulse. There is no need for intermediate electronics like a shaping amplifier, since the signal from the PMT is directly connected to the oscilloscope. Energy spectra are generated off-line in a software analysis, by integrating over each pulse. Before integration the baseline of each pulse is determined and subtracted from each pulse.

4.3.4 The Bi-Po trigger

One important contribution to background in low level background physics is the noble gas isotope ^{222}Rn. It is part of the ^{238}U decay chain and is continuously emanated from all solid materials containing traces of this primordial radio-isotope. ^{222}Rn and its daughters ^{218}Po and ^{214}Po are α emitters with α energies of 5.5 MeV, 6.0 MeV and 7.7 MeV respectively and its daughter ^{214}Bi undergoes β decay with a spectrum that extends beyond the RoI of the $0\nu\beta\beta$ decay (2038 keV) up to 3.27 MeV. These contributions are relevant background contributions for GERDA. Moreover the Po isotopes can precipitate onto surfaces and become surface impurities on the diodes itself. The ^{222}Rn decay chain contains a characteristic sequence of decays, however, which can be used to detect the presence of ^{222}Rn daughters. The daughter of the above mentioned isotope ^{214}Bi is ^{214}Po which decays with a half-life of 164 μs via α-decay. The energy of the emitted α is 7.7 MeV, high enough to be easily separable from the lower energy background. A decay in the β/γ range ($<$3.3 MeV) followed by a decay in the high-energy α range within the time of a few half-lives of ^{214}Po is therefore a signal for the presence of ^{222}Rn in the system. The half-life is long enough that the two decays are separable within the timescale of the LAr scintillation detection (order of μs) yet it is also short enough that the probability for random-coincidences within the time window is acceptable. This characteristic sequence of decays is called the the '^{214}Bi-Po coincidence'.

Figure 4.6 shows the electronic layout for detecting the Bi-Po coincidence, using the digital oscilloscope. The signal from the PMT is fed into a leading edge discriminator. The threshold is set just above the full height the single photo electron signal to exclude the dark noise. When a signal is detected, a gate is opened for a second leading edge discriminator. The gate length is chosen to be several half-lives of ^{214}Po long. The threshold for the second discriminator is set well above the end of the γ background spectrum at 3.3 MeV. Any signal detected in the second discriminator originates therefore either from an α decay or from the cosmic muon background. Depending on the gate length G used, the total counting rate in the low energy region $R_{\beta\gamma}$ and the rate of cosmic background events above the second threshold R_{cosm}, the rate of random coincidences R_{coinc} with cosmic background events can be calculated. $R_{coinc} = R_{\beta\gamma} \cdot R_{cosm} \cdot G$. The probability P_{coinc} that a detected event is a random coincidence depends on the coincidence rate and the rate of real ^{214}BiPo coincidences: $P_{coinc} = R_{coinc}/R_{BiPo}$. Everything aside from random coincidences is an α correlated to the previous decay in the β/γ energy scale and so a signal for the presence of ^{222}Rn.

4.3.5 Simultaneous readout of the last dynodes

In the first measurements the PMT was operated with positive high voltage. Later we changed the divider scheme to operate the PMT on negative HV, since this proved to improve the signal quality (see section 8.3) and to prevent overshoots that appeared due to AC coupling
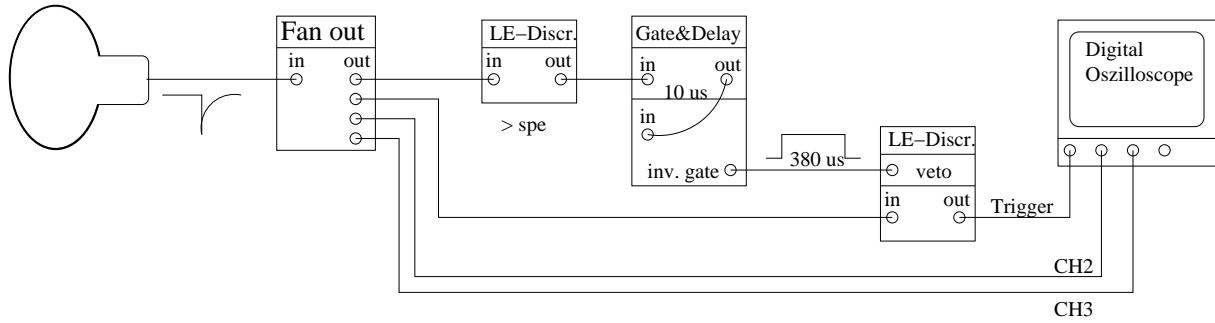
Figure 4.6: The front-end-electronics layout for measurements using the Bi-Po trigger.

in the voltage divider for positive HV. A further improvement of the electronic layout was the implementation of the readout of the last dynode of the PMT. When using only the anode, the linear dynamic range both of the PMT and especially of the digital oscilloscope proved to be insufficient to measure signals from γ and α-sources simultaneously in the linear range. When selecting a scale (i.e. internal gain factor) on the digital oscilloscope that allows the detection of single photo electrons (spe), or the spectroscopy in low energy ranges like the 60 keV ^{241}Am, the signals from α-s are cut off, which introduces a non-linearity of the energy scale in high energy ranges. Also the PMT, when operated at a high voltage that allows a good signal to noise ratio in the low energy range, is saturated in the α energy range.

Reading out the dynode for events of higher energy and using the anode for the low energy part of the measured spectrum increases the dynamic range in two ways. First, the gain of the last amplification step between last dynode and anode is a factor 2.7 with our voltage divider settings. This means the dynode signal is a factor 2.7 lower and is not saturated in the α energy range, even when operating the PMT at the voltage needed for a good separation of the spe signals from the noise. Second, the availability of a second signal output allows the use of a second oscilloscope channel that can be set to a larger voltage scale, i.e. a lower gain factor to record the untruncated alpha signals, while the first channel records the low energy range of the anode signal.

The readout of the dynode before the last was also implemented, but since the readout of the last dynode proved to be sufficient for the dynamic range needed for our experiment, the readout of the previous-to-last dynode was not necessary.

A further advantage of the readout of the last dynode is the possibility of an improved suppression of electronic noise. The signal detected on the last dynode is oriented in the opposite direction of the signal from the anode, since the dynode is read out via a capacitor. I.e. when the signal on the anode is negative, the signal on the dynode is positive. When both signal readout paths share the same DAQ electronics then both share the same electronic noise picked up after the PMT. That means the electronic noise on the anode channel is in phase to the electronic noise on the dynode channel. By adjusting the amplification in a way that both signals are of the same height and then subtracting the dynode signal from the anode signal in the off-line data analysis, real signals are amplified while the noise is reduced. Figure 4.7 shows an idealised schematic of the noise suppression principle. The electronic layout of the new voltage divider is shown in the appendix.

40
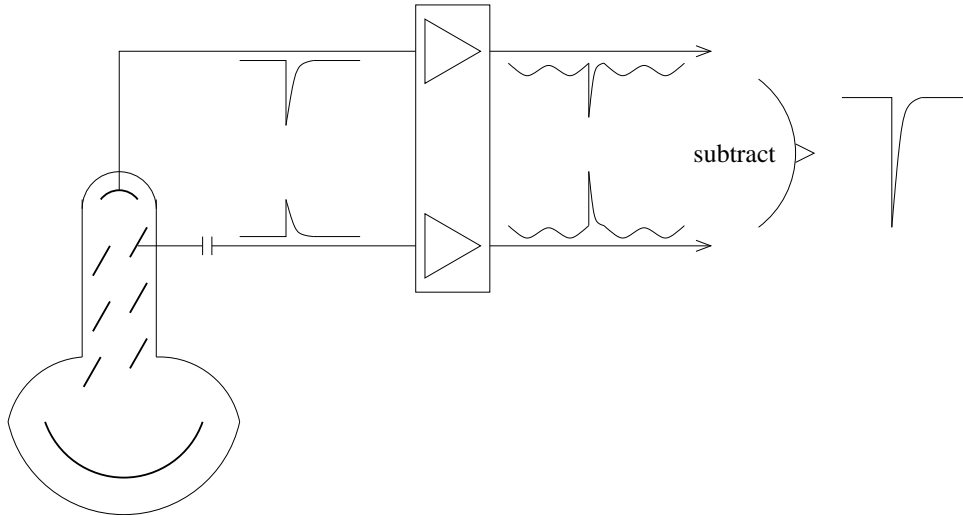
Figure 4.7: The principle of noise suppression by using the signal from the last dynode. The last dynode is read out via a capacitor. Real signals are in opposite phase. Electronic noise from amplifier + DAQ unit is in phase. Software subtraction acts as noise reduction.

4.4 Operations

4.4.1 Basic operations

Figure 4.8 shows schematic drawings of the system including the flow paths for LAr and gaseous argon (GAr) for different operations. The entire system, including all pipes, can be flushed with GAr. During normal operation however, the evaporation of the LAr inside the system proved to be sufficient to maintain the necessary overpressure of ∼50 mbar and to provide continuous flushing. One exit valve (1) is open and connected to a 'bubble bottle' during all operations to prevent pressure buildup. The 'bubble bottle' serves as precaution against a back-flow of air should the pressure in the system drop unexpectedly. It is filled with mineral oil with a low vapour pressure.

When filling the system through (2) a larger 1" release valve (3) is opened to allow a higher gas flow than the bubble bottle can handle (figure 4.8(a)). The system can be emptied via the inner flushing tube (4) by closing all exit valves and increasing the pressure in the system using GAr blown into the system through (5) (figure 4.8(b)). The valve between (4) and (5) is closed during this process. For more details on operations see [DPS05].

4.4.2 Doping of the LAr with Xe and Rn

The LAr in the system can be doped with other gases for various purposes. If the freezing point of the doping gas is higher than that of argon, GAr is necessary as carrier gas. GAr is flushed through the inner flushing tube into the LAr. The flow has to be low enough that the gas bubbles inside the system can liquefy inside the LAr volume. This is checked by monitoring the flow of the exhaust gas, which may not increase significantly.

In the case of Xe (also possible for other gases that are available in gas bottles) the doping gas is added through the second valve of the flushing tubes with a flow which has to be significantly lower than the flow of GAr. The combined gas bubbles liquefy inside the LAr volume, depositing the doping gas in the LAr. Figure 4.8(c) shows a schematic drawing of this doping process.
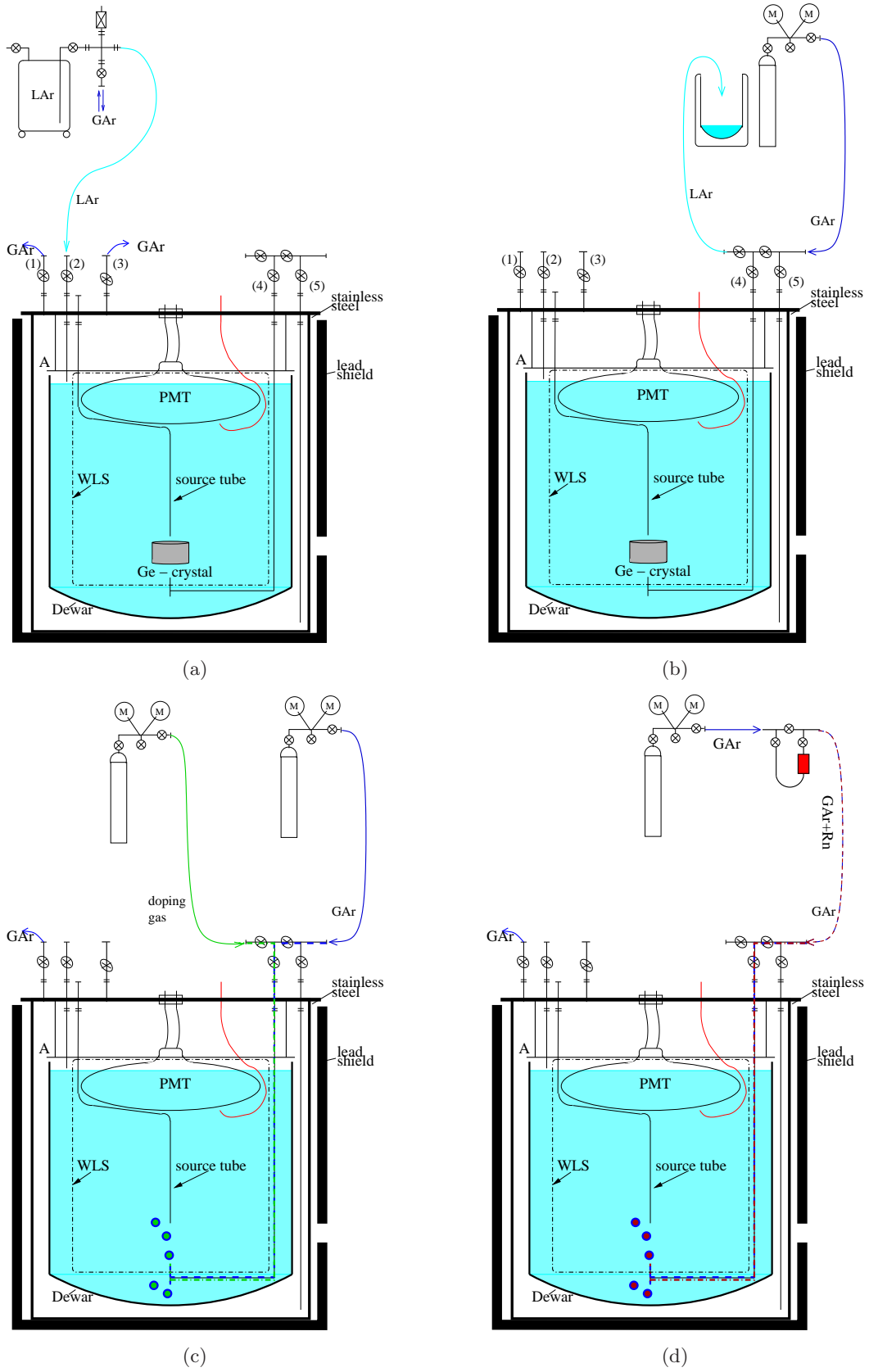
Figure 4.8: Schematic drawings of different operations. Filling (a), emptying (b), doping with Xe (c) and doping with Rn (d).

In the case of Rn doping a known quantity Rn is frozen onto an activated carbon trap. The trap is connected to the system and flushed with GAr as carrier gas, while the trap is still cold. Then the trap is slowly warmed up to release the Rn that is frozen onto the activated carbon. This method allows the insertion of a known quantity of Rn into the LAr. Figure 4.8(d) shows the schematic drawing for this process and a more quantitative description including an analysis of the transfer efficiency from the trap to the active volume can be found in section 10.1.2.

4.5   Notes on germanium diode handling

During the operation of different HP-Ge-diodes in LAr and LN_2 several caveats and difficulties were observed. First, the diodes are more sensitive to dust and moisture than originally thought. Even a short exposure to normal air may lead to leakage current when operating the diode the next time. The most critical moment is when dismounting the diodes. When the diode is still cold, any moisture will freeze unto the surface. While ice is in general less dangerous than water, it can still be detrimental to later detector performance. Several methods were tried and discarded. First the diodes were dismounted as fast as possible while still cold and then placed under vacuum to warm up. This was done to remove the ice by sublimation without going through the liquid phase. The second step was warming the system up with heated argon gas before opening. This prevents the condensation from happening. The third improvement was the addition of a flexible PVC-hood continuously flushed with nitrogen, to open the system under nitrogen flow. This method - warming up before opening, opening under gas flow, was used for most of this work. In the meantime however a new method of diode handling has been adopted from the Ge-diode manufacturer Canberra, Olen, in Belgium. The diode is dismounted, while still cold, under nitrogen atmosphere and is placed inside a methanol bath to warm up. After warming up the diodes are stored under vacuum (10^{-5} mbar).

Chapter 5

The photo electron yield for γ-sources

5.1 Definition of photo electron yield

For the detection of the scintillation light in the LArGe project photo-multiplier tubes (PMTs) are used. The process of light-detection using a PMT is that the photons create photo-electrons in the photo-cathode of the PMT via the photo-effect. Each photon has a finite probability to produce such a photo electron. This probability is called the quantum efficiency of the PMT. The photo electrons are then accelerated towards the first dynode, where they produce secondary electrons which are accelerated towards the next dynode and so on, so that each primary photo electron corresponds to an avalanche of electrons from the last dynode, that is collected by the anode and gives rise to a charge equivalent signal. The number of avalanche electrons collected by the anode per primary photo electron is called the gain factor. It depends on the PMT type and the operating high voltage and is of the order of $10^6 - 10^7$ in the setup used here. The minimal possible signal in a PMT is the production of only one photo electron on the photo-cathode. This one electron gives rise to a characteristic signal. The height of this signal depends on the gain-factor and its width is determined by the spread of the PMT. This characteristic, minimal signal is called the 'single photo electron (spe) signal'. With higher light-intensities the number of photo electrons produced on the photo-cathode increases. Since the light-intensity in a scintillator is a measure for the deposited energy, the average number of photo electrons registered in the PMT is also proportional to the energy deposited in the scintillator. The proportionality constant is called the photo electron yield Y. It depends on the light-yield of the scintillator, which is dependant on the ionisation density of the exciting radiation, and the quantum efficiency of detection. The photo electron yield is measured in number of photo electrons per unit of energy (e.g. pe/MeV). The quantum efficiency of detection in our system is a composition of the quantum efficiency of the WLS, the efficiency of the light collection and the quantum efficiency of the PMT. The efficiency of the light collection in turn depends on the geometry of the system, the reflectivity of the light guiding foil and the transparency of the LAr to the shifted light.

5.2 The principle of photo electron yield measurement

To determine the photo electron yield, the PMT is calibrated using a LED. When triggered, the LED emits a pulse of UV light (λ=380 nm) with a pulse width of ∼3 ns. The LED and

the DAQ-electronics are triggered by a common trigger (see section 4.3.2). The intensity of the LED is chosen such that only on one trigger out of 30 to the LED an event is registered by the PMT. The distribution of the number of photo electrons registered per trigger follows the Poisson statistic.

$$P_\lambda(N) = \frac{\lambda^N}{N!}e^{-\lambda}$$

with $P_\lambda(N)$ being the probability to detect N photo electrons and λ being the Poisson constant.

The probability to get any event at all is 1/30. So the probability for 0 photo electrons is given: $P_\lambda(0) = 29/30 = 0.9667$. From this the constant λ can be calculated:

$$\lambda = -ln(0.9667) = 0.034$$

and this gives the probability for one photo electron:

$$\rightarrow P_{0.034}(1) = 0.033$$

The probability to get more than one photo electron is then:

$$P_{0.034}(> 1) = 1 - P_{0.034}(1) - P_{0.034}(0) = 0.0003 \rightarrow P_{0.034}(> 1)/P_{0.034}(1) = 0.009 < 1\%$$

The probability to detect more than one photo electron when an event is registered is less than 1% which means that the total signal is dominated by the single photo electron signal. The spectrum of these signals is recorded and this 'spe-spectrum' has to be fitted to determine the number of channels per photo electron.

As said above, the number of photo electrons follows a Poisson statistic. Each photo electron gives rise to a characteristic charge signal in the anode, which is amplified, shaped and recorded by the ADC. Each ADC channel then corresponds to a certain charge collected at the anode and thereby to a certain number of primary photo electrons. This correlation between photo electrons and ADC signal can be summarised in one pe-to-ADC gain factor. The amplification is a statistical process, which is subject to a Gaussian spread. So the photo electron distribution in number of ADC-channels is a Poisson distribution multiplied by the gain factor and folded with a Gaussian. This distribution is added to the pedestal of the ADC system which is a simple Gaussian around the pedestal position. The final formula for the photo electron distribution in ADC channels is [H. 04]:

$$F(x) = N \cdot \left(\frac{e^{-\mu}}{\sqrt{2\pi}\sigma_P} exp\left[-\frac{1}{2}\left(\frac{x-P}{\sigma_P}\right)^2 \right] \right.$$

$$\left. + \kappa \sum_{n=1}^{m\gg1} \frac{e^{-\mu}}{\sqrt{2\pi}\sigma_{\gamma e}} \frac{\mu^n}{n!} exp\left[-\frac{1}{2}\left(\frac{x-(P+nG_{pe}^{ADC})}{\sqrt{n}\sigma_{\gamma e}}\right)^2 \right] \right) \quad (5.1)$$

with the overall normalisation N equal to the total number of events in the spectrum, the pedestal spread σ_P, the pedestal position P, a normalisation factor κ, the spread of the photo electron signal $\sigma_{\gamma e}$ and the gain factor G_{pe}^{ADC}, which summarises the gain factor of the PMT, the amplification of the charge signal by the spectroscopy amplifier and the conversion factor of signal height to ADC channel.

The fit proved to be more robust when the pedestal position P was not used as free parameter, but was fixed according to a separate measurement of the pedestal. N is fixed as well since the

total number of events is known. All other parameters are free. The first term of the equation is the Gaussian describing the pedestal for 0 photo electrons, the second term is the Poisson distribution convoluted with the gain factor and the Gaussian spread of the system.

The pedestal of the electronics is registered by delaying the trigger to the LED several μs with respect to the trigger to the DAQ system. The DAQ system then records only the baseline before the actual signal. In the next step the spectrum of a source with a known energy is recorded, along with the corresponding pedestal. From the fit of spe-spectrum the number of ADC channels per photo electron is known. With this the number of photo electrons in the full energy peak of the source can be calculated and since the energy of the peak is known, this can be translated to the number of photo electrons per unit energy:

$$Y = \frac{C_{src} - C_P}{G_{pe} \cdot E_{src}} \tag{5.2}$$

With C_P being the channel number of the pedestal, $G_{pe} = G_{pe}^{ADC}$ being the gain in ADC channels per photo electron, C_{src} being the mean channel number of the peak from the source used and E_{src} being the energy of the peak from the source used.

5.3   Results for the photo electron yield

The source selected in the following evaluations is ^{57}Co. It has a line at 122 keV with a relative intensity of 86% and a line at 136 keV with a relative intensity of 11%. The energy resolution of the system does not allow a separation of these lines, but they can be fitted as the sum of two Gaussians.

Figure 5.1 shows the pedestal of the DAQ-system. Figure 5.2 shows the single photo electron histogram taken with the LED-calibration system together with its fit. The spectrum is truncated because the pedestal is much higher than the spe-peak which wouldn't be visible in an untruncated spectrum. Figure 5.3 shows the spectrum from the ^{57}Co source. The fits on the data give the values for C_P, G_{pe} and C_{src}, which are summarised in table 5.1.

	C_{src}	C_P	G_{pe}	E_{src}
Value	2134	81.32	32.55	0.122 MeV
Stat. error	3.5	$4 \cdot 10^{-3}$	0.06	neg.
Syst. error	5	neg.	1	neg.

Table 5.1: The results from the fits of the spe-spectrum, the pedestal and the ^{57}Co spectrum.

Inserted into equation 5.2 these values give the photo electron yield Y=516.9 pe/MeV. The dominant contribution to the error on the gain factor comes from the fit of the spe-peak. The peak to valley ratio is limited by the shaping time used in the spectroscopy amplifier and the systematic error is larger than the statistic error given in the fit: Depending on the fitting range the gain factor G_{pe} varies by ± 1 channel (3%). The statistical error of 0.06 channels is therefore negligible. The relative statistical error and systematic error of the ^{57}Co peak position are 0.16% and 0.23% respectively, which is more than one order of magnitude lower than the systematic error on the gain factor. They are therefore negligible. The relative error on the pedestal is even smaller and can be neglected as well. With these considerations the total error on the photo electron yield is 16 so that the final result for the light-yield is:

$$Y = 517 \pm 16 \text{ pe/MeV}$$

Constant	1.90e5	
Mean	81.32	
Error	3.87e−3	
Sigma	4.936	
Error	3.78e−3	
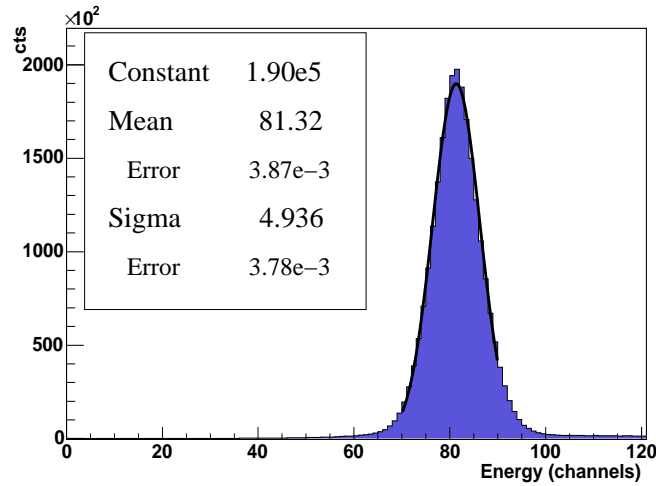
Figure 5.1: The pedestal of the DAQ-system that was used for the photo electron yield measurement.

In the first test setup mentioned in section 4.1 the photo electron yield was 250±8 pe/MeV so the photo electron yield is improved by more than a factor 2. The energy-resolution is also improved with respect to the first test system by a factor of 1.45, as expected from the increased photo electron statistics. Since the wavelength shifter, the photo-multiplier and the electronics used were the same, this increase of a factor 2 in photo electron yield is due to the improvement in liquid argon purity due to the improved air-tightness of the new system.

After the investigation of the background suppression power presented in the next chapter, some investigation of various methods of further improving the photo electron yield were undertaken. They are presented in chapter 8.
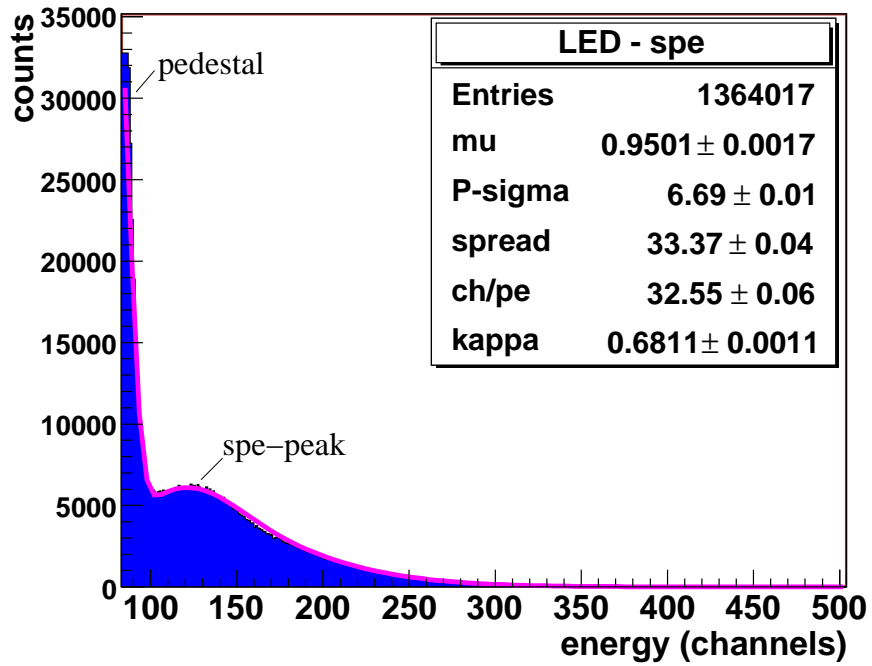
Figure 5.2: The single photo electron histogram of the LArGe@MPI-K system. The x-axis is truncated for better visibility of the spe signal.
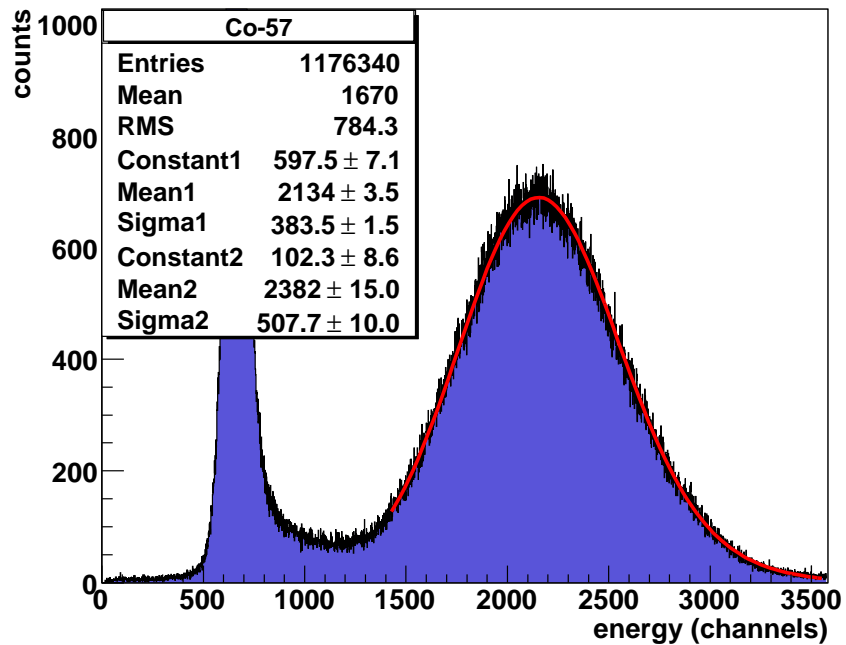
Figure 5.3: The spectrum of a ^{57}Co source. The mean energy of the peak is 123 keV. The apparent peak to the left is an effect of the threshold of the DAQ system.

Chapter 6

Measurements with γ-sources

In this chapter the results the investigation of the LAr scintillation anti-coincidence veto technique are presented. Following a basic test of the concept, the veto efficiencies for various sources in different locations have been measured. In the first half of the chapter the unsuppressed and suppressed spectra of various sources are shown and the second half of the chapter is dedicated to the analysis of the data and the determination of the suppression efficiencies from the recorded spectra.

6.1 Properties of the sources used

Table 6.1 lists the properties of the sources used for the experiments in this work. There are two locations in which the sources were used (see figure 4.1). Sources dubbed 'external' are placed in a window in the lead shielding at the height of the Ge-diode on the outside of the setup. 'Internal' sources are mounted/inserted close to the Ge-diode. The 'external' sources are used as a model for background contributions from outside the system, e.g. from uranium and thorium in the walls of the lab. The 'internal' sources are a model for background contributions from sources close to the Ge-diodes, i.e. impurities in the diode holders.

Further on we will refer to gammas from a source as 'coincident' or 'cascading gammas' when they are emitted in a cascade with a time constant that is small compared to the time resolution of the detection of energy deposition in the LAr. An example for this is the ^{60}Co-decay (figure 6.1). ^{60}Co decays with a branching ratio of 99.925% to the 2505 keV excited level (4+) of ^{60}Ni. This decays with a branching ratio of 99.9736% to the 1332 keV excited level which decays with a half life of 0.73 ps to the ground state. So the ^{60}Co-decay is dominated by the 1173 keV and 1332 keV γ-s which are emitted in a cascade with a time constant of the order of a pico-second. Within the width of the gate applied to the ADC for the detection of the energy deposition in the LAr (6 μs, see section 4.3) these gammas are detected in coincidence.

Conversely we refer to a gamma quantum as 'single', when it is not intrinsically coincident with any other decay that can be detected via the LAr scintillation within our time window. This either means that only one γ is emitted in the decay, or that the time constant of any cascade or chain of which the decay is part is long compared to the time-window of 6 μs or that the gamma is only coincident to decays that can not be detected by the LAr.

As discussed in section 2.3.2 when a gamma is Compton scattered in a diode it may deposit its remaining energy in the LAr. This means that the Compton continua are expected to be suppressed for all sources. Events where there is no energy deposition in the LAr, however, are not suppressed. This means that the full energy peaks of 'single' gammas are expected to

Source	nomin. activity	acquis. date	half life	current activity	LAr trigger rate	position	notes
None	N/A	N/A	N/A	N/A	1.2 kHz	N/A	natural background
^{241}Am	3 kBq	2006	432.2 y	3 kBq	1.94 kHz	internal	single 60 keV line
^{137}Cs	1 kBq	2005	30.07 y	1 kBq	2,78 kHz	internal	single 662 keV line
^{137}Cs	10.8 μCi	4.4.1969	30.07 y	170 kBq	48.3 kHz	external	
^{57}Co	43.5 kBq	1.8.2003	271.8 d	1.84 kBq	2.0 kHz	external	measure light-yield
^{60}Co	641 Bq	28.01.05	5.27 y	500 Bq	2.31 kHz	internal	2 coincident lines
^{60}Co	475 kBq	1.11.99	5.27 y	186 kBq	78.6 kHz	external	2 coincident lines
^{54}Mn	440 kBq	1.11.99	312.3 d	1.34 kBq	2.11 kHz	external	1 line 835 keV
^{226}Ra	936 Bq	5.9.2005	1600 y	935.9 Bq	3.2 kHz	internal	
^{228}Th	3 kBq	2006	1.91 y	2.12 kBq	8.14 kHz	internal	
^{228}Th	9 kBq	2006	1.91 y	6.36 kBq	19.7 kHz	internal	
^{232}Th	17.5 μCi	16.06.78	1.91 y	20.9 Bq	1.41 kHz	external	
^{232}Th	4.1 kBq	21.4.89	1.4e10 y	4.1 kBq	4.49 kHz	internal	homemade

Table 6.1: A list of the sources used in the measurements in this work.

be mainly suppressed by random coincidences. Their suppression by random coincidences is therefore a good model for the suppression of the $0\nu\beta\beta$ signal, which is a full energy deposition inside one diode as well. Full energy peaks from a 'coincident gamma' originating from a cascade, however, can be suppressed if a second gamma from the cascade deposits energy in the LAr.

The rate of random coincidences and the probability for a random energy deposition in the LAr for a given event in the HP-Ge diode can be calculated from the rates in the diode and the LAr. Table 6.2 summarises the trigger rates measured in the diode, those in the LAr, the rate of random coincidences and the probability to suppress an event in the HP-Ge diode by random coincidence for the internal sources used in the measurements below.

Source	R_{Ge} [Hz]	R_{LAr} [kHz]	R_{rnd} [Hz]	P_{rnd} [%]
Background	6.87	1.2	0.05	0.7
^{137}Cs	9.84	2.78	0.16	1.7
^{60}Co	12.1	2.31	0.17	1.4
^{232}Th	22.3	4.49	0.60	2.7
^{226}Ra	28.9	3.2	0.55	1.9

Table 6.2: A summary of the rates measured in the HP-Ge diode (R_{Ge}) and the LAr (R_{LAr}) and the random coincidence rate R_{rnd} and random coincidence probability P_{rnd} calculated from the measured rates.

6.2 First test of background suppression

A first test of the principle of background-suppression was performed in the pilot setup. A ^{54}Mn-source was mounted 4 cm above a 168 g p-type Ge-diode. ^{54}Mn decays under emission of a single gamma quant with an energy of 834.8 keV. Figure 6.2 shows the results of this first
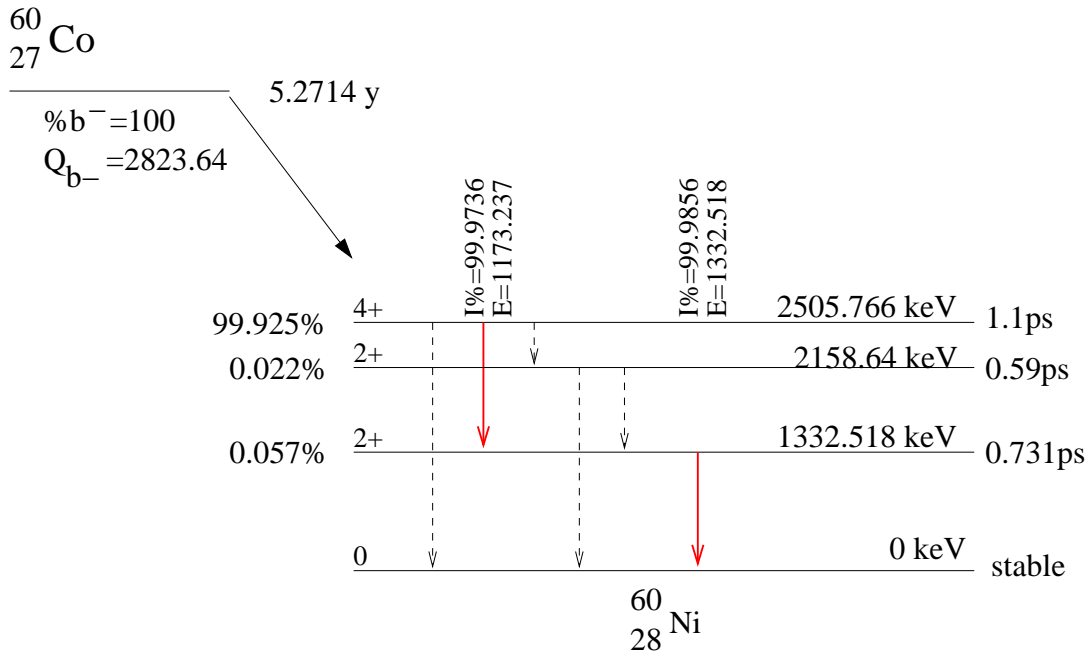
Figure 6.1: The decay scheme for the ^{60}Co-nucleus. An example for 'coincident γ-s' from a cascade.

test run. The spectrum in blue is the unsuppressed spectrum of the energy deposition in the Ge-diode. The spectrum in red is the spectrum remaining after the cut discarding all events with simultaneous energy deposition in the LAr. A suppressed spectrum obtained in such a way is generally referred to as anti-Compton spectrum. For the detection of energy deposition in the LAr a photo electron yield of 250 pe/MeV was achieved in this first test setup.

The suppression factor in the Compton region is approximately 5. The full energy peak is not suppressed, as it is expected from the suppression principle (see section 3.2). To our knowledge this has been the first time that a bare HP-Ge diode was operated in LAr, using the LAr scintillation light for background suppression. After this encouraging first step, an improved system was built for a more extensive investigation of various sources.
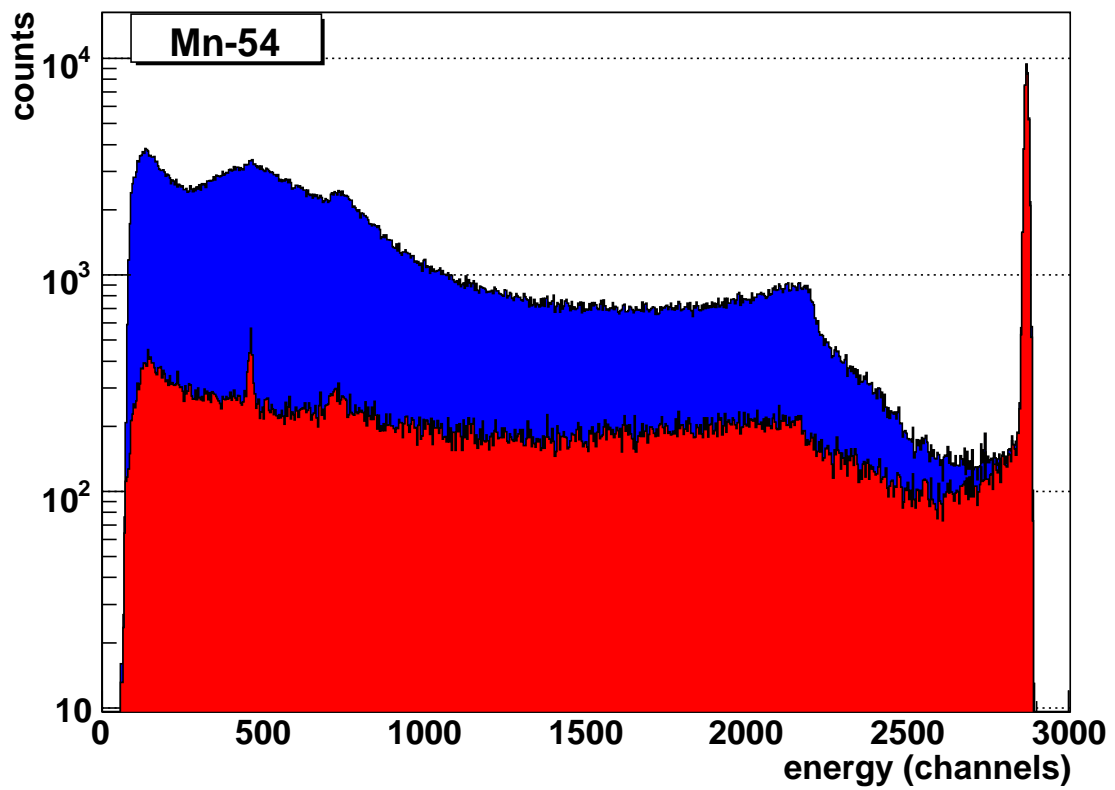
Figure 6.2: The pulse height spectrum of a ^{54}Mn source mounted 4 cm above the 168 g HP-Ge-diode in the LAr. Blue: unsuppressed spectrum. Red: spectrum remaining after the veto-cut on the detection of scintillation light. Plotted logarithmic scale.

6.3 Unsuppressed energy spectra and anti-Compton spectra for various γ-sources

The experimental data presented below were obtained with the improved system described in chapter 4 using a set of γ sources (for the properties of the sources see table 6.1). For each source first the unsuppressed raw spectrum in counts vs. ADC channel number is shown together with the corresponding energy calibration plot. γ-lines of known energy are chosen as calibration points to calculate the energy per channel. The measured pedestal of the DAQ system is selected as zero-point of the energy. The same calibration is applied to the anti-Compton spectrum from the same run. The spectra from different data-taking runs have to be calibrated separately, to be robust against changes in the DAQ electronics. After calibration and rebinning in 1 keV bins, the data from different runs can be added to increase the statistics. To be able to compare the different sources with the background and with each other all spectra are normalised to the data taking run time and are then shown in rate (counts per second per keV bin) vs. energy in keV. For each source the unsuppressed spectrum is shown in blue and the anti-Compton spectrum is shown in red.

6.3.1 Natural background

To determine the correct suppression factors for the sources investigated it is crucial to know the background of the system, without any artificial sources. Since the background varies from site to site, only the suppression of the contribution of known sources is a directly scalable to other experimental sites and setups. This means the measured background in the setup needs to be subtracted from the measured spectra from specific sources to determine the correct suppression efficiencies. This means that the first step was to measure the background in the setup in the Low Level Laboratory (LLL).

For the energy calibration there are two distinct, known lines in the natural background spectrum: The 1460.83 keV line from ^{40}K and the 2614.533 keV line from ^{208}Tl, which is part of the ^{232}Th decay chain. The third point is the measured pedestal as zero point. Figure 6.3 and 6.4 show the uncalibrated spectrum and the calibration plot respectively. The conversion factor between channels and energy is 0.741 ± 0.0015 keV/channel.

Figure 6.5 shows the calibrated background spectrum the system plotted in counts per second. The blue line is the total spectrum in the Ge-diode. The red line is the anti-Compton spectrum. The ^{40}K 1461 keV γ-line is not suppressed, as it is expected for single full energy lines. The ^{208}Tl 2614 keV γ-line is also unsuppressed since the ^{232}Th background from which it originates is mostly situated in the lab walls. This means that when one γ from the ^{208}Tl hits the diode, it is unlikely that a second γ from the same decay hits the detector simultaneously because of the distance of the background source from the setup

For comparison this background spectrum is shown in grey in the plots of the source spectra. The unsuppressed background is plotted in dark grey and the anti-Compton background spectrum is shown in light grey.

6.3.2 Spectra from ^{137}Cs-γ-sources

The expectation that the Compton continuum of a source spectrum is suppressed while the full energy peaks remain unsuppressed is easy to test by using a source where only one γ per decay is emitted. Such a source is ^{137}Cs, which has a single γ-line at 662 keV and was selected as the first source to be investigated. Figure 6.6 shows the decay scheme of ^{137}Cs.
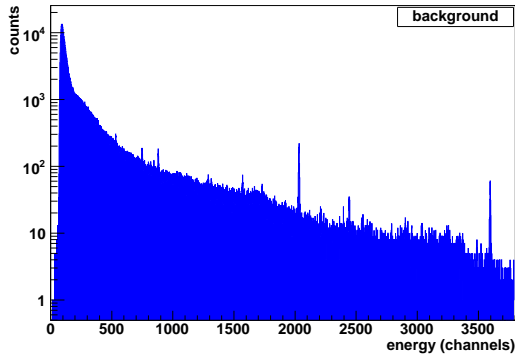
Figure 6.3: The uncalibrated background spectrum of our system, taken with the Ge-diode without veto. Plotted in energy in ADC-channels vs. total counts in logarithmic scale.

Figure 6.4: The energy calibration plot for the background spectrum. The data points are from left to right: pedestal, 1461 keV γ and 2614 keV γ. Plotted in channels vs. energy in keV.

Figure 6.7 and figure 6.8 show the uncalibrated ^{137}Cs spectrum and the calibration plot respectively. Since the source has only one line at 661.657 keV only that line and the pedestal as zero point are available for calibration. The conversion factor taken from the fit is 0.3038 $\pm$ 0.00065 keV/channel.

Figure 6.9 shows the spectrum from an internal ^{137}Cs-γ-source in linear scale. The suppression of the Compton-region is clearly visible. For better visibility of the anti-Compton spectrum and the background, the same spectrum is shown in figure 6.10 in logarithmic scale. The full energy peak appears mostly unsuppressed, but in linear scale a slight excess ($\mathcal{O}(1\%)$) of the unsuppressed spectrum over the anti-Compton spectrum is visible. This is due to random coincidences between the full energy deposition of the ^{137}Cs-γ in the Ge-diode and energy deposition from the background in the LAr.
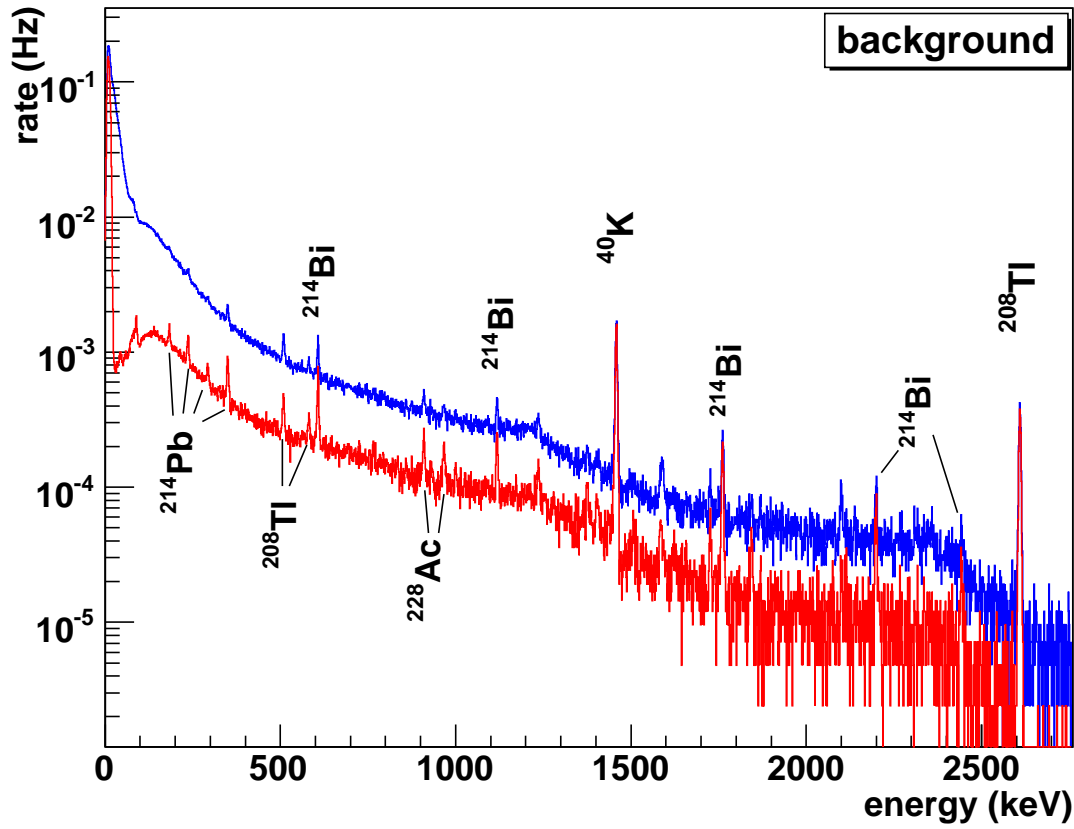
Figure 6.5: The background of the system in the LLL@MPI-K. Blue: unsuppressed data, red: data after applying the veto cut. Plotted in rate per keV vs. energy in 1 keV bins.
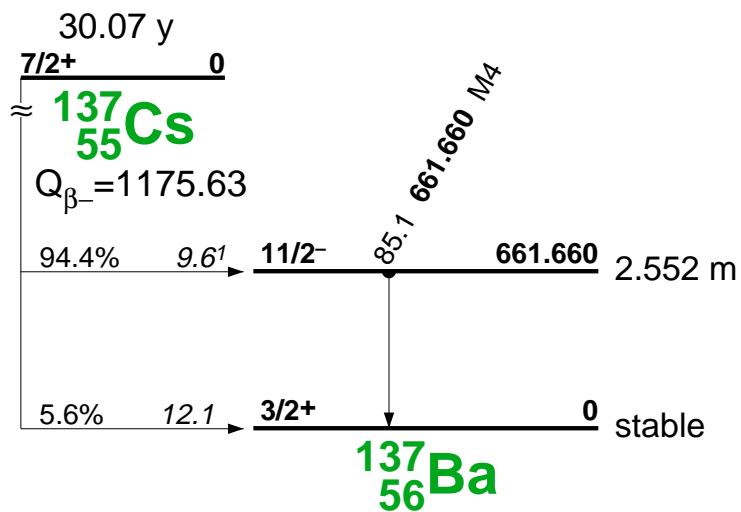
Figure 6.6: The decay scheme of ^{137}Cs [Fir96].
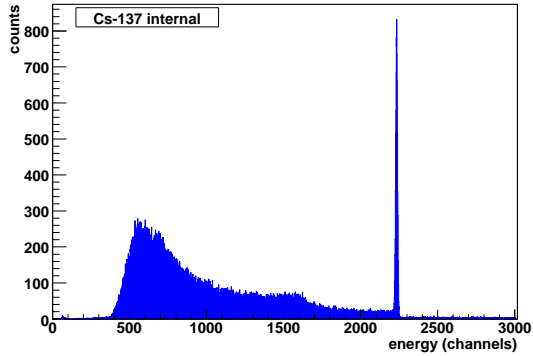
Figure 6.7: The uncalibrated ^{137}Cs spectrum taken with the Ge-diode without veto. Plotted in energy in DAQ-channels vs. total counts in linear scale.

Figure 6.8: The energy calibration plot for the internal ^{137}Cs-γ-source. The data points are from left to right: pedestal and 662 keV γ. Plotted in channels vs. energy in keV.
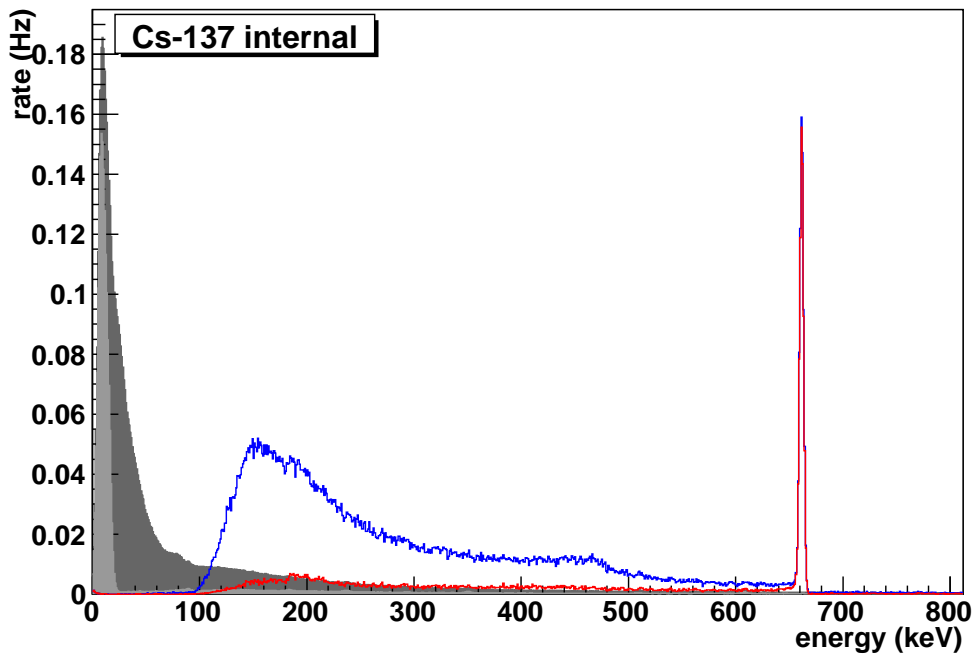
Figure 6.9: The unsuppressed energy spectrum (blue) and the anti-Compton spectrum (red) from an internal ^{137}Cs-γ-source in linear scale. The background of the system is shown in grey. The cutoff on the low energy side of the source spectra is an effect of the trigger threshold.
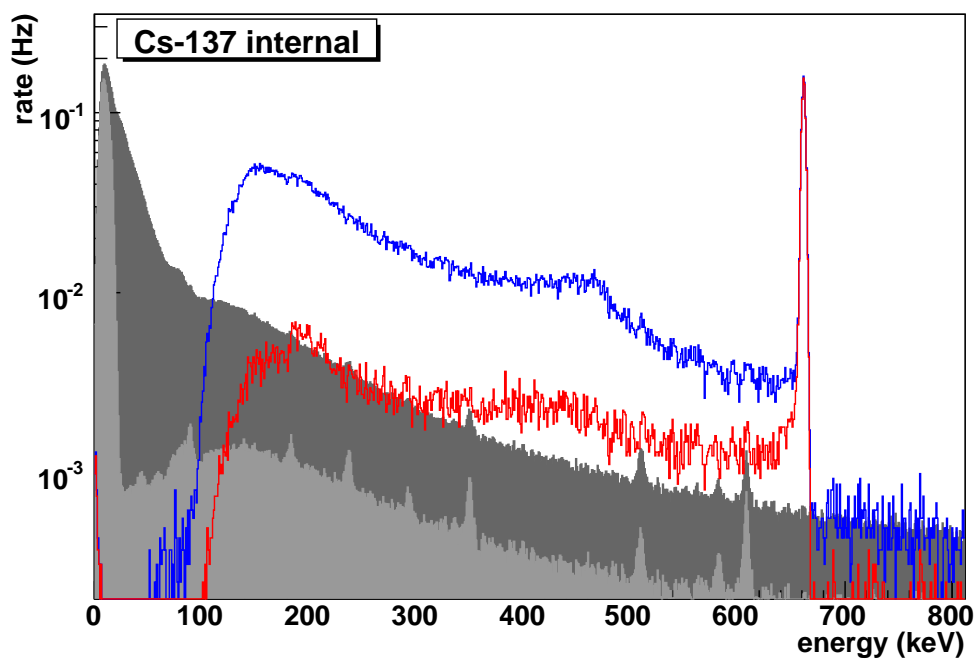
Figure 6.10: The same spectra from a ^{137}Cs-γ-source as seen in figure 6.9, plotted in logarithmic scale for better visibility of the background.

6.3.3 Spectra from ^{60}Co-γ-sources

Due to its cosmogenic production in germanium itself and in copper, which is used for the Ge-diode holders, ^{60}Co is one of the most crucial background isotopes in GERDA as discussed in section 2.3. While the energy of each of the γ-s emitted in the ^{60}Co-decay is below the energy-region of interest for the $0\nu\beta\beta$-decay (2039 keV), they can still contribute to the background in that region by summation. This is possible because, as discussed above, the gammas are emitted in a cascade with a time constant of 0.7 ps and are coincident within the time resolution of the HP-Ge-diodes. The summation spectrum extends up to the summation peak at 2505.8 keV. For the decay scheme of ^{60}Co see figure 6.1.

Figure 6.11 shows the uncalibrated spectrum from a ^{60}Co-source internal to the LAr, 4 cm above the diode (see figure 4.1 for source positions). Figure 6.12 shows the corresponding calibration plot. As calibration points the 1173.2 keV and the 1332.5 keV γ-lines from the ^{60}Co-decay are chosen, as well as the 1460.8 keV ^{40}K-γ-line and the 2614.5 keV ^{208}Tl-γ-line from the natural background. The calibration plot shows a linear dependence of channels to energy with a conversion factor of 0.7369 ± 0.0011 keV/channel.
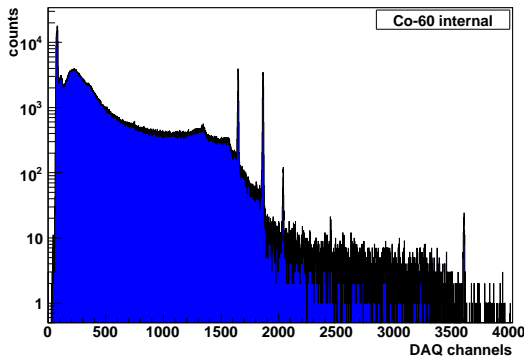
Figure 6.11: The uncalibrated spectrum from an internal ^{60}Co-γ-source taken with the Ge-diode without veto. Plotted in energy in ADC-channels vs. total counts in logarithmic scale.
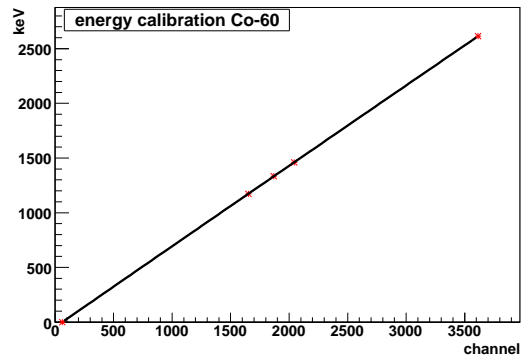
Figure 6.12: The energy calibration plot for the internal ^{60}Co-γ-source. The data points are from left to right: pedestal, 1173 keV γ, 1332 keV γ, 1461 keV γ and 2614 keV γ. Plotted in channels vs. energy in keV.

Figure 6.13 shows the calibrated and normalised spectrum in the Ge-diode from the internal ^{60}Co-γ-source. The energy scale is chosen such as to include the summation peak at 2506 keV and the ^{208}Tl peak at 2614 keV. Again the full spectrum is plotted in blue und the anti-Compton spectrum remaining after the veto cut is plotted in red.

Since the two gammas in the ^{60}Co-decay are emitted in a cascade as discussed above, we expect them to be suppressed for internal sources. When one of the γ-s deposits the energy in the Ge-diode and the source is inside the LAr volume, then there is a high probability that the other gamma deposits energy in the LAr. For external sources things look different. The probability that the second γ hits the active volume, when the first γ hits the Ge-diode, depends on the solid angle and thereby decreases with increasing the distance of the source from the LArGe detector. This means that the peak suppression is also expected to be the less the further the source is away from the detector.

Figure 6.14 shows the calibrated and normalised spectrum of an external ^{60}Co γ-source. The source is used as a model for far away sources. It was placed in front of the window in the lead
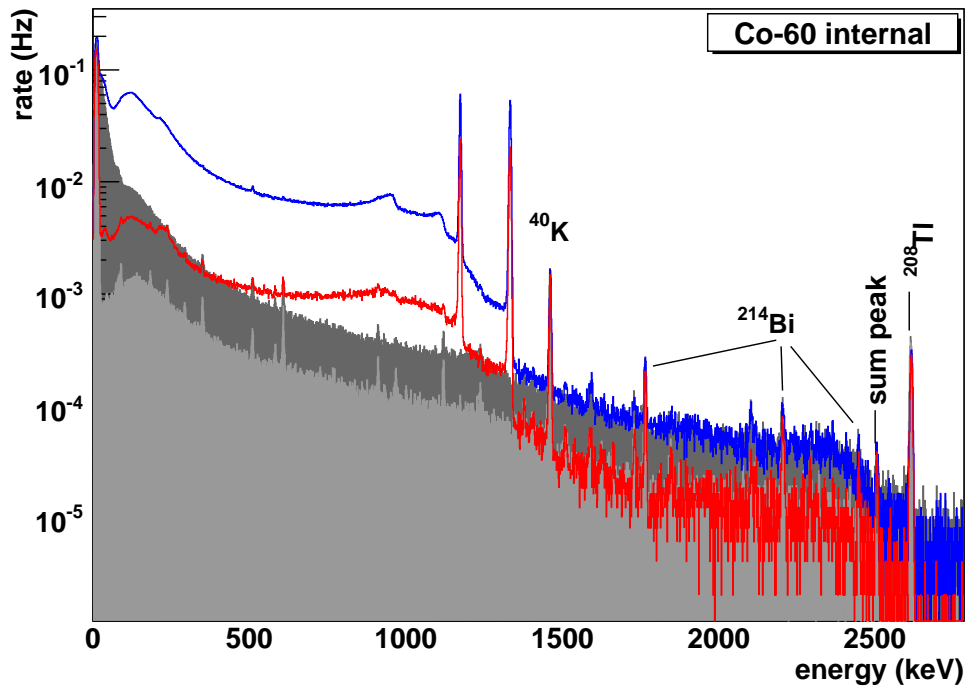
Figure 6.13: The spectra from an 'internal' ^{60}Co-γ-source in logarithmic scale. Including the summation peak at 2505 keV and the 2614 keV ^{208}Tl-line from the background.
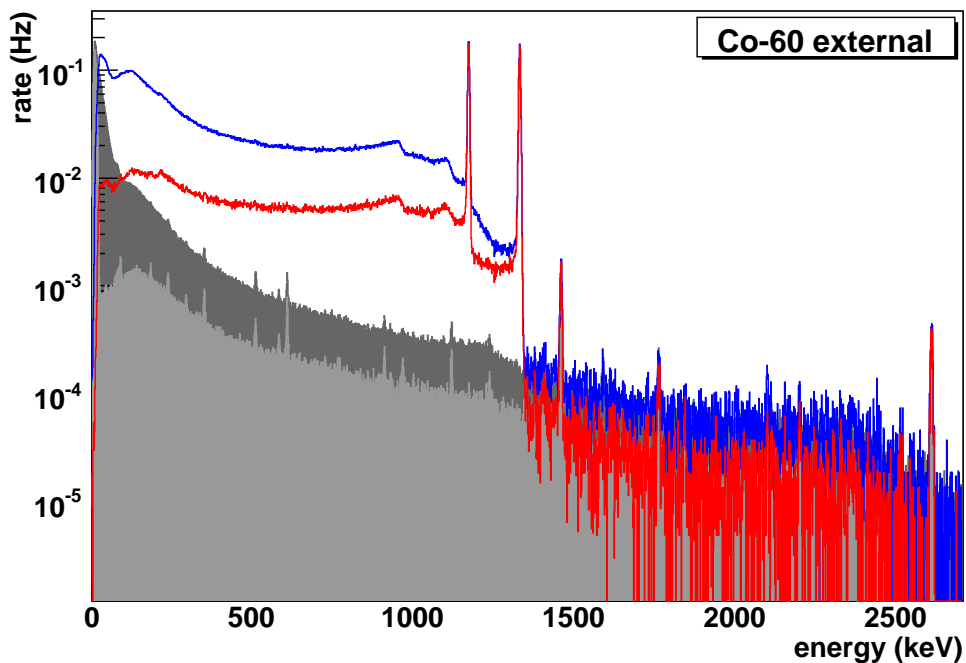
Figure 6.14: The spectra from an 'external' ^{60}Co-γ-source in logarithmic scale. The source was placed in 30 cm distance, irradiating the system through the window in the lead shield.

shield (see chapter 4) in 30 cm distance. The window measures 5x5 cm and serves as collimator, reducing the effective solid angle and thereby reducing the chance of both γ-s hitting the LArGe detector simultaneously.

Figure 6.15 and 6.16 show a comparison of the single-γ full energy peaks for an internal and an external source in linear scale. The peak suppression for the internal source is clearly visible, while for the external source the peaks are only slightly suppressed, mainly by random coincidences. The peak at 1173 keV appears to be more strongly suppressed than the peak at 1333 keV, but this apparent suppression has its origin in the Compton-plateau of the 1333 keV line, upon which the 1173 keV peak sits.
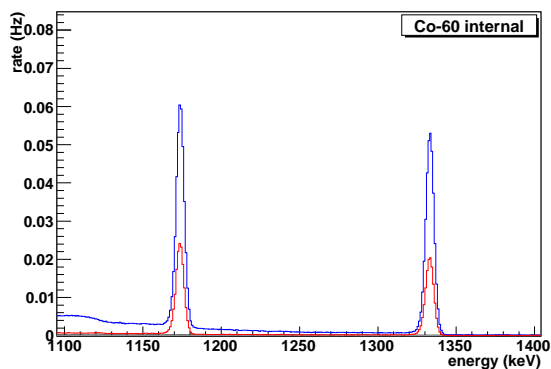
Figure 6.15: A zoom on the peaks from an internal ^{60}Co-γ-source. The unsuppressed peaks are plotted in blue and the peaks remaining after the veto-cut are plotted in red.
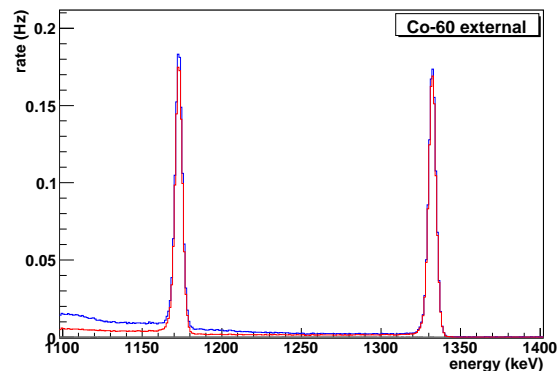
Figure 6.16: The same plot for an external ^{60}Co-γ-source. The peaks are only slightly suppressed, mostly due to random coincidences.

6.3.4 Spectra from ^{232}Th-γ-sources

Another very important isotope concerning the background in GERDA is ^{232}Th especially due to its progeny ^{208}Tl. ^{232}Th is an abundant natural radio-isotope and the gamma spectrum from the decay of ^{208}Tl, which is the dominant contribution to the gamma spectrum of ^{232}Th sources, extends up to 2614 keV, well beyond the RoI. The γ-line at 2614 keV has a branching ratio of 99%, but since it is coincident with several other γ-s (with time-constants of the order of ps), the full energy peak is expected to be suppressed for internal sources. The decay scheme of ^{208}Tl is shown in figure 6.17.
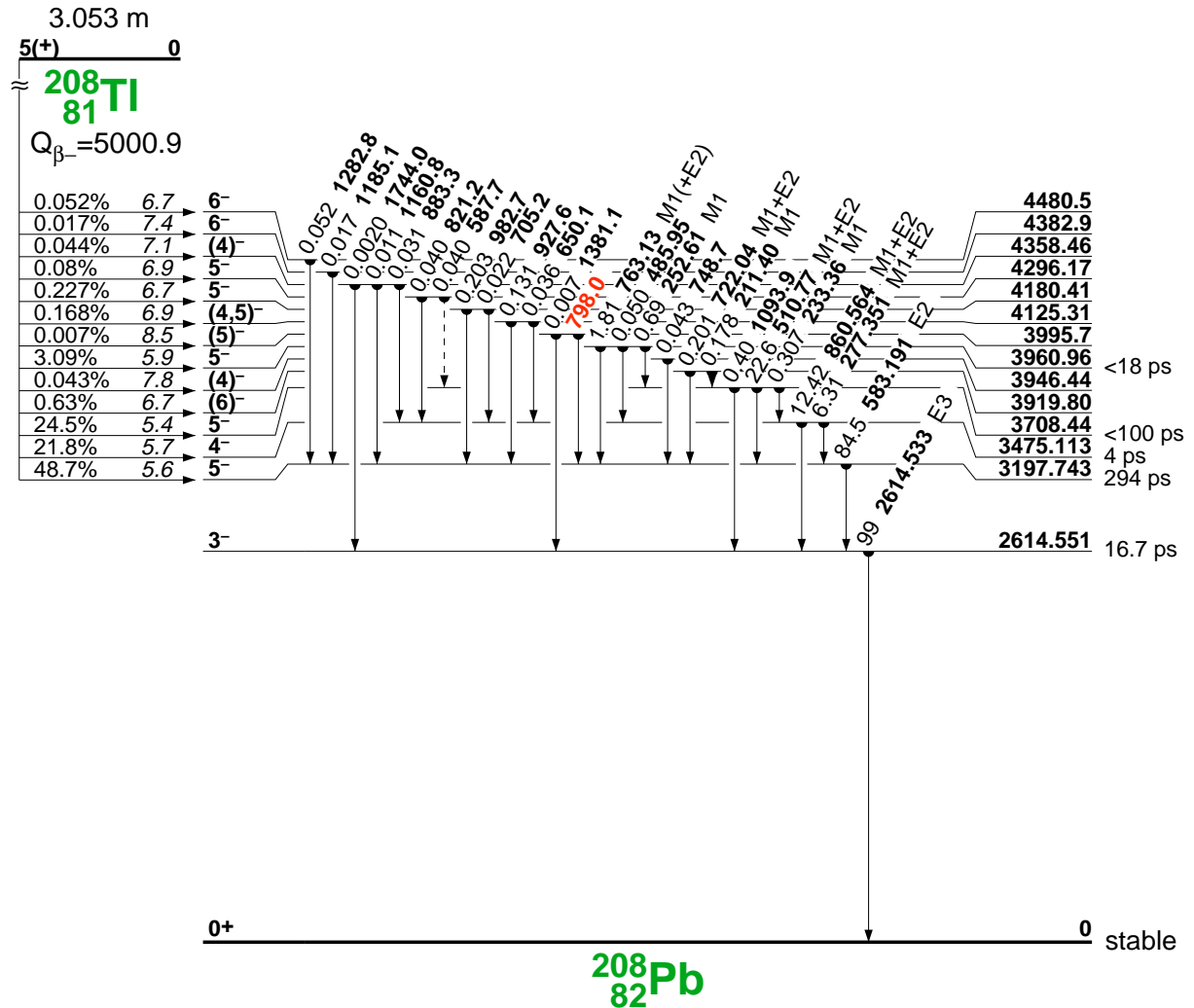
Figure 6.17: The decay scheme of the ^{232}Th progeny ^{208}Tl [Fir96].

Figure 6.18 and figure 6.19 show the uncalibrated spectrum and the energy calibration for the internal ^{232}Th source respectively. Calibration points are the pedestal and the γ-lines at 510.8 keV, 583.2 keV and 860.5 keV (^{208}Tl), 911.2 keV and 969.0 keV (^{228}Ac), 2614.5 keV (^{208}Tl) and the 1460.8 keV γ-line of ^{40}K from the natural background. The conversion factor from channels to keV taken from the fit is 0.7415 ± 0.0012 keV/channel.

Figure 6.20 shows the full spectrum in the Ge-diode from the ^{232}Th-source, again unsuppressed in blue and suppressed by the LAr-veto in red. Like in the other plots the background is shown in the same plot. The background without LAr-veto is drawn in dark grey and the
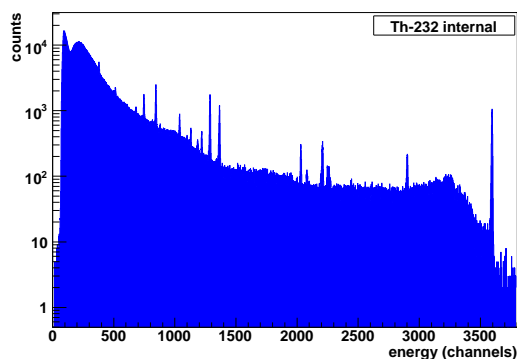
Figure 6.18: The uncalibrated spectrum from an internal ^{232}Th-γ-source taken with the Ge-diode without veto. Plotted in energy in DAQ-channels vs. total counts in logarithmic scale.
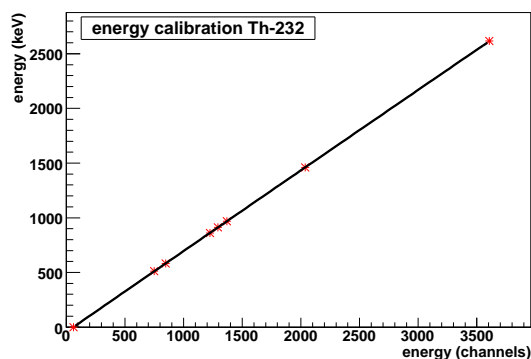
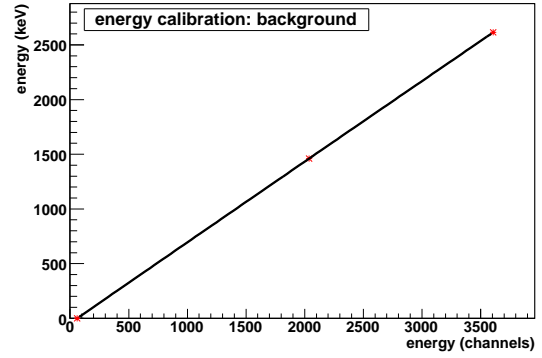Figure 6.19: The energy calibration plot for the internal ^{232}Th-γ-source. The data points are from left to right: pedestal, 510.77 keV, 583.191 keV 860.5 keV 911.205 keV, 968.971 keV, 1460.830 keV, 2614.533 keV.

background remaining after the veto is drawn in light grey. As one can see, the anti-Compton spectrum remaining from the ^{232}Th source after the veto-cut is close to the background of the system without any source.

Figure 6.21 shows a zoom on the RoI in linear scale. In this plot spectra are shown from which the background has been subtracted to allow a precise measurement of the suppression of the ^{232}Th-contribution only. The unsuppressed spectrum from which the unsuppressed background spectrum has been subtracted is shown in solid light blue. The suppressed spectrum from which the suppressed background spectrum has been subtracted is shown in yellow. For comparison the unsuppressed and suppressed spectra without background subtraction are shown in the same plot as blue and red line respectively. The suppression factor in the RoI determined from these background subtracted spectra is 17.2±0.6(stat). This means that only (5.8±0.2)% of the ^{232}Th-spectrum in the RoI remain after the veto-cut.
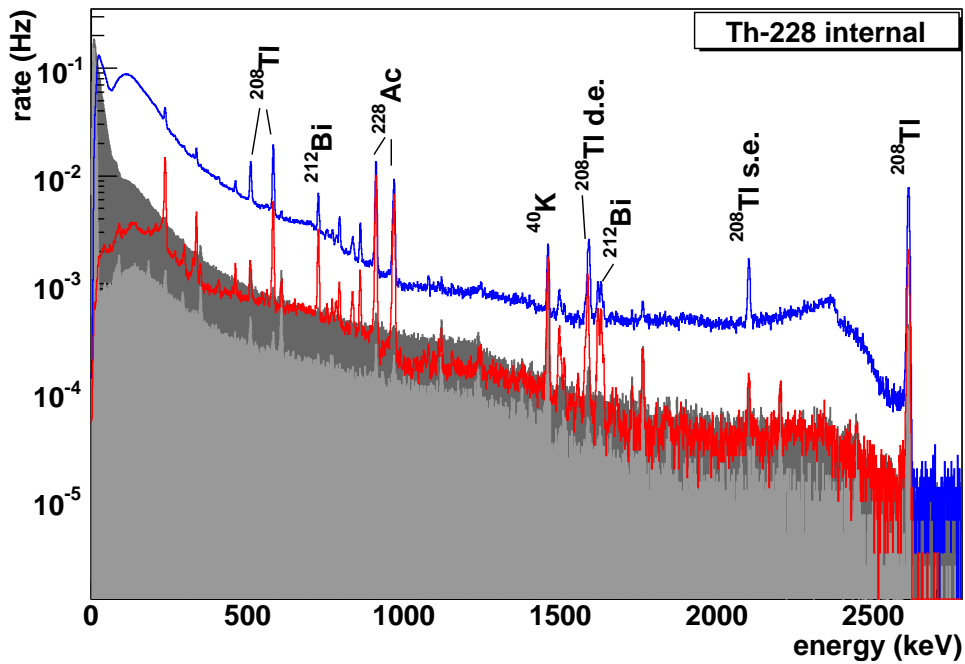
Figure 6.20: The spectra from an internal Th-γ-source. Blue: unsuppressed, red: anti-Compton spectrum. The more prominent lines are market with the isotope they originate from. 's.e.' and 'd.e.' stand for the single and double escape peak of the 2614 keV γ.
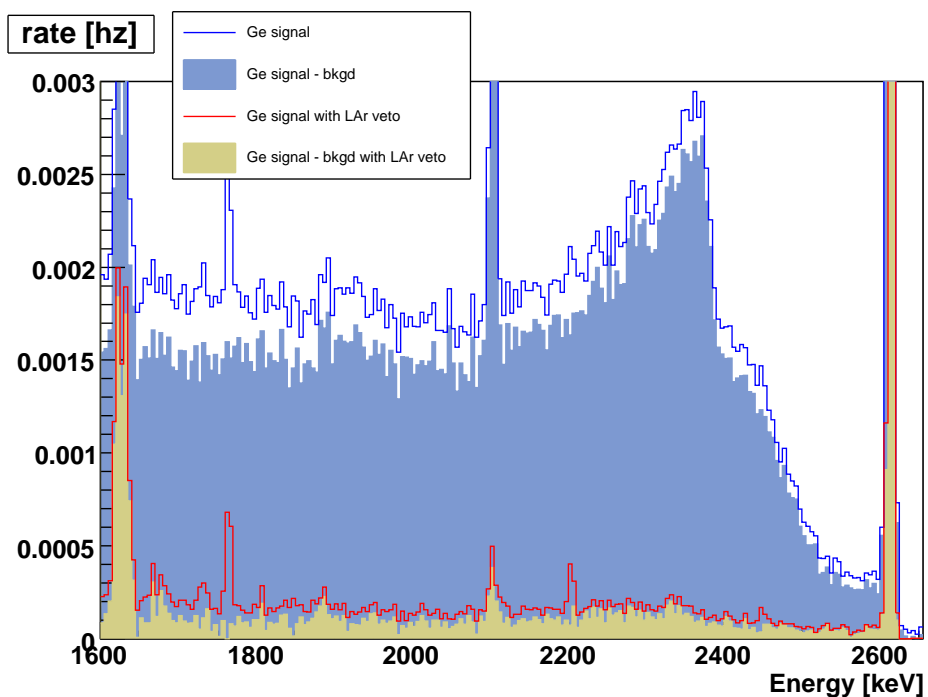
Figure 6.21: A zoom on the region of interest of the Th-spectra in linear scale. The solid spectra were obtained by subtracting the background from the raw data.

6.3.5 Spectra from a ^{226}Ra-γ-source

Another isotope that is important for the background estimation in GERDA and was investigated in this experiment is ^{226}Ra along with its daughter, the noble gas ^{222}Rn. They are part of the ^{238}U decay chain. ^{226}Ra is an α emitter and the γ-spectrum from ^{226}Ra sources is dominated by the contribution of its progeny ^{214}Bi. The γ-spectrum from ^{214}Bi extends up to 3270 keV with a line with a branching ratio of 1.6% at 2448 keV. This is above $Q_{\beta\beta}$ and can therefore contribute to the background in the region of interest. The lines in the high energy part of the spectrum down to 1730 keV are emitted 'single'. The lower energy lines are emitted in cascades and are detected in coincidence within our time-resolution. The decay scheme of ^{214}Bi is included in the appendix in section B since it would require too much space here.

Figure 6.22 and figure 6.23 show the uncalibrated spectrum and the energy calibration for the internal ^{226}Ra source respectively. Calibration points are the pedestal, the γ-lines at 609.3 keV, 1120.3 keV, 1764.5 keV, 2447.9 keV and the γ-lines from the natural background at 1460.8 keV (^{40}K) and 2614.5 keV (^{208}Tl). The conversion factor is 0.7396 ± 0.0012 keV/channel.
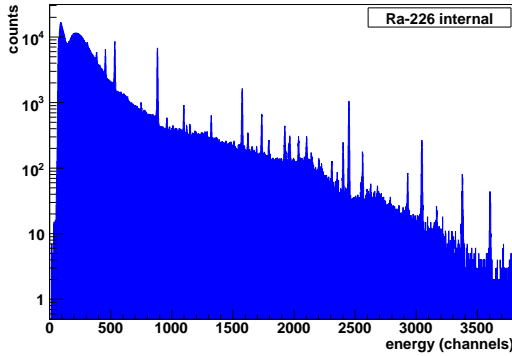
Figure 6.22: The uncalibrated spectrum from an internal ^{226}Ra-γ-source taken with the Ge-diode without veto. Plotted in energy in DAQ-channels vs. total counts in logarithmic scale.
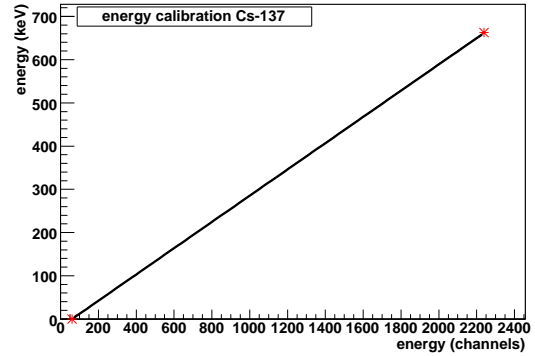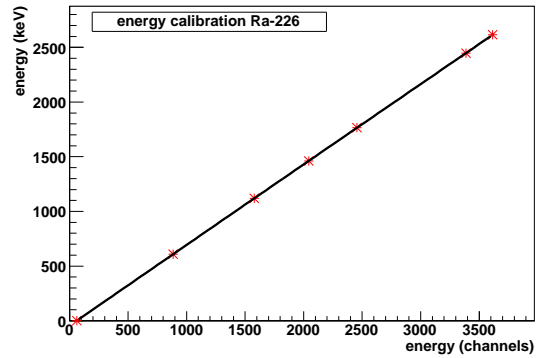
Figure 6.23: The energy calibration plot for the internal ^{226}Ra-γ-source. The data points are from left to right: pedestal, 609.312 keV, 1120.287 keV, 1460.83 keV, 1764.494 keV, 2447.86 keV and 2614.533 keV.

Figure 6.24 shows the spectrum of an internal ^{226}Ra source. As expected the high-energy lines show only slight suppression while the lines below 1.7 MeV are suppressed. It is noticeable that the lines from the source spectrum are also visible in the background spectra drawn in grey, which were taken without any artificial source present. The members of the ^{238}U decay chain and especially ^{222}Rn are dominant contributions to the natural background. It is also visible in the plot that the line at 2.6 MeV is not part of the ^{226}Ra-source-spectrum, but part of the natural background only: The peak in the background spectrum at 2.6 MeV is of the same height as it is in the source spectrum. This line is the ^{208}Tl 2614 keV gamma line from the ^{232}Th decay-chain.
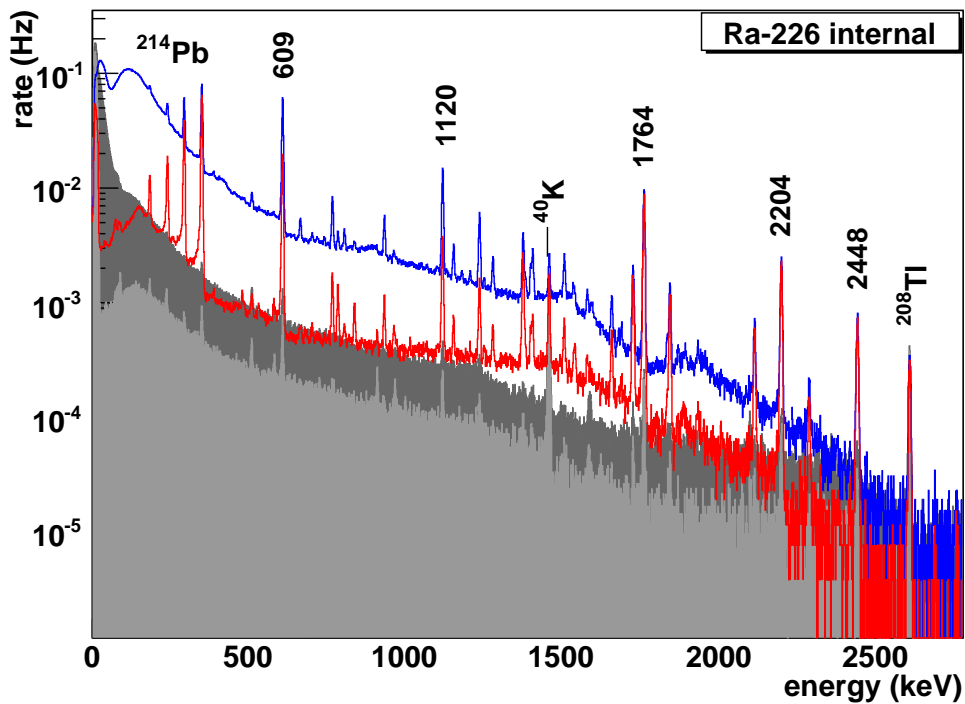
Figure 6.24: The spectra from an 'internal' ^{226}Ra-γ-source. Lines that are coincident within our time-window are suppressed (low energy lines). 'Single' lines are unsuppressed (high energy lines of the spectra). The dominant lines from ^{214}Bi are marked with their energy in keV, other prominent lines are marked with their respective isotope.

6.4 Data treatment

6.4.1 Stability monitoring

Every two days the dewar in the LArGe setup has to be refilled with LAr. For this process the PMT and Ge-diode were switched off. It takes several hours after refilling for the microphonic noise due to the boiling of the LAr to cease. Only then is the system in stable condition and can be used for precise measurements. This limits the effective data taking time for one run to ~40 hours. To increase statistics several data runs were merged. The stability of the peak rates and the energy resolution for the different runs were monitored. The following tables show the results of this monitoring for the background (table 6.3), ^{60}Co (table 6.4), ^{226}Ra (table 6.5) and ^{232}Th (table 6.6). For ^{137}Cs one run provided sufficient statistics since it is a comparatively simple source with just one γ-line.

Since the main goal of the LArGe setup was a test and investigation of the background suppression and not doing γ-spectroscopy the system was not optimised for energy resolution. This is the reason why the energy resolution of the HP-Ge diode cited here is worse than the energy resolution that can be achieved with similar HP-Ge diodes in other setups.

Source	Energy	Date	FWHM [keV]	rate [/h]	ratio
^{40}K	1461 keV	Oct. 29th	5.83	36.8±1.2	
		Nov. 9th	6.34	31.6±1.0	
		Nov. 21st	5.98	30.4±2.4	
		Nov. 28th	8.59	38.0±1.9	
^{208}Tl	2614 keV	Oct. 29th	6.66	10.8±0.6	0.29±0.02
		Nov. 9th	6.54	10.4±0.5	0.32±0.02
		Nov. 21st	8.81	7.1±1.3	0.23±0.05
		Nov. 28th	7.54	10.3±0.8	0.27±0.03

Table 6.3: The peak resolution and rates as well as the ratio of the ^{208}Tl peak to the ^{40}K peak for different background data taking runs.

The rates in the background peaks in absence of any source were found to vary significantly between different runs (table 6.3). However for the ^{40}K/^{208}Tl peak rates the error regions overlap. No convincing explanation for these variances in background rate has been found. However the average of the different background rates agrees with the average peak rates from background peaks recorded during the source runs (table 6.4). So the average over the background runs was taken as background for the source runs.

In table 6.4, which lists the peak rates in the ^{60}Co runs, it is noticeable that the rates in the peaks of the source from the runs from Nov. 14 and 16 are significantly lower than those from the runs from Dec. 8 and 10. The rates in the background peaks, however, don't show this increase in rate. This is an effect of source distance since the source was not inserted far enough into the source tube in the first two runs. As it is the goal of the measurements with internal sources to simulate background contributions from materials close to the Ge-diodes, only the runs from Dec. 8 and 10 were used for this evaluation.

For ^{226}Ra (table 6.5) the variance in rate between the runs is again somewhat bigger than the statistical error. The peak ratios between the different peaks, however, are stable. To achieve a high enough statistic the files were merged and the average of the rates was taken for evaluation.

Also between the two ^{232}Th runs the difference between the peak rates is a bit larger than

Source	Energy	Date	FWHM [keV]	rate [/h]
^{60}Co	1173 keV	Nov. 14th	6.08	1235±7
		Nov. 16th	6.05	1240±6
		Dec. 8th	6.31	1408±7
		Dec. 10th	5.88	1398±9
	1332 keV	Nov. 14th	6.00	1151±6
		Nov. 16th	5.94	1148±5
		Dec. 8th	6.42	1309±6
		Dec. 10th	5.85	1310±8
^{40}K ^{b}	1461 keV	Nov. 14th	6.52	36±1
		Nov. 16th	6.08	38±1
		Dec. 8th	7.33	35±1
		Dec. 10th	6.20	39±2
^{208}Tl ^{b}	2614 keV	Nov. 14th	7.25	8.9±0.6
		Nov. 16th	7.65	8.3±0.6
		Dec. 8th	8.45	9.0±0.6
		Dec. 10th	8.43	9.9±0.8

Table 6.4: The peak resolution and rates for different ^{60}Co data taking runs. The peaks marked with ^{b} are contributions from the background.

the statistical error. Within 2σ the rates agree, however, and the peak ratio is stable. Again the data from both runs were merged for increased statistics.

6.4.2 Background subtraction

As mentioned above it is necessary to subtract the background from the spectra for specific sources to get a valid estimation of the suppression efficiency for the contribution from the investigated source only. After calibrating the spectra as discussed above, rebinning them in 1 keV bins and normalising them to the duration of the respective data run, the subtraction is straightforward. This treatment also allows an easy comparison between data from different runs as well as their addition to increase statistics. The unsuppressed background spectrum

Energy	Date	FWHM [keV]	rate [/h]
609 keV	Oct. 25th	5.17	1139±12
	Nov. 18th	5.68	1145±7
	Nov. 20th	6.16	1088±9
1120 keV	Oct. 25th	5.34	283±6
	Nov. 18th	6.46	299±4
	Nov. 20th	6.55	253±5
1764 keV	Oct. 25th	5.55	220±5
	Nov. 18th	6.16	222±3
	Nov. 20th	6.95	206±3

Table 6.5: The peak resolution and rates for different ^{226}Ra data taking runs.

Energy	Date	FWHM [keV]	rate [/h]
911 keV	Nov. 4th	5.92	232±2.6
	Nov. 6th	6.01	227±3.2
	combined	5.95	229±2.1
2614 keV	Nov. 4th	6.71	167±2.2
	Nov. 6th	6.65	170±1.8
	combined	6.93	161±1.5

Table 6.6: The peak resolution and rates for different ^{232}Th data taking runs.

was subtracted from the unsuppressed source spectrum as were their respective anti-Compton spectra.

Ideally the subtraction of the background should not change the position or energy resolution of the peaks. Figure 6.25 shows a comparison of the 2614 keV ^{208}Tl-peak from the ^{232}Th source before and after the subtraction and the same comparison for the 609 keV ^{214}Bi peak from the ^{226}Ra source.

The peak position of the 2614 keV peak is unchanged at (2613.4±1.6) before and after background subtraction. The energy resolution is unchanged as well at σ=(2.95±0.02) keV → FWHM=(6.93±0.05) keV before and after background subtraction. The 609 keV peak is at (608.6±0.9) keV before and after subtraction with an energy resolution of (5.70±0.03) keV FWHM before subtraction and a resolution of (5.65±0.05) keV FWHM after subtraction. The peak positions and energy resolutions are stable under background subtraction. This means that the energy calibrations for the background and the source run data are in good agreement and that the method of background subtraction is reliable.

6.4.3 Determining suppression efficiencies

After normalising and the subtracting the background from the spectra, the determination of the suppression efficiency in a flat part of the spectrum, like the RoI, is straightforward. The integral over a fixed energy range in the unsuppressed spectrum is compared to the integral over the anti-Compton spectrum for the same energy range. We define the suppression factor as the factor by which the unsuppressed spectrum has to be divided to get the suppressed spectrum, i.e. $SF = I_{unsuppressed}/I_{suppressed}$. A suppression factor of 1 corresponds to no suppression at all. The inverse of the suppression factor is the survival probability, which gives the probability for an event induced by a γ from the investigated source to remain after the veto cut (to 'survive' the cut).

To determine peak suppression, however, the peak has to be corrected for the plateau background. The plateau background is the contribution of Compton-scattered γ-s with a higher energy from the same source that forms a plateau on which the peak sits. The integral of the spectrum over ±1σ around the peak is taken. Next the plateau background has to be subtracted. To determine it, the integral over a range corresponding to 2σ of the peak is taken in a distance equivalent to 4σ both below and above the peak. The average of these integrals, divided by the number of bins in the integral, is taken as the plateau background per bin and is subtracted from the integral over the peak. These corrected integrals are then used to determine the suppression factor and the survival probability for the peak.
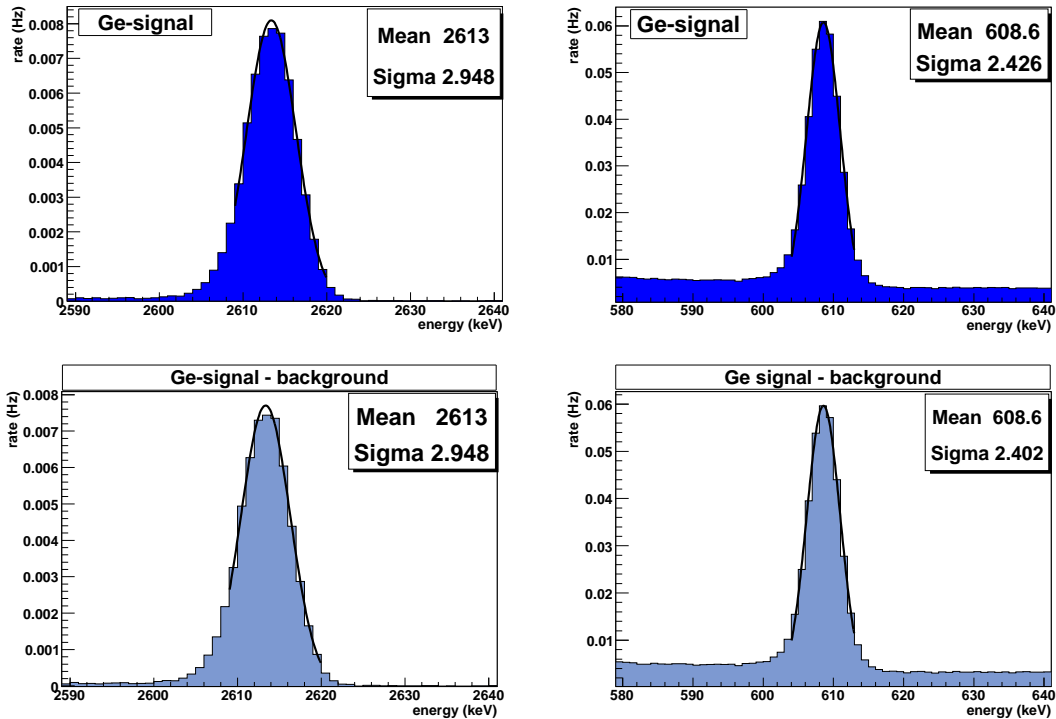
Figure 6.25: A comparison of the position and energy resolution of the 2614 keV ^{208}Tl peak (left) and the 609 keV ^{214}Bi peak (right) before and after background subtraction.

6.5 Summary of the suppression efficiency

Table 6.7 summarises the suppression efficiency, giving both the suppression factors and survival probabilities for the investigated sources in different energy regions.

The results of these measurements do not only show that the LAr-scintillation veto technique is a promising tool for background suppression. They also show that events that do not deposit energy outside the diode, like the full energy deposition of single γ-s like the ^{137}Cs-γ, are not suppressed. Within the error of $<1\%$ of the measurement for the ^{137}Cs source, no peak suppression is found. Since the $0\nu\beta\beta$ signal consists also of events that deposit all their energy inside the diode, no significant data loss is to be expected by applying the veto cut.

In the test system used in this section, the suppression efficiencies are limited by the 10 cm radius of the active volume. The attenuation length for 2.6 MeV gammas in LAr is 20 cm, that means that gammas that are scattered in the HP-Ge diode can escape the active LAr volume without depositing energy in the LAr. With an active volume that is large against the attenuation length the escape probability becomes negligible. The suppression efficiency is then limited only by non active materials close to the diode. These can be the detector support or, in the case of p-type diodes, the dead layer. These non-active materials can absorb γ-s scattered in the diode, thereby preventing them from depositing their energy in the LAr. To make quantitative predictions about the performance of a veto system with a larger active volume, a dedicated Monte Carlo study is necessary, which are presented in the next chapter.

Source	Region	Energy [keV]	suppr. factor	surv. prob.
Background	RoI	[2000-2080]	4.16±0.24	0.240±0.058
	^{40}K-peak	[1461]	1.025±0.026	0.976±0.025
	^{208}Tl-peak	[2614]	1.055±0.051	0.948±0.046
	full range	[0-2700]	3.19	0.313
^{137}Cs	peak	[662]	1.004±0.010	0.996±0.010
		[230-450]	6.536±0.085	0.153±0.002
	full range	[0-700]	4.73	0.211
^{60}Co int	peak	[1173]	2.47±0.01	0.405±0.002
	peak	[1332]	2.59±0.01	0.386±0.002
	RoI	[1900-2100]	2.86±0.24	0.35±0.03
	full range	[0-2700]	5.57	0.180
^{60}Co ext	peak	[1173]	1.025±0.006	0.976±0.006
	peak	[1332]	1.026±0.006	0.974±0.006
	RoI	[1900-2100]	3.41±0.26	0.29±0.02
	full range	[0-2700]	4.23	0.236
^{232}Th	peak	[511]	9.26±0.69	0.108±0.008
	peak	[2614]	4.52±0.10	0.221±0.005
	RoI	[1900-2080]	17.24±0.59	0.058±0.002
		[2125-2350]	15.87±0.50	0.063±0.002
	full range	[0-2700]	13.8	0.073
^{226}Ra	peak	[609]	2.98±0.003	0.336±0.003
	peak	[1120]	3.76±0.07	0.266±0.005
	peak	[1765]	1.07±0.01	0.93± 0.002
		[515-595]	9.62±0.09	0.104±0.002
		[970-1095]	6.45±0.08	0.155±0.002
	RoI	[1870-2080]	3.73±0.07	0.268±0.002
	full range	[0-2700]	7.92	0.126

Table 6.7: A summary of suppression factors and survival probabilities for different sources and energy ranges. A in both cases 1 means no suppression.

Chapter 7

Monte Carlo simulations

This chapter presents the results of Monte Carlo studies that had the goal of estimating the suppression efficiency for a larger system. The validity of the Monte Carlo code is tested by comparison with the experimental data acquired.

7.1 Simulation of suppression efficiency

The simulation of the suppression efficiencies for the various sources was done with MAGE. MAGE is a GEANT4 [AAA$^+$03] based Monte Carlo software package developed by a collaboration between MAJORANA and GERDA to simulate the energy deposition in Ge-diodes and the surrounding material. In the case of the LAr scintillation veto setup, the surrounding material is separated into the active volume and dead material like the diode holder. The major part of the work on the MAGE Monte Carlo code and the implementation of the LArGe geometry into it was done by Marie DiMarco, one of the developers of MAGE. Other help came from Davide Franco and Luciano Pandola. The event generator used was 'decay0' [PTZ00]. The simulation counts an event as 'vetoed' when energy above a selected threshold is deposited in the active LAr volume. Several different thresholds were tested but a one photo-electron threshold reproduces the experimental data best.

The average number of photo electrons produced depends on the energy deposited and the photo electron yield. For the MC simulations 400 pe/MeV were assumed, based on a first estimation of the photo electron yield at that time. The generation of photo electrons is a statistical process, so the photo electron yield gives the average number of photo electrons: $N_{pe}^{av}(E_{dep}) = E_{dep} \cdot 400 \ pe/MeV$ with E_{dep} the energy deposition inside the active LAr volume. The actual number of photo electrons generated follows a Poisson statistic around the average number of pe for small numbers of photo electrons. For large numbers of pe ($N_{pe}^{av} > 10$) this approximates to a Gaussian distribution.

MAGE produces ideal spectra with an energy resolution of 1 eV. To simulate real spectra, the simulated spectrum is smeared with a Gaussian centred around the simulated energy deposition with a sigma corresponding to the measured energy resolution. A similar Gaussian smearing is applied to the threshold for the registration of energy deposition in the Ge-diode. In the measurements this threshold is set by the trigger-electronics. However the threshold is not sharp, but fluctuates with the shape of the trigger signal. This means that the real spectra don't start with a sharp threshold, but with a slope at their threshold value. The Gaussian smearing of the simulated threshold reproduces this slope realistically.

7.2 Comparison with the experimental data

To compare the simulated spectra to the measured data it is necessary to take into account the natural background measured in the setup in the low level laboratory (LLL). There are two ways to do this. One is to compare the simulated spectra to measured spectra from which the background has been subtracted. These background subtracted measured spectra have been used to calculate the suppression efficiencies (see chapter 6) and this method is useful to compare the predicted and measured suppression factors. However in regions of low statistics, where the source signal is of comparable intensity as the background, this subtraction can lead to a vanishing signal. To compare the spectral shape and the peak to Compton ratios the background is therefore added to the simulated spectrum and this 'background added MC spectrum' is compared to the measured spectra.

Figure 7.1 shows the comparison for a ^{137}Cs-source. The left plot is the comparison for the unsuppressed spectrum, the right plot is the comparison for the anti-Compton spectrum. The plots show the raw Monte Carlo spectrum for a simulated ^{137}Cs-source (light blue and ochre respectively), the measured background (grey), the sum of both which is the background added Monte Carlo spectrum (cyan / brown) and the full measured data from the ^{137}Cs source (dark blue / red). It is visible that the overall spectral shape for both spectra is very well reproduced.

To fit the intensity of the simulated unsuppressed spectrum to that of the measured spectrum, however, a correction factor of 1.08 was necessary. This correction is larger than the uncertainty of the activity of the source, which was cited with a 3% error. An error in the source distance to account for the necessity of this correction factor could be excluded by comparing the peak-to-Compton ratio of the simulated spectrum to that of the measured spectrum. The peak to Compton ratio is the number of counts in a peak divided by the number of counts in an arbitrary chosen integral over the associated Compton plateau. It's absolute value has no physical meaning since it depends on the integration range over the Compton plateau chosen, but for a fixed integration range it depends on the size of the diode and on the distance of the source. Therefore it is a good tool for the comparison of the simulated and measured spectra to test whether the geometry of the diode and source was implemented correctly. In the measured data, the peak to Compton ratio is 0.236±0.002 and in the simulated spectrum it is 0.240±0.003. Within the errors these values agree, so it is assumed that the necessity of the correction factor of 1.08 is due to an error in source strength or to an error in the run-time of the measurement.

Using the same correction factor for the simulated suppressed spectrum, its intensity is slightly lower than that of the real anti-Compton spectrum.

Figure 7.2 shows the same comparison for an internal ^{60}Co source using the same colour scheme. Figure 7.3 shows the comparison of the simulated and real spectra for the internal ^{232}Th-source and figure 7.4 shows the comparison of the simulated and real spectra for the ^{226}Ra-source. A common feature is that the spectral shape is correctly reproduced, but that the suppression efficiency is systematically over-estimated. This over-estimation is strongest in the case of ^{60}Co.

In the ^{232}Th spectrum the source strength had to be corrected as well to fit it to the measured data. Here the correction factor was 0.74, but given that the source was home-made from ^{232}Th wire and the activity was only estimated and that the wire is far from the point-like source that has been used in the MC code, the correction factor is not surprising. In the comparison of the corrected spectrum it is still noticeable that the measured intensity in the low energy part is higher than the intensity predicted by MC. A possible reason for this is again that the source is homemade and was assembled just before the measurements. This means that the ^{232}Th progeny ^{228}Ac, which contributes the two lines at 911 keV and 969 keV and their associated
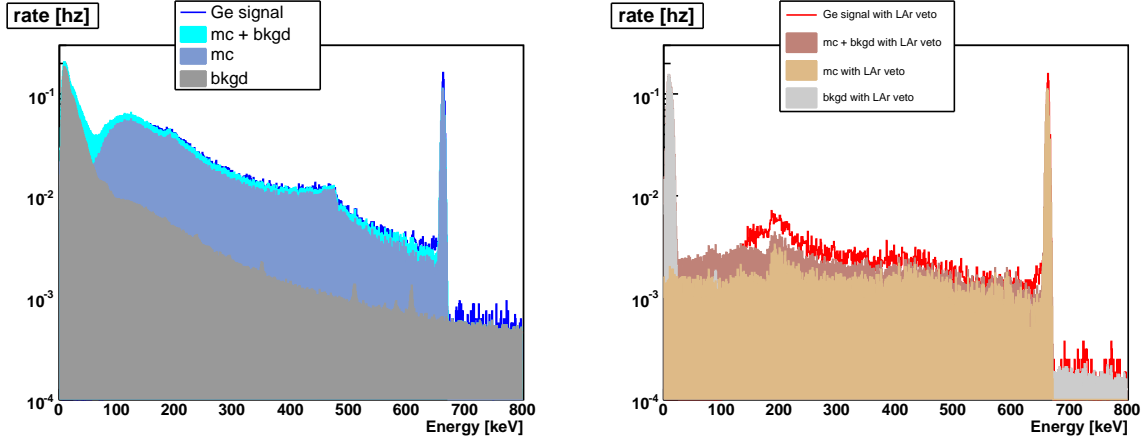
Figure 7.1: The comparison of the simulated full spectrum (left) and anti-Compton spectrum (right) with the measured real data for a ^{137}Cs-source.
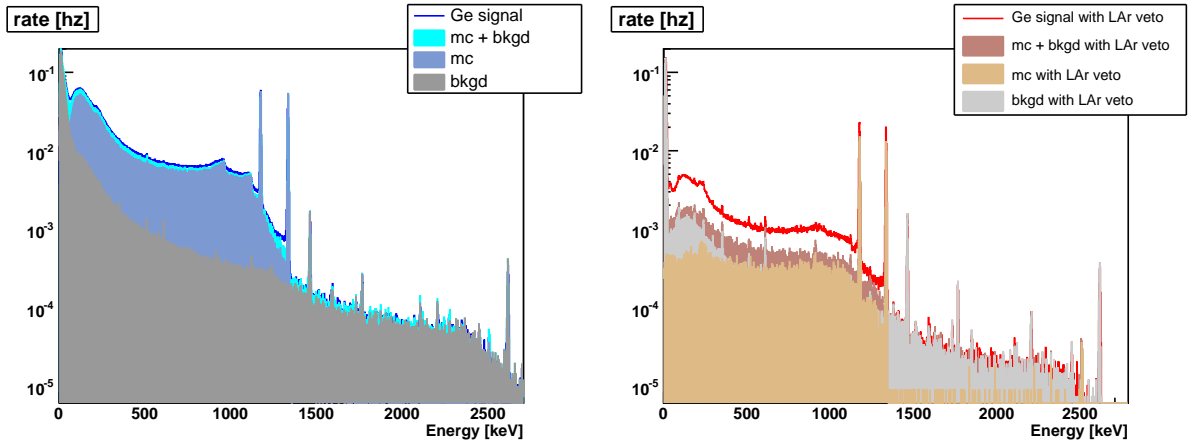
Figure 7.2: The comparison of the simulated full spectrum (left) and anti-Compton spectrum (right) with the measured real data for an internal ^{60}Co-source.

Compton continuum, might not be in secular equilibrium (the decay scheme of ^{228}Ac is included in the appendix).

For ^{226}Ra for simplicity only the ^{214}Bi decay, which is the only γ emitter in the high energy range and dominates the entire γ spectrum from the ^{226}Ra chain, was simulated. At low energies 4 lines are visible in the real data, that do not appear in the MC-spectra. These are the contribution from ^{214}Pb, the progenitor of ^{214}Bi, which was not simulated.

7.2.1 Quantitative comparison

For a quantitative comparison between the MC simulation data and the measured data the number of counts in the peaks, the RoI and selected Compton continua are compared. As a measure of the deviation between the simulated and measured data the ratios $R_{r/mc} = N_{real}/N_{mc}$ and $R_{r/mc}^{veto} = N_{real}^{veto}/N_{mc}^{veto}$ are defined, where N is the number of counts in the selected region. Table 7.1 lists the determined ratios.

It is noticeable that in the suppressed spectra the ratio is systematically larger than one for
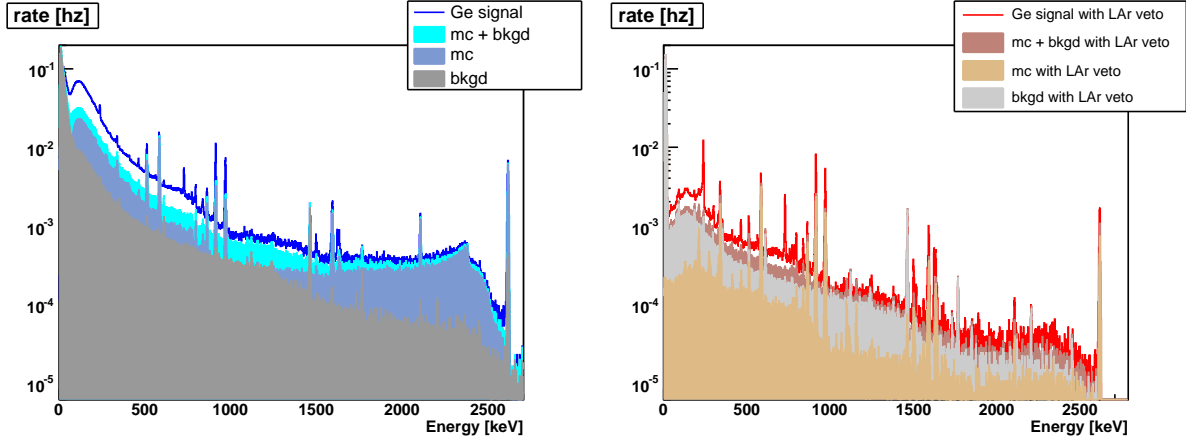
Figure 7.3: The comparison of the simulated full spectrum (left) and anti-Compton spectrum (right) with the measured real data for an internal ^{232}Th-source.
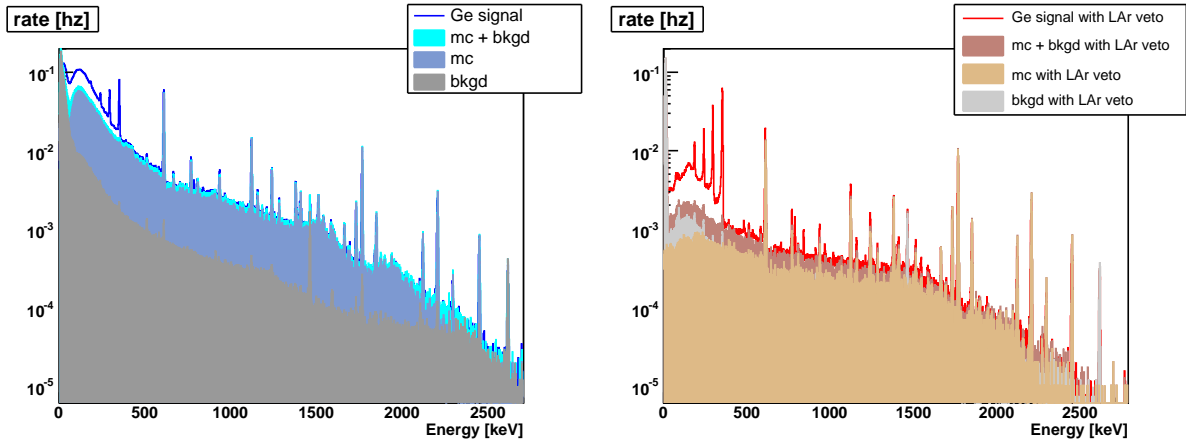
Figure 7.4: The comparison of the simulated full spectrum (left) and anti-Compton spectrum (right) with the measured real data for a ^{226}Ra-source.

most sources and energy regions. This means that the MC simulation predicts less events than measured or in other words that the simulated suppression efficiency is larger than the measured one.

7.3 Conclusions and predictions for increased active volume

The spectral shape of the different sources is reproduced by the MC simulation. Even for complex sources like ^{232}Th and ^{226}Ra. This shows that the geometry of the the system was correctly implemented into the simulation and that the Gaussian smearing of the simulated energy deposition to reproduce the energy resolution and the threshold on the energy deposition in the Ge-diode works very well.

Also the Poisson-smearing on the threshold for the energy detection in the LAr reproduces the real data. The best agreement is achieved for an average threshold of one photo electron, which corresponds with the assumed photo electron yield of 400 pe/MeV to an average energy

Source	Energy [keV]	$R_{r/mc}$	$R_{r/mc}^{veto}$
^{137}Cs [1]	662	1.0±0.01	0.98±0.01
	[230,450]	1.019±0.007	1.39±0.03
^{60}Co	1173	1.020±0.004	1.453±0.006
	1332	1.023±0.004	1.508±0.005
	sum [2505]	1.4±0.1	1.3±0.1
	[260,920]	1.110±0.001	3.19±0.01
	[935,1105]	1.120±0.002	3.01±0.02
	RoI [1900,2100]	1.19±0.07	2.92±0.55
^{226}Ra	609	0.995±0.006	1.30±0.01
	1120	0.92±0.01	1.55±0.04
	1765	0.92±0.02	0.90±0.03
	[515,595]	1.096±0.005	1.53±0.02
	[970,1095]	1.079±0.006	1.47±0.02
	RoI [1870,2080]	1.048±0.01	1.30±0.04
^{232}Th [2]	511	1.02±0.03	2.1±0.2
	2614	1.00±0.01	1.79±0.06
	RoI [1900,2080]	1.15±0.04	2.32±0.12
	[2125,2350]	1.16±0.02	3.2±0.2

Table 7.1: Comparison factors between real data and Monte Carlo simulation. R < 1 means the MC prediction is too high, R > 1 means the MC prediction is too low. [1]: source strength corrected by factor 1.08. [2]: source strength corrected by factor 0.74.

threshold of 2.5 keV.

The suppression efficiency is systematically over-estimated by the MC simulation. No final reason for this is yet proven, but a possible explanation might be an incomplete implementation of the diode holder into the MaGe geometry. The diode holder is a dead volume close to the diode which can absorb gammas that were scattered in the diode, thereby preventing the energy deposition in the LAr. The same is true for the dead layer of the diode. If the total dead volume assumed in the MC code is too small, this would lead to a systematic over-estimation of the suppression efficiency.

In the case of ^{60}Co the discrepancy between MC and real data is, however, significantly stronger than for the other sources. The reason for this may be that the angular correlation between the two γ-s ([JSD56, AMOY96]) was not implemented in the simulation. This correlation may influence the probability that one of the γ-s deposits energy in the active LAr volume when the other is detected in the Ge-diode. That means it can have an influence on the veto efficiency. Further MC studies with the correct source properties will be necessary in the future to validate this assumption.

The work on the MC code is not yet finished and will continue in the future. However, if the explanation for the deviation lies in an incorrectly implemented geometry of the holder, one can take the discrepancies as correction factors to the simulated suppression efficiencies. The current MC code then still allows a conservative estimation of the suppression efficiencies in a larger volume of LAr.

Figure 7.5(a) shows a MC simulated spectrum for a 2 kg HP-Ge diode suspended in a one ton active LAr volume ($\varnothing$=90 cm, h=155 cm) with a point-like ^{208}Tl gamma source inside the

LAr close to the diode (model for ^{232}Th contaminations in the diode holder). The unsuppressed spectrum in the diode is plotted in blue. The red spectrum is the anti-Compton spectrum remaining after the veto cut under the conservative assumption of a 100 keV threshold for the detection of energy deposition in LAr. Figure 7.5(b) shows the same plots for a ^{214}Bi source internal the LAr (model for contaminations from the ^{238}U chain in the holders).

(a)   (b)
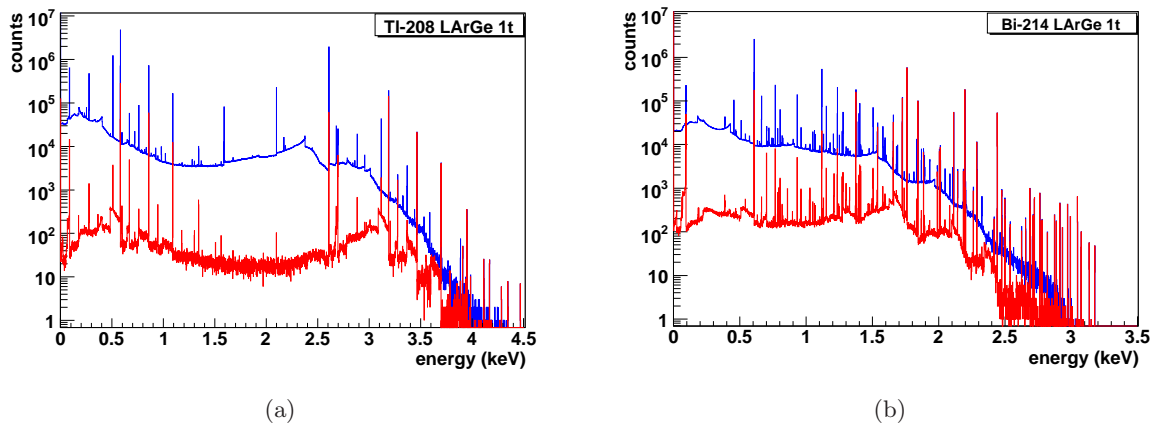
Figure 7.5: A MC simulation of the suppression efficiency in the GERDA-LArGe setup at the Gran Sasso laboratories (1 ton of active LAr volume) for ^{208}Tl (left) and ^{214}Bi (right). The unsuppressed spectra in the Ge diode are plotted in blue, the suppressed spectra are plotted in red.

The suppression factors predicted for the RoI are a factor 338±8 for the ^{208}Tl source and a factor 8.0±0.1 for ^{214}Bi. The corresponding survival probabilities are $(2.96 \pm 0.07) \cdot 10^{-3}$ and 0.125±0.002 respectively. Taking into account the discrepancies between the MC predictions and the measurements from table 7.1 as correction factors, these simulated factors become lower limits on the suppression efficiencies. These conservative values are a suppression factor of ∼145 for ^{208}Tl and a suppression factor of ∼6 for ^{214}Bi. The corresponding upper limits on the survival probabilities are: $6.9 \cdot 10^{-3}$ for ^{208}Tl and ∼0.16 for ^{214}Bi.

Chapter 8

Improving the system

The $\sim$500 pe/MeV photo electron yield achieved with the bare VM2000-foil (chapter 5) and even the 250 pe/MeV of the first test system allow for a sufficient background suppression for the HP-Ge diodes suspended in the LAr, as demonstrated above, with a threshold of $\sim$2 and $\sim$4 keV respectively. To estimate which energy threshold is strictly necessary for a veto, one can compare the energies of major background sources to the energy of the $Q_{\beta\beta}$ region. For example the summation energy of the two ^{60}Co gammas is 2505 keV. To get an energy deposition in the RoI (2039 keV) the remaining 466 keV have to be deposited somewhere else, outside the diode. This deposition will in most cases occur in the surrounding medium and therefore this remaining energy is available for background suppression. The same argument also holds for the 2614 keV gamma from ^{208}Tl. This means that a threshold of $\mathcal{O}(100)$ keV for the detection of energy deposition in the LAr would already be sufficient to suppress the contributions of these two major background isotopes.

However, a higher photo electron yield would allow not to use the full pulse for background suppression but to trigger only on the fast component. This would improve the time resolution from the order of the length of the slow component ($\mathcal{O}(\mu s)$) to that of the fast component ($\mathcal{O}(10)$ ns). A higher photo electron yield also improves the energy resolution of the LAr scintillation. This means that other applications of the LAr scintillation detection beyond veto-purposes become conceivable, for example spectroscopy for background identification. Together with a good pulse-shape discrimination (see chapter 3.3), which allows discrimination between particles of different ionisation densities and also depends on the photo electron yield achieved, the LAr scintillation becomes a powerful diagnostic tool for the investigation and monitoring of backgrounds. Moreover a high photo electron yield allows a close packing of the diodes in GERDA since it counteracts the shadowing effects of a closely packed cluster. For these reasons several methods of increasing the photo electron yield were tested.

8.1 Increasing the photo electron yield by improving the wave-length-shifter

8.1.1 Direct coating of the wavelength shifter with additional fluorescent dye

Following the results of investigations done by the WARP collaboration [BCC$^+$06] there is a possibility to increase the light-yield of a LAr scintillation system with VM2000 as wavelength shifter (WLS) by coating the VM2000 foil with an additional fluorescent dye. To test this approach it was necessary to find a suitable method of coating the foil. As a fist step different

solvents were tested on the foil, to find one which dissolves the fluorescent dyes under investigation as well as the material of the foil itself. The idea was, to dissolve the fluorescent dye and apply the solution to the foil. If the solution solubilises the surface of the foil, a compound of the fluorescent dye with the material of the foil can be formed with the evaporation of the solvent. The foil consists of poly-ethylene-naphtalate (PEN) and proved resistant to most common solvents. The organic solvent toluene however was found to weakly solubilise the foil and was used as a solvent in the subsequent studies. The next step was to find the best method to apply the solution to the foil. The resulting coating should be homogeneous, stable against weak mechanical forces (e.g. wiping) and resistant against cryogenic temperatures. Different methods of coating were tested. The best method was to use an airbrush to spray saturated solution of the fluorescent dye in toluene on the foil. The coating was most stable when the foil was heated up to (40-60)°C during the spraying. After that the foil samples were bathed in liquid nitrogen and wiped with a soft tissue to remove all parts of the coating that did not bond to the VM2000 foil. With this method samples of the foil were coated with different fluorescent dyes. To compare the coatings the samples were tested in a UV-Vis fluorescence spectrometer. A comparison by direct excitation at the LAr scintillation wavelength ad λ=128 nm was not possible since no light source in this extreme UV region (like for example a free electron laser) was available. Instead, a qualitative comparison was made with an UV Fluorimeter in different UV regions extending from λ=350 nm down to λ=190 nm, which is the limit of the Fluorimeter. While the absolute intensity of the fluorescence depends on the excitation wavelength, the relative fluorescence intensities of the different fluorescent dyes, barring excitation in an absorption peak of one of the fluorescent dyes, remained similar and especially the 'hierarchy' of the dyes remained the same throughout the measured region. Since nothing is known about absorption properties of any of the dyes in the XUV region, an intermediate region without absorption peaks of any of the dyes was chosen for this comparison.

Figure 8.1 shows the spectra of different fluorescent dyes on the VM2000 foil compared with the bare, uncoated VM2000 foil excited with an intermediate UV wavelength of λ=250 nm. The spectrum of the bare foil is shown in red. Some dyes like PMP (shown in blue) even reduced the overall light yield. Others, like BPO and Bis-MSB, did not bond to the foil and were almost completely removed by the LN$_2$ bath and wiping. The best fluorescence light-yield was achieved with tetra-phenyl-buthadine (TPB). The thickness of the coating was estimated by measuring the weight of a sample of the foil before coating and after coating. From the weight difference, the area of the sample and the density of TPB ($\sim$1 g/cm^2) the thickness can be calculated. For the chosen coating it was $\sim$0.9 μm.

The extinction thickness for UV light in this wavelength region in TPB is $\sim$0.5 μm. The extinction thickness is defined here as the thickness at which half of the light is absorbed. It is calculated from the extinction formula

$$I(x) = I_0 \cdot e^{-\epsilon \cdot c \cdot x} \tag{8.1}$$

with $I(x)$ being the intensity of the light after penetrating a layer of thickness x (in cm), I_0 being the initial intensity, c being the concentration (in mol/l) and ϵ being the molar extinction coefficient in ($l/(mol \cdot cm)$) taken from [Ber71].

The TPB formed a white coating on the foil and the impact of this coating on the reflectivity of the foil was investigated. Figure 8.2 shows the total reflectivity and the diffuse reflectivity component of the bare VM2000 foil and the foil with TPB-coating. The total reflectivity of the uncoated foil is shown in red and the diffuse component of the reflectivity is shown in blue. For the coated foil the total reflectivity and the diffuse component are shown in green and purple respectively.
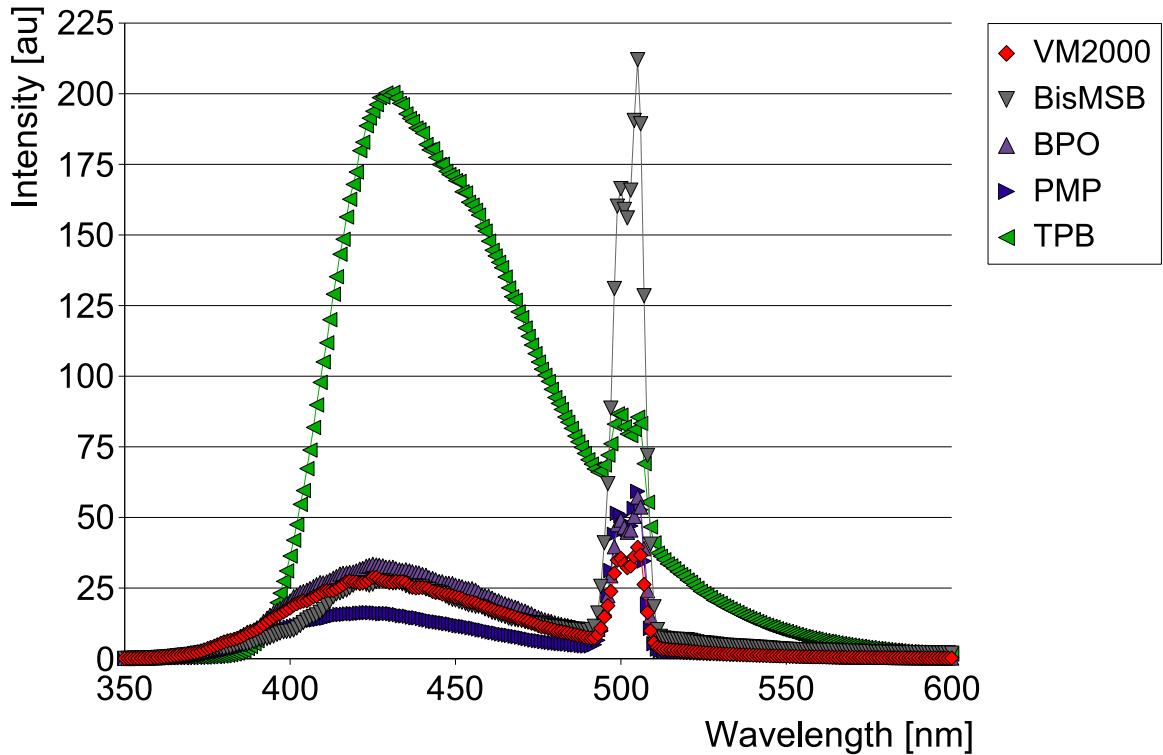
Figure 8.1: Fluorescence spectra of different fluorescent dyes sprayed on to the VM2000 foil. The apparent peak at 500 nm is due to scattered light from the excitation beam, which has a wavelength of λ=250 nm. Since a lattice is used as analysator, this light is also registered as second order peak at its double wavelength.

The reflectivity was measured using an integrating sphere. The sample is illuminated by a narrow (2.5 mm collimator width) beam of light with variable wavelength and the total light intensity inside the sphere is measured. For measuring the total reflectivity the sample is aligned such that the specularly reflected light is contained in the sphere (figure 8.3(a)). For measuring the diffuse component of the reflectivity the sample is aligned such that the specular reflection leaves the sphere (figure 8.3(b)).

Below $\lambda \simeq 375$ nm the foil is optically active. This means that the light in the UV region is not reflected, but absorbed and re-emitted by fluorescence. Above this reflectivity cutoff the reflection of the uncoated foil is mostly specular. This is visible from the fact that the diffuse component of the reflectivity (blue) is only around $\sim$3% of the total reflectivity (red). The total reflectivity of the coated foil (green) is around $\sim$96% of the total reflectivity of the uncoated foil. The main contribution is the diffuse component (purple). The specular component, which is the difference between the total and the diffuse reflectivity component, is reduced to (20-30)%.
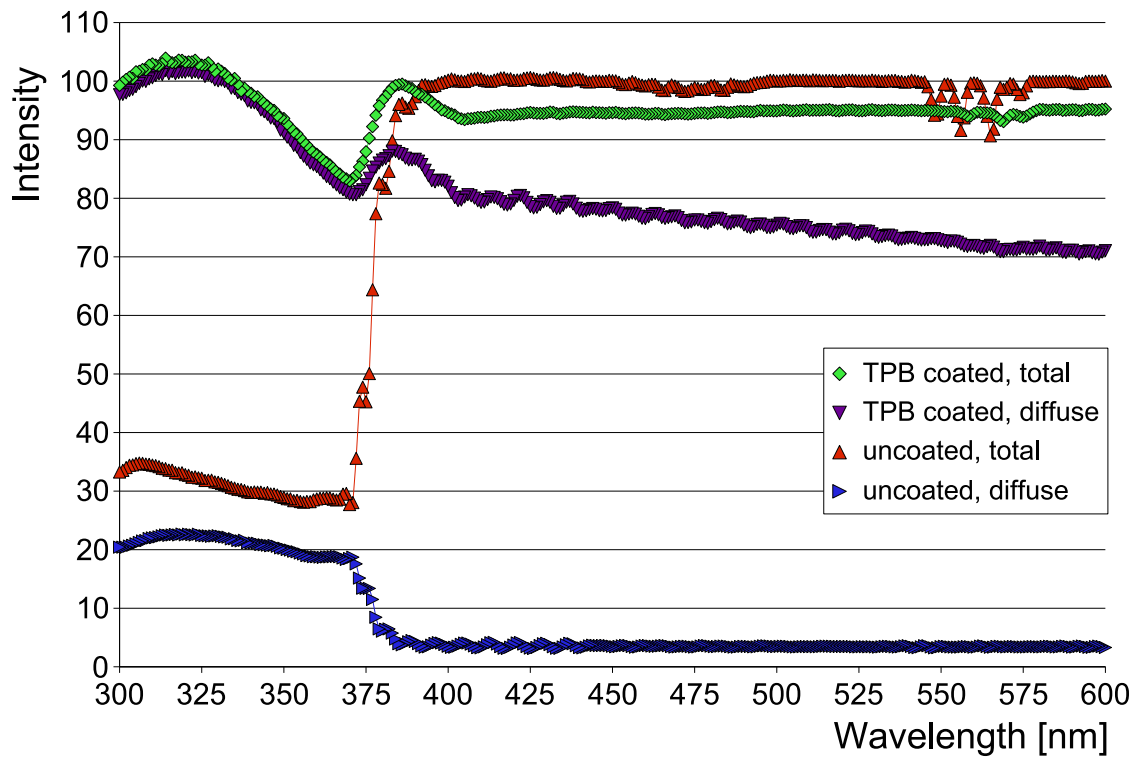
Figure 8.2: Total reflectivity and diffuse reflectivity component of the uncoated VM2000 foil (red and blue) and of the VM2000 foil spray-coated with TPB (green and magenta).
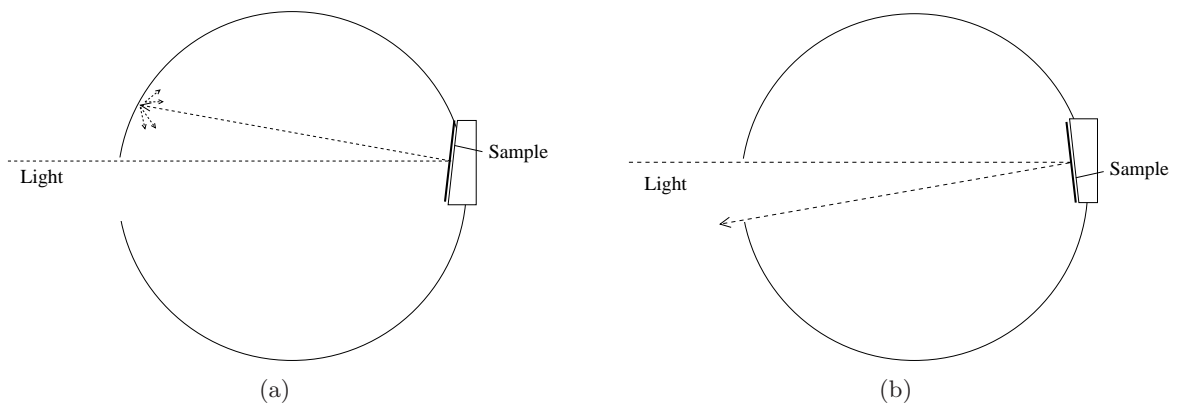
Figure 8.3: Schematic drawings of the integrating sphere for measuring the total reflectivity of a sample (left) and the diffuse component only (right).
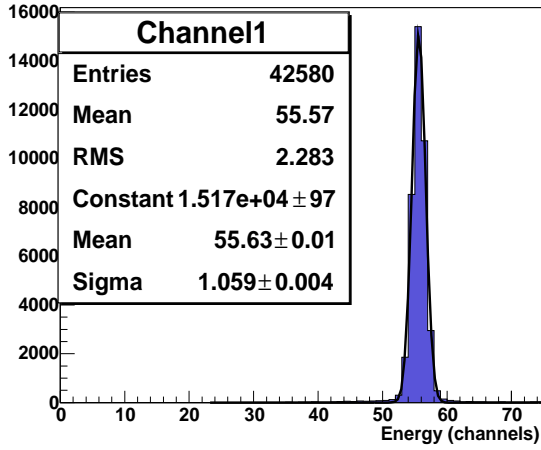
Figure 8.4: The pedestal for the photo electron yield measurement with the spray-coated WLS-foil.
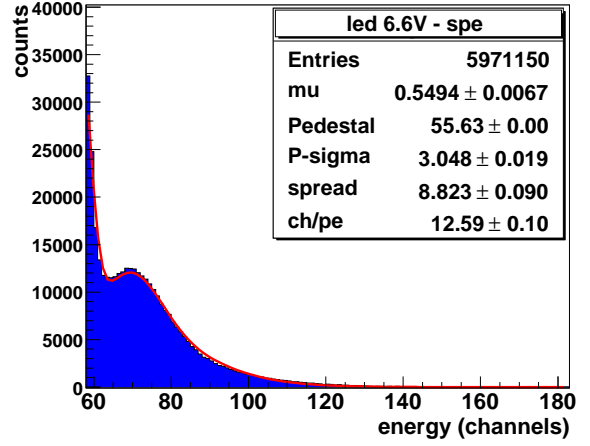
Figure 8.5: The single photo electron histogram for the photo electron yield measurement with the spray-coated WLS-foil.

Photo electron yield results

After the spray-coating the WLS-foil was mounted in the first test-system. To determine the photo electron yield the same procedure as described in chapter 5 was used. Figure 8.4 shows the pedestal of the DAQ electronics and figure 8.5 shows the single photo electron histogram. Figure 8.6 shows the spectrum from the external ^{57}Co-source used in the previous photo electron yield measurement. From these plots we take the values for the pedestal $C_P = 55.63\pm0.01$, the gain factor from photo electrons to ADC channels $G_{pe} = 12.59\pm0.10$ ch/pe and the position of the source peak in ADC channels $C_{src} = 2347\pm3.6$. The mean energy of the ^{57}Co-peak is E_{src} = 123 keV. The error on the pedestal is negligible and the fitted position of the single photo electron peak depends on the fitting method and parameters chosen by ±0.45 channels, which is taken as systematic error on G_{pe}. Since both errors are of the same order of magnitude, both must be taken into account. So $G_{pe}=(12.59 \pm 0.1(stat) \pm 0.45(sys))$ ch/pe. With these values entered into equation 5.2 $Y = (C_{src} - C_P)/(G_{pe} \cdot E_{src})$ the photo electron yield is:

$$Y = 1480 \pm 12(stat) \pm 53(sys) \text{ pe/MeV}.$$

Since the first test-system was used in this measurement, which had a photo electron yield of 250 pe/MeV with the uncoated WLS-foil, this result corresponds to an increase in photo electron yield by a factor of 6.

Stability of the coating

After the first refilling of the system the photo electron yield determination was repeated. Pedestal and single photo electron spectrum were unchanged. The ^{57}Co peak position however was shifted down to channel $C_{src}=1765\pm4.4$. The spectrum from the ^{57}Co-source is shown in figure 8.7. With this value for C_{src} the photo electron yield is:

$$Y = 1104 \pm 9(stat) \pm 39(sys) \text{ pe/MeV}.$$

83
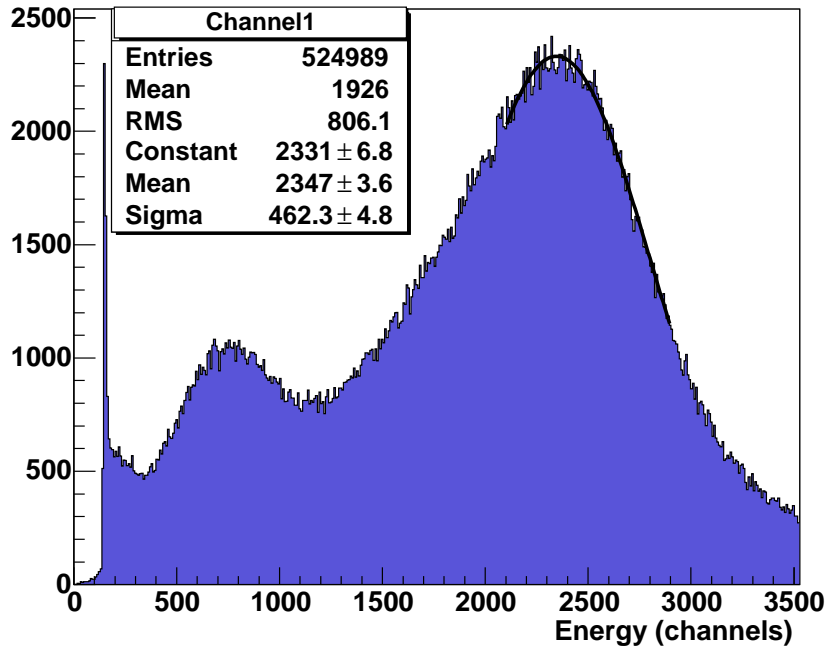
Figure 8.6: The spectrum from an external ^{57}Co-source. The mean energy of the peak is 123 keV.
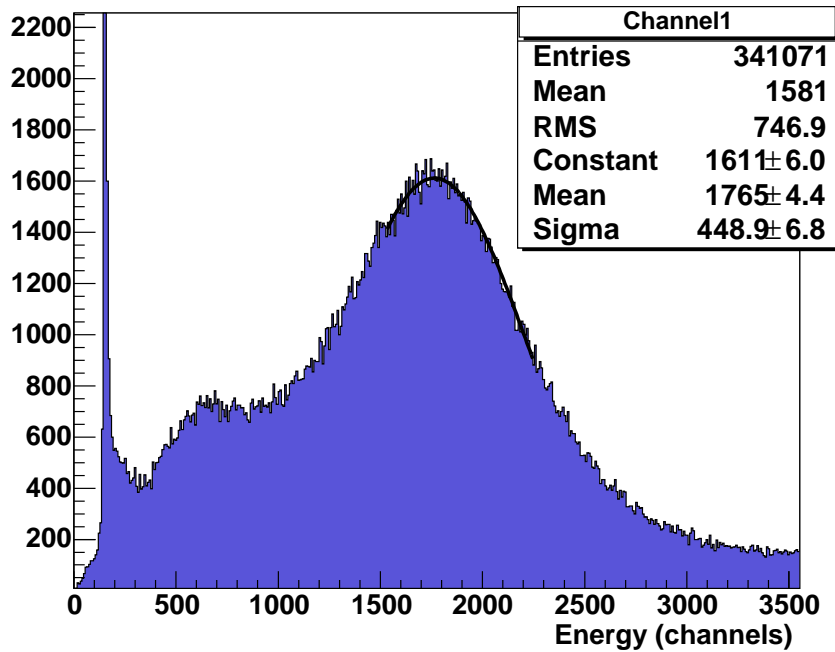
Figure 8.7: The spectrum from the external ^{57}Co-source after one refilling of the system with LAr.

This corresponds to a reduction of photo electron yield by more than 25% after one refilling. After this the photo electron yield dropped by 10% for the second refilling and by another 10% for the third. After this the measurement was stopped. The coating had proved to be unstable under the conditions associated with the refilling (boiling of the LAr or turbulences) and the spray-coating method for improving the WLS was therefore discarded.

8.1.2 Coating the WLS with a fluorescent dye, embedded in a polymer matrix

After the measurements with the γ-sources (chapter 6) a second attempt was undertaken to improve the WLS of the final system. The new concept of improving the WLS was to use a fluorescent polymer dissolved in toluene to coat the WLS-foil. The idea was that the polymerisation might create a stronger bond to the foil than the spray-coating technique. To achieve the increase in photo electron yield the polymer has to be doped with a fluorescent dye the emission of which lies in the sensitivity range of the PMT. The wavelength shifting process is then the following: the polymer absorbs the UV scintillation light from the LAr and transfers the absorbed energy non-radiatively to the dye, which then emits the energy in form of photons in the optical range. Some additional considerations limit the choice of polymer and fluorescent dye. First the energy transfer from the polymer to the fluorescent dye is important. This means that the energy levels of the two should have a good overlap. This can be tested by comparing the emission spectrum of the polymer with the absorption spectrum of the dye. Also the polymer has to be transparent to the emitted fluorescence light. The polymer as well as the dye have to be soluble in toluene, since this solvent weakly solubilises the material of the WLS-foil, PEN, which is resistant to most other common solvents. Two polymers fulfilling these requirements are poly-styrene (PST) and poly-vinyl-toluene (PVT).

Name		PST	PVT	BBO	bis-MSB	PMP	TFPB	TPB
Absorption max.	[nm]	260	265	340	350	300	320	345
Emission max.	[nm]	335	310	410	420	420	615	450
Fluorescence decay time	[ns]	23.0	14.0	0.92	1.35	3.4*	22.5	1.76

Table 8.1: Absorption- and emission maxima of the polymers and selected fluorescent dyes. The emission maximum of the fluorescent dyes lies in the optical range and their absorption spectrum overlaps with the emission spectrum of at least one of the polymers [Ber71], *[MEM96].

The extinction coefficients of PST and PVT in the XUV region around λ=128 nm are unknown. In the known UV region the range of the extinction coefficient for PST extends from ϵ=$\sim$50 l/(mol·cm) at λ=240 nm to ϵ=220 l/(mol·cm) in the absorption peak at λ=260 nm. This corresponds to an extinction thickness of 13.7 μm and 3.1μm respectively. For PVT the extinction coefficients extend from ϵ=$\sim$200 l/(mol·cm) at λ=240 nm to ϵ=$\sim$400 l/(mol·cm) in the absorption peak at 265 nm. This corresponds to an extinction thickness of $\sim$4 μm and $\sim$2 μm respectively.

Concerning the thickness of the polymer layer these numbers, combined with the consideration that nothing is known about the extinction coefficients at λ=128 nm and that it would be preferable to be on the safe side, lead to two conflicting requirements on the polymer-coating. The coating should be thick enough to absorb the LAr scintillation light and thin enough to remain flexible at LAr/LN$_2$ temperature. Some samples of the WLS-foil were coated with the selected polymers by dissolving the polymers in toluene and using a soft paintbrush to coat the foil with the solution. Other methods like spraying the solution on the foil or dipping the foil into the solution were also tried, but did not result in homogeneous coatings as good as the brushing method. The thickness of the coating was controlled by the concentration of the polymer in the toluene-solution and was measured by the difference in weight of the coated foil to the uncoated foil. The coated foil was then dipped into a LN$_2$ bath and investigated under a microscope for cracks. The results for PVT are: at 1.4 μm thickness the coating remains flexible and free of cracks after the LN$_2$ bath, the same at $\sim$2.0 μm. At 4.3 μm and above cracks

appear after the LN$_2$ bath and at 7.6 μm micro-crystals are visible under the microscope even before the bath. For PST the results are: no cracks visible after the LN$_2$ bath for 2.3, 2,7 and 4.2 μm. One sample with 5.7 μm showed no cracks after the LN$_2$ bath, but on another sample with 5.6 μm some small cracks appeared. At a thickness of 7 μm the PST coating was cracked after the LN$_2$ bath, but no micro-crystals were visible. Following these results the solution for the PVT coatings was kept at a concentration resulting in a coating thickness of 1-2 μm (this thickness range was confirmed by weighting for the different coatings) and the solution for the PST coating was kept at a concentration resulting in a thickness of $\sim$4 μm (the actual coating thickness varied between 3.5 and 4.2 μm).

Fluorescence spectra

A first comparison of the different coatings was again made with the UV-fluorimeter. As excitation wavelength the absorption maximum of the polymer of the matrix was chosen (λ=260 nm for PST and λ=265 nm for PVT). This maximises the energy absorbed in the polymer, which then is transferred to the fluorescent dye. For each combination of polymer and dye several samples were prepared with different concentrations of the fluorescent dye in the polymer. Figure 8.8 shows, as an example, the comparison for a $\sim$3 μm thick PST coating with different concentrations of TPB. The concentrations are given in weight % of TPB relative to PST. Up to 10% PST in TPB the fluorescence light-yield increases, above 10% PST in TPB the light-yield decreases again. The explanation for this behaviour is, that the extinction coefficient for TPB is larger in the UV region than it is for PST. It is around 4500 l/(mol·cm). The extinction thickness due to the TPB in the matrix decreases linearly with increasing concentration (see equation 8.1). At 0.5% concentration the added absorption due to the TPB is negligible (extinction thickness $\sim$30 μm), however at 10% concentration the absorption due to TPB is dominant. At this concentration the extinction thickness of the TPB is 1.5 μm, so at a coating thickness of $\sim$4 μm $\sim$85% of the intensity of the UV light are absorbed by the PST. Above 10% concentration the fluorescence light yield is reduced again due to self quenching.

After determining the best concentration for each fluorescent dye, the fluorescence spectra of the different dyes were compared. Figure 8.9 shows these spectra with the maximal light-yield achieved for a selection of fluorescent dyes. Some coatings, like for example PST+TFPB shown in purple, had even less light-yield than the uncoated foil shown in blue. From these fluorescence spectra we chose the PST+TPB coating as the optimal coating candidate.

Reflectivity

Another advantage of this technique of coating the WLS with a transparent polymer, is that the specular reflectivity of the foil should not be reduced as it was for the spray-coating method. To test this assumption we took the reflectivity spectra from foil-samples coated with PST, doped with different concentrations of TPB. Figure 8.10 shows the results. The pure PST coating (yellow line) doesn't change the reflectivity of the uncoated foil (red line). Up to 10% TPB in PST (green line) the cutoff is shifted to greater wavelengths (to about λ=410 nm). But the specular reflectivity in the range of the visible light above the cutoff and especially at the emission-wavelength of TPB at λ=450 nm is unchanged. At concentrations around 20% TPB in PST and above the specular reflectivity is reduced. At 25% TPB in PST a sharp drop in specular reflectivity has been observed. At this concentration the TPB is no longer fully embedded in the PST matrix and crystallisation occurs, turning the coating visibly white and opaque.
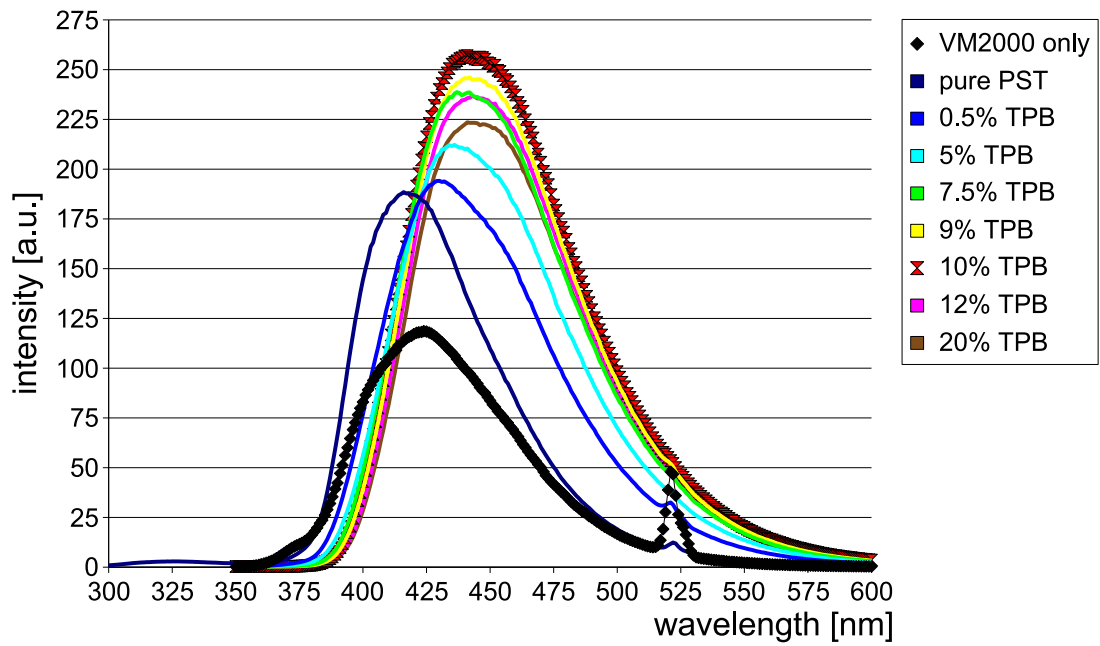
Figure 8.8: Fluorescence emission spectra of the WLS-foil, coated with PST doped with different concentrations of TPB. The excitation wavelength was 260 nm.
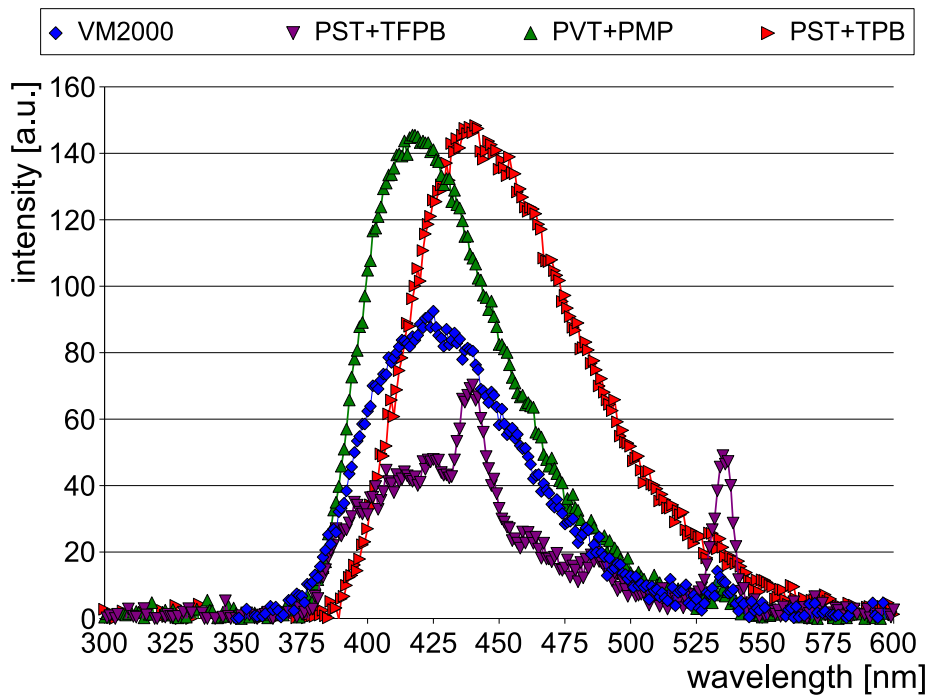
Figure 8.9: A comparison of the maximal light-yield fluorescence spectra for different combinations of polymer and fluorescent dye. The apparent peak on the right is again the second order peak of the scattered excitation light.
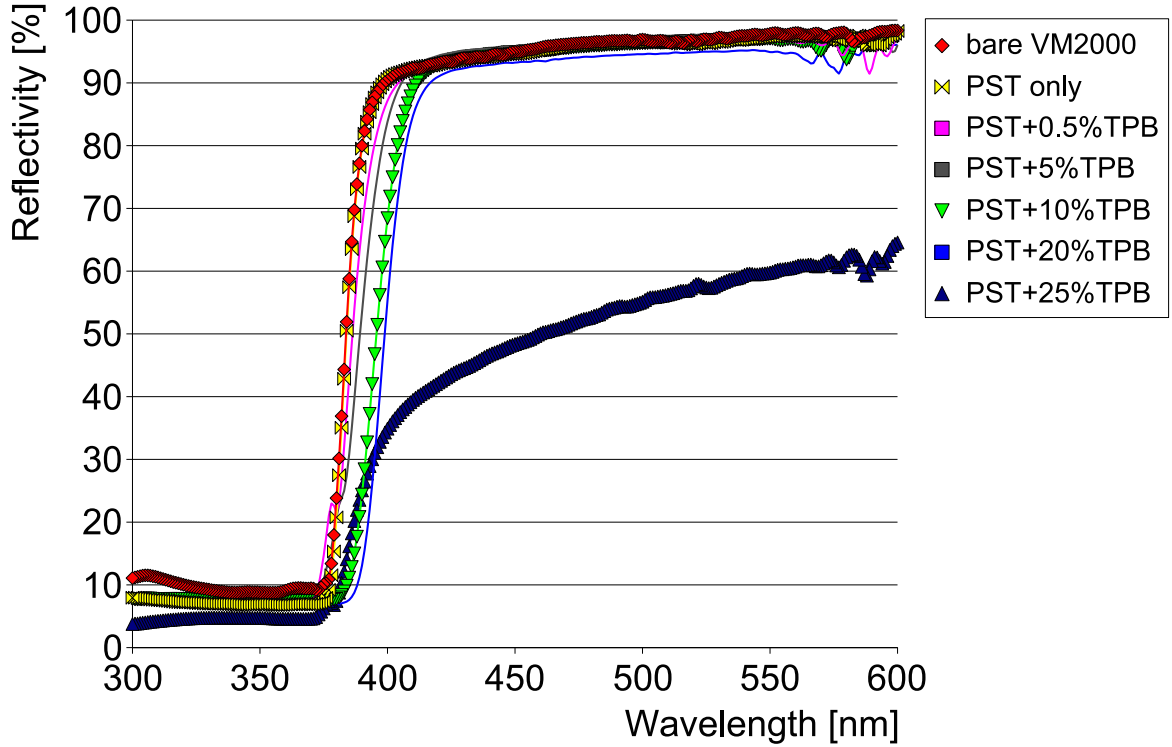
Figure 8.10: Specular reflectivity of the VM2000 foil coated with different concentrations of TPB embedded in PST. Concentrations are given in the percentage of TPB relative to PST, measured in weight.

Photo electron yield results

From the fluorescence and reflectivity measurements the PST coating doped with 10% TPB was chosen. After coating the WLS foil it was mounted in the system and a spe-spectrum was taken as described in chapter 5. However in these measurements a higher voltage setting than that used in the measurements presented in subsection 8.1.1 was chosen for a better signal to noise ratio in the single photo electron range. This had the effect that the peak of the ^{57}Co-source used in the previous measurements was beyond the dynamic scale of the ADC, when using the same settings that were used for recording the single photo electron spectrum. To use the ^{57}Co-source the signal had to be recorded a lower amplification, by a factor 2, on the spectroscopy amplifier. With this the uncertainty of the attenuation has to be included into the error calculation. As a cross check the non-attenuated spectrum from an internal ^{241}Am source was taken with the same settings as the spe-spectrum. The results of these measurements are displayed in figures 8.11 - 8.14.

The values taken from the fit of the spe-histogram and the pedestal measurement are: C_P=58 G_{pe}=16.36±0.14. For the spe-fit again the variance in G_{pe} depending on the fitting region chosen is taken as systematic error (±0.35). From the ^{241}Am spectrum the value C_{src}=1277±0.6 is taken. With these values entered into equation 5.2 the photo electron yield is

$$Y = \frac{C_{src} - P}{G_{pe} \cdot E_{src}} = (1242 \pm 27(sys) \pm 11(stat))\text{pe/MeV}.$$
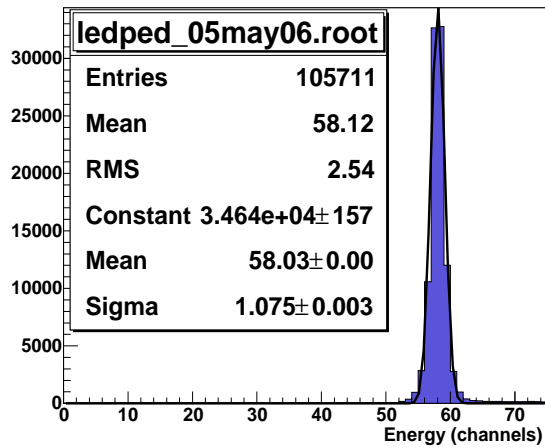
Figure 8.11: The pedestal for the photo electron yield measurement with the WLS-foil coated with PST + 10% TPB.
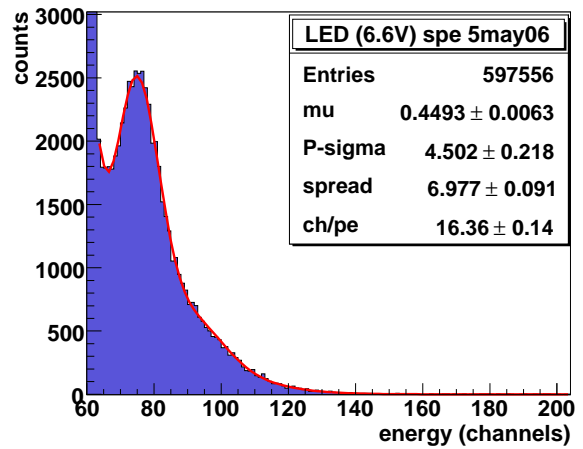
Figure 8.12: The single photo electron histogram for the photo electron yield measurement with the WLS-foil coated with PST + 10% TPB.
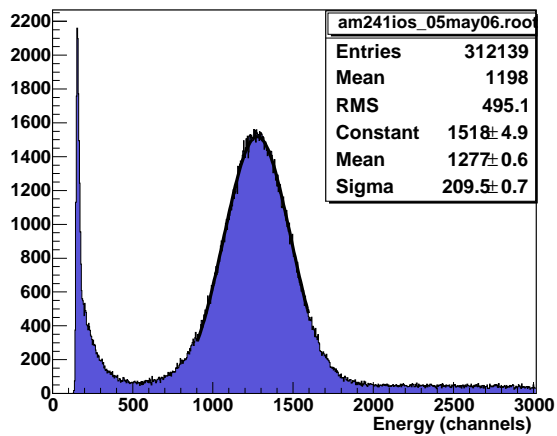
Figure 8.13: The spectrum of an internal ^{241}Am-source, taken with the same settings as the spe-histogram.
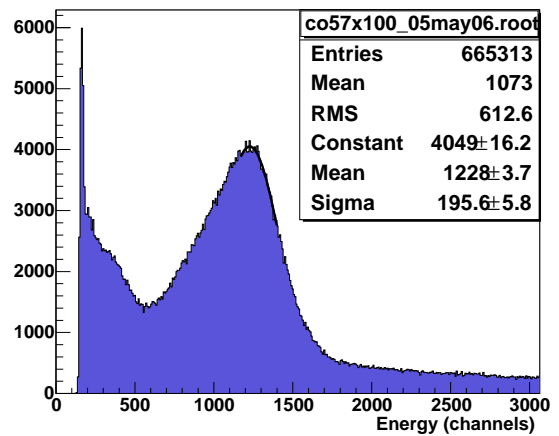
Figure 8.14: The spectrum of the external ^{57}Co-source. The amplification was reduced by a factor 2 with respect to the spe-histogram.

With the ^{57}Co-source and lower amplification by a factor 2 from the source peak is at C_{src}=2456±7.4(stat)±25(sys). With this the photo electron yield becomes: Y=(1221±29(sys)± 11($stat$)) pe/MeV taking into account an estimated systematic error of 1% due to the different amplifications. Within the error these two values agree and if one takes the average, the photo electron yield becomes (1232±20(sys) ± 17($stat$)) pe/MeV.

Stability of the coating

The PST + TPB coating proved to be very stable in time and robust against mechanical stress. Figure 8.15 and 8.16 show the single photo electron spectrum and the ^{241}Am spectrum respectively, taken after more than 6 months of operations with the system. These operations included several runs of data taking, during which the setup was refilled every two to three days with liquid argon (amounting to a total of 85 refills). The system was also three times opened during this time, one time to exchange the previous voltage divider for a new voltage divider for operating the PMT with negative HV (see below, section 8.3) and twice to fix some electronic problems that the new voltage divider had in the beginning. Before opening, the system has been emptied of LAr (see section 4.4) and warmed up to room temperature by flushing it with heated gaseous argon. After re-mounting, the setup was re-filled with LAr and the data taking continued.

During these 6 months we also changed the DAQ system from the pulse-height sensitive ADC to the data acquisition with the digital oscilloscope. (See section 4.3.3). Since in the data evaluation the baseline of each single pulse is subtracted before integration, the pedestal of these measurements is zero and does not appear in figure 8.15. In the fit function the pedestal contribution is set to zero as well. The fits on the histograms give the values C_{src}=2940±4.4 and G_{pe}=39.42±0.32. The statistical error on the spe fit is 0.5 channels, depending on the fitting range chosen. With these values entered into equation 5.2 the photo electron yield is

$$Y = (1243 \pm 10(stat) \pm 17(sys))\text{pe/MeV}.$$

This agrees very well with the photo electron yield determined in the previous section using the ^{241}Am γ-source (1242 pe/MeV) and also agrees within the error of measurement with the averaged photo electron yield determined there (1232 pe/MeV). This means that the photo electron yield has been very stable over a period of more than six months and is robust against the operations described above.
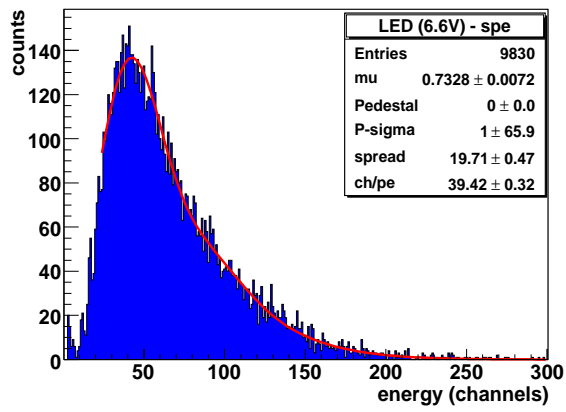
Figure 8.15: The single photo electron histogram taken with the digital oscilloscope.
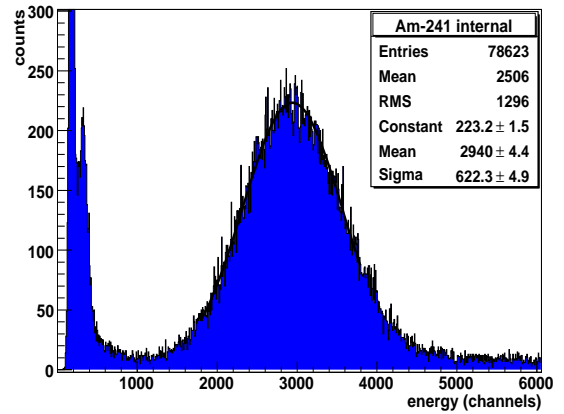
Figure 8.16: The LAr-scintillation spectrum of an internal ^{241}Am-γ-source. Taken after 6 month of operation with the WLS foil coated with PST + TPB.

8.2 Increasing the photo electron yield by addition of Xe

Another way to increase the photo electron yield of LAr scintillation detectors is the addition of small quantities of xenon [SHRK93]. For the most part this increase in photo electron yield is attributed to the fact that Xe works as additional wavelength-shifter, increasing the overall quantum efficiency of the wavelength shifting process. The emission from Xe peaks at 175 nm and this light is then further shifted to the optical range and guided to the PMT by the WLS/reflector foil.

To test this method of increasing the light-yield, the LAr was doped with different quantities of xenon, using the procedure described in section 4.4.2. With this Xe-doped LAr system the spectra of the internal ^{241}Am and an internal ^{228}Th source were taken and compared to the spectra taken without Xe (for the properties of the sources see table 6.1). After this measurement samples of the doped LAr were extracted and measured with a quadrupole gas-spectrometer to determine the Xe content.

Figure 8.17 shows a comparison of the ^{241}Am spectrum with pure LAr and with LAr doped with two different concentrations of Xe. All spectra were generated from data taken with the digital oscilloscope and were recorded with the same high voltage and the same settings on the digital oscilloscope. For the lower concentration only an upper limit can be given since the sensitivity of the gas spectrometer was limited due to technical problems that are not yet solved.

The ^{241}Am 60 keV γ-peak in the spectrum for pure LAr is at channel 10622±40 with a resolution of σ=1715±44 channels. For a concentration of <90 ppm Xe the peak position is channel 14482±51 and the σ is 2069±85. At 300±160 ppm Xe the peak is at channel 15530±68 with a σ of 2232±93.

The single photo electron-peak position for the Xe-measurements was the same as for the measurements with pure LAr, so the pe-yield scales linearly with the peak position of the γ-peaks relative the position of the peaks in the spectra without Xe. Table 8.2 lists the pe-yield results and measured Xe concentrations for these measurements.

Xe-concentration	pe-yield [pe/MeV]	resolution (σ) at 60 keV	resolution (FWHM) at 60 keV
0	1243±20	16%	37.6%
< 90 ppm	1695±27	14%	32.9%
(300±160) ppm	1817±29	14%	32.9%

Table 8.2: The photo electron yield and energy resolution measured at the 60 keV ^{241}Am peak for different Xe-concentrations in LAr.

The increase in pe-yield, when measuring with the digital oscilloscope, is a factor 1.4 for a concentration of <90 ppm and a factor 1.5 for a concentration of (300 ± 160) ppm Xe compared with pure LAr.

When a spectroscopy amplifier is used in the measurements, however, the apparent increase in pe-yield is larger. This is an effect of the reduced pulse length. Xe is a scintillator as well and the scintillation process is similar to that of Ar, however the time constants involved are shorter. They are (2.2±0.3) ns for the singlet state and (34±2) ns for the triplet state [KGW74]. This means that especially the 'slow component' of the Xe light emission is much shorter than it is for Ar: it is ∼2 orders of magnitude smaller than that of Ar-excimers. The Ar-excimers can transmit their energy non-radiatively to Xe. With increasing Xe concentration the probability for a non-radiative energy transfer per unit time becomes greater than the probability for the
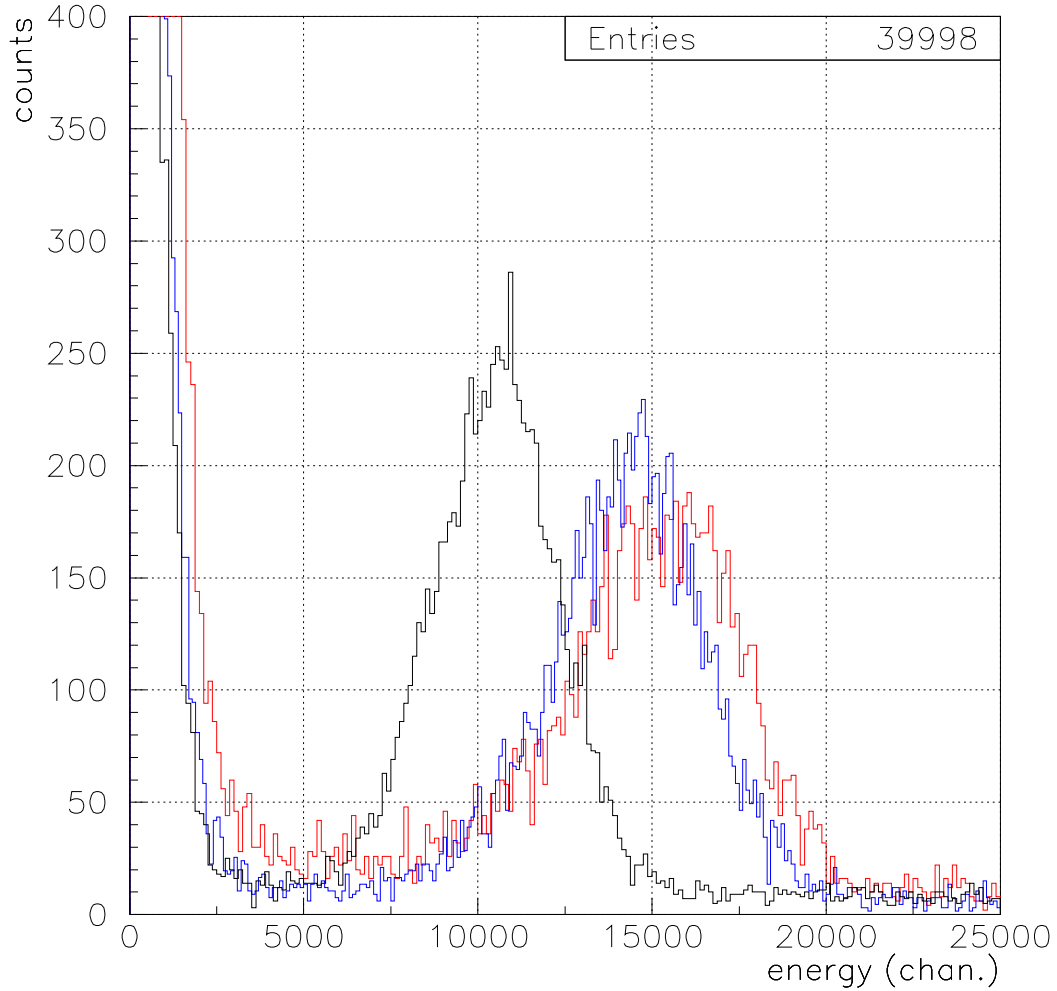
Figure 8.17: A comparison of the ^{241}Am spectrum with pure argon (black), <90 ppm Xe (blue) and 300 ppm Xe (red)

emission of a photon from the Ar triplet state. This means that the time constant of the slow component of the scintillation light emission of the combined Ar+Xe system approximates that of pure Xe for increasing Xe concentrations. The change in pulse-shape will be investigated in more detail in section 10.2. For the apparent photo electron yield when using spectroscopy amplifiers it is only important that the total pulse length becomes shorter with increasing Xe concentration.

With a spectroscopy amplifier using a shaping time for integration that is not large compared to the time-constant of the slow component of the LAr scintillation, a part of that slow component is lost, when measuring the scintillation light from pure LAr. Theoretically it would be possible to include the full slow component by choosing a shaping time that is long enough, however this would also mean the inclusion of additional noise, so that it is necessary to find a compromise. The time window is selected such that as much of the pulses is included as it is possible without deteriorating the energy resolution by the inclusion of too much noise. The

actual length of this ideal time window depends on the noise-level of the individual system.

The shortening of the pulses due to Xe now has the effect that, when using the same time window as determined for the use on LAr pulses to record the scintillation pulses from a LAr+Xe system, a larger fraction of the pulse is included in the time window. This leads to an apparent increase in light-yield, since less light is lost. Figure 8.18 shows a comparison of spectra taken with an MCA using a spectroscopy amplifier with a shaping time of 2 μs. The peak is at channel 1144±1 for pure LAr and at channel 2465±1 for LAr doped with <90 ppm of Xe. With this the apparent increase in light yield is a factor 2.15 compared to the real increase of a factor 1.36 in the photo electron yield determined above.
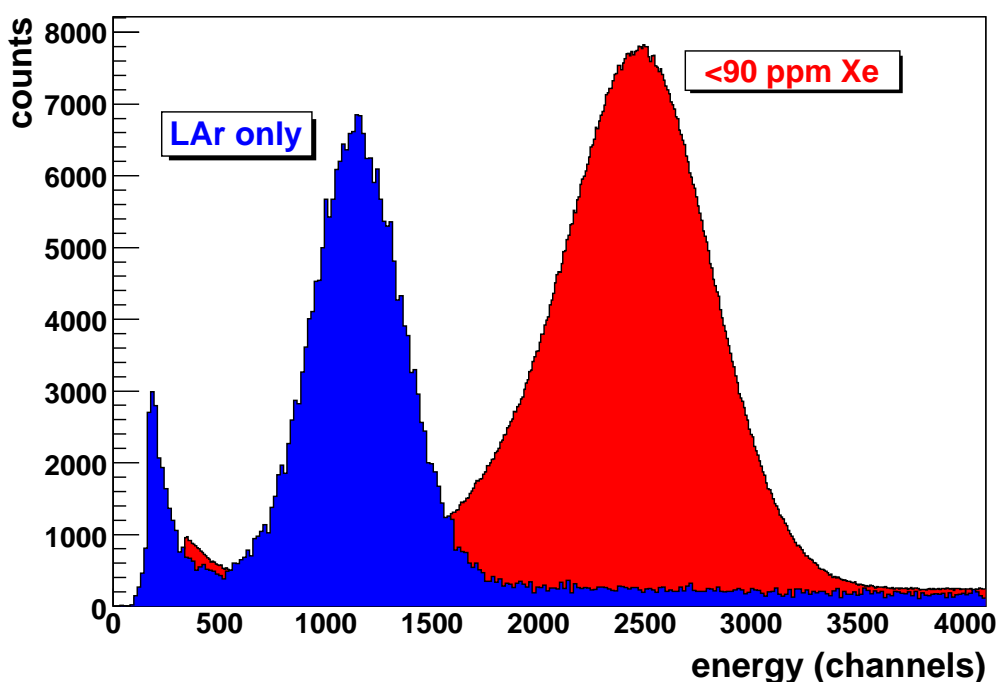
Figure 8.18: A comparison of the ^{241}Am spectrum with and without Xe taken with an MCA using a spectroscopy amplifier with a shaping time of 2 μs.

There are some unsolved challenges concerning the use of Xe doped LAr. The LAr in our system evaporates continuously and Ar and Xe have a different partial gas pressure. So it is a priori not clear how constant in time the Xe concentration is. Another challenge is controlling the exact amount of Xe that ends up in the active volume. At LAr temperature Xe is frozen. Although argon is used as a carrier gas during the doping procedure, an unknown part of the Xenon will freeze onto the walls of the tube through which the Xe is inserted. A third challenge is determining the homogeneity of the Xe distribution inside the LAr. The investigation of this will require the construction of a new test system dedicated to monitoring the local concentration of Xe in different places in the LAr. These challenges are topics for further studies.

8.3 Negative high voltage

When detecting light from liquid scintillators with PMTs it is a standard procedure to apply positive high voltage to the PMT. This has the advantage that the photo-cathode and other parts that are in contact with the scintillator are on ground.

With the PMT operated on positive HV there was a jitter on the signal due to AC-coupling in the voltage divider. Also in low energy pulses a sharp dip appeared and in some of the higher energetic pulses an overshoot over the baseline appeared. As an attempt to get rid of these effects the voltage divider for our PMT was modified for the use of negative HV. The modified voltage divider also includes the readout of the last dynode. The corresponding electronic layout is shown in the appendix (figure C.2). The HV was adjusted such that in the spe-signal was of similar height as in the positive HV case. With this setting the average pulse shape was recorded as well as spectra for different sources to compare the energy resolution to the spectra using positive HV. Figure 8.19 shows a comparison of the probability density function (pdf), which is the average pulse shape divided by its total area, averaged over ~5000 pulses and figure 8.20 shows the comparison of the energy resolution at the ^{241}Am 60 keV γ-peak. The average pulse shape is visibly smoother for negative HV than it is for positive HV and the relative energy resolution (1 σ) has improved from 21.15$\pm$0.67 % for positive HV to 16.06$\pm$0.44 % for negative HV.
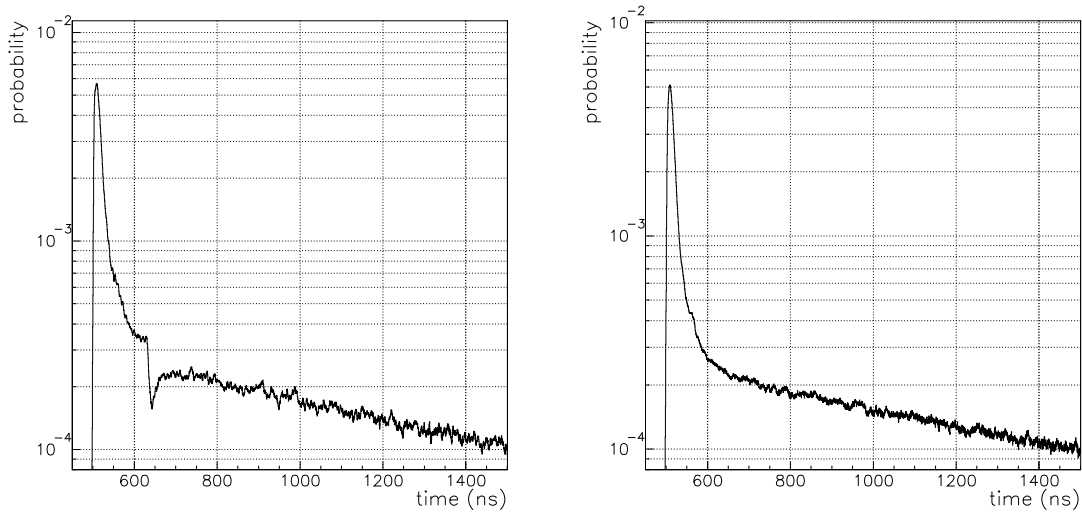
Figure 8.19: A comparison of the average pulse shape over ~5000 pulses for positive (left) and negative (right) HV. The sharp dip and the overall larger jitter of the negative HV pulse are visible.

8.4 Summary of the improvements

Table 8.3 shows a summary of the photo electron yield for the different configurations.

The technique of spray-coating of the 3M radiant mirror foil (aka. VM2000) with TPB or some other fluorescent dye is discarded due to instability of the coating. However the coating of the foil with a matrix of PST, doped with 10% of TPB has been stable now for more than six months. It has endured three cycles of unmounting and remounting the system for the purpose
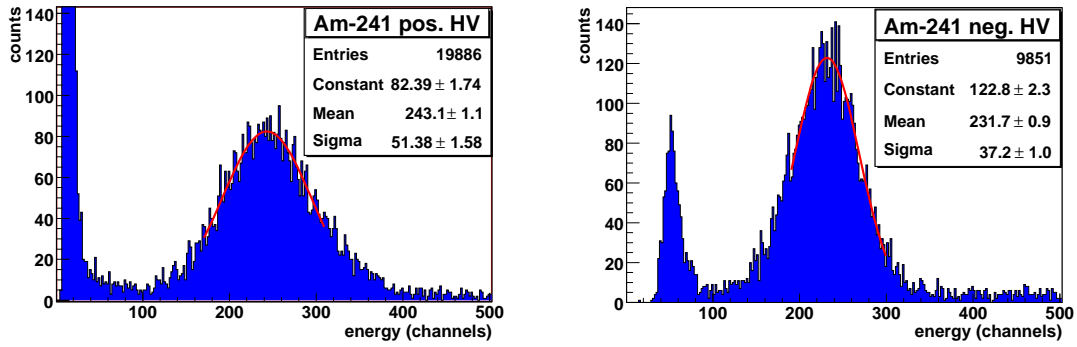
Figure 8.20: A comparison of the ^{241}Am 60 keV γ peak with positive (left) and negative (right) HV.

Description	pe-yield [pe/MeV]	notes
First test setup	250±8	not vacuum tight
Improved, vacuum tight system:		
Uncoated foil	517±16	stable
Spray-coated foil	1480±53	not stable
PST matrix + TPB	1242±27	stable, final configuration
PST(TPB)+ Xe doping	up to 1817	change of pulse shape

Table 8.3: A summary of photo electron yields for different configurations.

of exchanging or repairing the voltage divider of the PMT. This includes of course full removal of the LAr, warming up of the system, mechanical stress during the mounting process and, after remounting, the refilling of the system with LAr. After all these operations the photo electron yield remains at 1240 pe/MeV. The coating can be regarded as robust with respect to all normal operations and is taken as the finalised version of our wave-length-shifter / reflector.

Doping the argon with xenon further improves the photo electron yield but leads to a change of pulse shape which will be discussed in more detail in chapter 10. Also, as mentioned above, there are some challenges left, that are tasks for future work and the investigation of the xenon doping of LAr is continued in an ongoing diploma thesis [Pol07].

Using negative high voltage for the PMT improves the resolution and is adopted for future work. The dynode readout implemented in the new voltage divider is useful for increasing the dynamic range to the scale of α-decay energies. The following chapter presents the results of measurements making use of this increased dynamic range.

Chapter 9

Photo electron yield for α-sources

9.1 Theory of α-quenching

It is a well known fact that the relative light-yield of scintillating materials is different for particles of different ionisation densities [Bir64]. For minimal ionising particles with a low ionisation density the individual molecular or atomic excitations and ionisations are spaced several molecular/atomic distances apart along the particle path. Interactions between them can therefore be neglected. The light-yield is linearly dependant on the energy loss of the particle:

$$\frac{dL}{dr} = S\frac{dE}{dr}$$

where dL/dr is the specific fluorescence and dE/dr is the specific energy loss per path length dr and S is the absolute scintillation efficiency.

For particles of higher ionisation densities there are two processes that reduce the light-yield. One is the so-called ionisation quenching, the quenching of the primary excitation by the high density of ionised molecules/atoms around the particle. The second process is the bi-molecular (and multi-molecular) quenching. It is due to interactions between neighbouring excitons that lead to a non-radiative dissipation of the excitation energy as mentioned in section 3.1.2.

This quenching has the effect, that particles with a high ionisation density appear at a lower apparent energy in scintillation spectra than electrons or gammas of the same actual energy. For the case of α-particles the ratio between the apparent electron-equivalent energy of the α and its actual energy is referred to as α-quenching factor. A quenching factor of one would correspond to no quenching. The α-quenching factor depends, in general, on the energy of the α particle, but for the energy range which is relevant for our experiment (5-8 MeV) the values found by Hitachi et al. [HYDT87] are constant in the first approximation. In this chapter we determine the quenching factor for α-particles from the ^{222}Rn decay-chain.

9.2 Experimental determination of α-quenching for LAr

9.2.1 Method

To investigate the α-quenching the LAr was doped with ^{222}Rn. The basics of the doping procedure were described in section 4.4.2. Here some more details and an analysis of the transfer efficiency are presented. Figure 9.1 shows the part of the ^{238}U decay chain that is relevant for our experiment. Starting at ^{226}Ra it shows the main branch and is truncated at ^{210}Pb, which can be viewed as stopping point of the chain for our purposes, since its half-life (22.3 years) is

significantly longer than the time of the experiment. The alphas emitted from the chain starting at ^{222}Rn have energies of 5.5, 6.0, and 7,7 MeV.
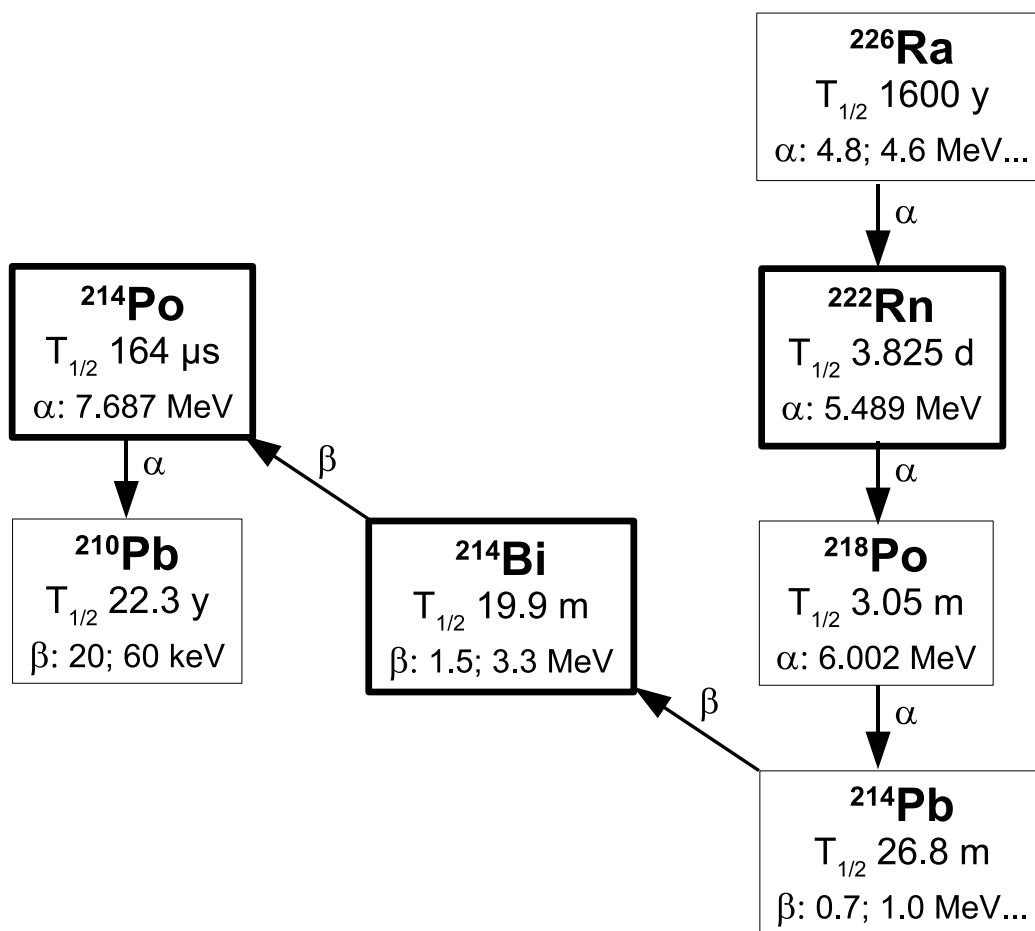
Figure 9.1: The decay chain of ^{226}Ra down to ^{210}Pb. Isotopes that are important for the experiment are marked with a thicker box-line.

To control the activity of the ^{222}Rn in the system the radon was extracted from a certified standard ^{226}Ra solution (HCL) with a total activity of 28.6 kBq. The solution is contained in a small glass vial that can be sparged (flushed) with a carrier gas like helium, nitrogen of argon. By flushing one can extract the radon from the solution with an efficiency of more than 98%. The extracted radon can be collected for example by freezing it onto an activated carbon trap.

Taking into account the fact that the ^{222}Rn is produced from the ^{226}Ra it is possible to obtain any desired activity in ^{222}Rn up to the nominal activity of 28.6 kBq simply by flushing the vial to remove all radon and then waiting until the desired activity has built up. The ^{222}Rn activity produced as a function of time is:

$$A_{Rn} = A_{Ra}(1 - e^{\lambda_{Rn} \cdot t})$$

with A_{Rn} being the activity in ^{222}Rn, λ_{Rn} being the ^{222}Rn decay constant and A_{Ra} being the activity in ^{226}Ra, which is constant within the timescale of the experiment considering its half-life of 1600 y.

After waiting the time necessary for the desired activity to build up, the procedure to transfer the radon from the source to the LAr in the system is the following:

- The source was connected to a column filled with silica gel and an activated carbon trap using vacuum tight tubes.

- The silica gel column was cooled down to -35 °C and the activated carbon trap was cooled in LAr to 87 K.

- The radon was extracted by flushing the source with helium as carrier gas.

- Water vapour from the source condensed and was retained in the silica gel and the radon was frozen onto the cold activated carbon.

- After the extraction the activated carbon trap was closed and disconnected from the source.

- The trap was connected to the LArGe system, while still being cooled with LAr.

- After cleaning all connecting tubes by flushing with gaseous argon, the activated carbon trap was opened and a low flow of gaseous argon was flushed through the trap into the LAr.

- The trap was slowly warmed up to release the radon frozen onto the activated carbon.

Comparison of the activity measured inside the system by the increase of the trigger rate with the activity inside the charcoal trap, shows that ∼35-39% of the doping gas is deposited inside the active volume. The rest may be partially froze onto the flushing tube where it is immersed in LAr and partially was distributed in the non-active volume outside the WLS.

A_i^{Rn}	$R_{\beta\gamma}^{max}$	$\Delta R_{\beta\gamma}^{meas}$	R_α^{max}	ΔR_α^{meas}	R_{Po}^{max}	ΔR_{coinc}^{meas}
3.1 kBq	15.5 kHz	6.0 kHz	9.3 kHz	3.4 kHz	3.1 kHz	2.3 kHz
ϵ_T:	39%		37%		74%	
1.8 kBq	8.9 kHz	3.2 kHz	5.4 kHz	1.9 kHz	1.8 kHz	1.2 kHz
ϵ_T:	36%		35%		60%	
130 Bq	650 Hz	241 Hz	390 Hz	141 Hz	130 Hz	51 Hz
ϵ_T:	37%		36%		39%	

Table 9.1: A table of trigger-rates in the LAr after ^{222}Rn insertion. A_i^{Rn} is the inserted activity in ^{222}Rn, ^{max} denotes the maximal rates which would result from a full deposition of the Rn in the active volume. ^{meas} are the measured rates. ϵ_T is the transfer efficiency to the active volume calculated from the measured rates.

Table 9.1 shows the rates measured in the LAr depending on the ^{222}Rn activity inserted. There are four short lived daughter isotopes in the ^{222}Rn chain, two of which are alpha emitters. Including the α decay of ^{222}Rn itself and assuming that the isotopes are in equilibrium this means that the total decay rate is five times the inserted activity. The detection efficiency for α-s and β-s from sources inside the argon is close to 100%. So the trigger rate resulting from a full deposition of the inserted radon ($R_{\beta\gamma}^{max}$) would be five times the inserted activity. The rate in the α range (R_α^{th}) would be three times the inserted activity and the ^{214}Po decay rate R_{Po}^{th} would be equal to the inserted activity. The ΔR in the table are the actually measured

increases in the counting rate above the background of the respective energy ranges. The rates were measured at least 3h after insertion of the radon to insure that the daughter isotopes are in equilibrium. The ratio between the total activity and the activity measured in the active volume is defined as the transfer efficiency ϵ_T. While the measured efficiencies in the $\beta\gamma$ region and the α region approximately agree with each other and show that 35-39% of the maximal activity was deposited in the active volume, the ^{214}Po rate measured appears to be significantly higher. This is due to random coincidences with alphas from the other two isotopes. The probability of random coincidences depends on the total activity and the apparent discrepancy disappears with decreasing activity. Overall this procedure proved to be a reliable, reproducible method of doping the LAr with a known activity of radon, controllable to $\sim$5%.

Figure 9.2 shows a spectrum taken with a spectroscopy amplifier and a multi-channel-analyser (MCA). The peaks of the α-s from the ^{222}Rn decay chain are visible. 5.5 MeV from ^{222}Rn, 6.0 MeV from ^{218}Po and 7.7 MeV from ^{214}Po. For comparison the internal ^{228}Th source was inserted and the high energy end of its γ spectrum is visible as well. When taking spectra using a spectroscopy amplifier, one needs to take into account the effects of the shaping time. The shaping time cannot be chosen too long, because otherwise too much noise will be included in the integration time window. The best energy resolution was achieved with a shaping time of 2 μs. At this shaping time however a significant part of the slow component, with its decay time of 1.6 μs, is lost. This leads to a non-linearity between pulses with different relative populations of the slow component. I.e. particles of high ionisation densities appear to be less quenched than they really are. To determine the real quenching factor it is therefore necessary to generate spectra by integrating over the full pulse. The pulses were recorded event-by-event with the digital oscilloscope as described in section 4.3.3. The spectra were then obtained by integrating over the recorded pulse shape by software in the off-line data analysis.

This method, while being true to the actual quenching, comes at a price. The data acquisition speed of the digital oscilloscope is limited to $\sim$30 events/second. This means the statistic is also limited. The long integration also makes this method more sensitive to baseline noise than the spectroscopy amplifier noise. The result is, that in the spectra generated from single pulses the 5.5 MeV and the 6.0 MeV α-lines are not separated.

To determine the α-quenching ratio both the signal from the anode and from the dynode of the PMT are recorded to increase the dynamic range. The anode is set to a scale where single photo electrons are visible with a good signal to noise ratio. This scale, which was 10 mV for these measurements, is used to evaluate the slow component of the pulses, which consists partially of single photo electron events in the tail. The dynode is used to evaluate the fast component of the pulse and is set to a scale where the pulses are not truncated for α-energies. In these measurements that scale was 200 mV. The scaling factor between the recorded dynode and anode signals is measured with sources of known energy. Using these factors the dynode signals are recalculated to anode-equivalent signals.

The system is calibrated using a ^{228}Th-source. The spectrum is generated by integrating over the total pulse from the anode in single photo electron equivalent scale. From the peaks in the ^{228}Th spectrum the correlation from channels to energy is calculated. This correlation is used to determine the apparent electron-equivalent E_{app} of α-peaks with the known energy E_{real}. The ratio $Q_\alpha = E_{app}/E_{real}$ is the quenching factor.

9.2.2 Result

Figure 9.3 shows the spectrum of the integral over the full anode-signals for an internal ^{228}Th-source and the corresponding energy calibration. The relation between channels and energy
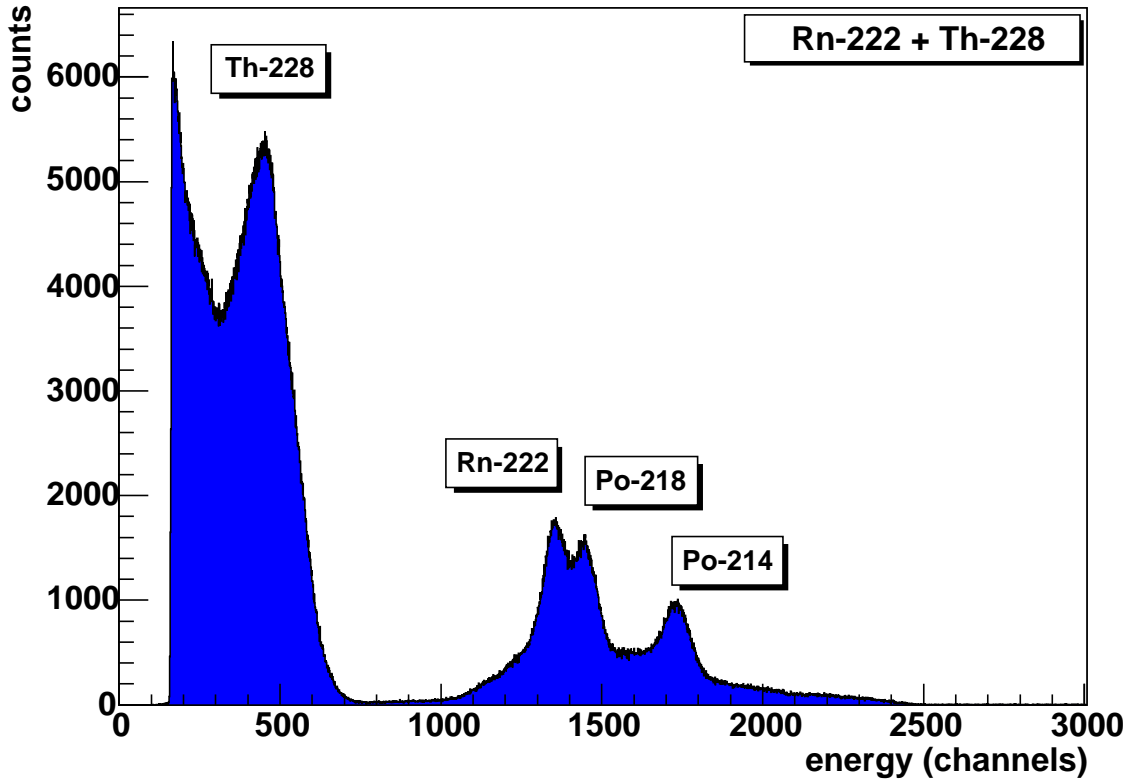
Figure 9.2: A spectrum of the LAr scintillation with ^{222}Rn inside the LAr taken with a MCA, using a spectroscopy amplifier. The α peaks at 5.5, 6.0 and 7.7 MeV are labelled with their associated isotope. The apparent peak on the left is the edge of the ^{228}Th γ spectrum.

is:

$$E = O + S \cdot C = -4.22 + 1.015 \cdot C \text{ [keV]}$$

in keV, with the offset O in keV, the slope S in keV/channel and C is the peak position in channels. The errors are $\Delta O = 1.03$ keV and $\Delta S = 0.029$ keV/channel (stat). The systematic error depending on different fitting ranges and initial fit parameters chosen is estimated as $\Delta S = 0.02$ keV/channel (sys).

Figure 9.4 shows the spectra taken from the anode (left) and dynode (right) by integrating over the fast component only. As an example the fits over the 238 keV peak are shown. For the anode spectrum the peak is at channel 69.31 ± 0.34 and for the dynode spectrum it is at channel 25.56 ± 0.11. The ratio between the peak positions in channels is the gain factor from the dynode to the anode for the fast component. The gain factor is $G_{d-a} = 2.712 \pm 0.018$.

To record pulses of a known energy the Bi-Po trigger (see section 4.3.4) was used. The following chapter discusses this method in some more detail including a test of its validity, making use of the pulse shape discrimination discussed there, but for now it is sufficient that it selects the α-events from the ^{214}Po-decay. The energy of the ^{214}Po α-s is 7.6869 MeV. Figure 9.5 shows the histogram of the integral over the slow component of pulses from ^{214}Po on the anode, recorded at a 10 mV scale with the digital oscilloscope. The peak position is channel
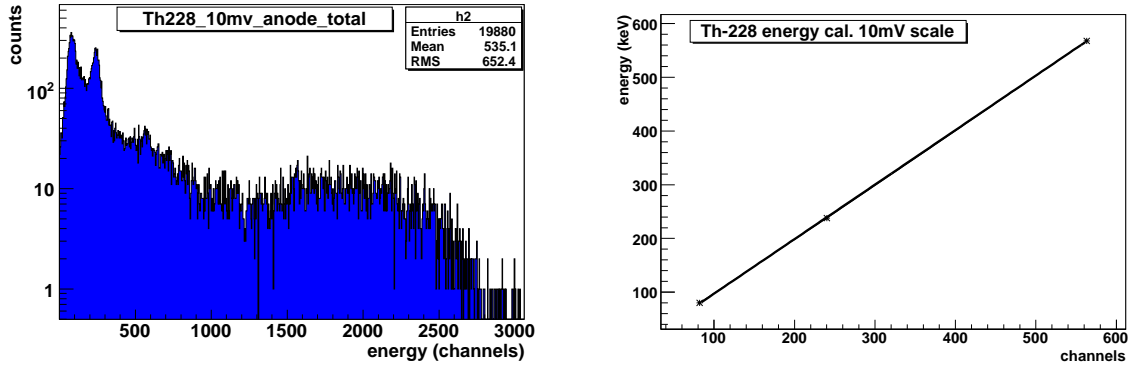
Figure 9.3: The pulse height spectrum of the anode signal from an internal ^{228}Th-source in logarithmic scale and the corresponding energy calibration.
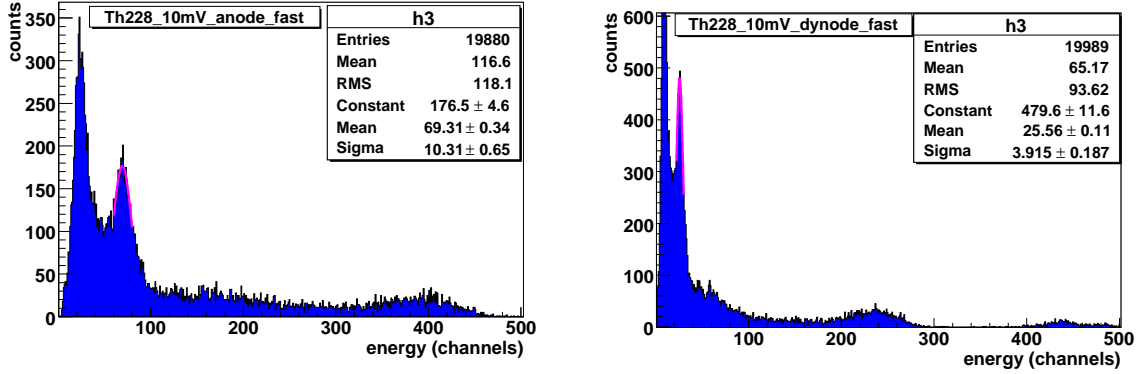
Figure 9.4: The pulse height spectrum of the fast component of the anode signal and of the dynode signal from an internal ^{228}Th-source. The fit over the 238 keV peak is shown in each spectrum.

$P_{slow}(Po) = 1555.0 \pm 3.8$. To the left of the ^{214}Po peak the contribution of random coincidences with other, lower energy α-s from the ^{222}Rn-chain is visible. Figure 9.6 shows the corresponding histogram of the integral over the fast component of the same pulses, but taken from the dynode at a 200 mV scale. To translate this to the full anode-equivalent integral, which was recorded at 10 mV scale, the dynode spectrum has to be multiplied by the scale factor of 20 determined by the oscilloscope settings and by the measured gain factor between dynode and anode. The scaled peak position is: channel $P_{fast}(Po) = 72.06 \cdot 20 \cdot 2.712 = 5464$. The combined error from the fit and the gain factor is 36 channels.

With the energy correlation determined above, the apparent electron-equivalent energy of the alpha peak is $E_{app} = P + Sl \cdot Ch = -4.22 + 1.015 \cdot 5464 = 5546$ keV. The error is 163 keV. With this the quenching factor becomes:

$$Q_\alpha = E_{app}/E_{real} = 5541/7686.9 = 0.721 \pm 0.021(stat) \pm 0.014(sys)$$

with E_{real} being the literature value for the energy of the α emitted by ^{214}Po.

This quenching factor agrees well with the factor of Q_α=0.73±0.04 found by Hitachi et al. in [HYDT87].

Po214_10mV_anode_slow	
Entries	19895
Mean	1535
RMS	443.3
Constant	786.8 ± 11.9
Mean	1555 ± 3.6
Sigma	200.2 ± 6.3

Po214_200mV_dynode_fast	
Entries	19992
Mean	70.97
RMS	12.18
Constant	1551 ± 23.0
Mean	72.06 ± 0.04
Sigma	2.459 ± 0.041

Figure 9.5: The ^{214}Po-spectrum taken from the anode at 10 mV scale. Slow component of the pulses only.
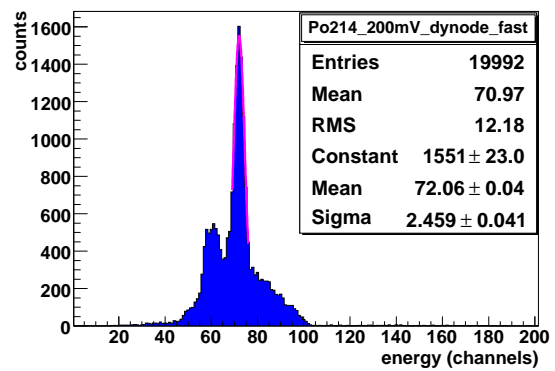
Figure 9.6: The ^{214}Po-spectrum taken from the dynode at 200 mV scale. Fast component of the pulses only.

Chapter 10

Pulse shape investigations

As discussed in sections 3.1.2 and 3.3 the properties of LAr scintillation allow for pulse shape discrimination. In this chapter the experimental results for different sources are discussed as well as the changes in pulse shape for Xenon doped LAr. For recording the pulses we used a digital oscilloscope as described in section 4.3.3.

10.1 Pulse shapes of LAr-scintillation for different sources

To compare the scintillation pulse shapes for different sources, the probability density function (pdf) is calculated for each source type. The pdf i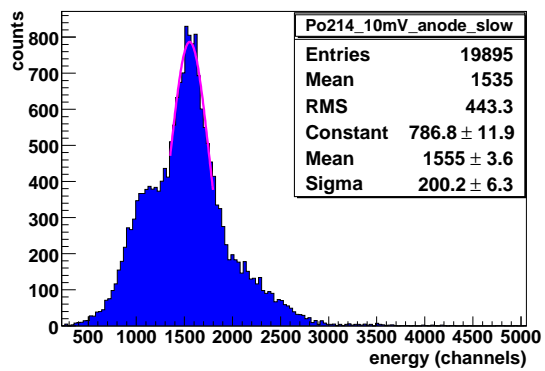s the average pulse shape for a certain source and energy window, normalised to a total area of unity. The pdf is plotted in the probability of the detection of an event vs. time. With high enough statistic for generating the average pulse shape (in this analysis $\mathcal{O}(10.000)$ pulses or more are used per pdf), each point in the pdf gives the probability for one photo electron to be generated and detected in the given time bin. To compare the pulse shapes for each single pulse and not only in the statistical mean, the ratio between the slow and the fast component is calculated. Since the fast component of the scintillation pulse shape is dominated by the emission from the singlet state and the slow component is dominated by the emission from the triplet state, the relative intensities of these two components are a good measure for the relative population of the excimer states. As discussed in the introduction (section 3.3) this population of the excimer states depends on the ionisation density of the particles. In this analysis the ratio slow/fast is used to avoid division by zero, since in some low energy events from particles with a high ionisation density, i.e. recoil nuclei from neutron scattering, the slow component vanishes. To visualise the ratio its value can be plotted for each pulse against the energy of that pulse. Pulses from sources of the same ionisation density, having roughly the same ratio, will then fall into a horizontal band in the ratio vs. energy plot.

10.1.1 γ-sources

In our investigation of the pulse shapes for gamma sources we used mainly two sources: ^{241}Am and ^{228}Th. ^{241}Am is used as internal source and has a single γ-line at 60 keV. This energy is low enough that the γ has a negligible probability of penetrating the 10 cm of LAr which is the active volume radius. That means that the γ is fully absorbed inside the active volume. ^{228}Th is convenient because its decay and that of its daughters provide several distinct lines at different energies, extending from 80 keV to 2.6 MeV. Figure 10.1 shows two samples of scintillation pulses taken directly from the PMT anode (no amplification or shaping). The pulses were recorded
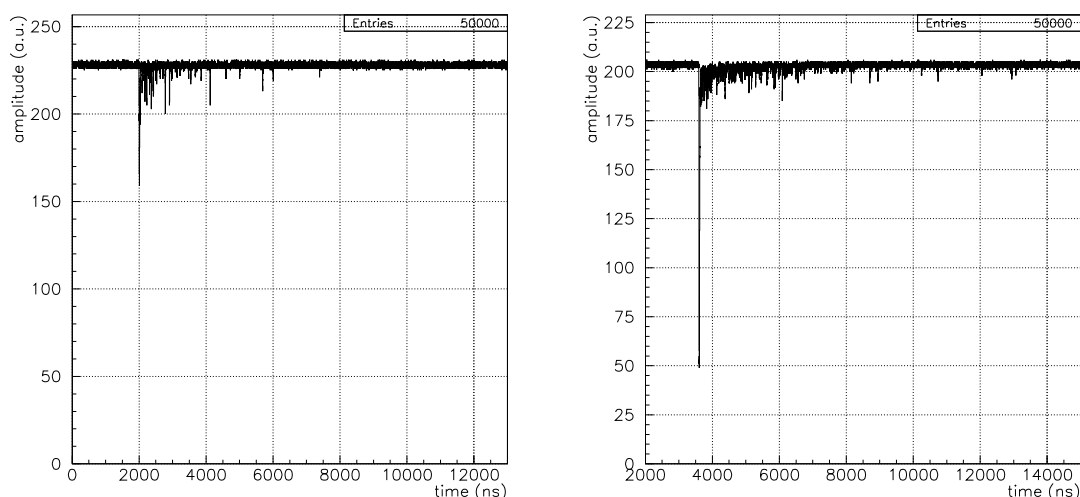
Figure 10.1: Sample pulses from γ-sources taken directly from the anode-signal of the PMT and recorded with the digital oscilloscope. Left: ^{241}Am, right: ^{228}Th. The time resolution is 400 ps.

with the digital oscilloscope with a time resolution of 400 ps per point. On the left is a typical pulse for the ^{241}Am source (60 keV) and on the right is a pulse of a comparatively higher energy from ^{228}Th. It is visible that, while the fast component constitutes an actual comparatively high peak, the tail of the slow component consists mostly of single photo electron events. The spacing of these single photo electron events depends on the total energy of the pulse and on the position (i.e. the time) in the tail. For a comparison of pulses of different energies it is necessary to create the probability density function mentioned above. Figure 10.2 shows the pdf for a ^{241}Am gamma source. The pdf was generated from events with a known energy deposition, selected by a cut on the associated pulse height spectrum selecting only events that fall into 2σ of the 60 keV peak. The x-axis (time in ns) is plotted in logarithmic scale for better visibility of the slow component.

Figure 10.3 shows a comparison of pdf-s from γ-s at different energies. They are obtained by making energy cuts on peaks in the ^{228}Th spectrum. All three pdf-s are generated from the data of the same run. The black line is the pdf for 80 keV γ-s, the red line is the pdf for 238 keV γ-s and the green line is the pdf for 583 keV γ-s. Again the pdf-s are plotted in logarithmic timescale. For a more detailed investigation it is necessary to look at the fast and the slow component separately. Figure 10.4 shows a zoom in a linear scale on the fast component of the pdf-s and figure 10.5 shows a zoom in a linear scale on a part of the slow component. The fast component shows the highest population for the low energy γ-s (black line) and increasingly lower population for higher energy γ-s (red and green). For the slow component the population is inverted: lowest for low energy and highest for high energy.

This behaviour is explainable by considering that the ionisation density of electrons depends on their energy and that higher energetic gammas also produce electrons with a higher energy in their interactions with LAr. This means that the average ionisation density for γ-events depends on the energy of the γ. The population of the fast and slow component depends on the ionisation density ([HTF$^+$83]), so low energy γ-events generate a slightly higher ionisation density and thereby a higher singlet/triplet ratio. This means the fast component of the scintillation is slightly stronger populated for low energy γ-s. Conversely a saturation effect or non-linearity of
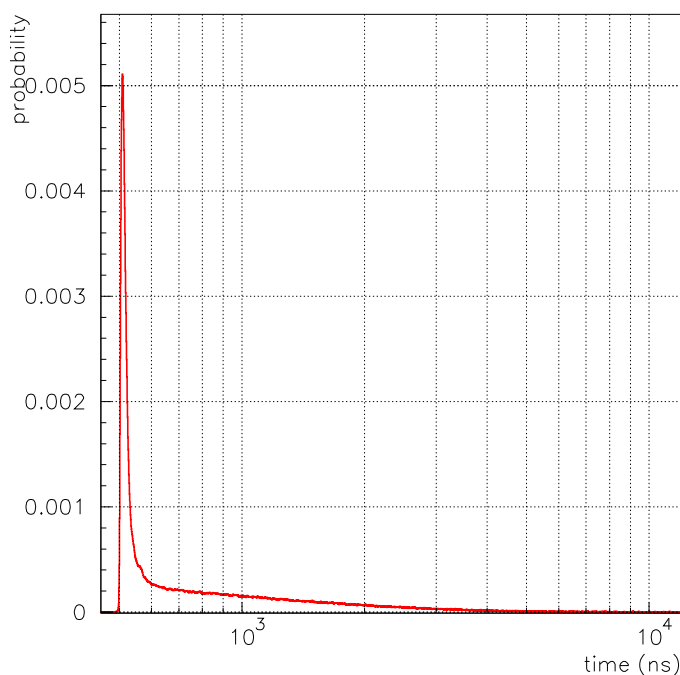
Figure 10.2: The probability density function for the scintillation pulses from an internal ^{241}Am γ-source. Plotted in probability per 400 ps bin vs. log. time [ns].

the PMT is unlikely, since the effect observed persists in the μs scale, where a saturation of the PMT, which might be assumed for higher energies, would have regenerated. The same is true for influences of pre-pulses, which might have an effect on the fast component similar to the one observed, but could not explain the difference between the pulses in the slow component. So the explanation that the effect of the γ-energy on the average ionisation density of γ-events can be seen in the pdf-s is the most plausible one.

The pdf is a tool to compare the statistic mean of different pulse shapes. Since it is not possible to generate a pdf from a single pulse, the ratio between the fast and the slow component of the scintillation becomes the main discriminating characteristic. In our analysis we define the charge collected in the first 48 ns as the fast component (8 half-lives of the singlet state) and the charge collected in the following 8 μs as the slow component (5 half lives of the triplet state). At this length most of the emissions from the triplet state are included in the evaluation window ($\sim$97%). At greater lengths the single photo electron noise from the PMT would be a non-negligible contribution. As mentioned above we use the ratio slow/fast component to avoid division by zero. Figure 10.6 shows the ratio plot for the ^{241}Am-source along with the corresponding spectrum figure 10.7. The ratio plot is in ratio vs. energy in bins. Each dot represents one event (one recorded pulse). The spectrum uses the same energy scale in bins. The peaks in the spectrum correspond to the accumulations of events visible in the ratio plot. Figure 10.8 and 10.9 show the same plots for the ^{228}Th source and Figure 10.10 shows an overlay of the ratio plot from ^{228}Th with the ratio plot from ^{241}Am. It is visible that the events from both sources fall into the same horizontal band.
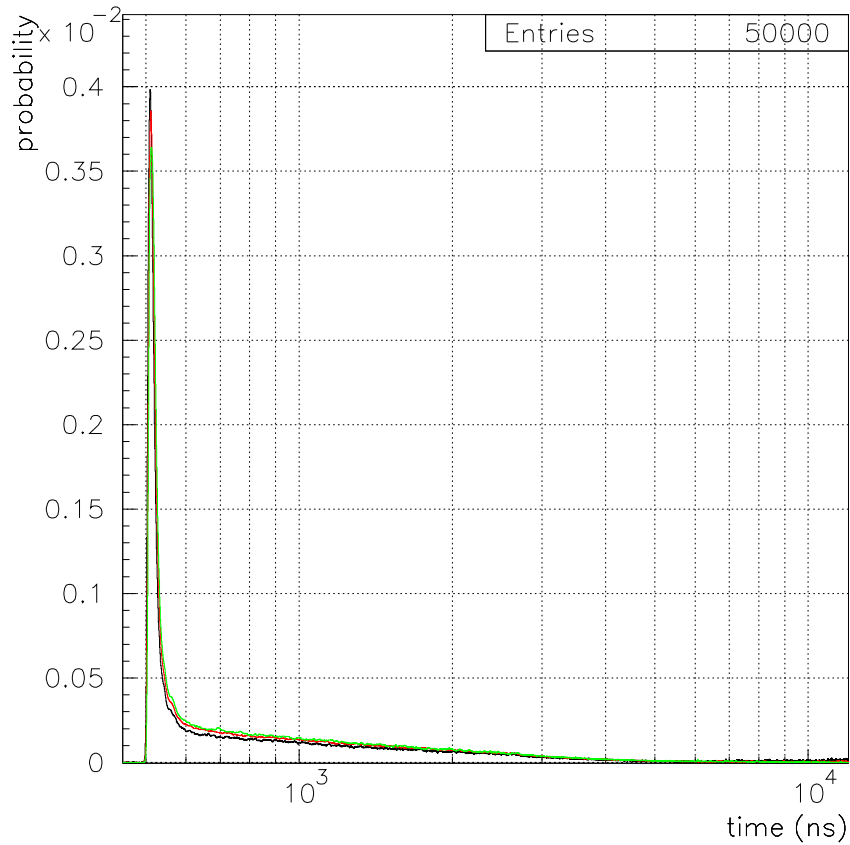
Figure 10.3: A comparison of pdf-s for different γ-energies plotted in probability per 400 ps bin vs. time in logarithmic scale. Black = 80 keV, red = 238 keV, green = 583 keV
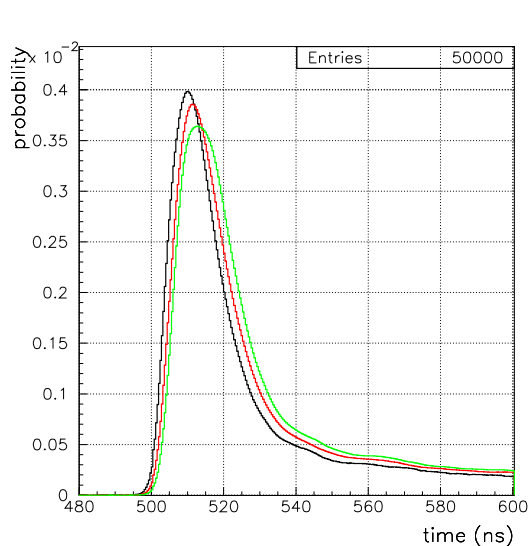
Figure 10.4: The fast component (first 100 ns) of the pdf-s shown in figure 10.3 in linear scale (same colour code).
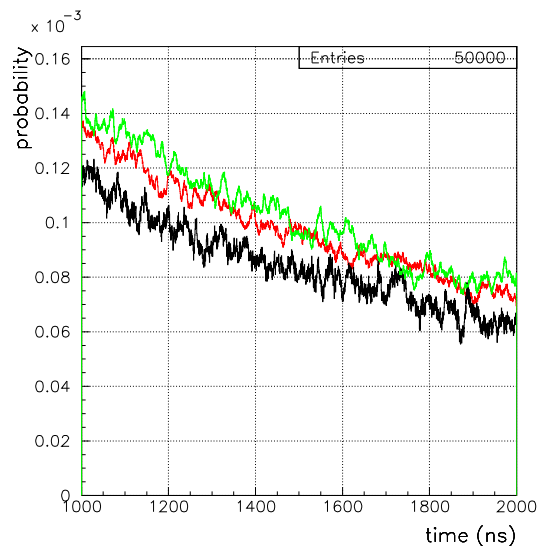
Figure 10.5: A zoom on the slow component of the pdf-s shown in figure 10.3 (same colour code).
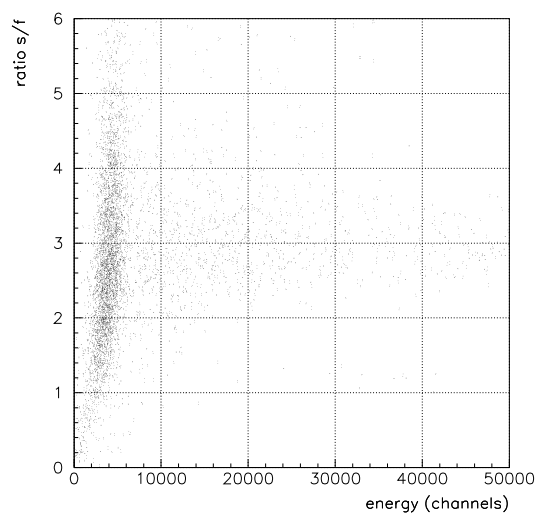
Figure 10.6: The ratio plot for the internal ^{241}Am-source. Plotted in ratio slow/fast component vs. energy in bins.
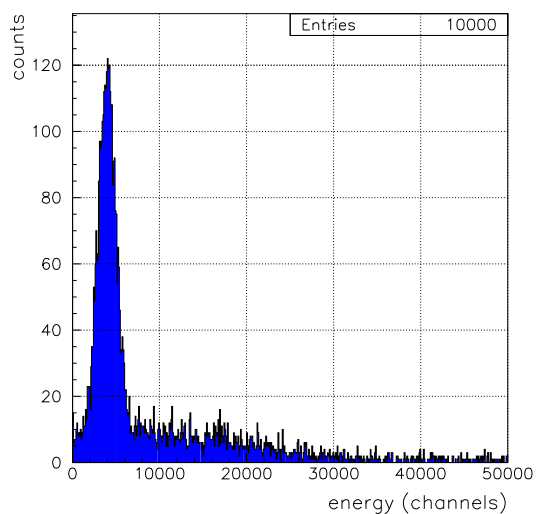
Figure 10.7: The spectrum of the internal ^{241}Am-source. Plotted in number of counts vs. energy in bins.
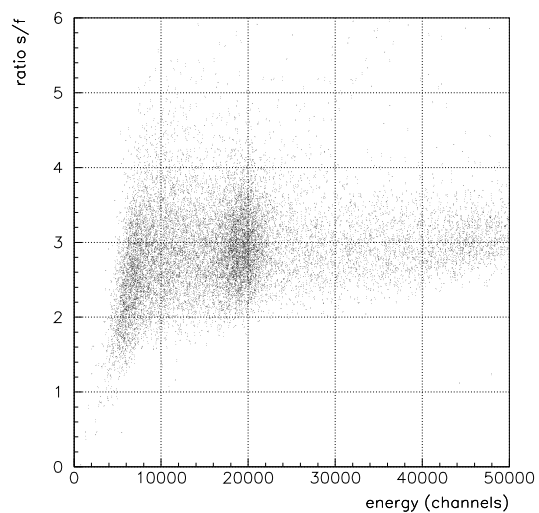
Figure 10.8: The ratio plot for the internal ^{228}Th-source. Plotted in ratio slow/fast component vs. energy in bins.
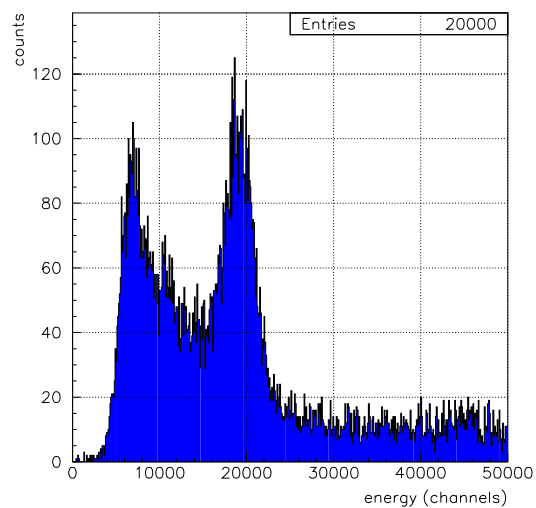
Figure 10.9: The spectrum of the internal ^{228}Th-source. Plotted in number of counts vs. energy in bins.
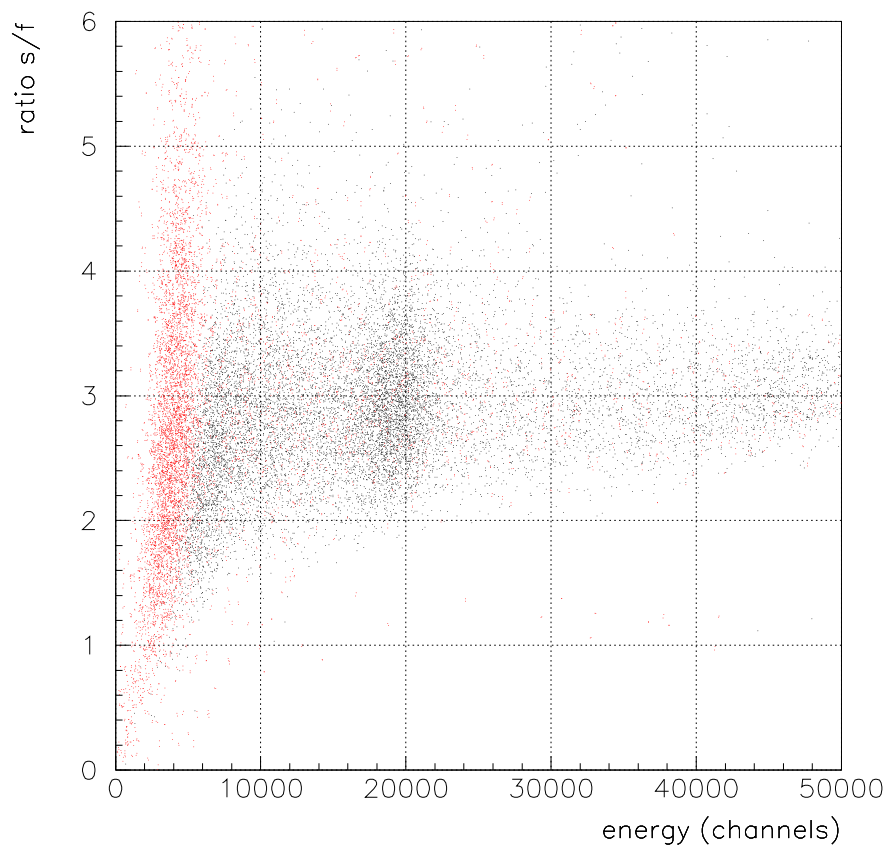
Figure 10.10: An overlay of the ratio plots of the ^{241}Am (red) and the ^{228}Th-source (black). The events from both sources fall into the same horizontal band. The '$\beta - \gamma$-band'.

10.1.2 α-particles

To investigate the scintillation pulse shape for the excitation of the LAr with α particles the LAr was doped with ^{222}Rn (see section 4.4.2 and chapter 9). The pulses were recorded with the digital oscilloscope and integrated by software. The limitation in energy resolution mentioned in chapter 9 is not a problem here, since the goal here is not spectroscopy or the determination of a quenching factor, but the investigation of the pulse shape and the ratio of the slow component to the fast component of the scintillation light.

Figure 10.11 shows a combined spectrum of the internal ^{228}Th source and the α-s from the ^{222}Rn inside the LAr. Figure 10.12 shows the corresponding ratio vs. energy scatter plot. The separation of two bands and their correlation with the energies of the γ-source and the α-s is clearly visible. Figure 10.13 shows the ratio histogram, plotted in ratio slow/fast component against number of counts, for the ^{228}Th-source before the insertion of ^{222}Rn (red) and for ^{228}Th and ^{222}Rn combined. The events from the 'γ-band' are centred around a mean ratio of $\overline{R} = 2.75 \pm 0.34$ with a σ of 0.37. The events in the 'α-band' are centred around $\overline{R} = 0.51 \pm 0.14$ with a σ of 0.083.
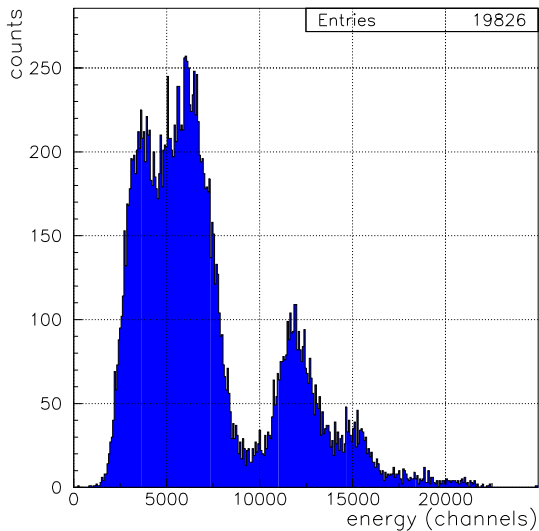
Figure 10.11: The spectrum of internal ^{228}Th and ^{222}Rn.
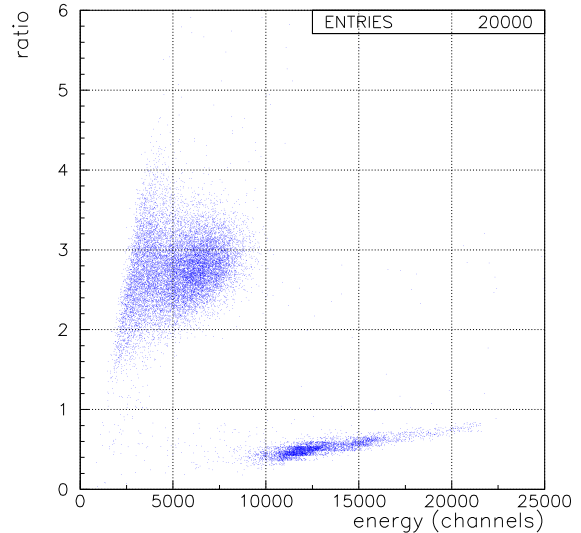
Figure 10.12: The ratio plot of the internal ^{228}Th-source and ^{222}Rn.

We define the separation S_σ between two ratio peaks as the distance between the peaks divided by the sum of the sigma-values for both peaks. This value is the distance of a point between the two peaks which is equally distant from each peak, when measured in units of the respective sigma: $M_n + S_\sigma \cdot \sigma_n = M_\gamma - S_\sigma \cdot \sigma_\gamma$. The separation of the ratio peak for the α-like events from that for the γ-like events in the ratio histogram in figure 10.13 is S_σ=4.9 sigma.

To calculate the overlap between the two ratio bands, the ratio distributions are assumed to be Gaussian. The probability for an event from one type of source to register in the ratio band of the other, that means the probability to identify a particle wrongly, is given by half the normalised overlap of the two Gaussians associated with the two ratio distributions. The normalised area of the overlap of two Gaussians is given by:

113
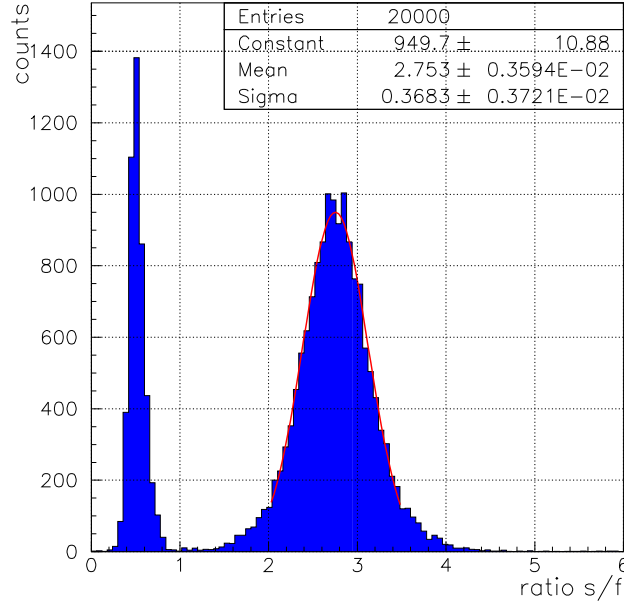
Figure 10.13: The ratio histogram for the ^{228}Th and ^{222}Rn measurements.

$$A_{overlap} = \int\limits_{-\infty}^{R_i} \frac{1}{\sqrt{2\pi}\sigma_2} \cdot exp\left(\frac{-(R-\overline{R}_2)^2}{2\sigma_2^2}\right) dR + \int\limits_{R_i}^{+\infty} \frac{1}{\sqrt{2\pi}\sigma_1} \cdot exp\left(\frac{-(R-\overline{R}_1)^2}{2\sigma_1^2}\right) dR \quad (10.1)$$

with R_i being the ratio where the two Gaussians overlap, $\overline{R}_1$ and σ_1 being the mean ratio and sigma of the 'left' Gaussian and $\overline{R}_2$ and σ_2 being the same for the 'right' Gaussian. This equation can be re-written as:

$$A_{overlap} = \frac{1}{2}erfc\left(\frac{R_i - \overline{R}_1}{\sqrt{2}\sigma_1}\right) + \frac{1}{2}erfc\left(\frac{\overline{R}_2 - R_i}{\sqrt{2}\sigma_2}\right)$$

and this can be approximated [RCP05] to:

$$A_{overlap} = erfc\left(\frac{\Delta R}{2 \cdot \sqrt{2} \cdot \sigma_m}\right) = \int\limits_{\frac{\Delta R}{2 \cdot \sqrt{2} \cdot \sigma_m}}^{\infty} \frac{2}{\sqrt{\pi}} \cdot e^{-u^2} du \quad (10.2)$$

with $erfc(x)$ being the error function, ΔR being the difference between the ratio peaks and σ_m being the average sigma: $\sigma_m = (\sigma_1 + \sigma_2)/2$. Solving the integral and inserting the separation $S_\sigma = \Delta R/(\sigma_1 + \sigma_2) = \Delta R/(2 \cdot \sigma_m)$ introduced above, yields:

$$A_{overlap} = \frac{\sqrt{2}}{S_\sigma \sqrt{\pi}} exp\left(-\frac{1}{2}S_\sigma^2\right) \quad (10.3)$$

With this the probability P_{mi} to mis-identify an event becomes:

$$P_{mi} = \frac{1}{2}A_{overlap} = \frac{1}{S_\sigma \sqrt{2\pi}} exp\left(-\frac{1}{2}S_\sigma^2\right) \quad (10.4)$$

114

With the value S_σ=4.9 determined above inserted into equation 10.4 the probability to wrongly identify an α as a γ or vice versa becomes: $P_{mi} = 5 \cdot 10^{-7}$. This means that the confidence level of the identification is 99.99995%.

To compare the statistical mean of the pulses and visualise the difference in pulse shape, the pdf of the α-pulses is generated. Figure 10.14 shows a comparison of the pdf-s for γ-sources shown in the last section with the pdf-s of pulses from the α-energy region. The different pdf-s are: Red=^{214}Po 7.7 MeV-α, selected by coincidence cut. Black=all ^{222}Rn-α-s, selected by energy cut. Blue = ^{228}Th (583 keV-γ) and green = ^{228}Th (80 keV-γ), selected by energy cuts on the full energy peaks. It is clearly visible that the pulses from α-particles show a stronger population of the fast component and a correspondingly weaker population of the slow component. Also it is visible, that while particles of the same kind but different energies show slight differences in the relative population of the slow and fast component, these differences are insignificant when compared to the difference between different kinds of particles.

As a crosscheck whether the events selected by energy cut on the spectrum are really mostly α-s, a different selection criterion can be used: the so-called Bi-Po trigger (see section 4.3.4). By selecting events that are above the γ-scale (> 3 MeV) and are correlated within 360 μs to a previous event, triggered with a low threshold in the $\beta - \gamma$-scale, there is a high probability that the selected event is a ^{214}Po-decay. The probability is given by the length of the correlation gate (360 μs) and the source- and random-trigger-rates (table 9.1).

Figure 10.15 shows a sample pulse-correlation on the digital oscilloscope. In the software analysis the high-energy 'delayed pulse' and the 'prompt pulse' are analysed separately. Figure 10.16 and 10.17 show the spectra of the prompt and delayed events. And figure 10.18 and 10.19 show the corresponding ratio plots. In the ratio plot of the prompt pulses two distinct groups are visible. One of lower energy with ratios in the $\beta - \gamma$ band and one high energy group with ratios in the α range. This means that a significant part of the prompt events are α-s.Since in a real Bi-Po event the prompt event has to be a β/γ event from ^{214}Bi these events are random coincidences. To test this assumption, the time distribution of the prompt and delayed signals is investigated. Real Bi-Po events should be distributed following the exponential decay equation

$$N(t) = N_0 \cdot e^{-\lambda \cdot t}$$

with $N(t)$ the number of events at a given time t, N_0 the number of events at time zero and the decay constant of $\lambda = ln(2)/T_{1/2} = 4.23 \cdot 10^{-3} \mu s^{-1}$ with $T_{1/2}(^{214}$Po$)$=164 μs. Random coincidences however are expected to be distributed linearly in all time intervals.

Figure 10.20 shows a histogram of the time distribution in number of events vs. time in μs. The cutoffs at 10 μs and 360 μs are given by the time window used. The distribution is fitted by a constant, to account for the random coincidences, plus an exponential decay: $f(t) = P1 + P2 \cdot exp(P3 \cdot t)$. The parameters are the constant contribution P1=C, $P2 = N_0$ and P3 = -λ.

The fit result for the decay constant is $\lambda = (4.38 \pm 0.68) \cdot 10^{-3} \mu s^{-1}$, which translates to $T_{1/2} = (158 \pm 25)$ μs. Within the error this agrees with the expected 164 μs half-life of ^{214}Po. The linear background is given as 23±11 counts.

To verify that the events with 'α-like' prompt signal are random coincidences, a cut on ratio vs. energy is made. The cut-requirement E$\geq$1500+4250$\cdot$R$_{s/f}$, with the energy in channels E and the ratio slow-/fast component R$_{s/f}$, selects events with the prompt signal in the α-band and high energy events well beyond the ^{214}Bi-β-range. The timing histogram of these events (Figure 10.21 shows indeed a linear distribution. This means that these events are not intrinsically correlated. The remaining events with a ratio in the $\beta - \gamma$ region show the time-
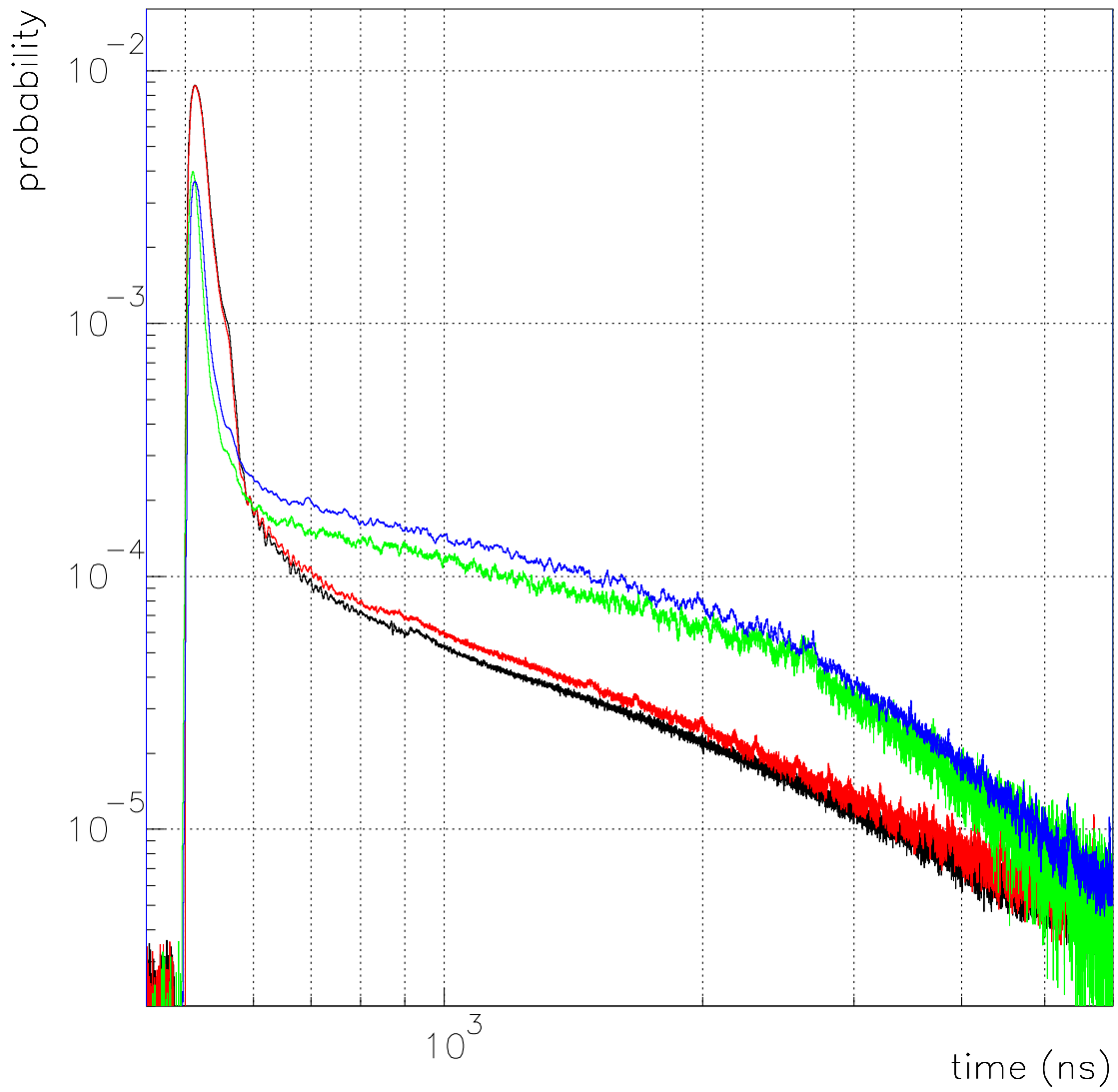
Figure 10.14: A comparison of the pdf-s for α-s and γ-s in log. probability per 400 ps bin vs. log. time. Sources: black=all ^{222}Rn-alphas, red=^{214}Po 7.7 MeV-α, green=^{228}Th 80 keV-γ, blue=^{228}Th 583 keV-γ
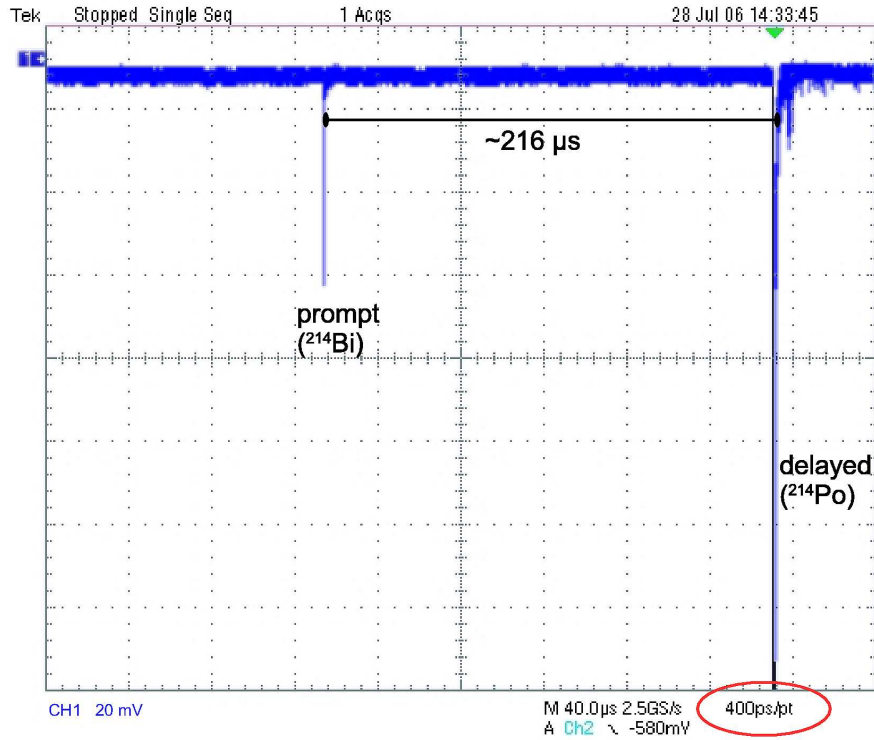
Figure 10.15: A sample of two correlated pulses (oscilloscope screenshot). A prompt pulse of lower energy and a delayed pulse in the higher α-energy scale. The x-axis is the time with 40 μs per box and the y-axis is the pulse height with 20 mV per box. The resolution selected is 400 ps/pt.

distribution shown in Figure 10.22. The linear background is reduced to 12±10 and the fit gives $\lambda = (4.35 \pm 0.57) \cdot 10^{-3} \mu s^{-1}$. The corresponding half-life is $T_{1/2} = (159 \pm 21)\mu s$.

The energy spectra and the corresponding ratio vs. energy plots are shown in figure 10.23. The plots from the prompt signals are shown in red and those from the delayed signals are blue. The contribution of random coincidences is visibly reduced. Figure 10.24 shows the ratio histograms for the prompt (red) and delayed signals (blue). The prompt signal ratio is centred around 2.857±0.013 with a 1σ of 0.596. The ratio of the delayed signals is centred around 0.5548±0.0009 with a 1σ of 0.073. These values agree with the ratios of the 'γ-band' and 'α-band' signals shown in plot 10.13 within the errors given there. However the errors of these 'cleaned' Bi-Po coincidence measurement are smaller. The spread (σ) of the prompt signal ratio distribution appears to be significantly larger than the sigma of the γ-band in figure 10.13. This is due to the different energy threshold. For the Bi-Po measurements a low threshold was used, to be sensitive to a large part of the ^{214}Bi-spectrum. While in the ^{222}Rn+^{228}Th-measurements a high threshold was used to avoid being dominated by the ^{228}Th signal.
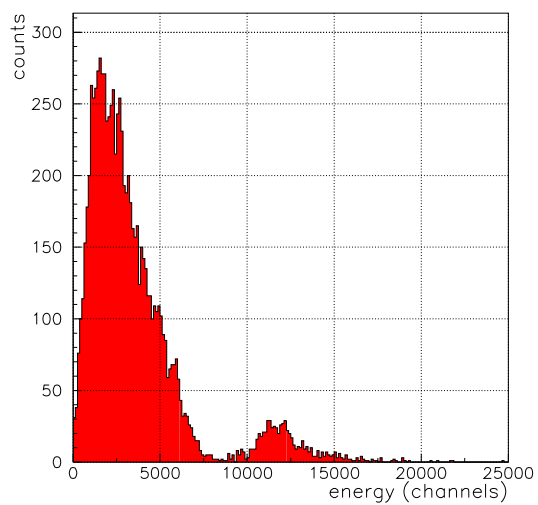
Figure 10.16: The spectrum of the prompt pulses from the Bi-Po measurement.
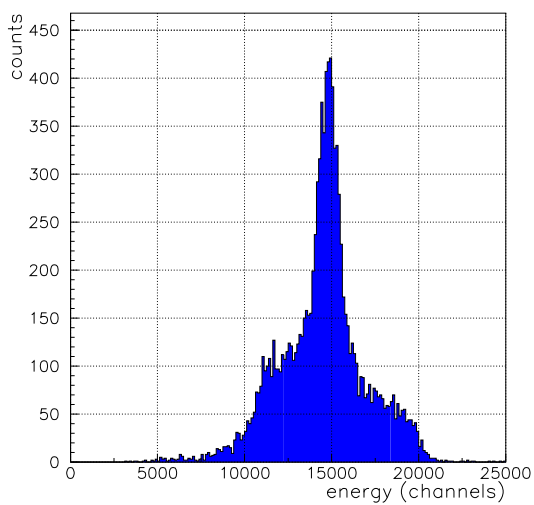
Figure 10.17: The spectrum of the delayed pulses from the Bi-Po measurement.
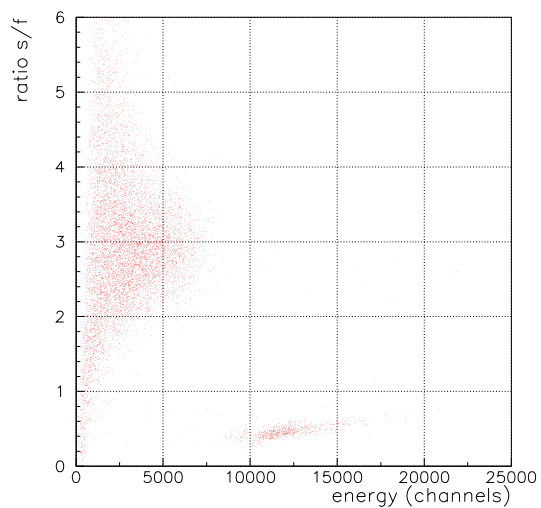
Figure 10.18: The ratio plot for the prompt events.
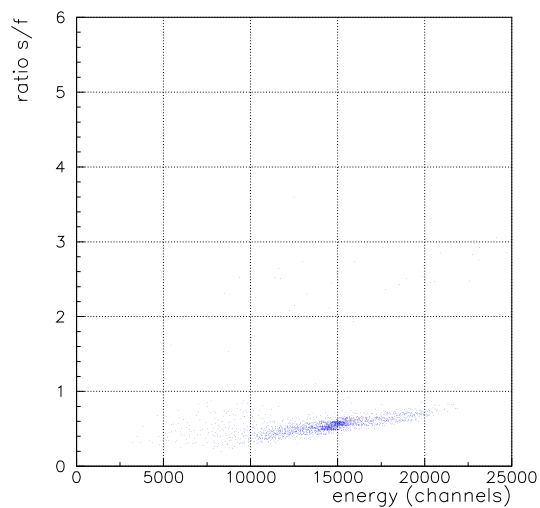
Figure 10.19: The ratio plot for the delayed events.

118
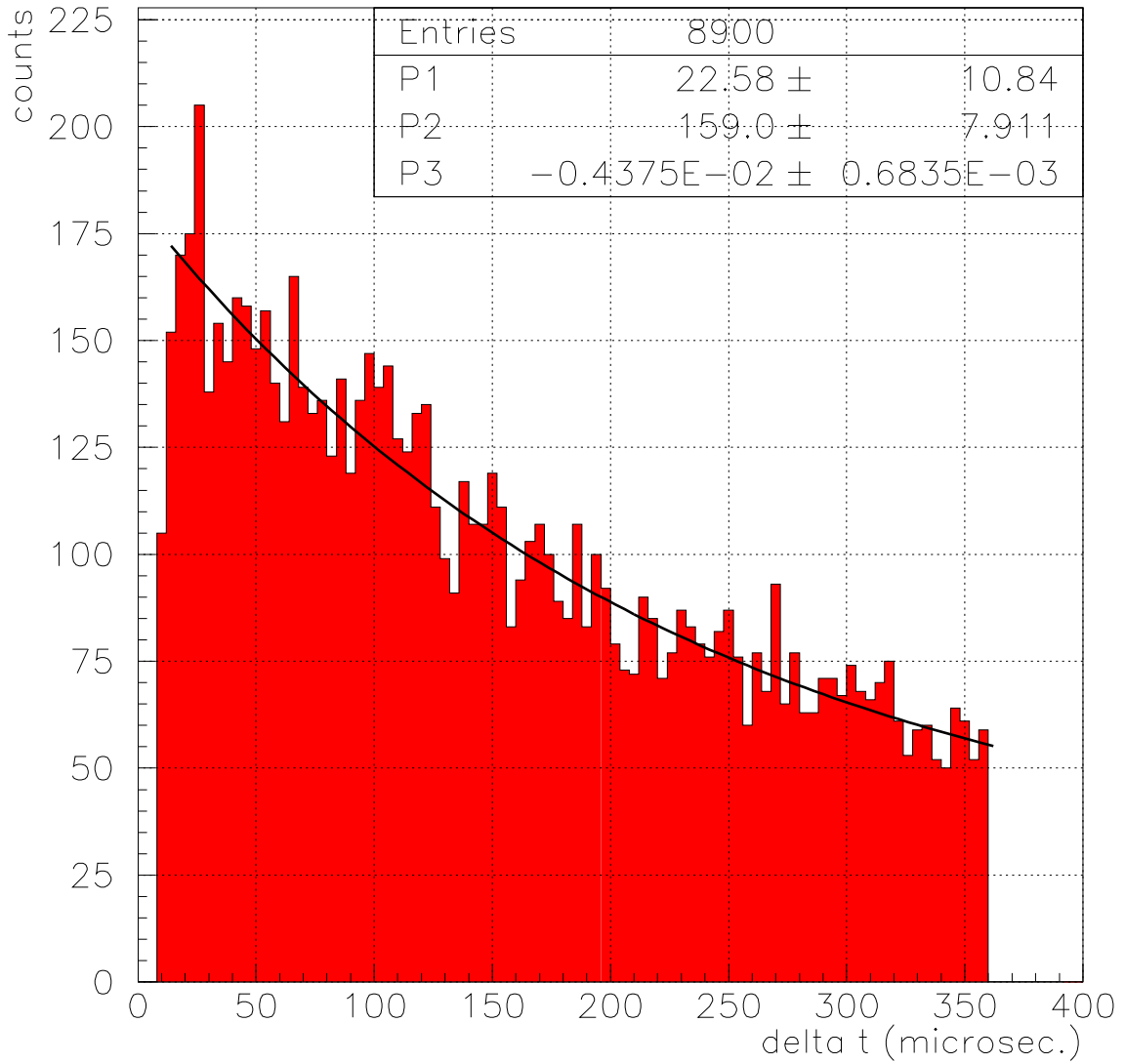
Figure 10.20: The timing histogram for the Bi-Po coincidences.With the fit $f(t) = P1 + P2 \cdot exp(P3 \cdot t)$
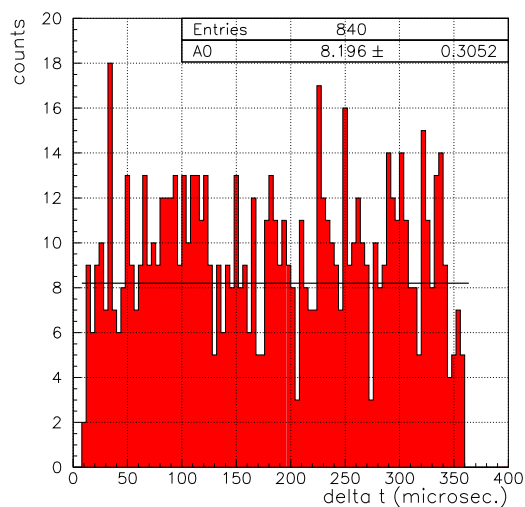
Figure 10.21: The timing histogram for the events with the prompt signal in the α ratio band with a constant as fit.
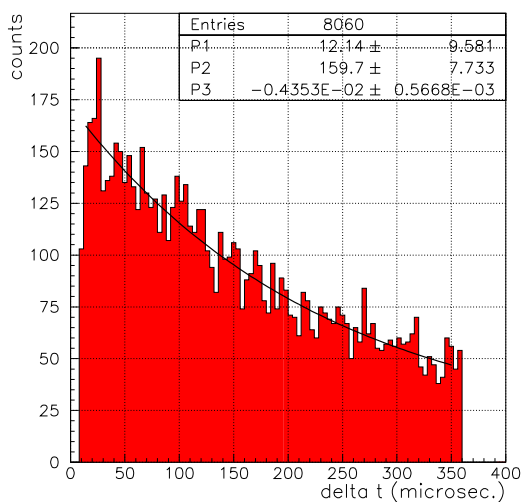
Figure 10.22: The timing histogram for events with the prompt signal in the $\beta - \gamma$ ratio band with the fit $f(t) = P1 + P2 \cdot exp(P3 \cdot t)$.
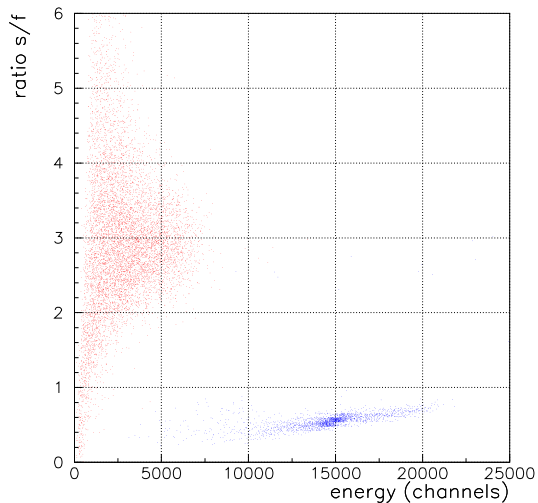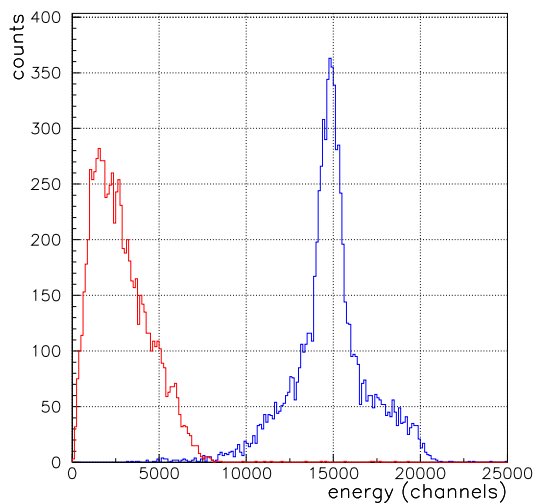
Figure 10.23: The spectra and the plot ratio s/f vs. energy of the cleaned Bi-Po data. Red: prompt signals, blue: delayed signals.
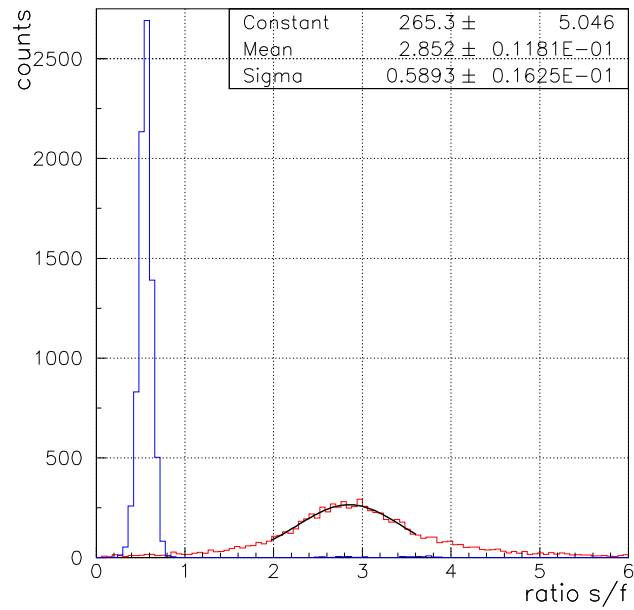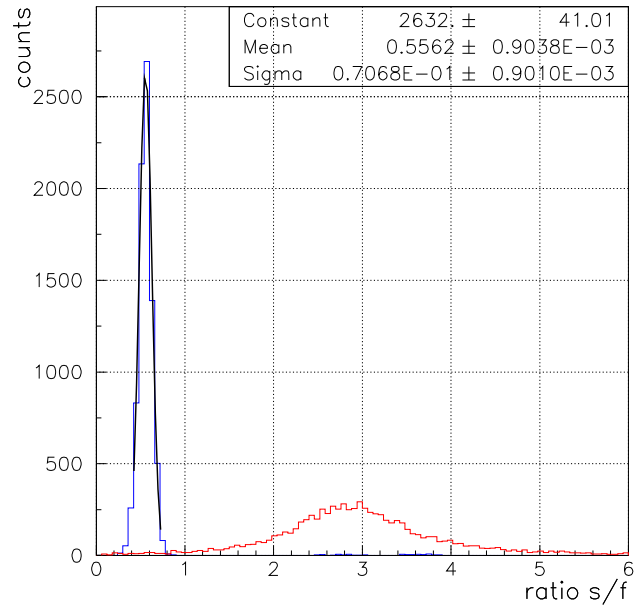
Figure 10.24: The ratio histogram for the prompt signal (red) and the delayed signal (blue). On the top plot the fit for the delayed signal is shown and on the bottom plot the fit for the prompt signals.

10.1.3 Neutrons / recoil nuclei

Neutrons are an important possible source of background that needs to be taken into account in GERDA (see section 2.3). Also they can be a signature of the creation of secondary radioactive isotopes by muon-induced spallation. Neutrons can be detected via inelastic interactions or elastic scattering on nuclei. The recoil nuclei from the elastic scattering process are charged particles of high ionisation density which induce scintillation light. The population of the singlet state relative to the triplet state should be even higher than for α-s, due to the higher ionisation density. The ratio of the slow/fast component of the scintillation is therefore expected to be lower than for α-s.

To test the detection of neutrons and determine the discrimination power between neutrons and γ-s an americium-beryllium (AmBe) neutron source was used externally. It contains a mixture of ^{241}Am and ^{9}Be. α-particles emitted from the ^{241}Am can be absorbed by the beryllium, emitting one neutron in the process $^9Be + \alpha \rightarrow^{12} C + n$. Table 10.1 lists the properties of the sources used. The energy of the neutrons peaks at $\sim$3 MeV and extends up to 10 MeV [NPRS69]. They deposit energy in the LAr by elastic scattering on Ar nuclei. The energy deposited depends on the scattering angle and the atomic weight of the nucleus (Ar: A=40). $E_{dep} = W_i - W_f$ with the deposited energy E_{dep}, the initial neutron energy W_i and the final neutron energy after scattering W_f.

$$W_f = W_i \cdot \frac{\sqrt{A^2 - 1 + cos^2\delta} + cos\delta}{(A+1)^2}$$

At 180° the energy transfer is maximal: $E_{dep} = W_i - W_i \cdot (A-1)^2/(A+1)^2 \simeq 0.1 \cdot W_i$. So we expect an energy spectrum which peaks at low energies and extends up to 1 MeV. The visible energy will be further reduced by an unknown quenching factor for recoil nuclei, which is assumed to be bigger than the quenching factor for α-s (chapter 9).

| Name	cited total activity	neutron activity	acquisition date	current total activity	current neutron activity
AmBe weak	1 mCi	$2 \cdot 10^3$ n/s	29.4.1983	0.964 mCi	$1.93 \cdot 10^3$
AmBe strong	30 mCi	$7 \cdot 10^4$ n/s	25.4.1968	28.23 mCi	$6.59 \cdot 10^4$ n/s

Table 10.1: The properties of the AmBe-neutron sources used in the neutron measurements.

The activity of the weak neutron source proved not to be enough to generate a significant statistic. Also, for both sources when used in the standard 'external' source position in the window in the lead shield, the signal was dominated by the γ-s emitted by the neutron source. The best results were achieved with the source shielded with 10 cm of lead against the system: The neutron flux is not significantly reduced due to the lead but γ-s are absorbed. There are additional γ-s produced due to bremsstrahlung and absorption, but the overall flux is reduced.

Figure 10.25 shows a comparison of the ratio plot for a ^{241}Am γ-source and a ratio plot for the ^{241}Am γ-source and the AmBe-neutron-source combined. The additional band at low slow/fast ratios appearing in the AmBe-ratio plot is clearly visible. It is attributed to the neutrons / nuclear recoils. It is visible that the separation of the two bands is dependant on the energy and that for energies below the 60 keV events from ^{241}Am there is no clear separation.

Figure 10.26 shows the ratio histogram of the AmBe-neutron source (black) and the pure ^{241}Am γ-source (red) with an energy cut of $E \geq 50$ keV, just below the full energy deposition of ^{241}Am gammas. The additional peak at low ratios in the ratio histogram for the AmBe

source corresponds to the 'neutron band' in the ratio scatter plot. It peaks around a ratio of 0.368 ± 0.004 with a sigma of 0.14. The ratios of the γ-s in this region peak around 2.873 ± 0.007 with a sigma of 0.58. The separation is S_σ=3.48 sigma. Inserted into equation 10.4 this yields a probability to mis-identify an event of $P_{mi} = 3\cdot10^{-4}$ and thereby a confidence level of the identification of 99.97%.

This discrimination is still two orders of magnitude from the required suppression for β/γ events in the nuclear recoil band required for the Dark Matter investigation. As mentioned in section 3.3 a sensitivity of 10^{-10} pb for WIMPs would require a suppression of 10^6, in other words a mis-identification probability of $P_{mi} \leq 10^{-6}$. However it might be possible to improve the separation by improving the pulse shape analysis algorithm and by improving the photo-electron yield further or by discarding events close to the crossover point R_i between the two ratio distributions. The investigation of the pulse shape discrimination as a tool of background suppression and the investigation of the WIMP detection sensitivity resulting thereof will be continued in the new GERDA-LArGe setup currently under construction in the Gran Sasso laboratories.
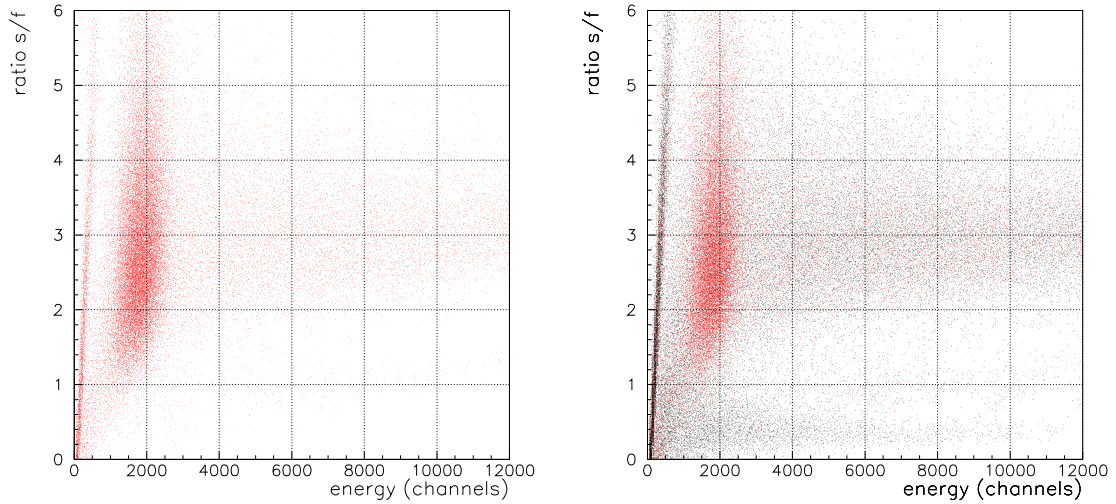
Figure 10.25: Left: the ratio scatter plot for the internal ^{241}Am γ-source. Right: the ratio scatter plot for the AmBe-neutron source (black) overlaid on that for ^{241}Am (red).

To investigate the dependence of the separation power on energy, the ratio histograms for different energy cuts are created. As energy calibration the ^{241}Am γ-peak is used, which is at channel 1819±2 at this energy scale. Figure 10.27 shows three of these ratio histograms. It is visible that the separation between the two ratio peaks increases with increasing energy.

For an energy cut on 50-100 keV the neutron ratio peaks at 0.42 with a sigma of 0.22 and the γ-ratio peaks at 2.62 with a sigma of 0.99. The separation is 1.8 sigma. For an energy cut on 100-150 keV the neutron ratio peaks at 0.38 with a sigma of 0.14 and the γ-ratio peaks at 2.77 with a sigma of 0.75. The separation is 2.7 sigma. For an energy cut on 150-200 keV the neutron ratio peaks at 0.36 with a sigma of 0.12 and the γ-ratio peaks at 2.84 with a sigma of 0.62. The separation is 3.4 sigma.

To generate the pdf for nuclear recoil events, events with a ratio within 1σ around the 'neutron' peak in the ratio histogram and with an energy >60 keV were chosen. Figure 10.28 shows the resulting pdf in comparison with the pdf-s for α-s and γ-s discussed in the previous
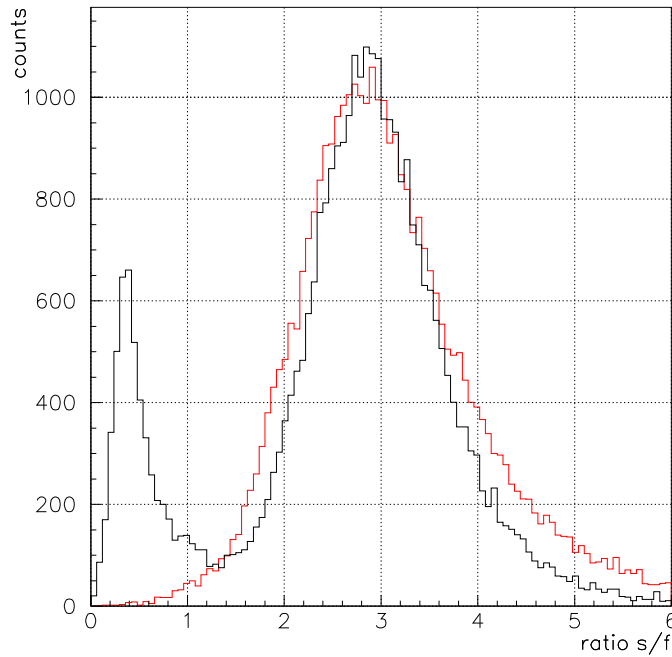
Figure 10.26: The ratio histogram for the AmBe-neutron source (black) and that for a pure ^{241}Am-γ-source (red). Both for events with $\geq$50 keV.

(a) 50-100 keV

(b) 100-150 keV

(c) 150-200 keV
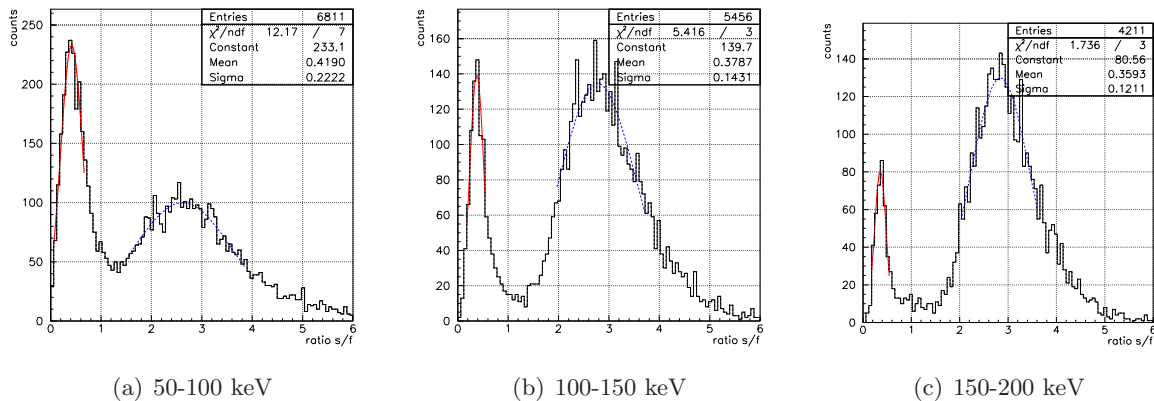
Figure 10.27: Ratio plots showing the separation between neutron- and γ-events for different energy cuts. The fit parameters displayed are those of the fit of the neutron ratio peak.

sections.

After the ^{222}Rn measurements discussed in the previous section, with the Rn still present inside the system, a new AmBe-neutron run was made and in the ratio vs. energy scatter plots a new class of events between the γ-band and the neutron-band had appeared. These events are attributed to degraded α-s from Rn-daughters embedded in the walls of the active volume. Figure 10.29 shows one of these ratio plots with the 'new' class of events marked. Figure 10.30 shows a continuation of this ratio plot to higher energy scales. At these high energies recorded in the settings for the low energy scale the high energy pulses are truncated by the oscilloscope.
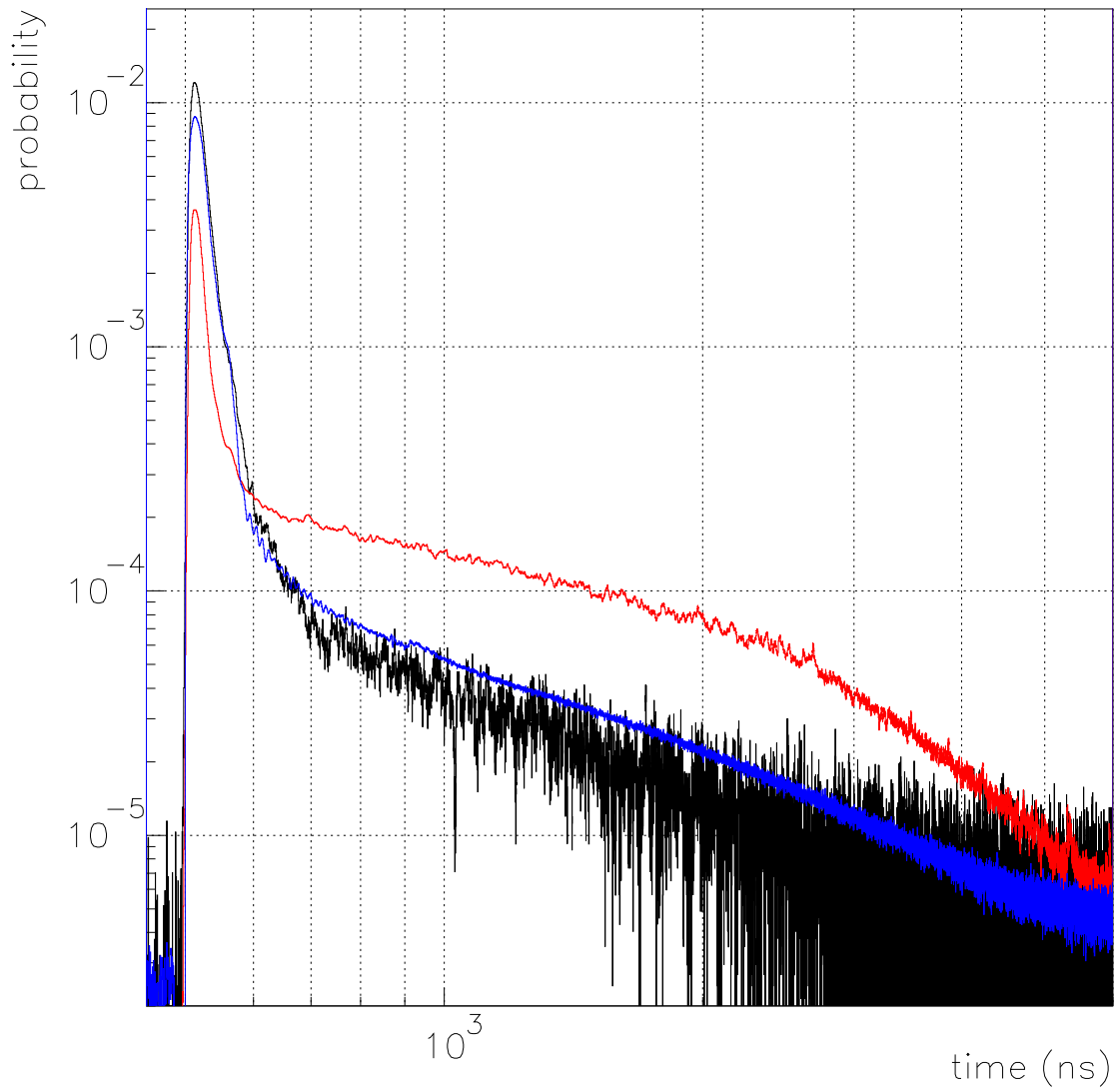
Figure 10.28: A comparison of the pdf-s for neutrons (black) α-s (blue) and γ-s (red) plotted in in log probability per 400 ps time bin vs. log time in ns.

This leads to the slope of the slow/fast component ratio bands, since the fast component is reduced by the truncation. It is however noticeable that the 'degraded α' events at low energies connect to the sloped α band. This is an evidence that the assumption that these events originate from degraded α-s is correct.
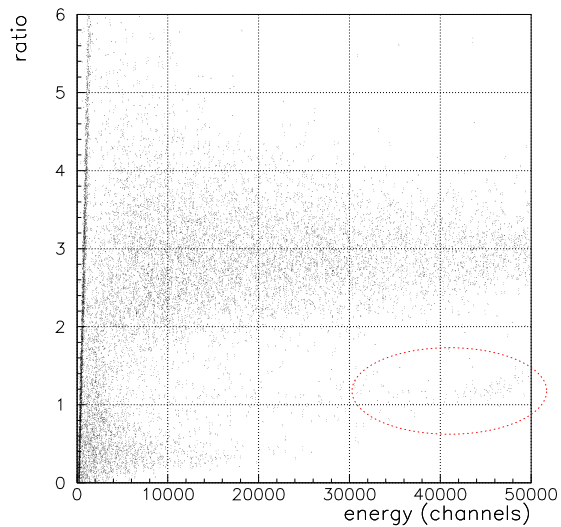
Figure 10.29: A scatter plot of the ratio slow/fast component vs. energy. The γ-band at a ratio of $\sim$3, the neutron band in the low energy range at $\sim$0.4 and the degraded-α-events in between are visible.
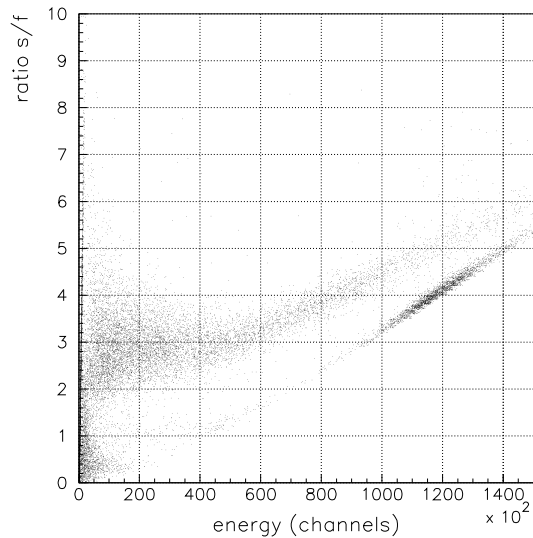
Figure 10.30: The continuation of the ratio vs. energy scatter plot to a higher (non-linear) energy scale, including the α band from the ^{222}Rn decay.

10.2 Influence of the Xe-doping on the scintillation pulse shape

10.2.1 γ-pulse shapes for different concentrations of Xe

As described in section 8.2 the LAr was doped with xenon to increase light yield. Xenon acts as additional wavelength shifter. Energy from the excited argon is transferred (radiatively and non-radiatively) to xenon, which then de-excites under emission of scintillation photons with a wavelength of $\lambda=175$ nm. Since xenon has different de-excitation time constants than Argon, an effect on the pulse shape is to be expected. Figure 10.31 shows a comparison of the probability density functions (pdf-s) of the scintillation of pure LAr (black), LAr doped with <90 ppm Xe (red) and with $\sim$300 ppm Xe for the excitation by γ-s.
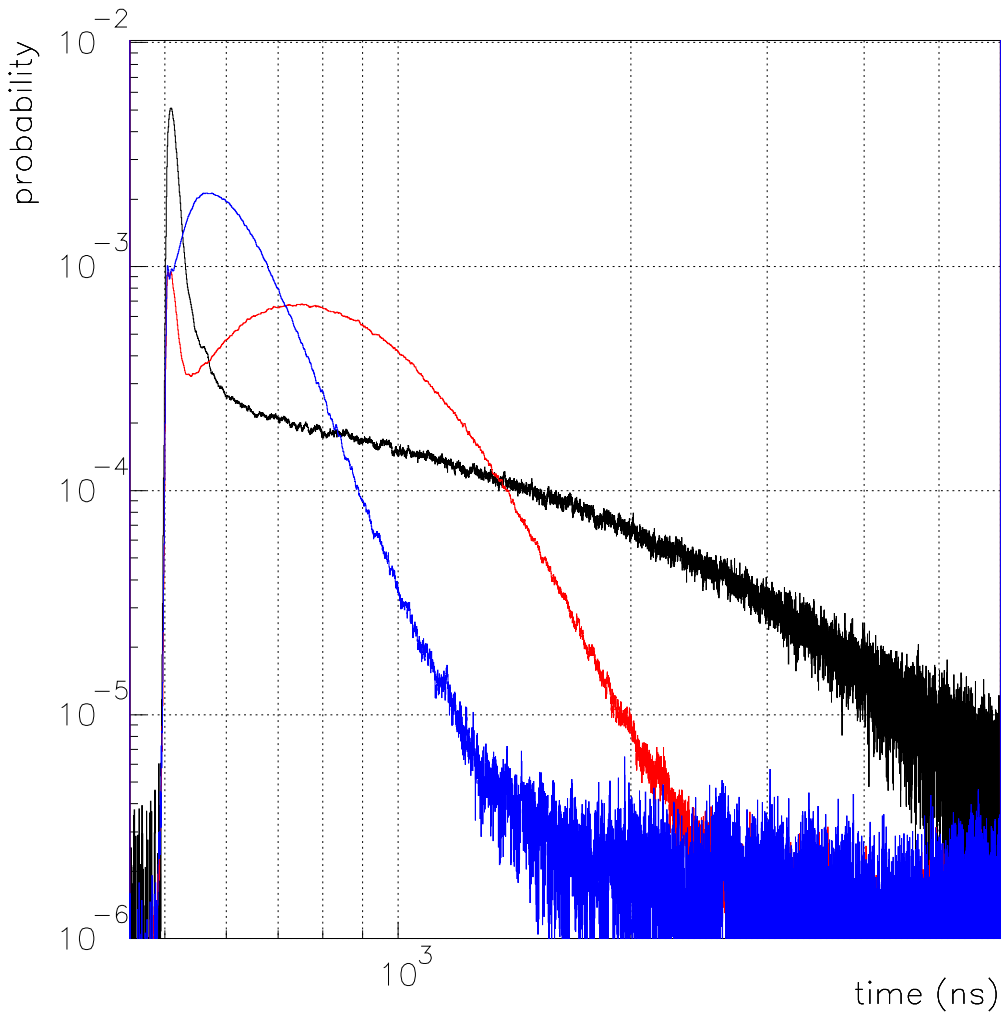
Figure 10.31: A comparison of the pdf-s for the ^{241}Am full energy deposition in LAr and in LAr doped with different concentrations of Xe. Plotted in double-logarithmic scale (probability per 400 ps bin vs. time). Black: pure LAr, red: < 90 ppm of Xe, blue: $\sim$300 ppm of Xe.

It is visible that the length of the pulses decreases with increasing Xe concentration and also that the fast component of the scintillation is decreased. The overall pulse shape is changed

as well with the slow component exhibiting a peak-like structure instead of a continuous decay. The effect of these changes on the pulse shape discrimination is investigated in the following two sections.

10.2.2 γ-neutron discrimination with Xe-doped LAr

To investigate the separation of neutron induced events from gamma induced events by pulse shape discrimination, the same methods as in the previous sections were used. Figure 10.32 shows the ratio plot for the scintillation of LAr doped with < 90 ppm of Xe. The events from the AmBe neutron source are printed in black and the events from the internal ^{241}Am source are printed in red. While there is still a band structure recognisable, the bands are clearly less separated than in figure 10.25 for pure LAr.

Figure 10.33 shows the corresponding ratio histogram for events with an energy of $E \geq 50$ keV. The neutron like events (black) are centred around a ratio of 4.6±0.1 with a sigma of 1.43±0.11. The mean ratio of the events from the gamma band (red) is 13.7±0.2 with a sigma of 4.23±0.25. The separation with these values is S_σ=(1.60±0.06) sigma. This is less than half the separation of that for pure LAr in the same energy range as shown in figure 10.26 above.
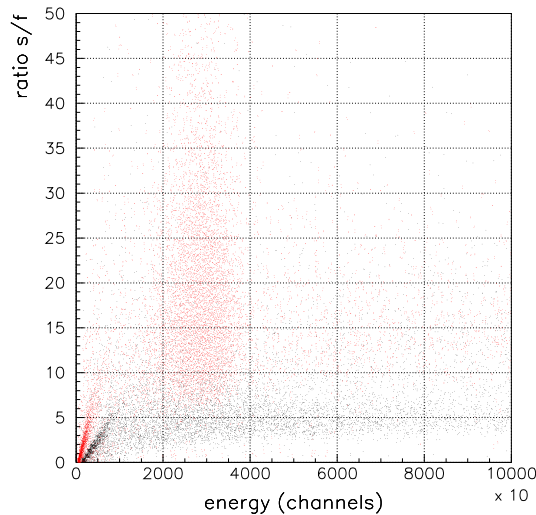
Figure 10.32: The ratio plot of an AmBe-neutron source (black) overlaid with that of a ^{214}Am γ source (red) for < 90 ppm of Xe in the LAr.
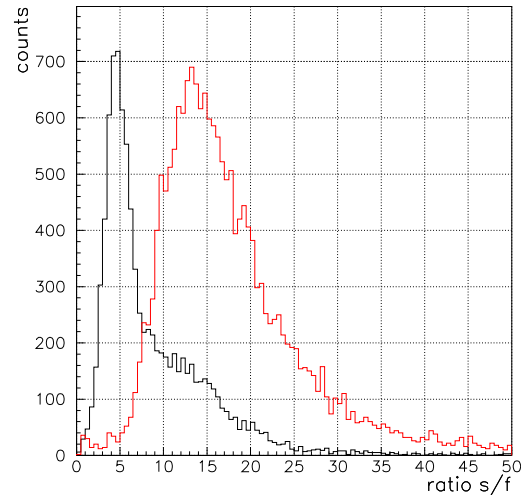
Figure 10.33: The ratio histogram of an AmBe-neutron source (black) and a ^{214}Am γ source (red) for < 90 ppm of Xe in the LAr.

With increasing Xe concentration the discrimination power decreases further. Figures 10.34 and 10.35 show the ratio scatter plot and ratio histograms for LAr doped with ∼300 ppm of Xe. The ratio scatter plot shows no recognisable discrimination between the events from the AmBe neutron source (black) and the internal ^{241}Am source. In the ratio histograms, while the histogram for the AmBe neutron source shows a slight excess on the low ratio side, there are no clearly defined two peaks any longer and no separation power can be sensibly deduced from the histogram.
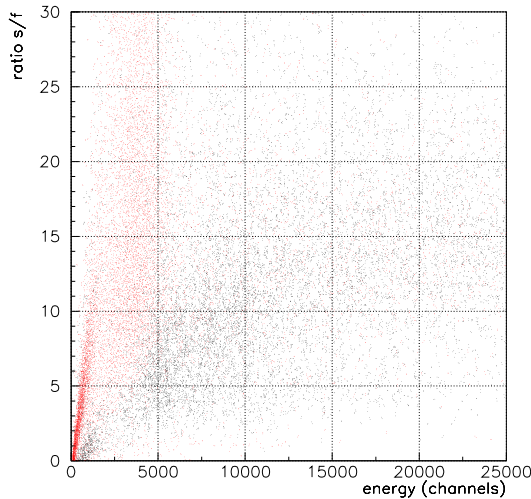
Figure 10.34: The ratio plot of an AmBe-neutron source (black) overlaid with that of a ^{214}Am γ source (red) for $\sim$300 ppm of Xe in the LAr.
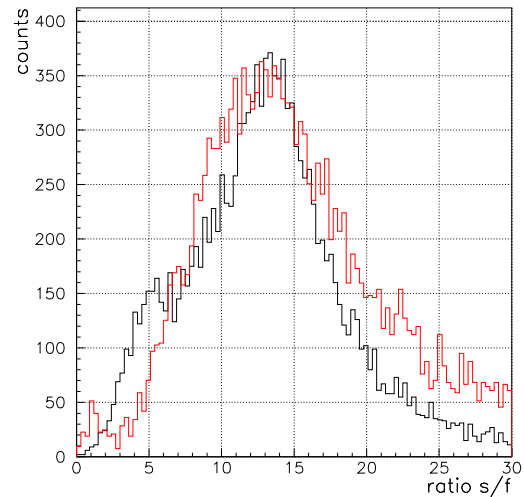
Figure 10.35: The ratio histogram of an AmBe-neutron source (black) for $\sim$300 ppm of Xe in the LAr.

10.2.3 α-γ discrimination with Xe-doped LAr

To investigate the influence on the α/γ discrimination the xenon doped LAr was again doped with radon as described in chapter 9. Figure 10.36 shows the ratio plots for LAr doped with < 90 ppm of Xe. Events from an internal ^{228}Th source are shown in red, events from ^{222}Rn taken with a high energy threshold are shown in black. While the gamma- and alpha-band are still visibly separated, one notices when comparing the plot to the similar plot for pure LAr (figure 10.12) that the relative distance of the bands has decreased due to the addition of xenon. Also an additional band of events is visible below the main alpha-band. The origin of these events is not yet clear. A theory is that they are due to direct excitation of xenon. The investigation of this is part of an ongoing study [Pol07]. There are also some events above the alpha band at a ratio of > 10. These events are attributed to showers induced by cosmic muons.

Figure 10.37 shows the similar ratio plot for LAr doped with $\sim$300 ppm of Xe. The relative distance of the bands decreased further and the additional band is still visible. In this case the measurement after the radon doping was taken with the ^{228}Th source still inserted as can be seen by the black events in the gamma band overlaid on top of the events from the ^{228}Th source only that are shown in red.

To answer the question if some other way of analysing the pulses than comparing their slow and fast components might counteract this loss of discrimination power, it was necessary to investigate the absolute difference between the pulse shapes. A tool for comparing the pulse shape independent of the definition of the slow and fast component is the cumulative density function (CDF). It is defined by

$$\mathrm{CDF}(T) = \frac{\int\limits_0^T I(t)\mathrm{d}t}{\int\limits_0^\infty I(t)\mathrm{d}t}$$

129
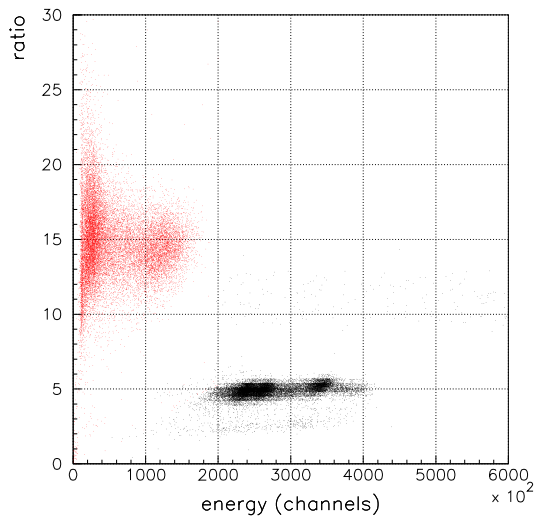
Figure 10.36: The ratio plot for LAr doped with < 90 ppm of Xe for ^{228}Th (red) and ^{222}Rn (black)
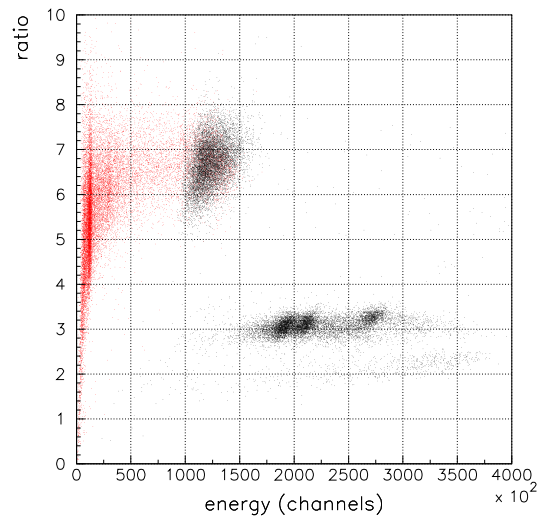
Figure 10.37: The ratio plot for LAr doped with $\sim$300 ppm of Xe for ^{228}Th (red) and with ^{222}Rn added (black)

with $I(t)$ being the intensity of the average pulse shape at a given time. The CDF gives for each point in time the fraction of the total area of the pulse that has been registered at that time.
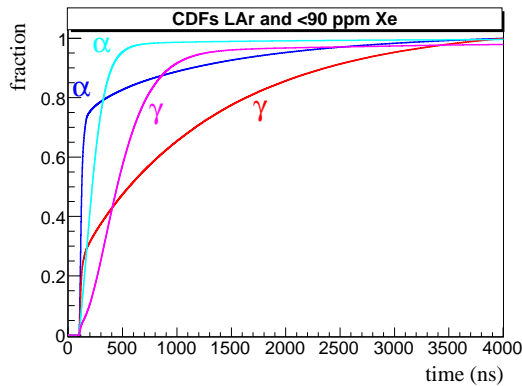
Figure 10.38: The CDFs with pure LAr for γ-s (red) and α-s (blue) and the CDFs with LAr doped with $<$90 ppm Xe for γ-s (magenta) and α-s (cyan)
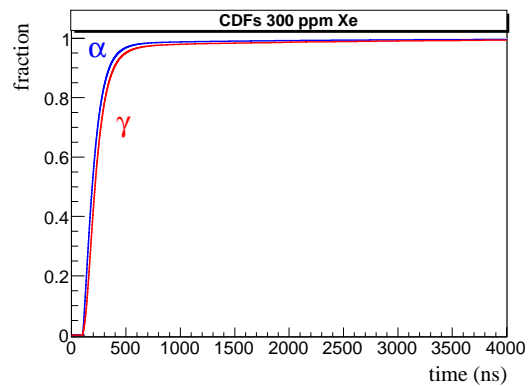
Figure 10.39: The same CDFs for LAr doped with $\sim$300 ppm of Xe for γ-s (red) and α-s (blue). The difference between the CDFs almost vanishes.

Figure 10.38 shows a comparison of the CDFs for excitation by gammas (red) and alphas (blue) for pure LAr and for LAr doped with $<$90 ppm of Xe. Figure 10.39 shows a comparison of the CDFs for $\sim$300 ppm Xe. It is visible that with increasing concentration of Xe the CDFs become more similar in shape and slope. This means that the absolute difference between the pulses for particles of different ionisation densities becomes smaller until at $\sim$300 ppm of Xe in the LAr the difference almost vanishes.

10.2.4 Considerations about the changed pulse-shape

As shown in this section, the addition of Xe to the LAr leads to a compression of the slow component to shorter times and a general alteration of the pulse shape. The CDFs show that the pulse-shapes are not only changed, but the absolute difference between the pulse shapes for particles of different ionisation densities is decreased with increasing Xe-concentration. Moreover secondary bands appear in the ratio plots, which seem to be pure Xe-emission. These additional bands further complicate the pulse-shape analysis.

The increase in statistics due to the increase in photo electron yield discussed in section 8.2 is not enough to offset the reduction of the difference of the pulse shapes. The total discrimination power between particles of different ionisation densities is strongly reduced with increasing Xe concentration.

Disregarding the pulse shape analysis, however, the reduction of the length in time of the pulses can be an advantage. Shorter pulses allow for shorter time-windows for the light-detection. This again reduces the dead time of the LAr detector and helps to overcome the ^{39}Ar limitation. With a high enough concentration of Xe ($\sim$2% [SHRK93]) the slow component of the LAr can be reduced to the same order of magnitude as the slow component of pure Xe scintillation (τ_t(Xe)=(34±2) ns [KGW74]). This allows for a correspondingly larger active volume. For pure anti-coincidence veto purposes the addition of Xe might therefore be an advantage.

10.3 Summary of pulse shape investigations

The pulse-shape analysis on the scintillation light of pure LAr proves to be a powerful tool for the discrimination between particles of different ionisation densities. This discrimination yields some efficient tools for improving the detector performance. The possibility to detect and recognise neutrons is an important achievement, since neutrons can give rise to secondary background via the creation of radio-isotopes by neutron capture, inelastic scattering or induced nuclear reactions. Due to the higher atomic weight the neutron moderation in LAr is not as efficient as it would be in LN$_2$. This means that the neutron background reaching the diodes is higher and that a reliable tagging of the neutrons is very important.

A second important application of the pulse-shape discrimination (PSD) is the detection and identification of ^{222}Rn impurities. The combination of the BiPo-trigger with the reliable identification of α-s by PSD gives the theoretical possibility to detect every single decay of a ^{222}Rn nucleus. The detection limit reached in the setup at MPI-K so far is a ^{222}Rn activity of 2 μBq/kg which corresponds to 3.3 μBq/m^3 (STP) in the gas phase. The possibility to detect degraded α-s is also very important to monitor surface contaminations of the Ge-diode or the walls of the active volume.

It could be shown that the admixture of traces of Xe to the LAr, while it increases the photo electron yield, decreases the efficiency of the PSD. This means this technique is discarded for LArGe to retain the possibilities mentioned above. In GERDA however it might be an option to go back to an admixture of Xe since the Xe-doping shortens the length of the pulses significantly as discussed above. An alternative would be to use only the fast component of the scintillation with pure LAr. Since the total volume of GERDA is in an order of magnitude where the dead time due to ^{39}Ar becomes dominant, a method of reducing the dead time might prove necessary if a reduction of the active volume proves to be impractical. The advantage of the Xe option would be the higher light yield. The disadvantage is the loss of the ability to discriminate between particles of different ionisation densities (depending on the Xe concentration) and thereby the loss of a tool of background diagnostics. Also it would exclude any Dark Matter detection

capabilities with the LAr. The drawback of using only the fast component of the scintillation of pure LAr would be an effective loss of light and possibly also a reduced discrimination power, depending on what fraction of the pulse can be used. However this decision will not be taken until Phase II of GERDA and will also be based on further studies.

Chapter 11

Summary and Outlook

As it was laid out in the introduction of this thesis, two of the most crucial questions in particle physics concern the particle-antiparticle symmetry of the neutrinos (Majorana particle) and the absolute neutrino mass scale. The $0\nu\beta\beta$ experiment GERDA sets out to try to answer these questions. In GERDA 17.9 kg of high purity germanium (HP-Ge) diodes (enriched to $\sim 86\%$ ^{76}Ge) will be operated in liquid argon (LAr) in Phase I. These diodes already exist and have been used in the the HdM and IGEX experiments. In Phase II newly produced diodes will be added. For this purpose 37.5 kg of germanium, enriched to $\sim 87\%$ ^{76}Ge, have been procured [GER06].

For Phase I, for which a total exposition 15 kg·y is planned, the required background of less than 10^{-2} cts/(kg·keV·y) can be reached with passive shielding and existing background suppression techniques. To reach the background level of less than 10^{-3} cts/(kg·keV·y) required for Phase II, new background suppression methods have to be implemented in GERDA and if at a later time a ton scale experiment is required, the background will have to be suppressed by another order of magnitude.

11.1   Background suppression ...

In this work a novel method was studied to suppress backgrounds in GERDA. LAr scintillates (see chapter 3) and the technique investigated in this work is the simultaneous readout of the diode signal and the scintillation light of the LAr. The detection of the scintillation light is then used as anti-coincidence signal for the HP-Ge diodes. For this purpose a Liquid Argon and Germanium (LArGe) hybrid detector has been developed, built and successfully operated in the low level underground laboratory at the MPI-K in Heidelberg. The active LAr volume was 13.5 l (h=43 cm, $\varnothing$=20 cm) which corresponds to 19 kg of LAr. In the first test system a 168 g p-type HP-Ge diode was operated, suspended in the LAr. In the improved system a 390 g p-type HP-Ge diode was used (chapter 4).

The investigations have been very successful and the power of the LAr scintillation anti-coincidence concept for background suppression could be demonstrated. With an active volume of 19 kg a suppression factor of ~ 3 for ^{60}Co and of ~ 17 for ^{232}Th has been reached in the region of interest (RoI) around $Q_{\beta\beta}$=2039 keV. Monte Carlo predictions are in reasonable agreement with the data (chapter 7). The suppression factors are limited by escaping γ-s from the active LAr volume (10 cm radius). For a larger active volume the escape probability becomes negligible and Monte Carlo simulations predict suppression factors of $\mathcal{O}(100)$ for ^{60}Co [GER04] and of ~ 340 for ^{208}Tl (active volume radius: 45 cm, see chapter 7).

Table 11.1 lists a comparison of suppression factors for different background suppression techniques. For a description of the various techniques see chapter 2.

Method	^{60}Co	^{208}Tl	acceptance	notes	ref.
diode anti-coincidence	2	1.5	n.d.	estimation	
segmented detector	5.3	1.8	n.d.	estimation	[GER04]
Ge-pulse shape	1.5	1.5	~80%	estimation	
Ge-pulse shape	1.7	1.7	88%	MC prediction	[KLM06]
diode anti-coincidence	3.2	2.6	n.d.	MC prediction	[KAA$^+$07]
segm. & diode anti-coinc.	38	13	87%	MC prediction	
LAr veto 19 kg	3	17	> 98%	measured	this work
LAr veto 1.4 t	100	340	> 98%	MC prediction	[GER04], this work

Table 11.1: A summary of suppression factors and the acceptance for the $0\nu\beta\beta$ for different techniques for ^{60}Co and ^{208}Tl. (n.d.: value not determined)

Even when taking the conservative lower limit on the suppression factors predicted for the one ton scale LAr active volume as discussed in chapter 7 the results of this study show, that the LAr scintillation anti-coincidence veto is a powerful background suppression technique which will allow a suppression of the background to the level required for Phase II.

Moreover this suppression technique is complementary to techniques that work on energy deposition internal to the diodes such as segmentation, anti-coincidence with neighbouring diodes and pulse shape discrimination on the diode signal (see chapter 2). This means that the LAr scintillation anti coincidence is effective in the cases where these other techniques are not effective and vice versa.

11.2   ...and beyond

Beyond the main goal of investigating the feasibility and efficiency of the LAr scintillation anti-coincidence veto, the LAr scintillation was also investigated as a tool for background diagnostics. As discussed in chapter 3 the scintillation light of argon is emitted from excited dimers (excimers) that are created in argon by ionising radiation. These excimers can be created in a singlet or a triplet state. The de-excitation times of these states are τ_s=6 ns and τ_t=1.6 μs respectively and their population depends on the ionisation density of the particle ionising the argon. This allows a discrimination between particles of different ionisation densities by analysing the pulse shape (i.e. the intensity in dependence of time) of the LAr scintillation. This principle has been successfully used in this work to discriminate between α-s and γ-s and between γ-s and neutrons with a probability to mis-identify an event of only $P_{mi}(\gamma\alpha) \simeq 5 \cdot 10^{-6}$ and $P_{mi}(\gamma n) \simeq 3 \cdot 10^{-4}$ respectively (see chapter 10).

The ability to identify α-s can be used in conjunction with the BiPo-trigger technique (chapter 10) for a high sensitivity radon detection and as a monitor against surface contamination by detecting degraded α-s. The ability to reliably detect and identify energy deposition from neutrons in the LAr allows for a detection of the thermalisation process of neutrons in the LAr. This ability can help to suppress secondary background (like ^{77}Ge) that is created by the capture of thermal neutrons.

Apart from these achievements a new wavelength shifter/reflector foil has been developed in the framework of this thesis, that has proven to be very stable and robust and allows the

detection of the LAr scintillation light with a standard borosilicate PMT with a photo electron yield of 1.2 pe/keV and a new voltage divider for the PMT operating on negative HV has been built, that improved the energy resolution by a factor 1.3 (chapter 8).

Also the addition of xenon to the LAr was investigated. A xenon doping of the LAr further increases the light yield, but this increase comes at the cost of a concentration dependent reduction of the efficiency of the pulse shape discrimination. However, if a combination of a high light yield and a short pulse length is desired, for example to reduce the dead time while still retaining a good energy resolution, the xenon doping is still an option, since for a Xe doping of $\sim 2\%$ the slow time constant of the scintillation of the doped LAr becomes similar to that of liquid xenon ($\tau_t(\text{Xe})$=34 ns).

For pure veto purposes it is also possible to use only the fast component as veto signal. As discussed in chapter 8 a 100 keV veto threshold would be sufficient for the veto in GERDA. About 23% of the total scintillation light output is emitted in the fast component for the excitation by minimal ionising particles (see table 3.1). With the 1.2 pe/keV achieved, requiring the detection of 10 pe as a veto signal would result in a 36 keV veto threshold if only the fast component is evaluated, so the restriction to the fast component is feasible.

11.3   Outlook

This work has been part of the GERDA-LArGe project and has successfully proven the efficiency of the LAr scintillation as a tool for background suppression and background diagnostics. The investigations presented here will be continued with an active volume of the scale of one cubic meter (1.4 tons) of LAr in the new LArGe setup that is currently under construction in the Gran Sasso laboratories. Figure 11.1 shows a schematic drawing of the new setup in which a cluster of HP-Ge diodes will be operated in the LAr. Nine PMTs of the type used in this work (ETL 9357-KFLB) will be used to detect the scintillation light. They will be operated on negative HV and a dynode readout will be implemented using the new voltage divider described in chapter 8. The high purity copper cryostat will be lined with the improved wavelength shifter and reflector foil developed in this work. The setup will be shielded by a graded shield consisting of 20 cm poly-ethylene, 23 cm steel, 10 cm lead and 15 cm copper with increasing radio-purity.

The goals of the new GERDA-LArGe setup will include the testing of the HP-Ge-diodes for purity before they are mounted in GERDA and the continued investigation of the possibilities offered by the LAr scintillation that were shown in this work. One part of these investigation will be the operation of segmented n-type HP-Ge-diodes in LAr with simultaneous light readout to investigate the combined efficiency of these two complementary methods. Another part will be the continued investigation of the pulse shape analysis on the LAr scintillation light with respect to background diagnostics, neutron tagging and other applications beyond pure veto purposes.

As a final word can be said, that an exciting and successful period of experiments comes to a conclusion. However the work will be continued and new questions are already waiting to be answered and for GERDA-LArGe and GERDA the exciting time has just begun.
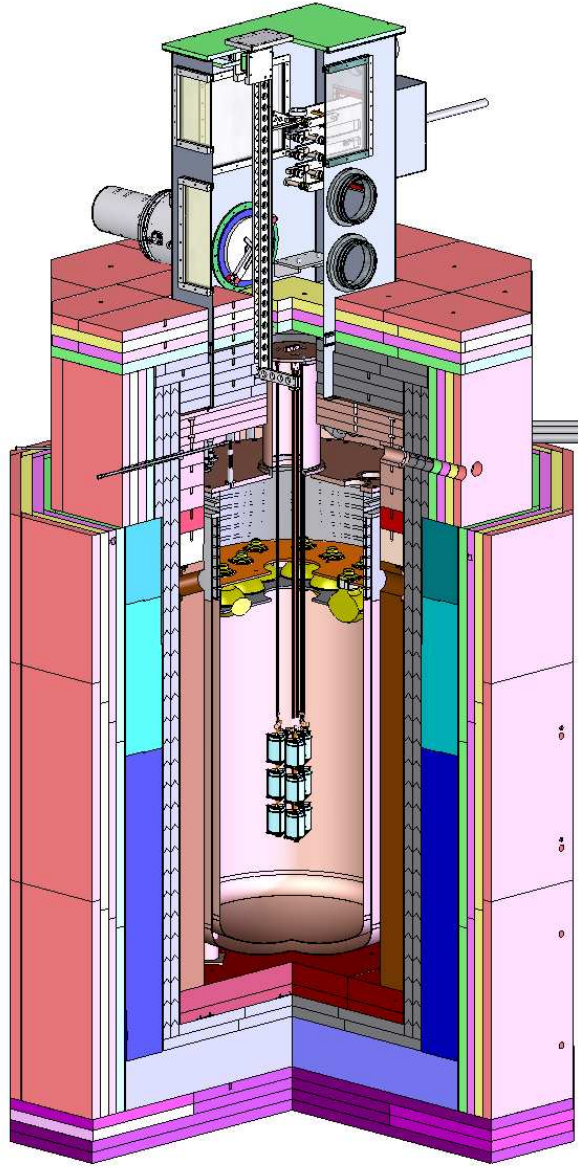
Figure 11.1: A schematic drawing of the GERDA-LArGe setup, showing the cluster of HP-Ge diodes and some of the PMTs.

Glossary

0νββ-decay - The neutrinoless double beta decay

(2ν)ββ-decay - (two neutrino) double beta decay

ADC - Analog to Digital Converter

CDF - Cumulative Density Function

cts - Counts

DAQ - Data Acquisition

ECEC - Double electron capture

FWHM - Full Width at Half Maximum

GAr - Gaseous argon

GEANT4 - a MC simulation software package

GERDA - Germanium Detector Array

HP-Ge - High purity germanium

LAr - Liquid argon

LArGe - Liquid Argon and Germanium hybrid detector

LLL - Low level laboratory - an underground lab at the MPI-K

LMA - Large Mixing Angle parameter space of the neutrino oscillations

LNGS - Laboratori Nationale di Gran Sasso

MAGE - MAJORANA -GERDA - jointly developed MC simulation based on GEANT4

MC - Monte Carlo - a simulation method

MCA - Multi Channel Analyser

MSW - Mikheyev-Smirnov-Wolfenstein effect - matter enhanced neutrino mixing

NIM - Network Interface Machine - a standard for electronics

NME - Nuclear Matrix Element

pdf - here: probability density function

pe - Photo electron

PEN - Poly ethylene naphthalene

PMNS - Pontecorvo-Maki-Nakagawa-Sakata matrix - the 'neutrino mixing matrix'

PMT - Photo multiplier tube

ppm - Relative concentration in parts per million ($10^{-4}\%$)

PSD - Pulse shape discrimination

PST - Poly-styrene

$Q_{\beta\beta}$ - Energy of the double beta decay

RoI - Region of Interest - here the energy region around $Q_{\beta\beta}$

SNU - Solar Neutrino Unit - 10^{-36} ν captures per target atom per second.

SM - Standard Model

spe - Single photo electron

SS - Stainless steel

SSM - Standard Solar Model

STP - Standard Temperature and Pressure (0°C, 1013 mbar)

TPB - Tetra phenyl buthadiene - a fluorescent dye

TTL - Transistor-transistor logic - a logic circuit standard

VM2000 - older trade name of the '3M radiant mirror foil'

VME - VERSAcard Modified for Eurocard - a computer and electronics standard

WIMP - Weakly Interacting Massive Particle

WLS - Wavelength shifter

XUV - Extreme ultra violet

Appendix A

Decay chains
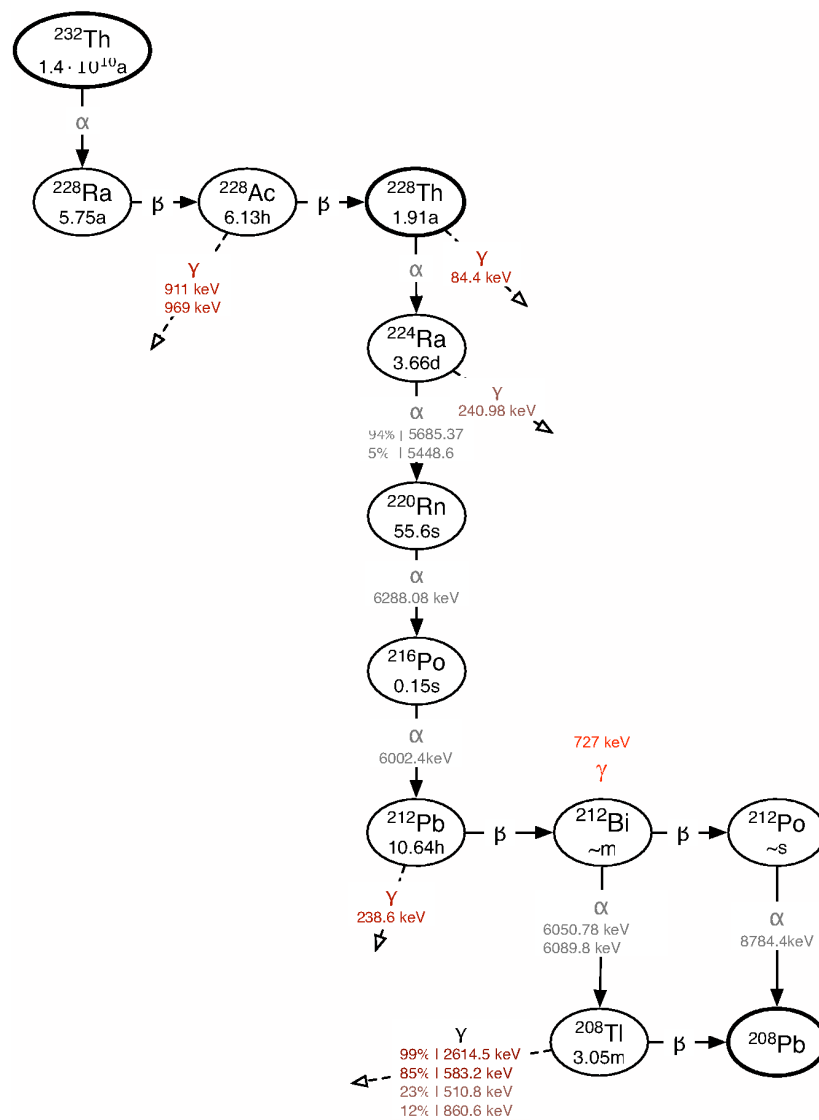
Figure A.1: The decay chain of ^{232}Th. Decays that were important in this work are marked in red.
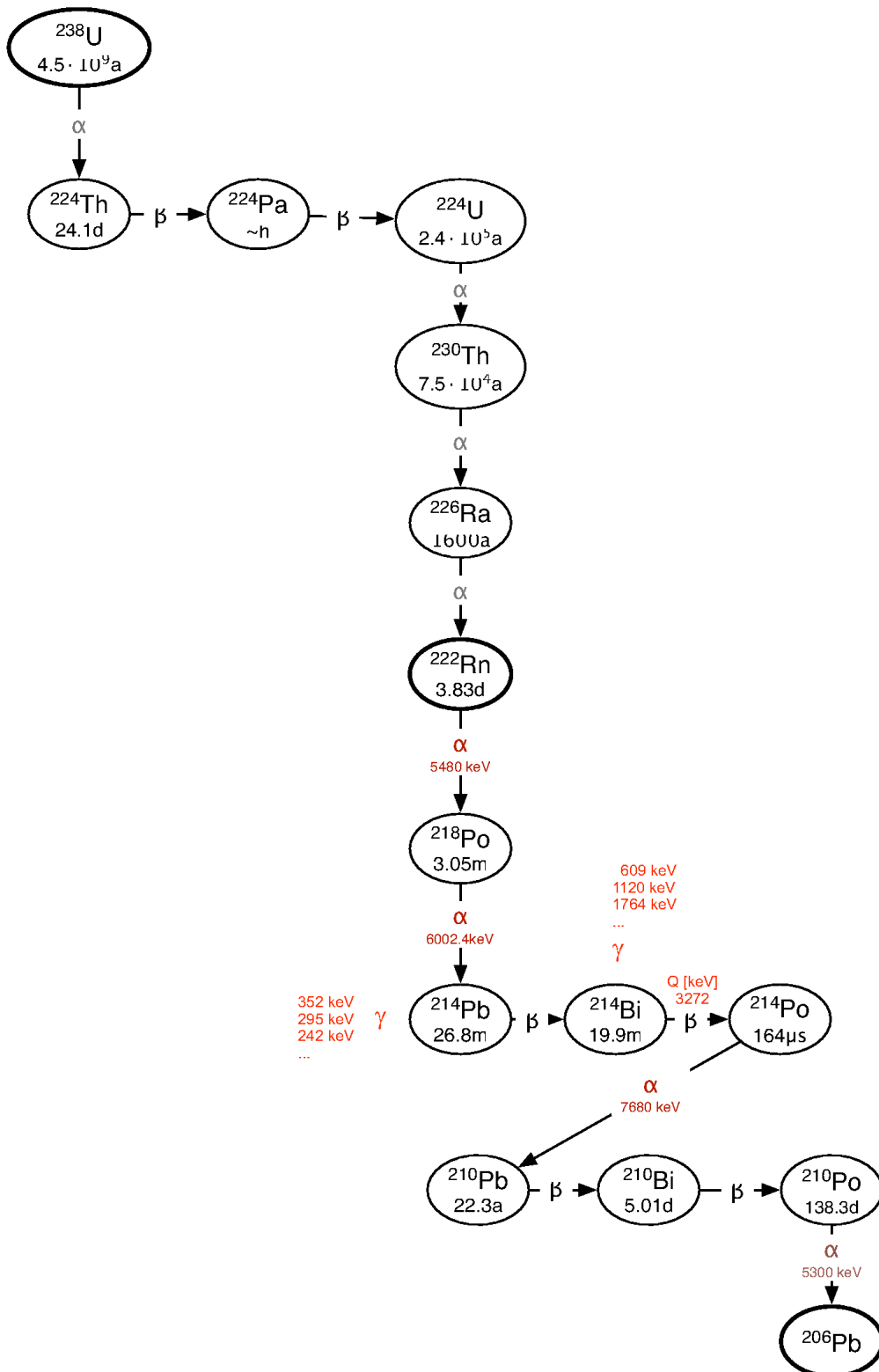
Figure A.2: The decay chain of ^{238}U. Important decays (for this work) are marked in red.

Appendix B

Decay schemes
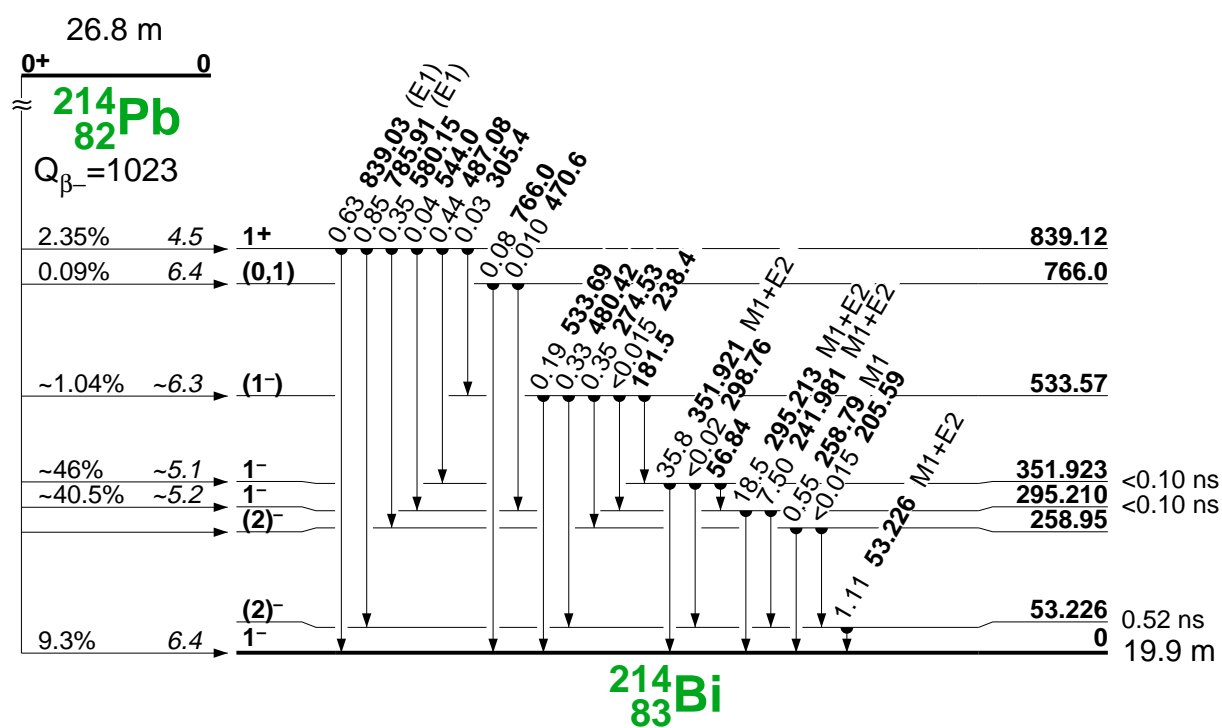
Figure B.1: The decay scheme of ^{214}Pb [Fir96].

Figure B.2: The decay scheme of ^{214}Bi, part 1 of 3 [Fir96].

Figure B.3: The decay scheme of ^{214}Bi, part 2 of 3 [Fir96].
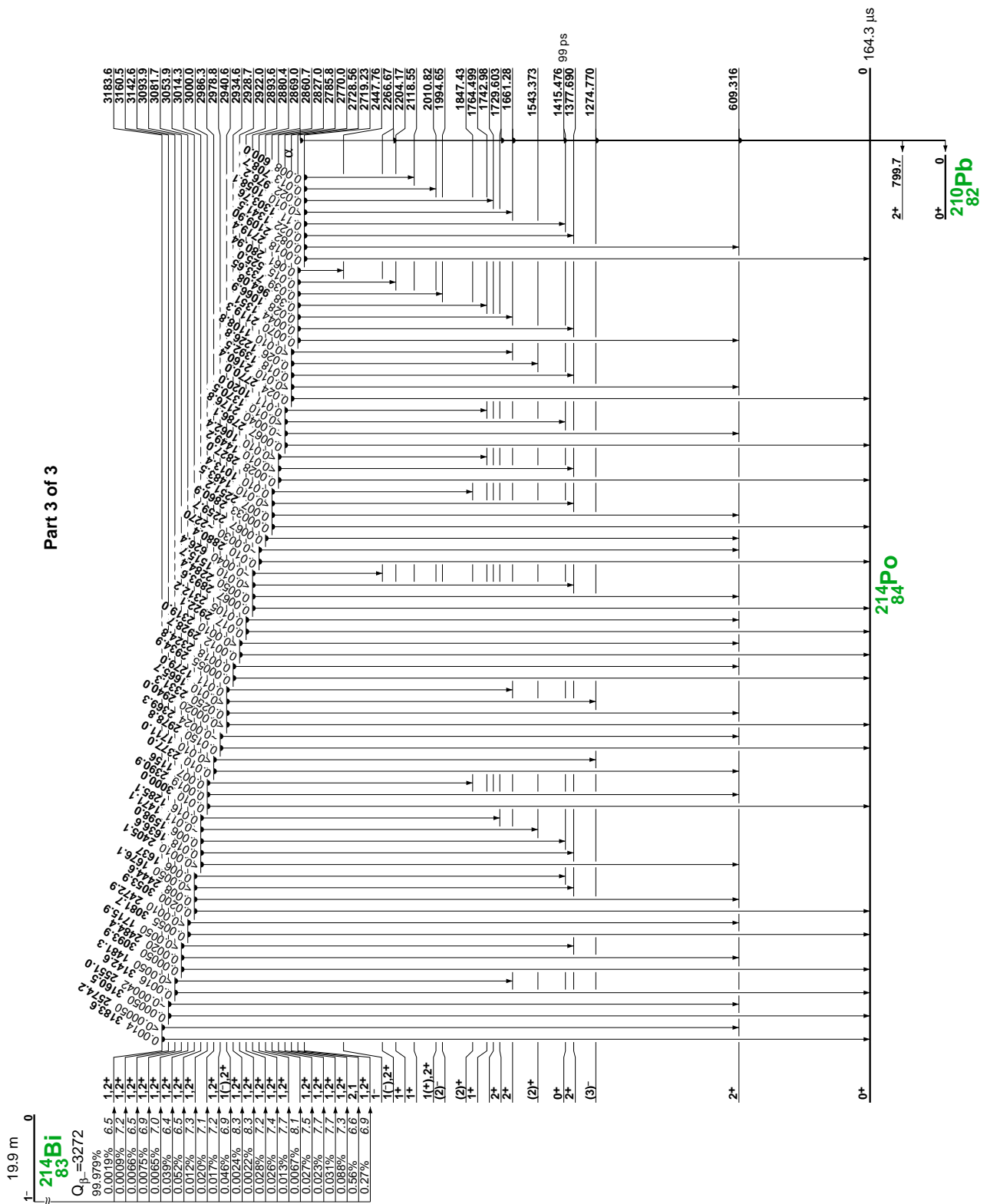
Figure B.4: The decay scheme of ^{214}Bi, part 3 of 3 [Fir96].

Figure B.5: The decay scheme of ^{228}Ac, part 1 of 4 [Fir96].

145

Figure B.6: The decay scheme of ^{228}Ac, part 2 of 4 [Fir96].

Figure B.7: The decay scheme of ^{228}Ac, part 3 of 4 [Fir96].

Figure B.8: The decay scheme of ^{228}Ac, part 4 of 4 [Fir96].

Appendix C

Electronic layouts

Figure C.1: The layout of the voltage divider for the operation of the PMT with positive high voltage.

Figure C.2: The layout of the voltage divider for the operation of the PMT with negative high voltage and dynode readout.

Figure C.3: The layout of the DSG pre-amplifier for the HP-Ge diode voltage supply and signal readout.

Bibliography

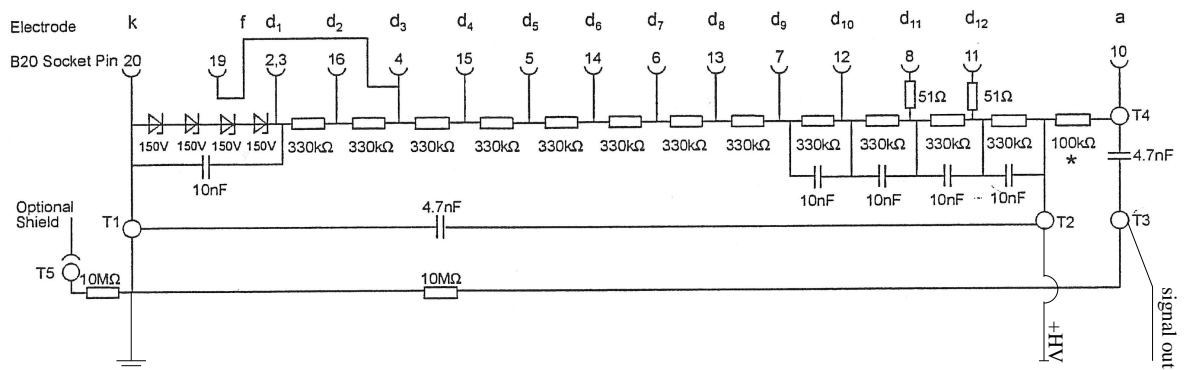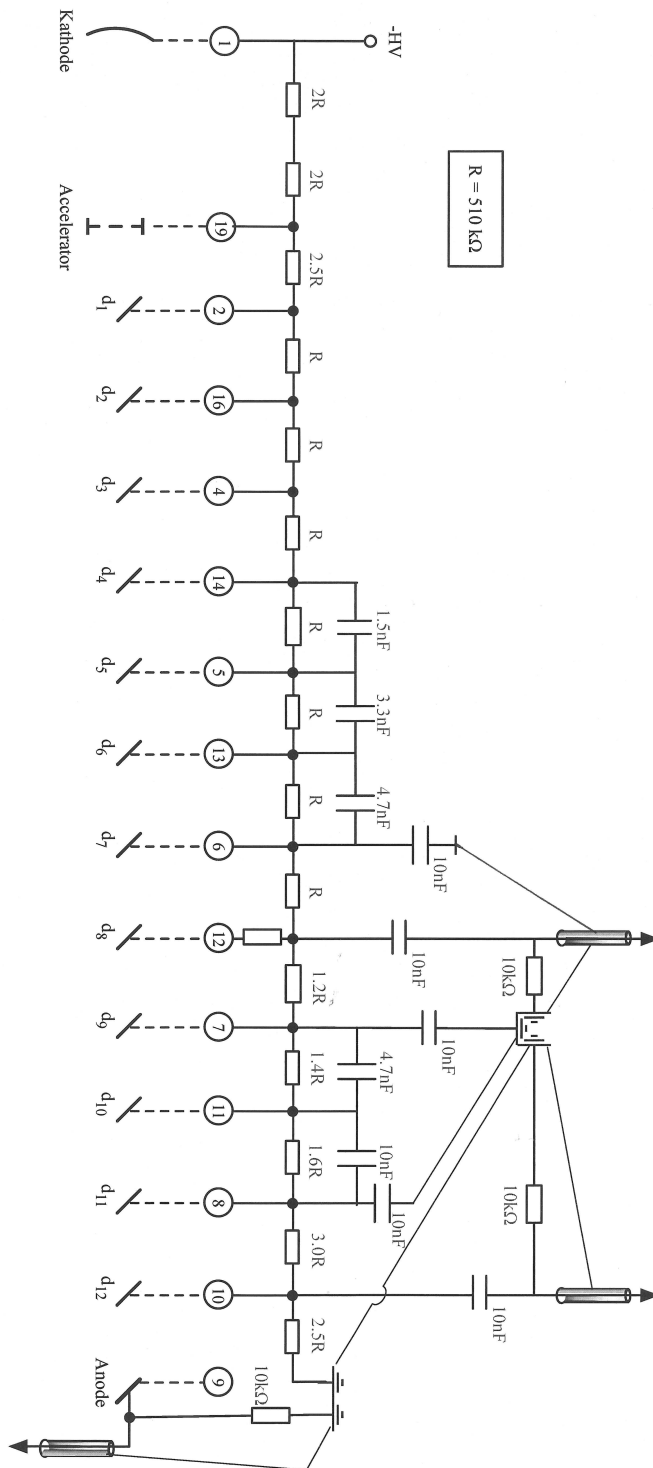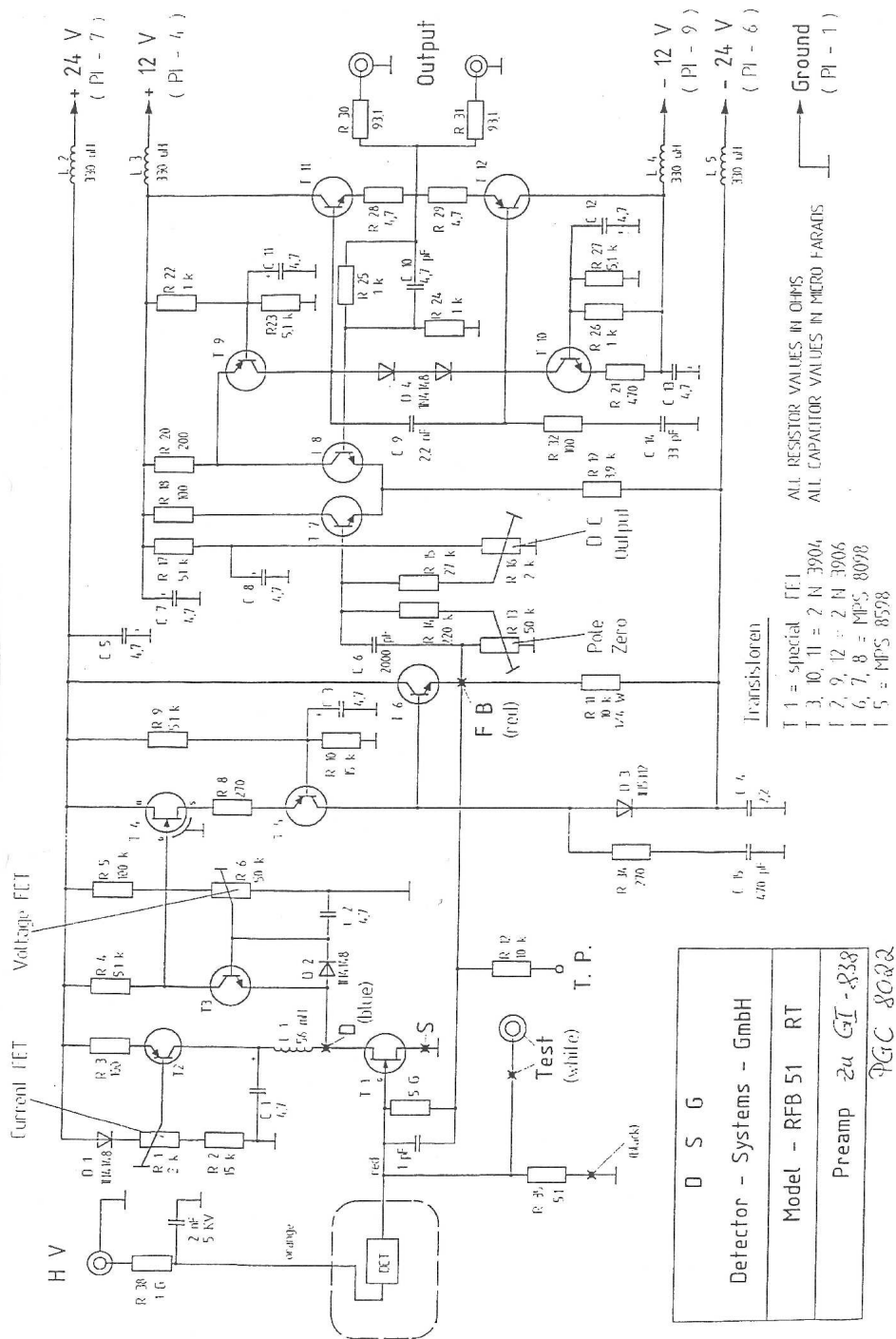[A+00]   C.E. Aalseth et al. *Recent results of the igex 76ge double-beta decay experiment.* Physics of Atomic Nuclei, 63 (2000), 1225–1228. doi:10.1134/1.855774.

[AAA+02]   Q. R. Ahmad, R. C. Allen, T. C. Andersen, et al. *Measurement of day and night neutrino energy spectra at sno and constraints on neutrino mixing parameters.* Phys. Rev. Lett., 89 (2002), no. 1, 011302. doi:10.1103/PhysRevLett.89.011302.

[AAA+03]   S. Agostinelli, J. Allison, K. Amako, et al. *G4–a simulation toolkit.* Nuclear Instruments and Methods in Physics Research A, 506 (2003), 250–303. doi:10.1016/S0168-9002(03)01368-8.

[AAA+05]   E. Aliu, S. Andringa, S. Aoki, et al. *Evidence for muon neutrino oscillation in an accelerator-based experiment.* Physical Review Letters, 94 (2005), no. 8, 081802. URL http://link.aps.org/abstract/PRL/v94/e081802.

[AAB+01]   A. Aguilar, L. B. Auerbach, R. L. Burman, et al. *Evidence for neutrino oscillations from the observation of $\overline{\nu}_e$ appearance in a $\overline{\nu}_\mu$ beam.* Phys. Rev. D, 64 (2001), no. 11, 112007. doi:10.1103/PhysRevD.64.112007.

[AAB+04]   S. N. Ahmed, A. E. Anthony, E. W. Beier, et al. *Measurement of the total active b solar neutrino flux at the sudbury neutrino observatory with enhanced neutral current sensitivity.* Physical Review Letters, 92 (2004), no. 18, 181301. URL http://link.aps.org/abstract/PRL/v92/e181301.

[AB+03]   M. Apollonio, A. Baldini, et al. *Search for neutrino oscillations on a long baseline at the CHOOZ nuclear power station.* The European Physical Journal C, 27 (2003), 331–374. doi:10.1140/epjc/s2002-01127-9.

[ABB+05]   GNO Collaboration: M. Altmann, M. Balata, P. Belli, et al. *Complete results for five years of gno solar neutrino observations.* Physics Letters B, 616 (2005), 174. URL http://www.citebase.org/abstract?id=oai:arXiv.org:hep-ex/0504037.

[AEE+05]   T. Araki, K. Eguchi, S. Enomoto, et al. *Measurement of neutrino oscillation with kamland: Evidence of spectral distortion.* Physical Review Letters, 94 (2005), no. 8, 081801. URL http://link.aps.org/abstract/PRL/v94/e081801.

[AHI+05]   Y. Ashie, J. Hosaka, K. Ishihara, et al. *Measurement of atmospheric neutrino oscillation parameters by super-kamiokande i.* Physical Review D (Particles and Fields), 71 (2005), no. 11, 112005. URL http://link.aps.org/abstract/PRD/v71/e112005.

[AMOY96] Y. Asano, S. Mori, Y. Ohta, et al. *Sum-peak method and angular correlation correction for a ^{60}Co source by a ge(tl) detector.* Japanese Journal of Applied Physics, 35 (1996), 4117–4120.

[B$^+$06] P. Benetti et al. *Measurement of the specific activity of ar-39 in natural argon* (2006).

[Bar05] A.S. and the NEMO Collaboration Barabash. *Nemo-3 double beta decay experiment: Present status.* Nuclear Physics B - Proc. Suppl., 138 (2005), 207–209. doi:10.1016/j.nuclphysbps.2004.11.049.

[BBB$^+$05] A. M. Bakalyarov, A. Ya Balysh, S. T. Belyaev, et al. *Results of the experiment on investigation of germanium-76 double beta decay. experimental data of heidelberg-moscow collaboration november 1995 - august 2001.* PISMA FIZ.ELEM.CHAST.ATOM.YADRA, 2 (2005), 21. URL `http://www.citebase.org/abstract?id=oai:arXiv.org:hep-ex/0309016`.

[BCC$^+$05] R. Brunetti, E. Calligarich, M. Cambiaghi, et al. *WARP liquid argon detector for dark matter survey.* New Astronomy Reviews, 49 (2005), 265–269.

[BCC$^+$06] P. Benetti, F. Calaprice, E. Calligarich, et al. *Measurement of the specific activity of ar-39 in natural argon* (2006). URL `http://www.citebase.org/abstract?id=oai:arXiv.org:astro-ph/0603131`.

[Ber71] Isadore B. Berlman. *Handbook of fluorescence spectra o aromatic molecules* (Academic Press, 1971).

[BFGS05] S. M. Bilenky, Amand Faessler, Thomas Gutsche, et al. *Neutrinoless double beta-decay and neutrino mass hierarchies.* Physical Review D (Particles and Fields), 72 (2005), no. 5, 053015. URL `http://link.aps.org/abstract/PRD/v72/e053015`.

[BGW$^+$04] W.B. Brudanin, K.Ja. Gromow, S.I. Wassuljew, et al. *Gamma-lutschi c energijei bolsche 2000 kew w zepotschke raspadow ^{238}U.* Picma w ETschAJa - Particle Physics letters, 122 (2004), 84–87. Translation: Gamma quanta with energies above 2000 keV in the ^{238}U decay chain.

[BHH$^+$03] C. L. Bennett, M. Halpern, G. Hinshaw, et al. *First year wilkinson microwave anisotropy probe (wmap) observations: Preliminary maps and basic results.* The Astrophysical Journal, 148 (2003), 1. URL `http://www.citebase.org/abstract?id=oai:arXiv.org:astro-ph/0302207`.

[BHP80] S.M. Bilenky, J. Hosek, and S.T. Petcov. *On the oscillations of neutrinos with Dirac and Majorana masses.* Physics Letters B, 94 (1980), no. 4, 495–498. doi: 10.1016/0370-2693(80)90927-2.

[Bir64] J.B. Birks. *The Theory and Practice of Scintillation Counting* (Pergamon Press, 1964).

[BKS95] John N. Bahcall, Marc Kamionkowski, and Alberto Sirlin. *Solar neutrinos: Radiative corrections in neutrino-electron scattering experiments.* Physical Review D, 51 (1995), 6146. URL `http://www.citebase.org/abstract?id=oai:arXiv.org:astro-ph/9502003`.

[Bor02]   G.Alimonti et al. for the Borexino Collaboration. *Science and technology of Borexino: a real-time detector for low energy solar neutrinos.* Astroparticle Physics, 16 (2002), 205–234. doi:10.1016/S0927-6505(01)00110-4.

[BP04]   J.N. Bahcall and M.H. Pinsonneault. *What do we (not) know theoretically about solar neutrino fluxes?* Phys. Rev. Lett., 92 (2004), 121301.

[BPB01]   John N. Bahcall, M. H. Pinsonneault, and Sarbani Basu. *Solar models: current epoch and time dependences, neutrinos, and helioseismological properties.* The Astrophysical Journal, 555 (2001), 990. URL http://www.citebase.org/abstract?id=oai:arXiv.org:astro-ph/0010346.

[BPY05]   W. Buchmuller, R. D. Peccei, and T. Yanagida. *Leptogenesis as the origin of matter.* Annual Review of Nuclear and Particle Science, 55 (2005), 311. URL http://www.citebase.org/abstract?id=oai:arXiv.org:hep-ph/0502169.

[BSBC$^+$92] R. Becker-Szendy, C. B. Bratton, D. Casper, et al. *Electron- and muon-neutrino content of the atmospheric flux.* Phys. Rev. D, 46 (1992), no. 9, 3720–3724. doi: 10.1103/PhysRevD.46.3720.

[BV92]   F. Boehm and P. Vogel. *Physics of Massive Neutrinos* (Cambridge, UK: Cambridge University Press, 1992), 2nd edition.

[C$^+$98]   B. T. Cleveland et al. *Measurement of the solar electron neutrino flux with the homestake chlorine detector.* Astrophys. J., 496 (1998), 505–526.

[CBC$^+$93]   M.T.F. da Cruz, D.W. Bardayan, Y. Chan, et al. *Thick-target yields of iodine isotopes from proton interactions in te, and the double-β decays of $^{128,130}te$.* Phys. Rev. C, 48 (1993), no. 6, 3106–3109. doi:10.1103/PhysRevC.48.3106.

[CEF99]   S.Y.F. Chu, L.P. Ekstrm, and R.B. Firestone. *LNBL/Lund Nuclear Data search* (1999). URL http://nucleardata.nuclear.lu.se/nucleardata/toi/radSearch.asp.

[Cer37]   P. A. Cerenkov. *Visible radiation produced by electrons moving in a medium with velocities exceeding that of light.* Phys. Rev., 52 (1937), no. 4, 378–379. doi: 10.1103/PhysRev.52.378.

[DGRS97]   A. Dementyev, V. Gurentsov, O. Ryazhskaya, et al. *Production and transport of hadrons generated in nuclear cascades initiated by muons in the rock (exclusive approach).* Technical Report INFN/AE-97/50, INFN (September 1997).

[DHH68]   R. Davis, D.S. Harmer, and K.C. Hoffman. *Search for neutrinos from the sun.* Phys. Rev. Lett., 20 (1968), 1205–1209.

[DHK$^+$02]   Tadayoshi Doke, Akira Hitachi, Jun Kikuchi, et al. *Absolute scintillation yields in liquid argon and xenon for various particles.* Jpn. J. Appl. Phys., 41 (2002), 1538–1545. doi:10.1143/JJAP.41.1538.

[DKK03]   C. Dörr and H. V. Klapdor-Kleingrothaus. *New Monte-Carlo simulation of the HEIDELBERG-MOSCOW double beta decay experiment.* Nuclear Instruments and Methods in Physics Research A, 513 (2003), 596–621. doi: 10.1016/j.nima.2003.07.018.

[DPS05]   Marie Di Marco, Peter Peiffer, and Stefan Schönert. GERDA *scientific/technical report*. Technical Report GSTR-05-001, Max-Planck-Institut für Kernphysik (2005).

[EV02]   Steven R. Elliott and Petr Vogel. *Double beta decay*. Annual Review of Nuclear and Particle Science, 52 (2002), no. 1, 115–151. doi: 10.1146/annurev.nucl.52.050102.090641.

[F+01]   The Super-Kamiokande Collaboration: Y. Fukuda et al. *Solar ^8B and hep Neutrino Measurements from 1258 Days of Super-Kamiokande Data*. Phys. Rev. Lett., 86 (2001), 5651.

[FHI+96]   Y. Fukuda, T. Hayakawa, K. Inoue, et al. *Solar neutrino data covering solar cycle 22*. Phys. Rev. Lett., 77 (1996), no. 9, 1683–1686. doi: 10.1103/PhysRevLett.77.1683.

[FHI+99]   Y. Fukuda, T. Hayakawa, E. Ichihara, et al. *Measurement of the flux and zenith-angle distribution of upward throughgoing muons by super-kamiokande*. Phys. Rev. Lett., 82 (1999), no. 13, 2644–2648. doi:10.1103/PhysRevLett.82.2644.

[Fir96]   Richard B. Firestone. *Table of Isotopes* (Wiley-Interscience, 1996). Ebook.

[FLM+04]   G. L. Fogli, E. Lisi, A. Marrone, et al. *Observables sensitive to absolute neutrino masses: Constraints and correlations from world neutrino data*. Physical Review D (Particles and Fields), 70 (2004), no. 11, 113003. URL http://link.aps.org/abstract/PRD/v70/e113003.

[FM04]   J. A. Formaggio and C. J. Martoff. *Backgrounds to sensitive experiments underground*. Ann. Rev. Nucl. Part. Sci., 54 (2004), 361–412.

[FS98]   Amand Faessler and Fedor Simkovic. *Double beta decay*. Journal of Physics G: Nuclear and Particle Physics, 24 (1998), no. 12, 2139–2178. URL http://stacks.iop.org/0954-3899/24/2139.

[FSV03]   Ferruccio Feruglio, Alessandro Strumia, and Francesco Vissani. *Addendum to: "Neutrino oscillations and signals in [beta] and 0[nu]2[beta] experiments" [Nucl. Phys. B 637 (2002) 345]: First KamLAND results*. Nuclear Physics B, 659 (2003), 359–362.

[G+00]   D.E. Groom et al. *Review of particle physics*. Eur. Phys. J. C, 15 (2000), 1.

[GAL99]   W. Hampel et al. for the GALLEX collaboration. *GALLEX solar neutrino observations: results for GALLEX IV*. Phys. Lett. B, 447 (1999), 127–133.

[Gal05]   H. Gallagher. *Experimental Evidence for Atmospheric Neutrino Oscillations: MACRO, Soudan 2 and the Future*. Nuclear Physics B - Proceedings Supplements, 143 (2005), 79–86. doi:10.1016/j.nuclphysbps.2005.01.091.

[GER04]   I. Abt et al. for the GERDA collaboration. GERDA *The GERmanium Detector Array for the search of neutrinoless $\beta\beta$ decays of ^{76}Ge at LNGS* (2004). URL http://www.mpi-hd.mpg.de/ge76/.

[GER05]   I. Abt et al. for the GERDA collaboration. *Progress Report to the LNGS Scientific Commitee.* Technical report, GERDA collaboration (September 2005). URL `www.mpi-hd.mpg.de/ge76`.

[GER06]   I. Abt et al. for the GERDA collaboration. *Progress Report to the LNGS Scientific Commitee.* Technical Report LNGS-EXP 33/05 add. 3/06, GERDA collaboration (October 2006). URL `www.mpi-hd.mpg.de/ge76`.

[GMC$^+$03]   D. Gonzalez, J. Morales, S. Cebrian, et al. *Pulse shape discrimination in the igex experiment.* NUCL.INSTRUM.METH.A, 515 (2003), 634. URL `http://www.citebase.org/abstract?id=oai:arXiv.org:hep-ex/0302018`.

[GNO00]   M. Altmann et al. for the GNO collaboration. *GNO Solar neutrino observations: results for GNO I.* Phys. Lett. B, 490 (2000), 16–26.

[H. 04]   H. E. S. S. Collaboration: F. Aharonian. *Calibration of cameras of the h.e.s.s. detector.* Astroparticle Physics, 22 (2004), 109. URL `http://www.citebase.org/abstract?id=oai:arXiv.org:astro-ph/0406658`.

[H$^+$89]   (The Kamiokande Collaboration) H. Hirata et al. *Observations of ^8B solar neutrinos in the Kamiokande-II detector.* Phys. Rev. Lett., 63 (1989), 16.

[HDM92]   A. Hitachi, T. Doke, and A. Mozumder. *Luminescence quenching in liquid argon under charged-particle impact: Relative scintillation yield at different linear energy transfers.* Phys. Rev. B, 46 (1992), no. 18, 11463–11470. doi: 10.1103/PhysRevB.46.11463.

[Heu95]   G Heusser. *Low-radioactivity background techniques.* Annual Review of Nuclear and Particle Science, 45 (1995), no. 1, 543–590. doi: 10.1146/annurev.ns.45.120195.002551.

[HK00]   J. Hellmig and H. V. Klapdor-Kleingrothaus. *Identification of single-site events in germanium detectors by digital pulse shape analysis.* Nuclear Instruments and Methods in Physics Research A, 455 (2000), 638–644.

[HTF$^+$83]   Akira Hitachi, Tan Takahashi, Nobutaka Funayama, et al. *Effect of ionization density on the time dependence of luminescence from liquid argon and xenon.* Phys. Rev. B, 27 (1983), no. 9, 5279–5285. doi:10.1103/PhysRevB.27.5279.

[HTH$^+$81]   A. Hitachi, T. Takahashi, T. Hamada, et al. *Scintillation response of liquid argon to fission fragments.* Phys. Rev. B, 23 (1981), no. 9, 4779–4781. doi: 10.1103/PhysRevB.23.4779.

[HYDT87]   Akira Hitachi, Akira Yunoki, Tadayoshi Doke, et al. *Scintillation and ionization yield for α particles and fission fragments in liquid argon.* Phys. Rev. A, 35 (1987), no. 9, 3956–3958. doi:10.1103/PhysRevA.35.3956.

[JSD56]   P. S. Jastram, R. C. Sapp, and J. G. Daunt. *Angular correlation of gamma radiations from oriented nuclei.* Phys. Rev., 101 (1956), no. 4, 1381–1388. doi: 10.1103/PhysRev.101.1381.

[K⁺05]   C. Kraus et al. *Final results from phase II of the Mainz neutrino mass searchin tritium b decay.* The European Physical Journal C, 40 (2005), no. 4, 447–468. doi:10.1140/epjc/s2005-02139-7.

[KAA⁺07]   K. Kröninger, I. Abt, M. Altmann, et al. *Background reduction in neutrinoless double beta decay experiments using segmented detectors - A Monte Carlo study for the GERDA setup.* Nuclear Instruments and Methods A, 570 (2007), 479–486.

[KGW74]   J. W. Keto, R. E. Gleason, and G. K. Walters. *Production mechanisms and radiative lifetimes of argon and xenon molecules emitting in the ultraviolet.* Phys. Rev. Lett., 33 (1974), no. 23, 1365–1368. doi:10.1103/PhysRevLett.33.1365.

[KHSR79]   Shinzou Kubota, Masahiko Hishida, Masayo Suzuki, et al. *Dynamical behavior of free electrons in the recombination process in liquid argon, krypton, and xenon.* Phys. Rev. B, 20 (1979), no. 8, 3486–3496. doi:10.1103/PhysRevB.20.3486.

[KKBH⁺99] H. V. Klapdor-Kleingrothaus, L. Baudis, G. Heusser, et al. *Genius - a supersensitive germanium detector system for rare events* (1999). URL http://www.citebase.org/abstract?id=oai:arXiv.org:hep-ph/9910205.

[KKDB⁺01] H.V. Klapdor-Kleingrothaus, A. Dietz, L. Baudis, et al. *Latest results from the heidelberg-moscow double beta decay experiment.* The European Physical Journal A - Hadrons and Nuclei, 12 (2001), 147–154. doi:10.1007/s100500170022.

[KKDKC04] H. V. Klapdor-Kleingrothaus, A. Dietz, I. V. Krivosheina, et al. *Data Acquisition and Analysis of the 76Ge Double Beta Experiment in Gran Sasso 1990-2003.* NUCL.INSTRUM.METH.A, 522 (2004), 371. URL http://www.citebase.org/abstract?id=oai:arXiv.org:hep-ph/0403018.

[KKKC04]   H.V. Klapdor-Kleingrothaus, I.V. Krivosheina, and O. Chkvorets. *Search for neutrinoless double beta decay with enriched ^{76}Ge in Gran Sasso 1990-2003.* Physics Letters B, 586 (2004), 198–212. doi:10.1016/j.physletb.2004.02.025.

[KL05]   K. Kröninger and X. Liu. *Initial results from the GERDA Monte Carlo Simulation of internal background - Update 1.* Technical Report GSTR-05-019, GERDA collaboration (November 2005). URL www.mpi-hd.mpg.de/ge76/internal.

[KLM06]   K. Kröninger, X. Liu, and B. Majorovits. *A Method for Selecting Single- and Multi-site events.* Technical Report GSTR-06-014, GERDA collaboration (March 2006). URL www.mpi-hd.mpg.de/ge76/internal.

[KSR80]   Shinzou Kubota, Masayo Suzuki, and Jian-zhi Ruan(Gen). *Specific-ionization-density effect on the time dependence of luminescence in liquid xenon.* Phys. Rev. B, 21 (1980), no. 6, 2632–2634. doi:10.1103/PhysRevB.21.2632.

[LMP01]   Thierry Lasserre, Dario Motta, and Peter Peiffer. *A multi-purpose data acquisition system for the lens pilot phase* (2001). Internal document.

[Lob02]   V.M. Lobashev. *Study of the tritium beta-spectrum in experiment Troisk-ν-mass.* Progress in Particle and Nuclear Physics, 48 (2002), 123–131. doi:10.1016/S0146-6410(02)00118-7.

[Mai96]   Bernhard Maier. *Der Ausbau des Heidelberg-Moskau Doppelbetaexperimentes auf fnf angereicherte 76Ge-Detektoren und quantitative Beschreibung des Untergrundes.* Ph.D. thesis, Universität Heidelberg (1996).

[Maj03]   The Majorana collaboration. *White paper on the majorana zero-neutrino double-beta decay experiment* (2003). URL `http://www.citebase.org/abstract?id=oai:arXiv.org:nucl-ex/0311013`.

[Mar71]   Marlo Martin. *Exciton self-trapping in rare-gas crystals.* The Journal of Chemical Physics, 54 (1971), no. 8, 3289–3299. URL `http://link.aip.org/link/?JCP/54/3289/1`.

[MEM96]   F. Masetti, F. Elisei, and U. Mazzucato. *Optical study of a large-scale liquid-scintillator detector.* Journal of Luminescence, 68 (1996), 15–25.

[Min07]   Aguilar-Arevalo et al. for The MiniBooNe Collaboration. *A Search for Electron Neutrino Appearance at the Δm^2 1 eV^2 Scale* (April 2007). To be submitted; url=http://www-boone.fnal.gov/publicpages/prl8.pdf.

[MKK99]   B. Majorovits and H. V. Klapdor-Kleingrothaus. *Digital pulseshape analysis by neural networks for the heidelberg-moscow-double-beta-decay-experiment.* European Physical Journal A, 6 (1999), 463. URL `http://www.citebase.org/abstract?id=oai:arXiv.org:hep-ex/9911001`.

[MNS62]   Ziro Maki, Masami Nakagawa, and Shoichi Sakata. *Remarks on the Unified Model of Elementary Particles.* Progress of Theoretical Physics, 28 (1962), no. 5, 870–880.

[Mot04]   Dario Motta. *Feasibility Analysis and Prototype Measurements of a Novel Approach for the Real-Time Spectroscopy of Low Energy Solar Neutrinos.* Ph.D. thesis, University of Heidelberg (May 2004).

[MS80]   Rabindra N. Mohapatra and Goran Senjanovic. *Neutrino mass and spontaneous parity nonconservation.* Phys. Rev. Lett., 44 (1980), no. 14, 912–915. doi: 10.1103/PhysRevLett.44.912.

[MS85]   S.P. Mikheyev and A.Y. Smirnov. *Resonance enhancement of oscillations in matter and Solar Neutrino spectroscopy.* Soviet Journal of Nuclear Physics, 42 (1985), 913–917.

[MTK+74]   M. Miyajima, T. Takahashi, S. Konno, et al. *Average energy expended per ion pair in liquid argon.* Phys. Rev. A, 9 (1974), no. 3, 1438–1443. doi: 10.1103/PhysRevA.9.1438.

[Mul70]   Robert S. Mulliken. *Potential curves of diatomic rare-gas molecules and their ions, with particular reference to xe[sub 2].* The Journal of Chemical Physics, 52 (1970), no. 10, 5170–5180. URL `http://link.aip.org/link/?JCP/52/5170/1`.

[NPRS69]   S. Notarrigo, F. Porto, A. Rubbino, et al. *Experimental and calculated energy spectra of Am-Be and Pu-Be neutron sources.* Nuclear Phsysics A, 125 (1969), 28–32.

[Ons38]   L. Onsager. *Initial recombination of ions.* Phys. Rev., 54 (1938), no. 8, 554–557. doi:10.1103/PhysRev.54.554.

[Pan06]   Luciano Pandola. *Study of the muon-induced background in the GERDA backup design with stainless-steel cryostat*. Technical Report GSTR-06-013, GERDA collaboration (April 2006). URL `www.mpi-hd.mpg.de/ge76/internal`.

[PCF04]   L. Pandola, C. Cattadori, and N. Ferrari. *Neural network pulse shape analysis for proportional counters events*. Nuclear Instruments and Methods A, 522 (2004), 521–528. doi:10.1016/j.nima.2003.12.003.

[PMSS05]   P. Peiffer, D. Motta, S. Schönert, et al. *Operation of bare HP-Germanium detectors in liquid argon (LAr)*. Nucl. Phys. B - Proc. Suppl., 143 (2005), 511.

[Pol07]   Tina Pollmann. *Diploma thesis* (2007). To be published, University of Heidelberg.

[Pon46]   B. Pontecorvo. *Inverse β process*. Technical Report PD205, Chalk River Laboratory (1946). Reprinted in *B. Pontecorvo - Selected Scientific Works*, Societa Italiana di Fisica (1997), 21.

[Pon57]   B. Pontecorvo. *Mesoniums and antimesoniums*. J.Exp.Theoret.Phys., 33 (1957), 549. English translation: Sov.Phys.-JETP 6 (1958) 429.

[PR59]   H. Primakoff and S.P. Rosen. *Double Beta Decay*. Rep. Progr. Phys., 22 (1959), 121.

[PTZ00]   O. A. Ponkratenko, V. I. Tretyak, and Yu. G. Zdesenko. *Event generator decay4 for simulating double-beta processes and decays of radioactive nuclei*. Physics of Atomic Nuclei, 63 (2000), 1282–1287. doi:10.1134/1.855784.

[RC$^+$56] F. Reines, C.L. Cowan, et al. *Detection of the free neutrino: A confirmation*. Science, 124 (1956), 103.

[RCP05]   Nitin Rathore, Manan Chopra, and Juan J. de Pablo. *Optimal allocation of replicas in parallel tempering simulations*. The Journal of Chemical Physics, 122 (2005), no. 2, 024111. URL `http://link.aip.org/link/?JCP/122/024111/1`.

[RFSV03]   V. A. Rodin, Amand Faessler, F. Simkovic, et al. *Uncertainty in the $0\nu\beta\beta$ decay nuclear matrix elements*. Phys. Rev. C, 68 (2003), no. 4, 044302. doi: 10.1103/PhysRevC.68.044302.

[SA00]   Jr Robert C. Singleterry and Thibeault Sheila A. *Materials for low-energy neutron radiation shielding*. Technical report, National Aeronautics and Space Administration - NASA (2000).

[SAG99]   J.N. Abdurashitov et. al. for the SAGE collaboration. *Measurement of the solar neutrino capture rate by SAGE and implications for neutrino oscillations in vacuum*. Phys. Rev. Lett., 83 (1999), 4686–4689.

[SAG02]   J.N. Abdurashitov et. al. for the SAGE collaboration. *Solar neutrino flux measurements by the soviet-american gallium experiment (sage) for half the 22-year solar cycle*. Journal of Experimental and Theoretical Physics, 95 (2002), 181–193. doi:10.1134/1.1506424.

[Sch03]   Stefan Schönert. *Multi Purpose Detectors/Targets for Low Energy Particle and AstroPhysics (LEPAP)* (November 2003). Talk at Journees Neutrinos, Paris.

[Sch05] Stefan Schönert. *Low energy neutrino and cold dark matter detection.* In *Proceedings of the International Conference on the SeeSaw Mechanism* (World Scientific, 2005), pages 195–206. SeeSaw 25, Paris 2004.

[SHRK93] M. Suzuki, M. Hishida, J. Ruan(Gen), et al. *Light output and collected charge in xenon-doped liquid argon.* Nuclear Instruments and Methods in Physics Research A, 327 (1993), 67–70. doi:10.1016/0168-9002(93)91412-G.

[Sim05] Hardy Simgen. *Adsorption techniques for gas purification.* In Bruce Cleveland, Richard Ford, and Mark Chen (editors), *TOPICAL WORKSHOP ON LOW RA-DIOACTIVITY TECHNIQUES: LRT 2004*, volume 785 (AIP, 2005), pages 121–129. URL http://link.aip.org/link/?APC/785/121/1.

[SVP+03] D. N. Spergel, L. Verde, H. V. Peiris, et al. *First year wilkinson microwave anisotropy probe (wmap) observations: Determination of cosmological parameters.* The Astrophysical Journal, 148 (2003), 175. URL http://www.citebase.org/abstract?id=oai:arXiv.org:astro-ph/0302209.

[TF37] I.E. Tamm and I.M. Frank. *Coherent radiation of fast electrons in a medium.* Dokl. Akad. Nauk. SSSR, 14 (1937), 107.

[WJRv04] H. Wulandari, J. Jochum, W. Rau, et al. *Neutron flux at the gran sasso underground laboratoryrevisited.* Astroparticle Physics, 22 (2004), 313. URL http://www.citebase.org/abstract?id=oai:arXiv.org:hep-ex/0312050.

[Wol78] L. Wolfenstein. *Neutrino oscillations in matter.* Phys. Rev. D, 17 (1978), 2369–2374.

[ZPT01] Yu G. Zdesenko, O. A. Ponkratenko, and V. I. Tretyak. *High sensitivity gem experiment on double beta decay of 76-ge.* J.PHYS.G, 27 (2001), 2129. URL http://www.citebase.org/abstract?id=oai:arXiv.org:nucl-ex/0106021.

Acknowledgements

Addendum

On page 10 and all other occurrences the phrase:
There is a claim of a 4.2 σ evidence ... by a part of the Heidelberg-Moscow (HdM) collaboration ...

is replaced by the phrase:
There is a claim of a 4.2 σ evidence ... by the remaining part of the Heidelberg-Moscow (HdM) collaboration ....

Also on page 10 the corresponding paragraph:
There is a claim of a 4.2 σ evidence for a detection of the $0\nu\beta\beta$ decay of ^{76}Ge by a part of the Heidelberg-Moscow (HdM) collaboration [KKKC04]. However, these results are still under debate ([BBB$^+$05]) and need to be checked by an independent experiment.

is changed to:
There is a claim of a 4.2 σ evidence for a detection of the $0\nu\beta\beta$ decay of ^{76}Ge by the remaining part of the Heidelberg-Moscow (HdM) collaboration [KKKC04]. However, the former members of the Moscow-part of the HdM collaboration found no such evidence [BBB$^+$05]. The issue is still under debate [Fio06] and needs to be checked by an independent experiment.

Bibliography addendum

[Fio06]   E.Fiorini, *Double beta decay: experiments*, Journal of Physics: Conference Series, 39 (2006), 243-249